A photometric survey of the Small Magellanic Cloud

Ki Won LEE

Thesis submitted for the Degree of Doctor of Philosophy
of the University of London

Department of Physics & Astronomy
UNIVERSITY COLLEGE LONDON

December 2005

ProQuest LLC
789 East Eisenhower Parkway
P.O. Box 1346
Ann Arbor, MI 48106-1346

To my parent, sisters and brother

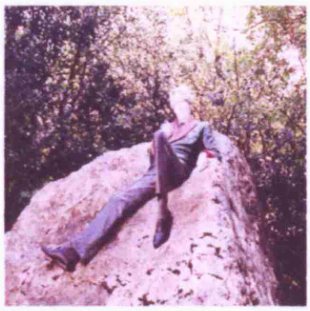

We are all in the gutter, but some of us are looking at the stars.

Oscar Wilde *(1854 - 1900).*

This is not the end. It is not even the beginning of the end. But it is, perhaps, the end the of the beginning.

Winston Churchill *(1874 - 1965).*

Abstract

The initial mass function (IMF) is defined as the fraction or number of stars born per unit mass interval and is the one of key parameters in astronomy. Since Salpeter (1955)'s work, there have been many studies, and most of them show the universality of the IMF regardless of systems, mass ranges, and metallicity within observational errors, although recently there are some suggestions of its variation. The main aim of this thesis is to test the IMF universality, based on a photometric study of the SMC.

In order to study the IMF of massive stars and the star formation history, we perform a BVR photometric survey of the Small Magellanic Cloud (SMC), chosen for its proximity and low metallicity. The observational data were acquired at Siding Spring Observatory, Australia during the 5 - 11 September & 26 - 31 October 2001 and 9 - 17 November 2002, covering essentially the whole SMC area. Details of the instruments, characteristics of each run, and the procedures of data reduction are presented. We catalogued 0.76 million SMC stars brighter than 18 magnitude in B from total 1.3 millions. Regarding to the accuracy, we found 0.1 arcsecond in astrometry and 0.1 magnitude at B and V and 0.2 at R in photometry.

Together with spectroscopic data, we investigate the basic parameters of the SMC such as colour excess, reddening and distance modulus, and compare them with other studies. Based on these parameters, we study the IMF and star formation histories using population synthesis techniques. In contrast to other authors, we transform the theoretical quantities into observable ones, and use Bayesian inference in the comparison of the various IMF models. The procedures and background concepts for the generation of models incorporating the same constraints as observed samples, are also described.

According to model calculations, a continuous star formation model with an IMF slope of -1.6 offers the best representation of the SMC stars. Therefore we suggest that our result is one of the implications for the variation of the IMF, at least for hot stars.

Acknowledgements

The work presented here would not have been possible without the help of many people. First and most importantly, I deeply would like to thank my supervisor, Ian Howarth, for his guidance and long-standing patience until data reduction is over. In addition to his academic teaching and advise, I had been greatly benefitted from his careful concerns to finish my course and to live in here. My thanks also go to Raman Prinja for reading my thesis and giving many good suggestions, and to Mike Barlow for giving kind advise when I applied to PhD course. I must thank Chris Evans, was a second supervisor, for his practical assistance and corrections for the better English expressions. Furthermore, I would like to thanks to A25 society; to Rich Townsend for his vast knowledge of computer skills, to Adam for giving detailed explanations whatever I asked, to Fab and Mark for their good favours and kindness. Other notable mentions include the past and present astronomy group guys, namely Rich Price, Tammay, Barbara, Rich Norris, Jay, Roger, Sam Thompson, Durgan, Rob, Jo, Sam Searle, and Sarah.

Considering financial, I am deeply appreciate to Korean government for supporting the three year postgraduate studies and to Perren who granted a scholarship to a strange overseas student. As well, I many thanks to Department funding for supporting the final months of my writing up period.

A special thanks should go to Regent Park for being there. Whenever I feel alone or I was stuck, it was alway there and make me comfortable.

Finally, endless thanks to my parent, sisters and brother for their love and encouragement. Without their support, there is not what I am. Again huge thanks, Mum.

Contents

List of Figures

List of Tables

CHAPTER 1

Introduction

The main property which determines the fate of a star is its mass, although other factors such as metallicity, mass-loss rate, rotation and magnetic field strength play a role (Maeder and Meynet, 2003, 2004). Once the mass of star is known, we can, in principle, estimate such quantities as luminosity, radius, and effective temperature at any phase of stellar evolution, with the distribution of masses giving clues to understanding galaxy evolution. The accurate determination of the initial mass function (hereafter IMF) and its variation in space and time provides fundamental constraints on star formation in the Galaxy and external galaxies, dynamical evolution of stellar clusters, and the chemical evolution of the universe.

In a pioneering work, Salpeter (1955) investigated the IMF in the solar neighbourhood, finding a value of $\Gamma = -1.35$ (refer to section 1.2 for the definition of Γ). Since then, there have been advances in this subject from the development of data reduction techniques (*e.g.* DAOPHOT), observational facilities (*e.g.* single or mosaic CCDs), and new theoretical works (*e.g.* using new radiative opacities and consideration of convection and overshooting). Although recently there is some evidence for the variation of the IMF (Evans, 2001; Kroupa, 2001), most studies still appear to show universality, even in different environments (Kennicutt, 1998).

Turning to the study of the Small Magellanic Cloud (SMC), Humphreys (1983) studied the luminous-star population in this very metal-poor galaxy and constructed a luminosity function which showed a steeper function for the highest luminosities (and therefore the highest masses). Laney and Stobie (1986) performed infrared photometry and found a

distance modulus of 19.05. More recently, Hill *et al.* (1994*a*,*b*,*c*) used UBV photometry of stars in 14 associations in the Magellanic Clouds to derive the IMF and presented an average slope of $\Gamma = -2.0 \pm 0.5$ for $M > 9m_{\odot}$ with the conclusion that there is no strong evidence for a significant variation in the slopes from one association to another. Massey *et al.* (1995*c*) also investigated the massive star populations of the Magellanic Clouds, with an emphasis on the field population, and found that the slope of the field-stars IMF is very steep, $\Gamma = -4.1 \pm 0.2$ and $\Gamma = -3.7 \pm 0.5$ for the LMC and SMC respectively. As well, Evans (2001) suggests $\Gamma = -3.2 \pm 0.3$ based on his 2dF spectroscopic data analysis for the whole SMC area. However, Hill *et al.* (1994*a*) and Massey *et al.* (1995*c*) observed only in selected regions of the SMC, while Evans (2001) derived the IMF from only spectroscopic data. Uncertainties in relating the spectroscopic sample to the total population was a significant stumbling block for Evans (2001).

Therefore, we have performed a BVR photometric survey, for the whole of the SMC, to accurately determine the slope of the IMF, as a step to testing its universality.

1.1 Aim of thesis

As mentioned above, Massey *et al.* (1995*c*) studied the IMF of massive stars in the field and associations of the SMC. They found the slope of the IMF of the field stars in the SMC to be very steep, $\Gamma = -3.7 \pm 0.5$, compared with $\Gamma = -1.3 \pm 0.3$ for the associations. Also in the same paper, they presented the need for spectroscopic data in determination of the IMF for hot stars. Generally the major source of uncertainties in determination of the massive star IMF arises through poor sampling of stars and the absence of spectroscopic data.

Evans (2001) conducted a spectroscopic survey of the SMC using 2dF and completed MK classification of over 4000 stars. He analyzed the results for the slope of the IMF and his provisional result was $\Gamma = -3.2 \pm 0.3$. It seems to support the Massey *et al.* (1995*b*) result of $\Gamma = -3.7 \pm 0.5$ in field SMC stars. As he pointed out, however, the spectroscopic data have relatively poor photometry because he used Automatic Plate Measuring (APM) data from the photographic survey plates of UK Schmidt (UKST). One important consequence was that the relationship of the spectroscopic sample to the full sample was not defined precisely.

The aim of this thesis is to undertake a precise determination of the IMF for massive

stars in a very metal-poor environment, the SMC, using a large photometric survey to ascertain the completeness of the spectroscopic data.

1.2 The Initial Mass Function

The IMF, $\phi(m)$ is defined as the fraction or number of stars born per unit mass interval dm at birth. In practical applications, the most commonly adopted form is the power law distribution:

$$\phi(m) = \phi_0 m^{\gamma}. \tag{1.1}$$

It is convenient in practice to replace the IMF $\phi(m)$, by $\xi(\log m)$ which gives the fraction or number of stars born per unit logarithmic (base ten) mass interval $d\log m$ at birth (*e.g.*, Salpeter, 1955). The relation between two functions

$$\xi(\log\, m)d\log m = \phi(m)dm \tag{1.2}$$

so,

$$\xi(\log\, m) = (\ln 10)m\phi(m) = \xi_0 m^{\gamma+1} = \xi_0 m^{\Gamma}. \tag{1.3}$$

where $\gamma = \Gamma - 1$. In this equation, the IMF found by Salpeter is $\Gamma = -1.35$ or $\gamma = -2.35$.

It is difficult to estimate the IMF, even in the solar neighbourhood, although the equations appear simple. Prior to determining the IMF, we should know about the present-day mass function (PDMF) and the star formation rate (SFR). A primary method to determine the PDMF is to obtain the luminosity function (LF) and convert it into the mass function using a known mass-luminosity relation (MLR), with corrections for evolved stars, metallicity variation, binarity and so on. However, the uncertainties of the MLR increase toward upper (and/or lower) end of the range of stellar masses. So a different method to determine the PDMF for the massive stars is to construct a theoretical Hertzsprung-Russell diagram with sample stars and then count the number of stars between theoretical evolutionary tracks computed for models with different masses. The IMF is then derived from the PDMF and SFR. Although a constant SFR is preferred, the SFR is less certain than the MLR.

The IMF is one of the fundamental parameters in studies of star formation and evolution in the Galaxy and external galaxies. In general, IMF studies focus on targets such

as the field population, clusters and associations, and on different mass ranges. In the following subsection we give a brief introduction of recent studies of the IMF with respect to mass ranges. In regard to the IMF, excellent reviews have been given by Miller and Scalo (1979) and by Scalo (1986). Some further studies can be found in Gilmore and Howell (1998).

1.2.1 The IMF of low-mass stars

The low-mass range deals with stars from $0.1m_{\odot}$ to $1.2m_{\odot}$. Because of the low luminosities, most IMF studies in this range are limited to nearby stars. Using an empirical mass-M_V relation for the stellar samples within 5.2 parsecs of the Sun, Kroupa *et al.* (1993) found that the IMF can be well approximated by power laws divided into three mass ranges (see Table 1.1). Méra *et al.* (1996) found a similar IMF slope ($\Gamma \sim -1 \pm 0.5$) for $m < 0.6m_{\odot}$, from the same sample but using a theoretical MLR. Based on the analysis of WFPC2 data on HST, Gould *et al.* (1997) showed a change of the IMF slope at $0.6m_{\odot}$, from a near-Salpeter IMF of $\Gamma = -1.21$ to $\Gamma = 0.44$. However, Scalo (1998) suggested that the break in the IMF index at $m \sim 0.6m_{\odot}$ is caused by the uncertainty of the MLR; in this mass range, stars are too young to be on the main sequence, so the significant fraction of pre-main sequence stars with an uncertain age distribution introduces a poorly-defined MLR. On the other hand, Reid and Gizis (1997) compiled parallax samples within 8 parsecs of the Sun, covering 106 systems, and found a slightly shallower IMF ($\Gamma \sim 0$) in the range $0.1m_{\odot} < m < 1.0m_{\odot}$ with evidence for a decline ($\Gamma > 0$) below $0.1m_{\odot}$, but no evidence for a steeper IMF ($\Gamma = -1.2$) in the $0.5 \sim 1m_{\odot}$ mass range, such as that found by Kroupa *et al.* (1993). Despite much debate, it therefore seems that there is some convergence in the sense that most recent estimates give $\Gamma = 0$ to -0.5 for the lowest mass range.

1.2.2 The IMF of intermediate mass stars

In general, the intermediate mass range is considered to be $1m_{\odot} < m < 15m_{\odot}$. In this range, the study of the IMF for clusters has many advantages because the main sequence is well defined, the MLR is well understood, the effect of unresolved binaries is less severe and the SFR is less uncertain. For these reasons, there have been a large number of studies on the open-cluster IMFs in this mass range; *e.g.*, Phelps and Janes (1993) estimated the IMF for 8 open clusters and found $\Gamma = -1.40 \pm 0.13$ over the mass range $1.4m_{\odot} < m < 7.9m_{\odot}$. A number of recent IMF studies for this mass range has been

devoted to clusters and associations in the LMC. Sagar and Richtler (1991) estimated IMFs for five LMC clusters, with a reasonably large number of mass bins, and found an average $\Gamma = -1.1$ for $2m_{\odot} < m < 14m_{\odot}$. They also found that the IMF was steeper by 0.3 when the sample was corrected for incompleteness. Subramaniam and Sagar (1995) compared Γs for four LMC clusters using different types of evolutionary models and suggested that the uncertainties with respect to different models are quite large, up to 0.55 in Γ. Scalo (1998) concluded that the LMC clusters can be fit by a single power, $\Gamma = -1.5$; however it is not possible to say at present whether or not there is a significant difference between the IMF of Galactic and LMC clusters in this mass range.

1.2.3 The IMF of high-mass stars

Massive stars are usually considered to be those with masses greater than $10 \sim 15m_{\odot}$. However, there is no clear upper limit (although the Pistol star is considered to be one of the most massive stars, $\sim 200m_{\odot}$; Figer *et al.*, 1998). The IMF of massive stars is the most difficult to determine for several reasons: Firstly, because of their short life time on the main sequence they are relatively rare; and from the very definition of the IMF there are also fewer of them, so there are poor statistics involved in the determination of the IMF. Second, there are no well-defined MLRs because the bolometric correction is a very steep function of effective temperature, and because the stars evolve to cooler temperatures; that is, stars at a given M_V represent a mixture of masses. Lastly, as Massey *et al.* (1995*c*) pointed out, spectroscopic data are required due to the degeneracy of the near-UV and optical colours at high temperatures.

Garmany *et al.* (1982) determined gradients of the IMF slope for O-type stars in the disc of the Milky Way (MW); $\Gamma = -1.3$, and $\Gamma = -2.1$, inwards and outwards of the solar circle respectively. Massey *et al.* (1995*b*,*c*) summarised their results for massive stars in clusters and associations in the MW and the Magellanic Clouds (MCs) and found no difference in the IMF slopes between the MW and MCs, suggesting universality of the IMF, and specifically no effect of metallicity in the IMF for high-mass stars. However, for massive field stars in the MCs, Massey *et al.* (1995*c*) derived a very steep IMF, with Γ between -3 and -4. More recently, Evans (2001) also suggested a steep IMF for field hot stars in the SMC: $\Gamma = -3.8 \pm 0.4$, implying non-universality of IMF.

1.2.4 A summary of the IMF slope

It is half a century since Salpeter's (1955) study, but the value of the IMF slope in different environments is still very uncertain. There are no known reasons that the IMF should be universal, although there are suggestions on the three-fold IMF due to distinct physical processes during the star formation (Elmegreen, 2004). However, most recent studies appear to show a universal IMF within the relevant uncertainties, *i.e.*, a Salpeter slope ($\Gamma \sim -1.3$), regardless of mass ranges, metallicities, and environment, although some studies do suggest evidence for variations of the IMF in the extreme mass bins. In Table 1.1, we summarises the IMF studies mentioned in this section.

1.3 The Small Magellanic Cloud

Because of its brightness in apparent magnitude ($m_v = 2.3$), the SMC was certainly known to the ancient southerner. However, it became known to us following Magellan in 1519. The equatorial coordinates of the SMC are $\alpha = 00^h : 52^m : 00^s$, $\delta = -72^d : 50^m : 00^s$ and it covers about 280 × 160 arcmin on the sky.

The SMC is an irregular dwarf galaxy in the southern constellation of Tucana, and the main body of the SMC was designated NGC 292 in the New General Catalogue. With the Large Magellanic Cloud (LMC), the SMC is a satellite galaxy to the Milky Way. The true distance modulus of the SMC is reported as 18.9 (van den Bergh, 2000) or 19.1 (Massey *et al.*, 1995*c*; Jacoby *et al.*, 1990). Recently Harries *et al.* (2003) and Hilditch *et al.* (2005) published a precise distance modulus of the SMC, 18.91, from the studies of eclipsing binaries.

It was Arp (1962) who first noted that the SMC has a different metallicity compared to the solar neighbourhood. According to Lequeux *et al.* (1979), the metallicity of the SMC is $Z_{SMC} = 0.1 Z_{\odot}$. Because of its proximity and low metallicity, there have been many studies of the SMC. For example, Azzopardi and Vigneau (1975) presented a catalogue of 506 SMC stars, subsequently updated and expanded to contain 524 stars including UBV and spectroscopic data (Azzopardi and Vigneau, 1982). Schaller *et al.* (1992) and Maeder and Meynet (2001) calculated grids of stellar models with a metallicity that is appropriate for the SMC. More recently, Evans (2001) used intermediate-resolution 2dF spectroscopy to classify 4054 stars in the MK system, and Zaritsky *et al.* (2002) presented a $UBVI$ photometric survey of the central 18 deg^2 of the SMC. Now the SMC is one of the most

Table 1.1: The summary of the IMF slopes (Γ) discussed here.

Reference	index (Γ)	Mass range	Remark
Salpeter (1955)	-1.35	$0.4\ m_\odot < \mathrm{m} < 10\ m_\odot$	solar neighborhood
Garmany *et al.* (1982)	-1.3	$\mathrm{m} > 20\ m_\odot$	inside of solar circle
	-2.1	m	outside of solar circle
Scalo (1986)	-1.45	$\mathrm{m} > 10\ m_\odot$	
	-2.27	$1\ m_\odot < \mathrm{m} < 10\ m_\odot$	
	-0.83	$\mathrm{m} < 0.2\ m_\odot$	
Sagar and Richtler (1991)	-1.1	$2\ m_\odot < \mathrm{m} < 14\ m_\odot$	5 LMC clusters
Kroupa *et al.* (1993)	-3.7	$\mathrm{m} > 1\ m_\odot$	within 5.2 pc of the Sun
	-1.2	$0.5\ m_\odot < \mathrm{m} < 1\ m_\odot$	
	-0.2	$\mathrm{m} < 0.5\ m_\odot$	
Phelps and Janes (1993)	-1.40 ± 0.13	$1.4\ m_\odot < \mathrm{m} < 7.9\ m_\odot$	8 open clusters
Massey *et al.* (1995*b*,*c*)	$-1.1 \pm 0.1 / -1.3 \pm 0.3$	$\mathrm{m} > 7\ m_\odot$	associations in MW / MCs
Massey *et al.* (1995*c*)	$-4.1 \pm 0.2 / -3.7 \pm 0.5$	$\mathrm{m} > 15\ m_\odot$	field stars in LMC / SMC
Méra *et al.* (1996)	-1.0 ± 0.5	$\mathrm{m} < 0.6\ m_\odot$	within 5.2 pc of the Sun
Reid and Gizis (1997)	-0.05	$0.1\ m_\odot < \mathrm{m} < 1\ m_\odot$	within 8 pc of the Sun
Gould *et al.* (1997)	-1.21	$\mathrm{m} > 0.6\ m_\odot$	Groth Strip
	0.44	$\mathrm{m} < 0.6\ m_\odot$	
Evans (2001)	-3.2 ± 0.3	$\mathrm{m} > 10\ m_\odot$	SMC

well-studied galaxies, but there is still debate concerning its structure, the evolutionary status, the effect of lower metallicity, and so on. More general reviews of the SMC can be found in van den Bergh (2000) and Westerlund (1997).

1.4 Photometric Systems

Our study is fundamentally a photometric one, so we outline the important underlying principles here. Photometric systems are classified by their effective wavelength $\lambda_{\rm eff}$ as defined in Equation 1.4 and bandpass, $\Delta\lambda$ ($= \lambda_2 - \lambda_1$).

$$\lambda_{\rm eff} = \frac{\int_{\lambda_1}^{\lambda_2} \lambda E(\lambda) S(\lambda) d\lambda}{\int_{\lambda_1}^{\lambda_2} E(\lambda) S(\lambda) d\lambda} \tag{1.4}$$

where $S(\lambda)$ is a response curve and $E(\lambda)$ is a spectral energy distribution; λ_1 and λ_2 are the lower and upper wavelength limits for the response curve, defined as full width at half maximum, respectively. According to the bandwidths, in general, there are three main types of system: wide ($\Delta\lambda \simeq$ 100nm), intermediate ($\Delta\lambda \simeq$ 10nm), and narrow ($\Delta\lambda \simeq$ 1nm) band.

1.4.1 Wide band systems

A commonly used wide band system is the UBV system – ultraviolet (U), blue (B), and visual (V) – developed by Johnson and Morgan (1953) to complement the visual classification of stellar spectra in the MK system. The B and V regions correspond to the photographic and visual responses, and the U region is violet and (ground-based) ultraviolet. All three filters are scaled such that the colours for unreddened A0 V stars (*e.g.* Vega) are zero. It was extended into the red (R) and infrared (I) by Johnson and colleagues, and revised definition of RI passbands have been proposed by Kron and Cousins.

In order to clarify the filter system used in R and I, usually J (Johnson) and C (Cousins) subscripts are used. Cousins (1980) provided transformation equations between his system and Johnson's which is valid for stars earlier than M type:

$$\begin{aligned} (V-R)_C &= 0.715(V-R)_J - 0.02 \\ (V-I)_C &= 0.77(V-I)_J + 0.01 \end{aligned} \tag{1.5}$$

Bessell (1983) extended these transformation equations into the far red, for M dwarfs and giants:

$$\begin{aligned}(V-R)_C &= 0.6(V-R)_J + 0.12 \\ (R-I)_C &= 1.045(R-I)_J - 0.094 \end{aligned} \tag{1.6}$$

The advent of CCDs and requirements of astrophysics have led to several new photometric systems, but the UBV system is still widely in use. Not only do its colour indices give information on interstellar extinction and on stellar temperatures over a wide range of magnitudes, but it also has many well-established standard stars such as the Landolt standards (Landolt, 1983, 1992) around the celestial equator, and E-region standard stars (Menzies *et al.*, 1989) in southern hemisphere. Menzies *et al.* (1991) pointed out that there are small differences between the Landolt and E-region standards, and Bessell (1995) showed how to transform between them.

The $JHKLM$ photometric system, based on the conception of Johnson's near infrared photometric system, is an extension of the UBV system into the infrared region. Elias *et al.* (1982) published $JHKL$ standard stars and Koornneef (1983) has provided intrinsic colours for main sequence, giant, and supergiant stars in infrared indices: $(V-K)$, $(J-K)$, $(H-K)$, $(K-L)$, and $(K-M)$.

In Table 1.2, we summarises the effective wavelengths and bandpasses of the wide band $UBVRIJHKLM$ system (from Kitchin, 2003).

At present, wide band infrared and optical photometric systems have reached a level of comparability so reliable intrinsic colour indices can be determined on a subset of the wide band $UBVRIJHKLM$ system.

As large data sets become available due to the development of astronomical instruments, two other wide band filter systems, those of the Hubble Space Telescope (HST) and the Sloan Digitial Sky Survey (SDSS), are now widely in use as well.

1.4.2 Intermediate band systems

Among the intermediate pass band systems, the most widespread is Strömgren-Crawford $uvby\beta$ system (Strömgren, 1963, 1966; Crawford, 1966). The filters were devised in order to give better discriminations of stellar temperatures, gravities, and metallicities compared to wide band systems. The specifications for the $uvby\beta$ system are given in Table 1.3 (from Hilditch, 2001). The u bandwidth is below the Balmer discontinuity and above

Table 1.2: The effective wavelengths and bandpasses of the wide band $UBVRIJHKLM$ system.

Band	Effective Wavelength (λ_{eff})	Bandpass ($\Delta\lambda$)
U	365 nm	70 nm
B	440 nm	100 nm
V	550 nm	90 nm
R_J	700 nm	220 nm
I_J	900 nm	240 nm
J	1220 nm	213 nm
H	1630 nm	307 nm
K	2190 nm	390 nm
L	3450 nm	472 nm
M	4750 nm	460 nm

Table 1.3: The specifications for the $uvby\beta$ system.

Filter name	Symbol	λ_{eff} (nm)	$\Delta\lambda$ (nm)	Filter type
Ultraviolet	u	350	38	glass
Violet	v	410	20	interference
Blue	b	470	20	interference
Yellow	y	550	20	interference
Narrow β		486.1	3	interference
Wide β		486.1	10	interference

the atmospheric cut-off so it differs significantly from U in UBV system. The v band is selected to include the Fe I and II absorption lines and to be above the region of crowding of the hydrogen lines except $H\delta$ so it provides an indicator of the metallicity. The b band is centred at 470 nm, longward of B, in order to avoid the blanketing effects of the metal lines. The y band measures the continuum in the yellow region of the spectrum and can be easily transformed into V magnitude of the UBV system. Lastly two β filters were devised to measure the flux densities at Hβ, wide β (f_w), and the strength of the Hβ line,

Table 1.4: The main features for the DDO system.

Filter name	λ_{eff} (nm)	$\Delta\lambda$ (nm)	Filter type
48	488.6	186	interference
45	451.7	76	interference
42	425.7	73	interference
41	416.6	83	interference
38	381.5	330	glass
35	346.0	383	glass

narrow β (f_n). The β index is then defined as following;

$$\beta = -2.5 \log_{10}[\frac{f_n}{f_w}] \tag{1.7}$$

Therefore, the colour indices give the following information for stars:

- $(b - y)$; stellar temperatures over the spectral-type range OB – G.
- $m_1 = (v - b) - (b - y)$; metallicity.
- $c_1 = (u - v) - (v - b)$; influence of the metal-line blanketing.
- β index; temperature discrimination for the stars between A2 and G, and luminosity or surface-gravity discrimination for B and O stars.

Another intermediate band photometric system is the DDO system, developed at the David Dunlap Observatory by McClure and van den Bergh (1968). The DDO system is complementary to the *uvbyβ* system for studies of G, K, and M type stars, and is used to determine the stellar temperatures, luminosities, metallicities, and ultraviolet excess values. The filter name, central wavelength and bandwidths of DDO system are shown in Table 1.4.

1.4.3 Narrow band systems

The purpose of narrow band systems is to isolate specific spectral features. No single system is in general use; however, Hα and Hβ are common choices. A pair of filters which lie at the line and having different bandwidths are studied in which one isolates the spectral features, with the other centred on a nearby continuum section.

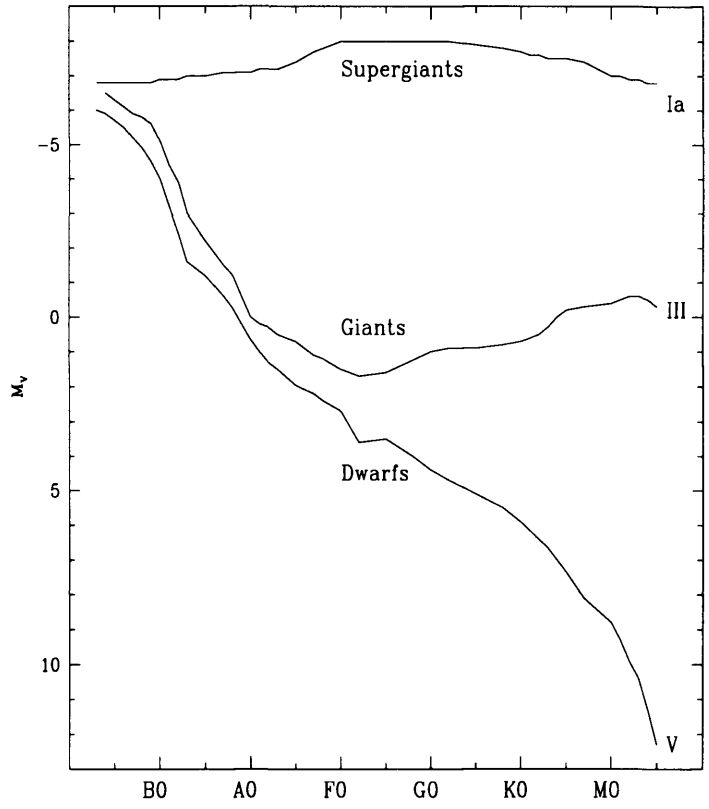

Figure 1.1: An observational H-R diagram of MK spectral class (Schmidt-Kaler, 1982). The luminosity classes are marked at right for each curve.

1.5 The Hertzsprung-Russell Diagram

An essential tool for the studies of stellar evolution is the Hertzsprung-Russell (H-R) diagram, which was developed independently by Ejnar Hertzsprung and Henry Russell. In 1911 Ejnar Hertzsprung noted that there was a pattern between absolute magnitudes of stars and their colour indices. Two years later, Henry Russell found a similar relation between the absolute magnitudes and their spectral types as well. In its original form, an observational H-R diagram is a plot of the absolute magnitude of observed stars against their spectral types; an example is shown in Figure 1.1. In this figure, the stars in the diagonal band are called the main sequence and they correspond to luminosity class V dwarfs in the MK system. However care must be taken in interchangeable use of the main sequence and dwarfs, because giants and subgiants are 'main sequence stars' in OB-type

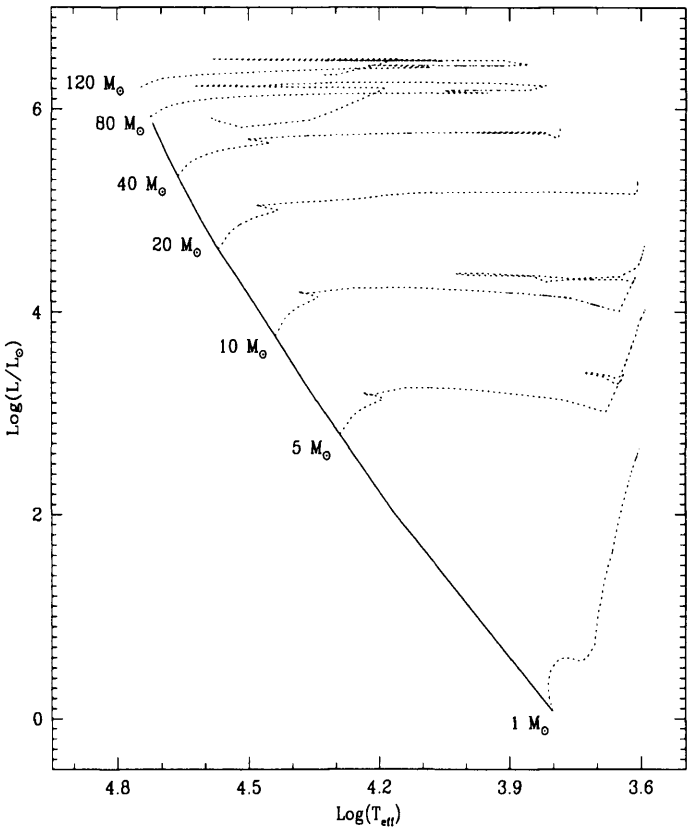

Figure 1.2: An theoretical H-R diagram with evolutionary tracks (dotted lines) according to masses in the unit of solar mass and with zero age main sequence (solid line) acrossing the diagram. The used evolutionary model is Geneva group for $Z = 0.004$ (Charbonnel *et al.*, 1993).

spectra in the sense that they are burning hydrogen in their core.

On the other hand, a theoretical H-R diagram is normally plotted as luminosity or absolute bolometric magnitude versus effective temperature. Figure 1.2 shows a theoretical H-R diagram with evolutionary tracks labelled according to masses in units of solar mass. For comparison with observations, the theoretical H-R diagram can be translated into an observational diagram, or vice versa. Those comparisons give us great information about studies of stars. For instance, we can determine the mass distribution by counting stars between evolutionary tracks, or estimate the age by fitting isochrones.

In photometry, the physical quantities we obtain from stars are magnitudes in each filter band. Because a colour or colour index defined as the magnitude difference between

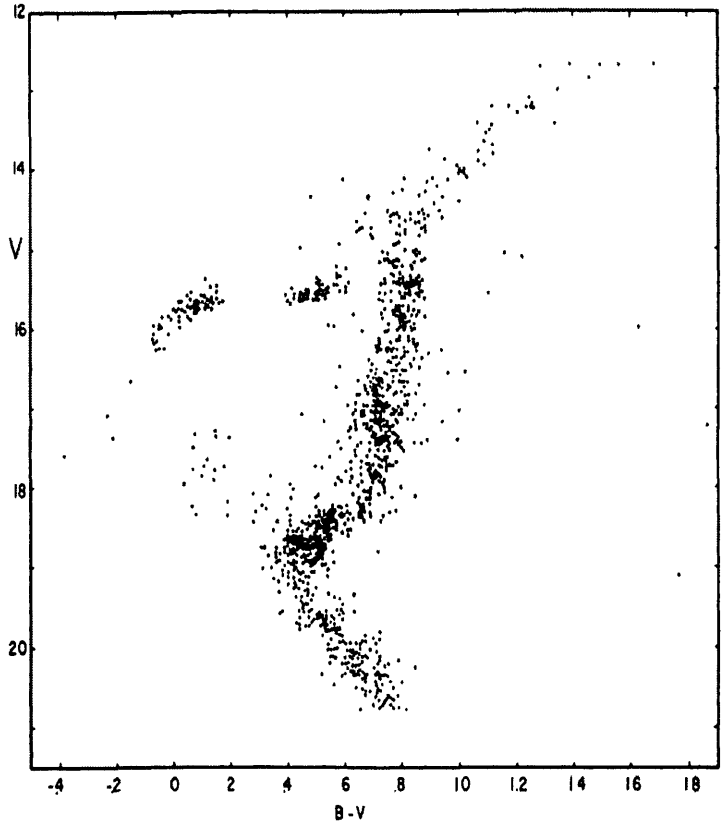

Figure 1.3: An example of the C-M diagram for a typical globular clusters (Johnson and Sandage, 1956).

two filters (for example, $B-V$ in UBV system) is roughly correlated with spectral type, we may construct a similar diagram. This is called a colour-magnitude (C-M) diagram. An example of a C-M diagram is presented in Figure 1.3. This figure shows a quite similar features to Figure 1.2.

In order to construct a theoretical H-R diagram from observational or colour-magnitude diagrams, however, we have to first know the distance of stars (because the absolute magnitude is defined as the magnitude at a distance of 10 pc). Moreover, because the UBV magnitude represents the flux density only in each filter's bandwidth, we must convert it into a bolometric magnitude over all wavelengths. Therefore the bolometric correction (BC), the difference between bolometric and photometric magnitudes, is required to estimate bolometric magnitude of stars. As well we have to know relations between colour, etc and T_{eff} with good accuracy from empirical relations or theoretical atmospheric model calculations.

CHAPTER 2

Observations

In an effort to investigate the IMF of massive stars and the effect of metallicity on galaxy evolution, we have performed a photometric survey of the SMC in B, V, and R bands. These passbands were chosen as a compromise between astrophysical information content and observing efficiency. The SMC is a useful target due to its proximity and low metallicity.

One of the greatest advances in observational astronomy has been the invention of Charge Coupled Devices (CCDs). The size of a single CCD has now seemingly reached its technological limit, therefore to get wide-field data, multiple-CCD instruments (mosaic CCDs) have been developed at many sites. The SMC covers about $280' \times 160'$ on the sky so a mosaic CCD mounted on the relatively small telescope is good for a whole area survey.

Observations were made at the 40 inch telescope at Siding Spring Observatory (SSO), in Australia, using the Wide Field Imager (WFI) during 5 - 11 September and 26 - 31 October 2001 and 9 - 17 November 2002.

In this chapter, we will describe used instruments, remarkable features of data taken each observation, and properties of basic frame such as bias, dark, and flat frames.

2.1 Instruments

The telescope is cassegrain with a 40 inch primary mirror and f/8 (or f/18) secondary mirror. The optics and mount system of the telescope are Ritchey-Chreitien and German equatorial type, respectively.

The WFI is a focal-plane CCD system with a detector size of 123 by 123 mm, 8192 by 8192 pixels, comprising a 4 × 2 array of 2048 × 4096 pixel, thinned, back-illuminated CCDs. The full array image yields ~ 140 MB of data (one CCD is 17.5 Mb), which doubles in size when processed. Each CCD covers 13′ × 26′ on the sky, giving a 52′ × 52′ field. The pixel size is 15 microns, giving 0.375 arcsec/pixel (at f/8). The gain is 1.5 ~ 2.1 electrons/ADU and the readout noise is 3.5 ~ 5.5 electrons (Shobbrook and Shobbrook, 2001). Most usefully of all, the two controllers read out the entire array in only 55 seconds. Figure 2.1 shows the layout of the WFI CCDs in the telescope's focal plane. In chip #1 there are several bad columns at the left edge and few hundred ADU bright columns near the centre. Chips #2, 3, 5, 7 and 8 have no bright columns but low level bias structure. There are dead pixels at the right top corner on chip #4 (see as well Figure 2.15). Although the instrument scientists refer to chip #6 as clean and the best quality chip in the whole array, we found that there are several bad columns in the left side and it shows abnormally high intensity in the centre array for some data during November 2002 run (see more detail in subsection 2.2.3). Table 2.1 shows saturation level, gain, read out

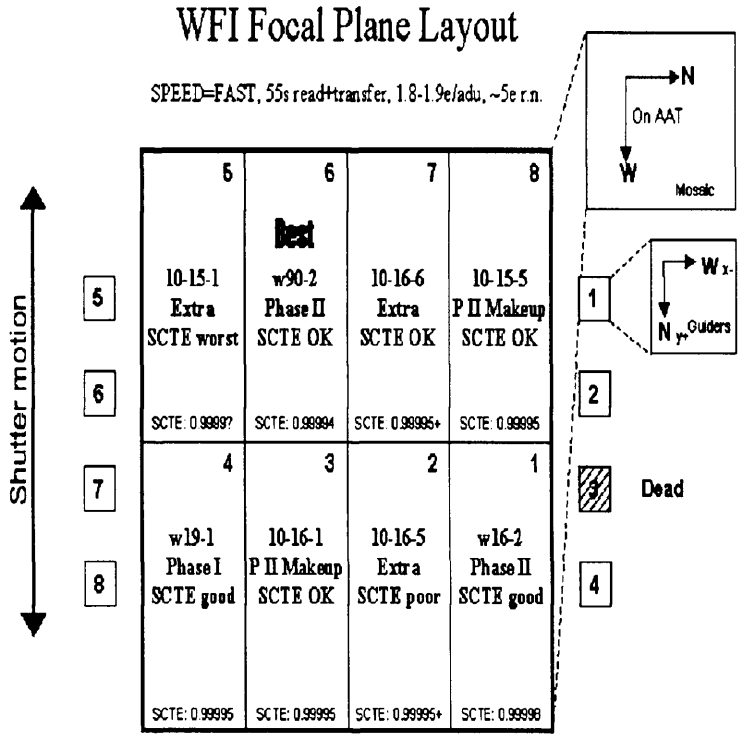

Figure 2.1: A systematic diagram shows assigned number, quality, and manufacture for each CCD chip.

Table 2.1: Basic characteristics of WFI CCDs.

CCD	Saturation level (ADU above bias)	Gain (e/ADU)	Readout noise (e)	Full well (kph)
#1	56,000	1.45	5.2	81.2
#2	53,000	1.70	5.9	90.6
#3	42,000	1.94	5.7	82.3
#4	52,000	1.73	4.9	89.4
#5	44,000	2.00	4.7	88.9
#6	56,000	1.67	4.7	93.5
#7	54,000	1.88	4.2	101.5
#8	55,000	1.68	4.0	92.9

noise and full well depth for the each CCD chip. Full details of the WFI can be found on the website: *http : //www.aao.gov.au/wfi/commission_plan.html.*

The basic characteristics of the WFI filter system are summarised in Table 2.2 and the predicted filter throughputs are shown in Figure 2.2 from the WFI schott glasses used in their manufacture. These do not consider the effects of reflection at the filter surfaces, which will reduce by $\sim$ 8% the overall throughputs, including the peak values indicated in column 5 of Table 2.2. In Figure 2.2, the solid lines and the dotted lines represent WFI CCD #6 and scaled Bessell (1990) B, V, and R filter throughputs, respectively. Bessell (1990) tabulated two B system responses in his paper and we plot the B response in which extinction is not corrected. The passband of the WFI B filter is shifted slightly toward the blue compared to Bessell's but the peak values match well. Similarly the WFI V filter is $\sim$ 10 nm shifted toward shorter wavelengths with respect to Bessell's. The R filters however are in very good agreement. In summary the B and V filters are similar to those of Johnson and Morgan (1953) system and the R filter is comparable to that of Cousins (1980).

2.2 Observations

To obtain multicolour photometry of the entire SMC, we observed 35 fields and used B, V, and R filters with two different exposure times (60 and 600 seconds); the shorter exposures

Table 2.2: Basic characteristics of the WFI B, V, and R filter system.

Filter	Thick (mm)	Size (mm)	Details	Peak (%)
B	5	165 × 165	1mm GG395+3mm BG37+1mm BG39	77.9
V	4	165 × 165	1mm GG495+2mm BG39	94.7
R	4	165 × 165	2mm GG570+2mm KG3	85.3

Notes: The peak value of WFI filter profile data is predicted one not measured. See text more details.

permit photometry of the stars saturated in the longer observations. As well, in order to compensate for the gap between each CCD ($\sim 20 - 30$ arcseconds), bad pixel and so on, we obtained two or three dithered frames, shifting $\sim 15'$ and $\sim 5'$ in RA and DEC, respectively. As a result, our work has at least 1,400 times the data (35 field × 2 exposure times × 2 or 3 dithers × 8 CCD chips) compared to a usual single-CCD observation using three filters with one exposure time. So in order to process this huge dataset, we required

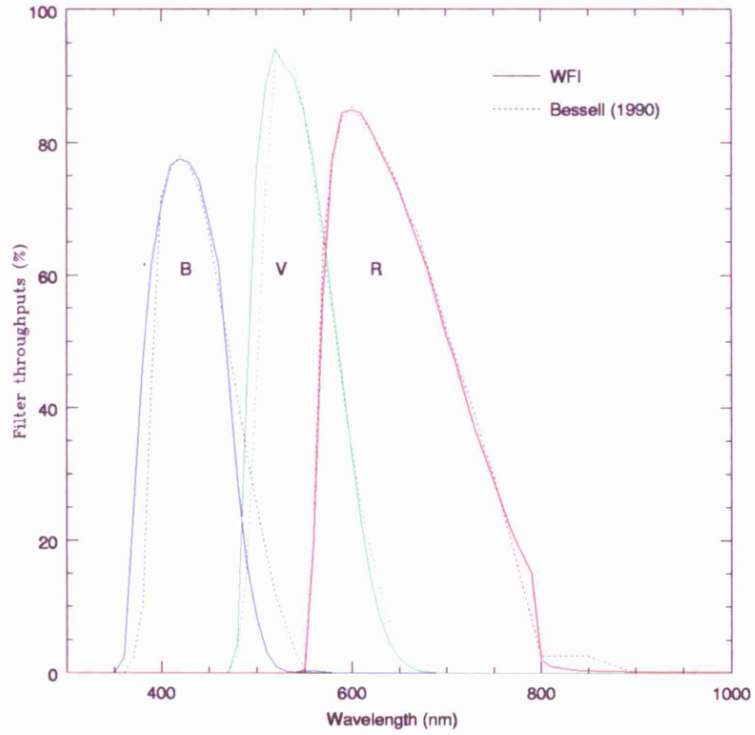

Figure 2.2: Predicted throughputs of the WFI CCD #6 for B, V, and R filters. The solid lines are WFI and the dotted lines are from Bessell (1990).

over 200 GB hard disk space.

To cover the whole SMC area, three observing runs were required: 5 - 11 September (by I. D. Howarth and C. J. Evans) and 25 - 31 October 2001 (by C. J. Evans and R. D Cannon) and 9 - 17 November 2002 (by K-W. Lee and C. J. Evans). In the 2002 observations we also obtained repeat exposures of some previously observed fields for the purpose of checking systematic differences between the two epochs and investigating further the frame-matching in the overall mosaic image.

The bias and dark frames are usually taken during non-photometric nights. We did not take dome flat frames but we took twilight flat frames after sunset and before sunrise whenever the weather permitted. In acquiring the twilight flats, the telescope was pointed about 20° away from the zenith in the direction opposite to where the Sun was setting or rising, with slightly moving positions to minimise possible contamination from stars. Generally we kept charge intensity of flat frames at about $10,000 \sim 30,000$ ADU to avoid non-linearity at the low and high count levels.

Evans (2001) investigated the IMF of massive stars in the SMC with a spectroscopic survey acquired using the 2dF instrument and with APM photometry. He found that there is a systematic offset in B and R magnitudes (especially for a faint B magnitudes). Massey (2002) presented a $UBVR$ CCD survey of the SMC for 7.2 deg^2, but it does not cover the full extent of Evans' spectroscopic survey area. Zaritsky *et al.* (2002) presented a U B V, and I stellar photometry of the central 18 deg^2 area of the SMC, but their data do not include R magnitudes. Therefore one of the important purposes of this study is to provide accurate B and R magnitudes and a world coordinate system for Evans' data. To get accurate faint B magnitudes , we took two 600s B exposures for each field.

Figure 2.3 depicts the selected areas and the observation log is presented in Table 2.3. In Figure 2.3, white boxes and the big black box are our SMC fields and Evans (2001)'s 2dF spectroscopic survey area. The lower characters in the observational log (a, b, and c) represent dithered fields for a given grid. The values of central right ascension and declination of each grid are given in Appendix A. The important features of each observation are noted in the following subsections.

2.2.1 September 2001 data

The most notable feature of these data is that there was a readout problem in the #01a, #01b, #02a, and #02b observations, because of which the parts of each CCD image are

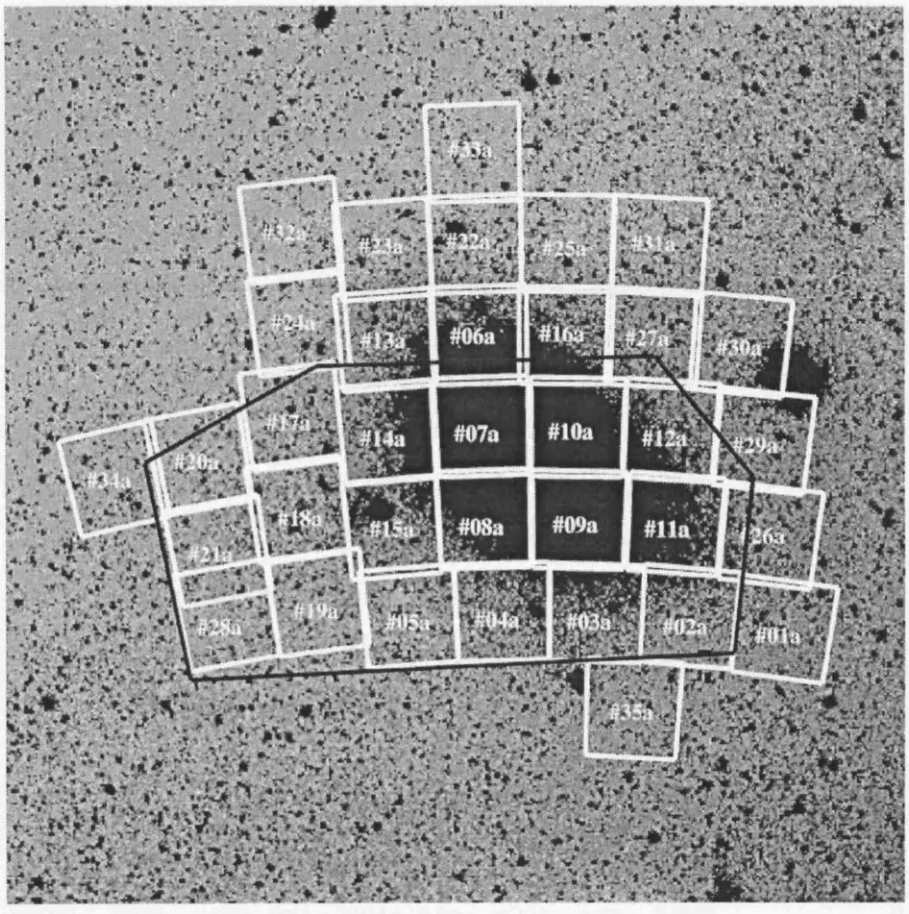

Figure 2.3: Outlines of our grid fields (small white colour boxes) and Evans's (2001) 2dF spectroscopic area (big black colour box) are shown against this image of the SMC. Only each '*a* field' is shown for the purpose of illustration. North is to the top and east is to the left.

shifted into the next CCD especially in #1 – #4 CCDs. To correct those frames, we found each boundary of the shifted parts by eye and moved them into the correct CCD chips.

Another problem is the omission of air-mass information in frame header files. Fortunately in this case, there is zenith distance information in the header files so we calculated air-mass values by the following equations (Hilditch, 2001);

$$\sec z = (\sin\phi \sin\delta + \cos\phi \cos\delta \cos H)^{-1} \tag{2.1}$$

$$X = \sec z - 0.0018167(\sec z - 1) - 0.002875(\sec z - 1)^2 - 0.0008083(\sec z - 1)^3 \tag{2.2}$$

where z is zenith distance, ϕ is the latitude of the observatory, H and δ are the hour angle and declination of the field centres respectively, and X is the air-mass. The SSO is located

Table 2.3: Observational log – The 'a', 'b' and 'c' characters next to field number represent the dithered frames.

Date	Field number	Ave. FWHM(″)
05 Sept. 2001	#01*a*,#01*b*,#01*c*,#01*a*,#02*b*,#02*c*	4.8
06 Sept. 2001	#03*a*,#03*b*,#04*a*,#04*b*,#05*a*,#05*b*	2.1
07 Sept. 2001	Only bias and dark frames	
08 Sept. 2001	#06*a*,#06*b*,#07*a*,#07*b*,#08*a*,#08*b*,#09*a*	3.9
09 Sept. 2001	#09*b*,#10*a*,#10*b*,#05*a*,#11*a*,#11*b*,#12*a*, #12*b*	2.1
10 Sept. 2001	#13*a*,#13*b*,#14*a*,#14*b*	2.2
11 Sept. 2001	Only bias and dark frames	
25 Oct. 2001	#14*b*	3.6
26 Oct. 2001	#14*b*,15*a*,#15*b*,#16*a*,#16*b*,#17*a*,#17*b*, #18*a*,#18*b*	3.4
27 Oct. 2001	#19*a*,#19*b*,#20*a*,#20*b*	2.2
28 Oct. 2001	#20*a*,#20*b*,#21*a*,#21*b*,#22*a*,#22*b*, #23*a*,#23*b*	2.6
29 Oct. 2001	#24*a*,#24*b*,#01*a*,#01*b*,#02*a*,#02*b*,#25*a*	3.9
30 Oct. 2001	#25*b*,#26*a*,#26*b*,#27*a*,#27*b*,#28*a*,#28*b*, #29*a*	2.5
31 Oct. 2001	#29*b*,#19*b*,#30*a*,#30*b*,#31*a*,#31*b*, #6*a*,#32*a*,#32*b*	2.8
09 Nov. 2002	#01*a*	2.9
10 Nov. 2002	Only bias and dark frames	
11 Nov. 2002	#01*b*,#02*a*,#02*b*,#04*b*,#05*a*,#05*b*, #06*a*,#19*b*	4.9
12 Nov. 2002	#09*b*	2.7
13 Nov. 2002	#09*a*,#14*b*,#33*a*,#33*b*,#34*a*,#34*b*, #35*a*,#35*b*	3.6
14 Nov. 2002	Only bias and dark frames	
15 Nov. 2002	#06*c*,#07*c*,#08*c*,#09*c*	5.1
16 Nov. 2002	#10*c*,#11*c*,#12*c*,#13*c* ,#16*c*,#14*c*,#15*c*,#18*c*	5.7
17 Nov. 2002	Only bias and dark frames	

at 31° 16′ 24″ south and 149° 03′ 45″ east. The field-of-view (FOV) in one mosaic image is 52′, so the maximum difference in air-mass across the mosaic is $\Delta X \sim 0.001$. Therefore we used a single value for all CCD chips (the air-mass value at the centre of the mosaic image) through entire data reduction.

A more serious problem in these observations is that some CCD chips have no good point spread function (PSF) stars in a given exposure due to the bad weather and low number of stars in a chip. For those chips, we used other PSF stars from other exposures of the same chip and the same exposure time taken on same day.

The average full-width half-maximum (FWHM) of stellar images in this run is 8.1 pixels, corresponding to 3.0 arcseconds.

2.2.2 October 2001 data

Some of the October 2001 data also have no air-mass information. Moreover, they do not have zenith-distance, hour angle and local sidereal time information in the header file either. Therefore we firstly calculated the Julian date (JD) and sidereral time (ST) using following equations (Henden and Kaitchuck, 1982);

$$\begin{aligned} \text{JD } (0^{\text{h}}\text{ UT}) &= 2415020 + 365(\text{year} - 1900) + (\text{days from start of year}) \\ &+ (\text{no. of leap years since } 1900) - 0.5 \end{aligned} \tag{2.3}$$

$$\begin{aligned} \text{ST} &= 6.6460556 + 2400.0512617(\text{JD} - 2415020)/36525 \\ &+ 1.0027379(\text{UT}) - \text{longitude (hours)} \end{aligned} \tag{2.4}$$

Next, with local sidereral time (LST) and right ascension (RA), the hour angle (H) is given by

$$H = \text{LST} - \text{RA}. \tag{2.5}$$

Lastly we estimated air-mass using equation 2.1 and 2.2.

In order to compensate for the problems in field #01a, #01b, #02a and #02b during the September 2001 run, we re-observed those areas in the middle of these observations (29th October). In this run, the average FWHM is again 3.0 arcseconds.

2.2.3 November 2002 data

The main purpose of these observations was to finish the remaining fields of the SMC and to take second-epoch observations mostly for the Evans' (2001) 2dF spectroscopic area

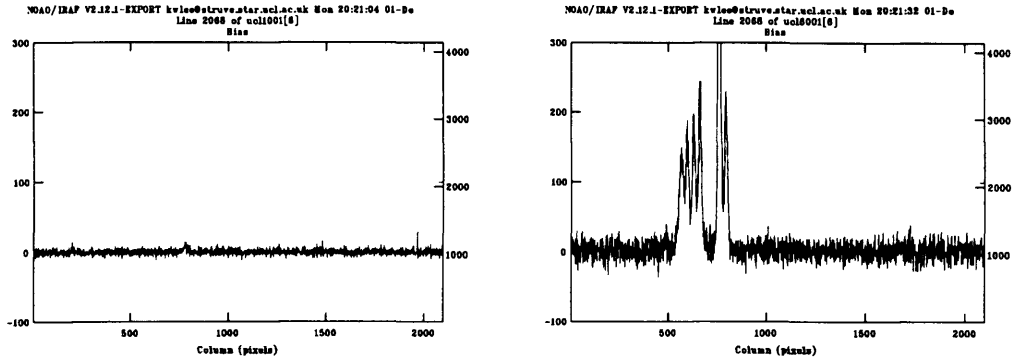

Figure 2.4: Plot of count levels along columns for the overscan corrected bias frames in CCD chip #6 to show the positions and the amount of counts level. Right panel (November 2002*b*) is 9th November data and left one (November 2002*a*) is 14th November data.

(see Figure 2.3).

The prominent characteristic of these observations was the sudden appearance of hot pixels between 550 – 820 columns in CCD chip #6 from 14 November onwards (see Figure 2.4) and the increase of bias levels (over 100 ADU) in CCD chip #1, #3 and #5 (refer to Table 2.4). In consideration of this matter, we made two master bias and master dark frames then separately applied them to corresponding data frames. In order to distinguish these two sets of data, we suffix *b* and *a* in the year, *e.g.* November 2002*a*, for *b*efore and *a*fter from 14th November 2002.

In the November 2002 data some of the frames have no air-mass information, similar to the two previous observations. Moreover, in November 2002*a*, some of data have no exposure time information in the header, either.

The average FWHM of these observations was 4.2 arcseconds which is the largest average value amongst runs (the worst was 5.7 arcseconds at 16th November 2002).

2.3 Properties of the basic frames

Every CCD system has its unique properties, and they change with respect to time. So it is important to check the characteristics of basic frames (*e.g.*, bias, dark, and flat frames) taken at the same run with astronomical frames in order to correct astronomical frames as accurately as possible. The WFI chips also exhibit a variety of idiosyncrasies. Here,

we discuss and characterise some properties of the basic frames of the WFI system as a preface to the data reduction (*i.e.*, Chapter 3).

2.3.1 Bias Frame

Generally, when the true signal is amplified before its digitisation by the Analogue-to-Digital Converter (ADC), a false signal (or bias) is also generated. This bias level depends upon the electronical properties of each CCD and changes with time and observational environments. In order to estimate and correct the bias, usually two techniques are used in CCD data reductions.

2.3.1.1 Overscan correction

Although the CCD controller only reads out a CCD, without sampling any of its stored charges, it contains false signal or bias. Nowadays in astronomical CCDs, there are usually overscan strips on either side of the chip to record this kind of bias and all CCD frames have to be corrected.

In Table 2.4, we determine the average and standard deviation of median bias levels of different CCDs. As mentioned in subsection 2.2.3, we divide the November 2002 data into two groups, before and after the appearance of sudden bad pixels in CCD #6. Note that chips #5 and #6 have large standard deviations in the September and October 2001 data. As well chips #1 and #3 show abnormally large standard deviations in the November 2002 data and the difference of mean values between 2002*b* and 2002*a* is over 100 ADU in CCDs #1, #3, and #6. We can account for this for CCD #6 from the appearance of hot pixels, but the reasons are unknown for CCDs #1 and #3.

In conclusion, the examination of bias levels from the three runs shows that bias levels are very different between CCDs and runs, and that therefore careful overscan subtraction is important in the data reduction.

Figure 2.5 illustrates the variation of overscan bias levels with time in each CCD chip for 29th September 2001. In the WFI CCDs the overscan area is [2075:2098, 5:4098] in chips #1 – #4 and [1:24, 39:4132] in chips #5 – #8. Δ (Julian day) in the x-axis is Julian day subtracted from 52211.41253443 days and Δ in y-axis is the difference of each median value from their mean value. On the average, CCD #4 and #5 have the largest (4635 ADU) and smallest (2858 ADU) values respectively in overscan bias levels amongst chips. In standard deviation, CCD #5 and #6 have the largest value (0.28) and #2 has the

Table 2.4: The mean and standard deviation (S.D) of median bias levels for each CCD.

	September 2001 (12 frames)		October 2001 (16 frames)		November 2002*b* (28 frames)		November 2002*a* (30 frames)	
CCD	Mean	S.D	Mean	S.D	Mean	S.D	Mean	S.D
#1	3537.2	0.54	3453.4	0.25	3744.9	10.08	3615.4	5.99
#2	4095.2	0.43	4018.3	0.21	4117.0	0.22	4109.5	0.26
#3	4022.2	0.43	4006.6	0.40	4071.6	10.61	4187.4	0.81
#4	4649.7	0.57	4632.8	0.50	4768.3	0.51	4767.9	0.44
#5	2874.1	0.64	2858.1	0.57	2796.6	0.38	2787.6	0.36
#6	3373.6	0.67	3372.2	0.55	3319.8	0.48	3470.5	0.61
#7	4039.7	0.37	4015.5	0.33	4081.6	0.49	4073.1	0.26
#8	4533.2	0.16	4523.1	0.20	4539.4	0.15	4537.0	0.15

smallest (0.10). Figure 2.6 shows the overscan bias level pattern of an object frame taken on 29 September 2001 for each CCD chip along the columns which are read out. Except in CCD #4 there are no peculiar patterns so it is reasonable to fit as a value, the median (instead of the mean to reject the effect caused by cosmic rays).

Figure 2.7 shows the time variations of the bias levels for the overscan-corrected bias frames from November 2002. The signal outside of the bias strip for these frames gives us an indication of how well a single bias strip approximates the 'global' bias level. Overall, the overscan-corrected bias frames have less than 4 ADU variations over time so it is believed that overscan correction is essential in data reduction and that median filtering of the overscan is satisfactory for bias correction.

2.3.1.2 Master bias frame correction: readout noise

We can study the bias further by examining the statistical distribution of the bias 'signal'. A bias frame has zero exposure time so it is also called a zero frame. Although no light is incident on the detector in zero exposure time, the electronics always generate some 'readout noise'. Typically in order to correct read out noise, several bias frames are taken, overscan corrected and combined with a proper value (median in our data reduction), then

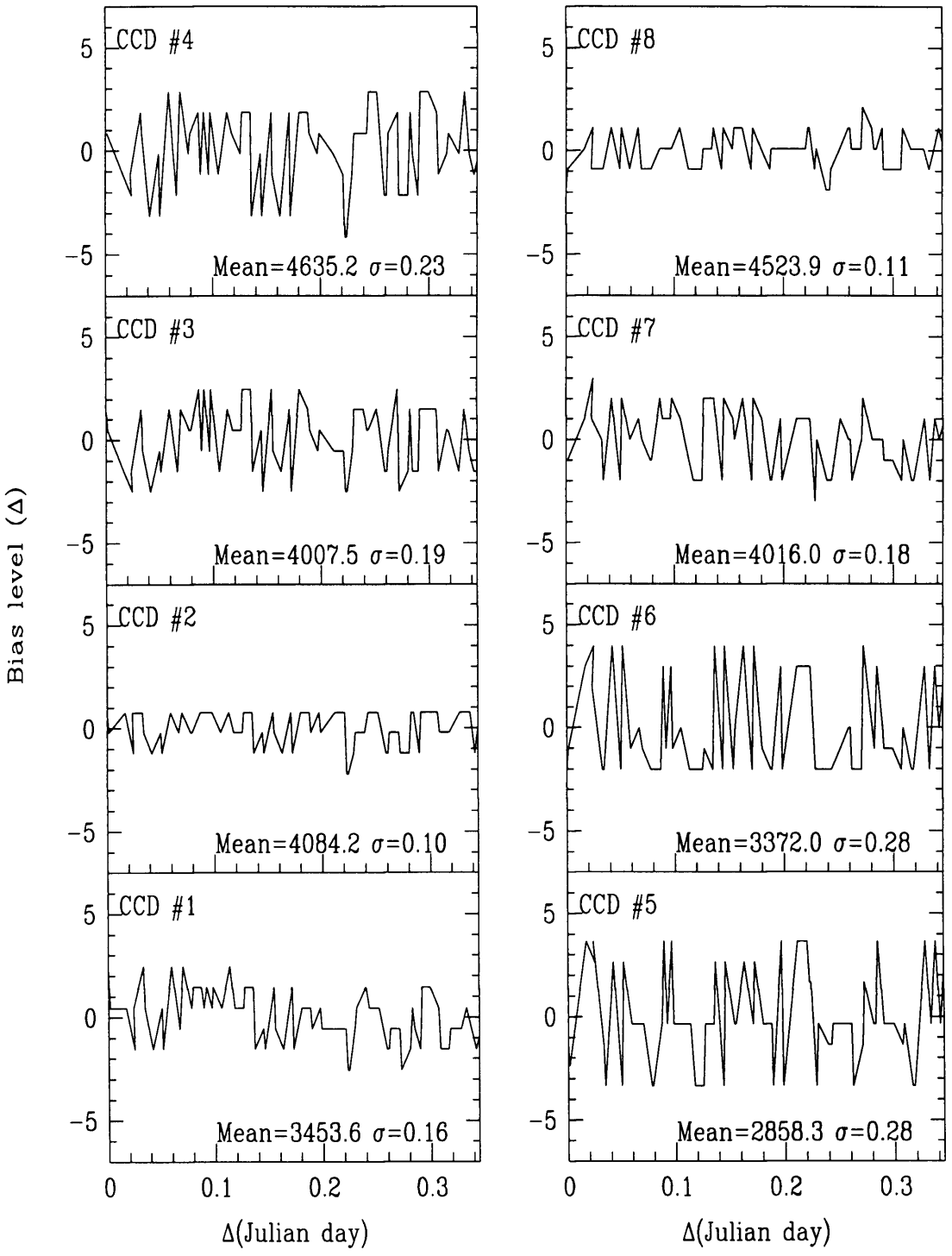

Figure 2.5: Overscan bias level – The variations of overscan bias level with time for each CCD chip on 29 September 2001 data. Δ (Julian Day) is Julian day subtracted from 52211.41253443 days and Δ is the difference of each median value from mean value.

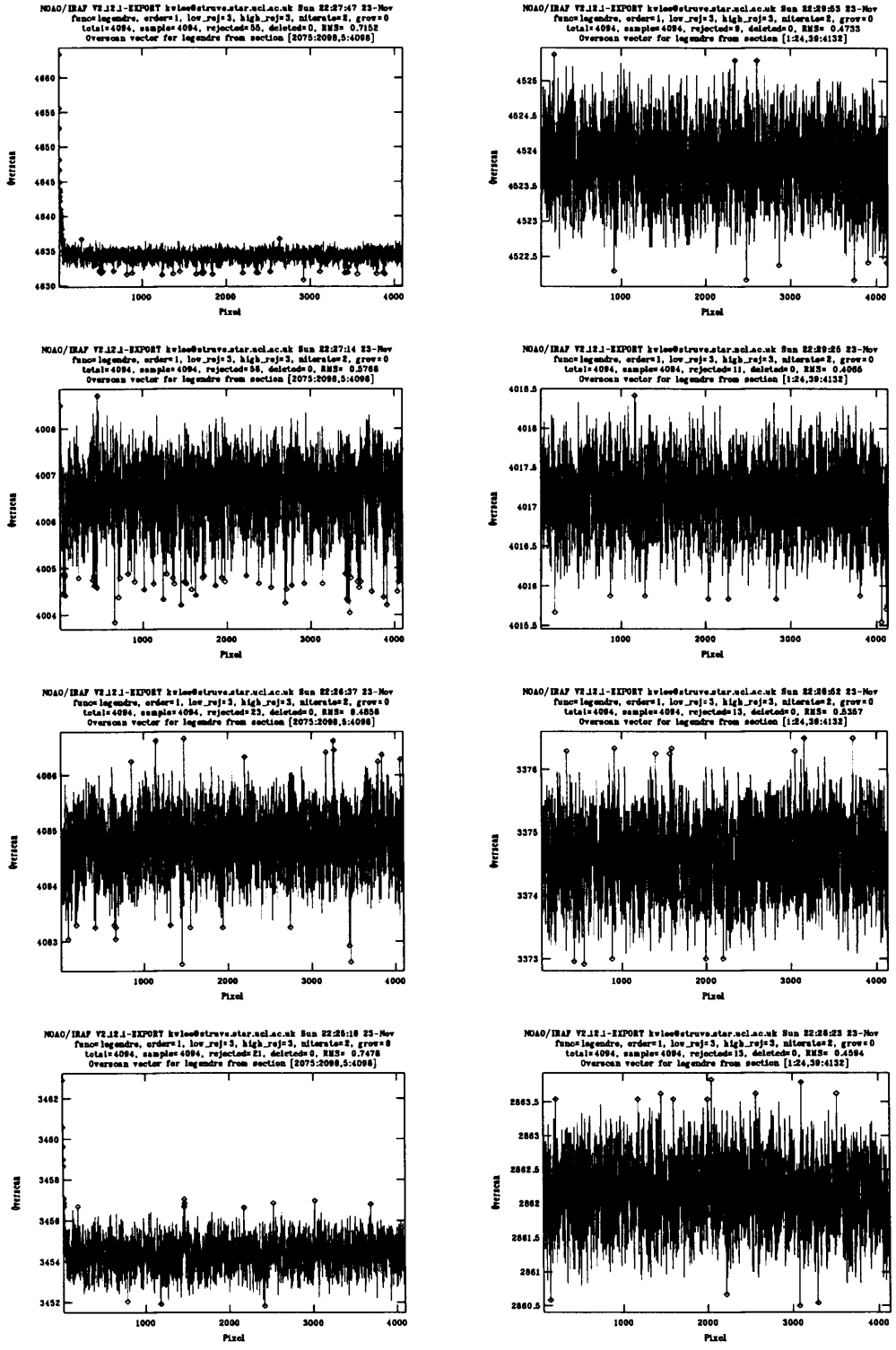

Figure 2.6: Overscan pattern – An example of overscan area pattern in an object frame taken 29 September 2001. The horizontal and vertical axes are pixels along each column and bias levels, respectively. Plots are laid out as in Fig 2.5 for each CCD.

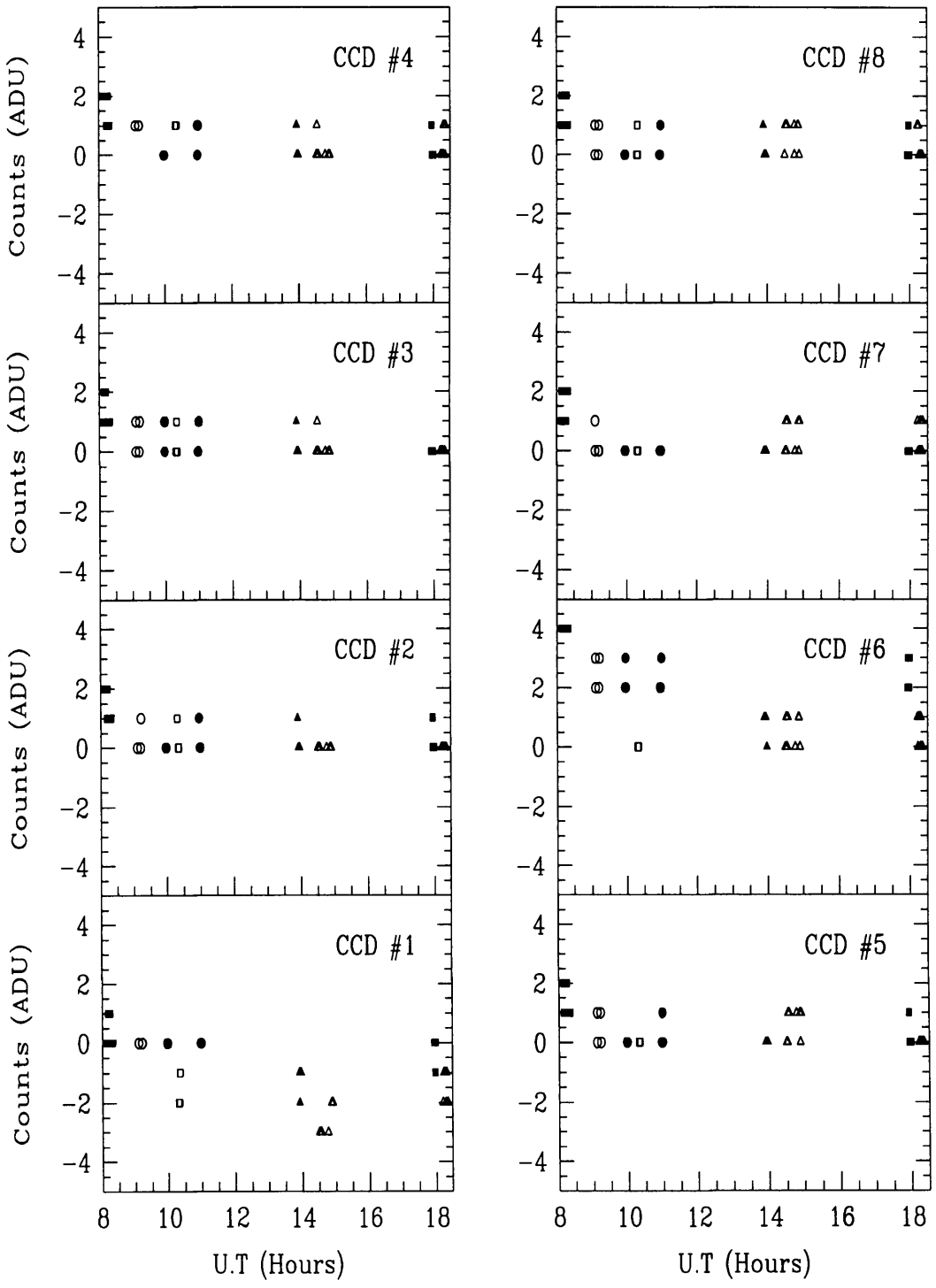

Figure 2.7: The time variations of overscan-corrected bias frames taken from the November 2002 data. Open triangle (20 points), filled triangle (5 points), open square (3 points), filled square (19 points), open circle (5 points), and filled circle (6 points) symbols are 9, 10, 12, 15, 16, and 17 November 2002 data, respectively.

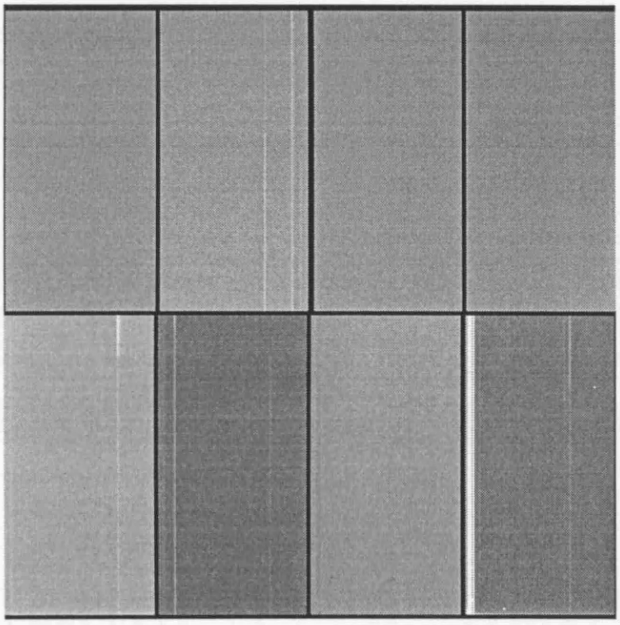

Figure 2.8: A master bias frame from median combination of 16 bias frames taken in September 2001.

applied to all frames. A good bias frame has a Gaussian for the number distribution of counts with respect to the mean value and the standard deviation is given by (Massey and Jacoby, 1992);

$$\sigma^{S}_{ADU} = \frac{RON}{GN} \tag{2.6}$$

where the upper script S means single frame and RON and GN are readout noise and gain, respectively. However, for a master bias frame constructed from N frames, we have to use readout noise $= \sqrt{N} \times RON$ and gain $= N \times GN$. Therefore, for a master frame made from N frames, Equation 2.6 can be rewritten:

$$\sigma^{N}_{ADU} = \frac{\sqrt{N}\ RON}{N\ GN} = \frac{\sqrt{N}}{N} \cdot \sigma^{S}_{ADU}. \tag{2.7}$$

For the WFI data most CCD chips have σ^{N}_{ADU} which is less than 1 ADU (see Table 2.1 for the WFI gain and readout values). As an example, we present the September 2001 master bias frame in Figure 2.8 and its histogram for the central window area ([800:1000, 1400:2000]) is given in Figure 2.9. This master bias (or zero) frame seems flat within ± 2 ADU (except for hot pixel regions described in section 2.1) and has a well-shaped Gaussian distribution satisfying the σ^{N}_{ADU} values.

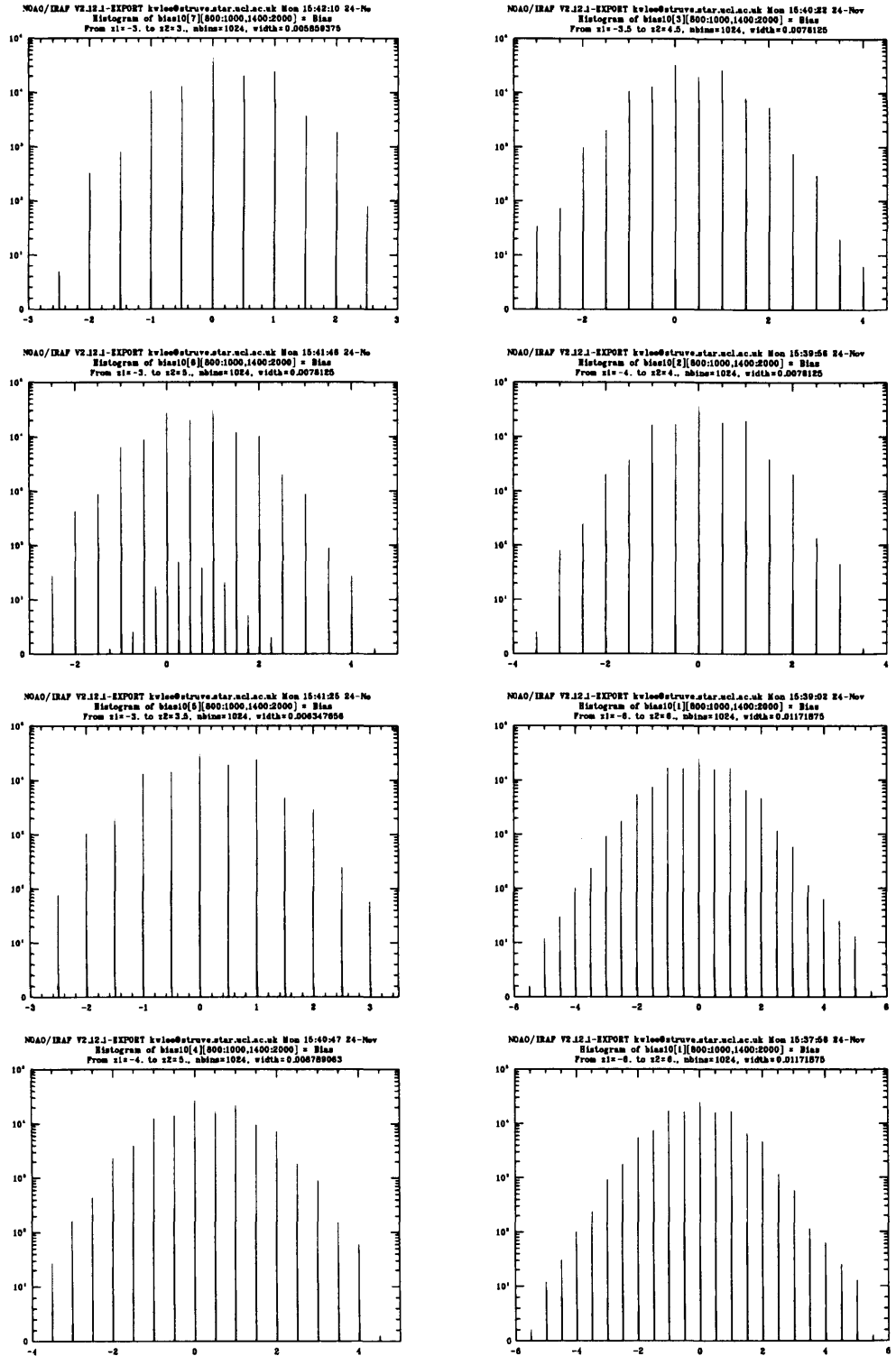

Figure 2.9: The number distribution for the master bias frames (*e.g.* Figure 2.8) with respect to mean value for each CCD. These distributions show a well-shaped Gaussian.

2.3.2 Linearity

One of the great advantages of CCDs in comparison to photographic plates is their linearity. However all CCD chips, including those in WFI, are not perfectly linear, especially in higher ADU levels. This fact necessitates use of a linearity correction procedure in the data reduction. In Figure 2.10 we present the polynomial linearity calibration for each WFI CCD calculated by the Anglo-Australian Observatory (AAO) from 2 February 2001 data. The area the AAO used was [420:597, 415:560] for each CCD, plotting counts against exposure time to derive the linearity correction for i filter (see Table 3.1 for the coefficients used in the polynomial linearity calibration). As can be noticed in Figure 2.10, most CCDs have quite significant non-linearity; for example, CCD #4 is non-linear over all count levels. (actually we need a uniform light source to test the linearity of each CCD; even the dome flat lamp used by the AAO has light variations).

In Figure 2.11 we plot logarithmic mean counts against logarithmic variance for the same sections as the AAO, linearity corrected V filter flat frames from our September 2001 data to check the fitness of the linearity correction. Although there is some suggestion of non-linearity over 32000 ADU in CCD #8, Figure 2.11 in general shows a good linearity. Therefore although it is evidently necessary to apply a linearity correction for the WFI data, the published corrections appear satisfactory.

2.3.3 Dark Frames

Theoretically, a dark current is always generated in every electronic device above zero Kelvin, and is proportion to integration time. Most modern CCDs are cooled below $-100°$C by liquid N_2 and the dark current is very low, and generally invariant with time, so is often neglected in data reduction. However, in order to increase charge transfer efficiency (CTE), the WFI has a relatively warm ($\sim$ 183 K) operating temperature for the focal-plane. The penalty for this is an increased dark current. Figure 2.12 presents dark-count variations with respect to time, using bias (and linearity) corrected dark frames taken in 2002 10, 12 (say November 2002*b*), and 17 November (say November 2002*a*). CCD #4 shows the highest overall level and #3 the lowest; CCD #2 displays the most consistent level. On average, 60-second frames have almost zero counts (except CCD #1); counts for the 600-second frames are 4 – 6 ADU (except CCD #4 and #8). In general, the dark level is independent of time, although there are some small scale fluctuations.

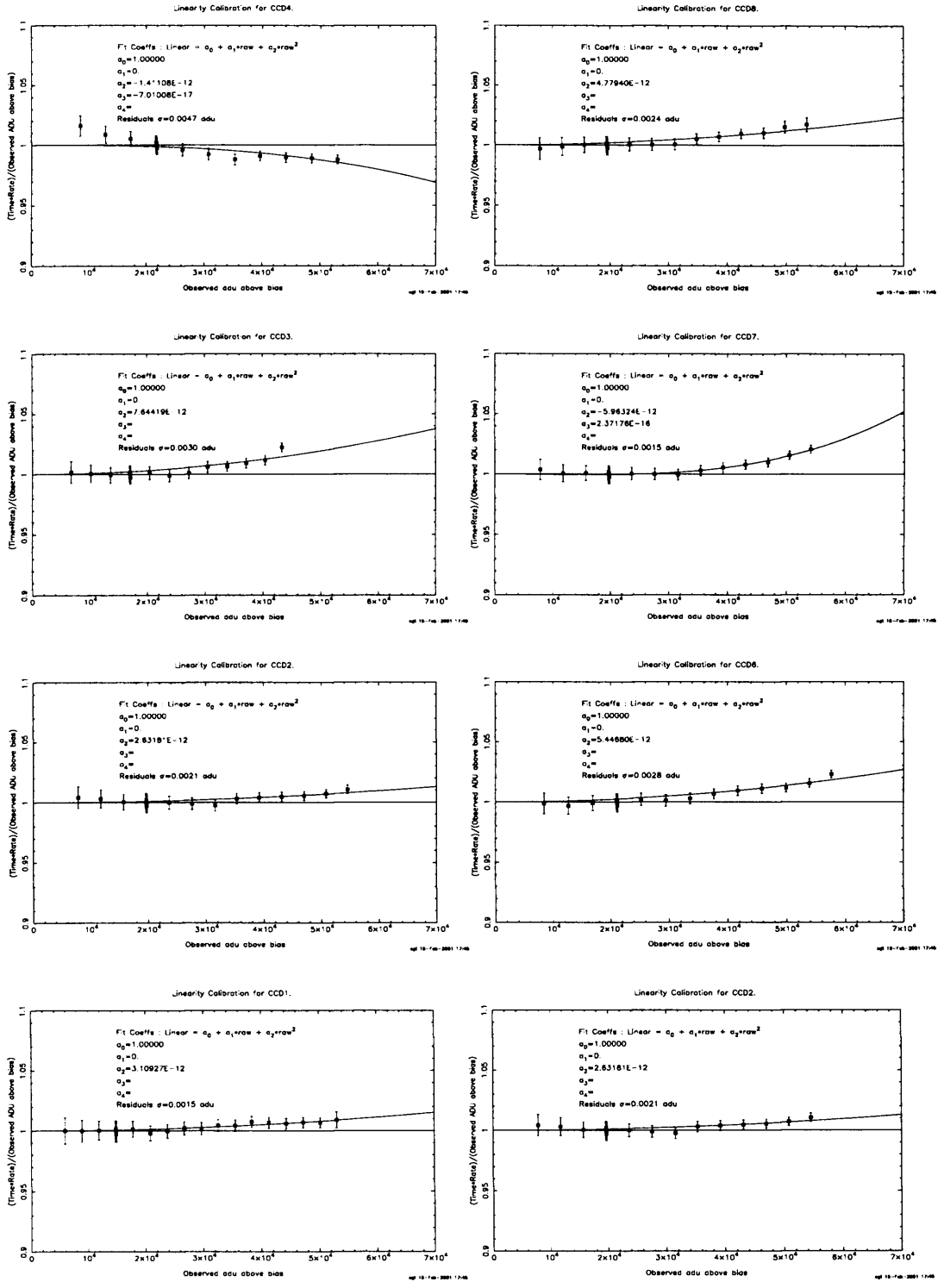

Figure 2.10: WFI linearity corrections calculated by the AAO from 2 Feb 2001 data for each CCD in i filter.

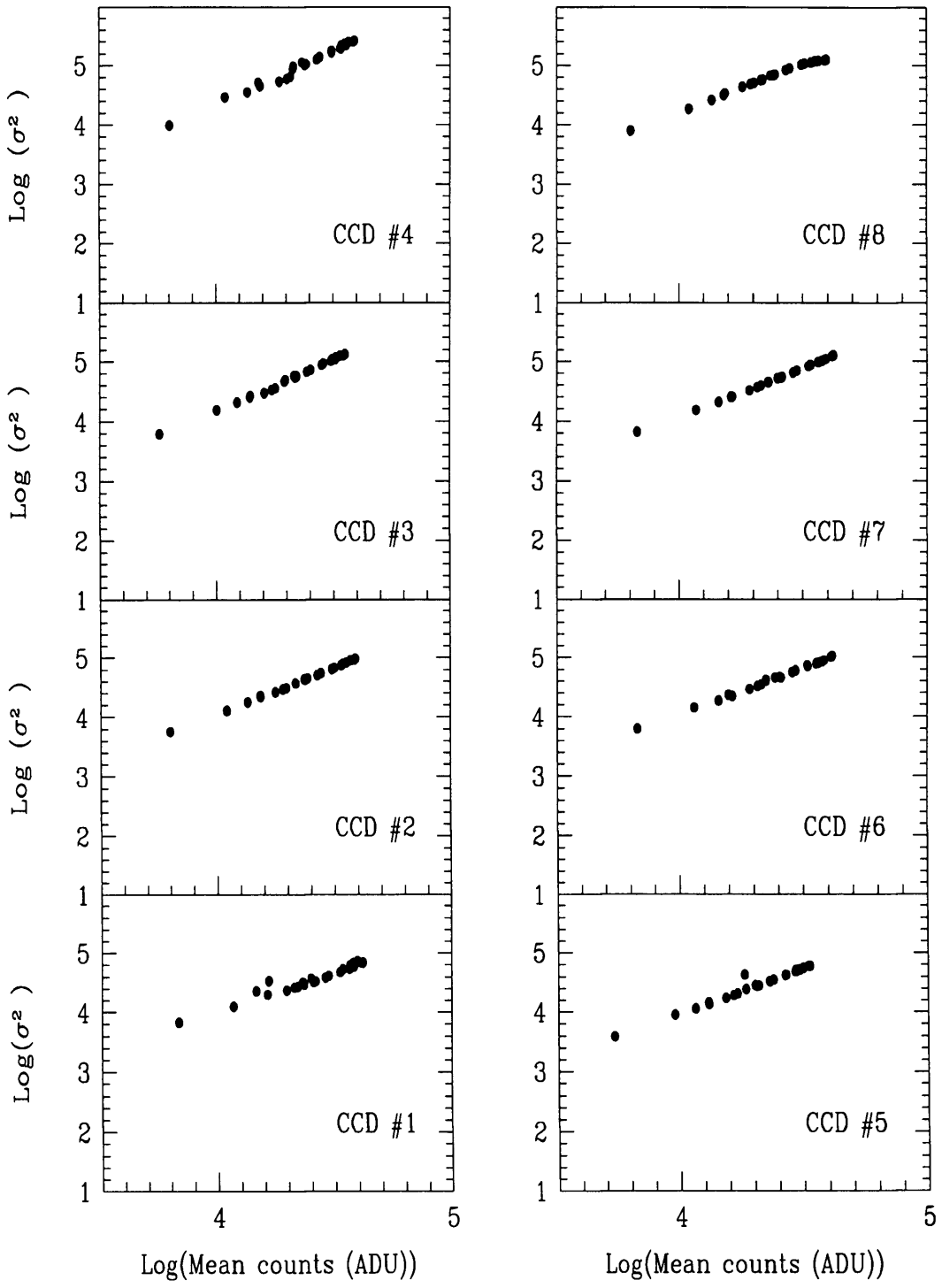

Figure 2.11: WFI linearity for our data using linearity corrected flat frames taken September 2001 for each CCD (V filter).

Figure 2.13 shows the dark level as a function of exposure time (60s, 240s, 300s and 600s) using master dark frames taken in September 2001. In Figure 2.13, the solid line is a least-square fit (*e.g.* $y = a + b \times x$), b is the slope and χ^2 is chi-square. CCD #4 has the steepest gradient (b=0.016) and the worst fit ($\chi^2 = 0.65$). On the other hand, CCD #3 has the the lowest (b=0.006) slope and the best fit ($\chi^2 = 0.03$). However, throughout all the chips, the dark count level seems to linearly increase with exposure time and is negligible ($<$ 1 ADU) in all 60s frames. In Table 2.5 we summarise the dark current rates in a central window [800:1000, 1400:2000] area for the 60 and 600 second master dark frames taken for each observation run. Except for the 60-second frames of November 2002*a*, dark current rates are around 1 ADU in the 60 second exposures. However they become significant (twice the readout noise level), in the 600-second frames. Regarding the single negative value of dark current, we think that it is caused by the originally low rate ($\sim$ 1 ADU), an abnormally higher bias level (see Table 2.4) in November 2002*b*, and low statistics (only 6 frames).

Overall, based on Figure 2.12, Figure 2.13 and Table 2.5, the dark count level is essentially invariant with time for a given chip. In conclusion, dark current can be neglected in the 60 second exposures, but it becomes comparable to readout noise level in the 300-second frames, and important in the 600-second frames.

In our data reduction, we created a master dark frame for each exposure time and for the consistency of reductions and applied it to all appropriate data. Figure 2.14 is an example of a 600-second master dark frame, made from 16 dark frames taken over the September 2001 run, with median-value combination. The bright regions on the edges of CCD #1, #4, #5 and #8 are due to the turning on of the guide CCDs and some white regions in CCD #2, #5, #7, and #8 show higher dark current levels than average. Therefore the acquisition of dark frames and correction with a master dark frame is essential to WFI data reduction.

2.3.4 Flat-field Frames

As mentioned in section 2.1, the WFI mosaic CCD is composed of eight CCD chips, each of which is has 2k $\times$ 4k pixels. Because each chip has a different response function (dependence on wavelength), separate flat fielding is required in data reduction with respect to each filter. In our discussion of flat field frames, we define four types – dome flats, twilight flats, sky flats and 'super (dark) sky' flat frames:

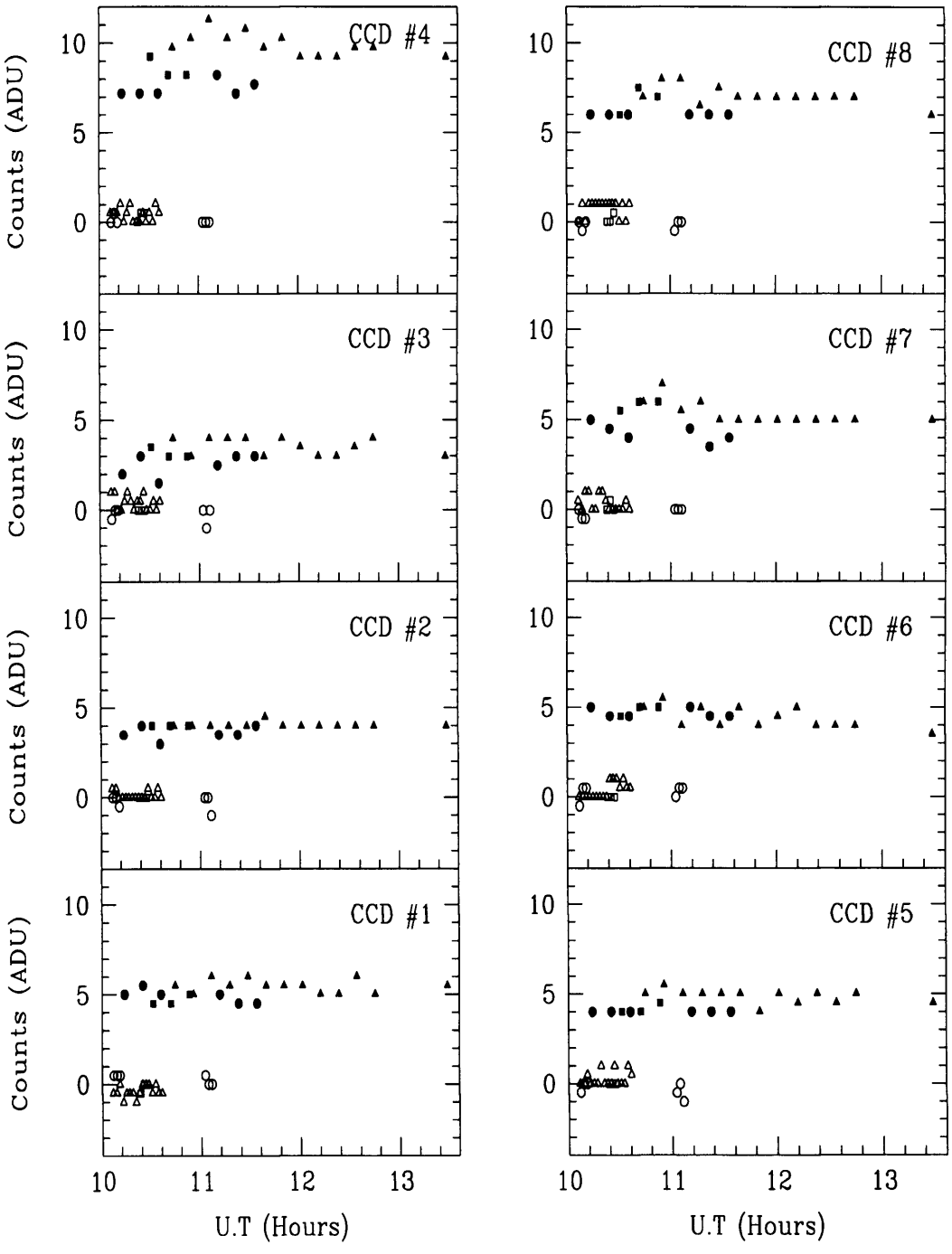

Figure 2.12: Dark-count level with respect to time for each CCD, from linearity-corrected dark frames taken in November 2002. Open and filled symbols denote 60 and 600 second frames. Triangles, rectangles, and circles represent 10, 12, and 17 November 2002 data frames, respectively.

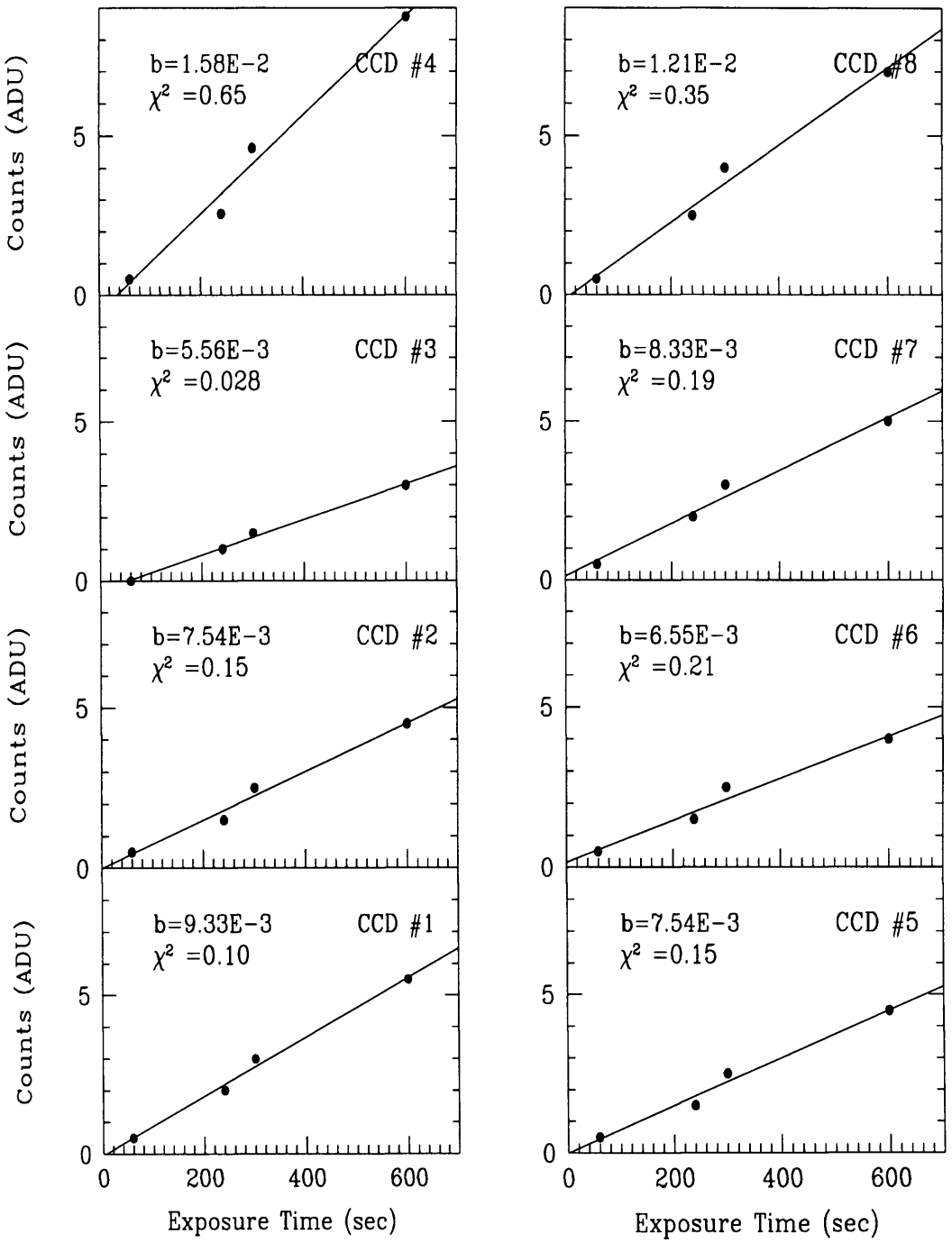

Figure 2.13: Dark-count level with respect to exposure time for the CCD using the master dark frames taken in September 2001. Solid lines are least square fits, b is the slope of line.

Table 2.5: Dark current rate in central window [800:1000, 1400:2000] in each CCD chip for the three observation epochs.

	September 2001		October 2001		November 2002*b*		November 2002*a*	
	(16)	(16)	(16)	(16)	(19)	(16)	(6)	(6)
CCD	e/60s	e/600s	e/60s	e/600s	e/60s	e/600s	e/60s	e/600s
#1	0.5	6.5	1.2	8.0	0.1	6.8	0.8	6.1
#2	0.5	7.4	0.7	7.0	0.1	6.7	-0.2	6.1
#3	0.3	5.9	0.5	7.1	0.7	6.7	-0.1	5.8
#4	0.6	13.8	1.2	16.0	0.4	15.7	0.1	12.5
#5	0.7	9.7	1.1	8.4	0.3	10.0	-1.0	8.3
#6	0.5	6.7	0.1	6.2	0.4	7.9	-0.5	6.4
#7	1.1	10.8	1.2	10.0	0.8	11.1	-0.5	8.3
#8	0.9	11.8	0.6	11.2	1.0	12.1	-0.5	10.2

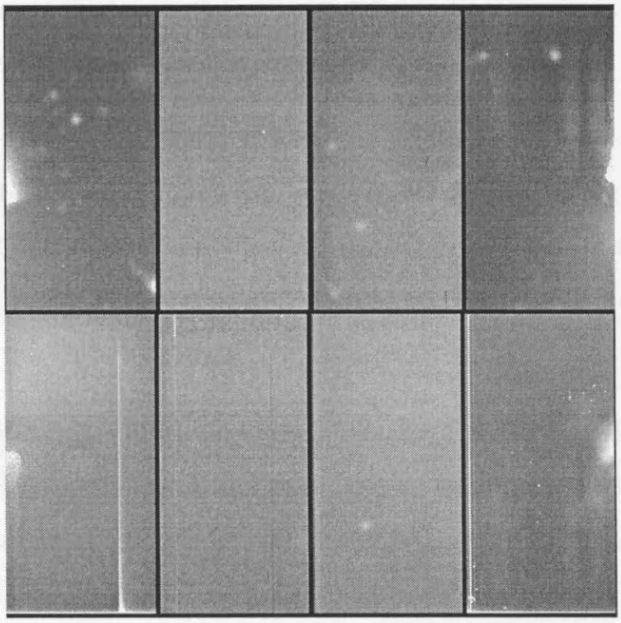

Figure 2.14: A master dark frame – This is an example of 600 second master dark frame made from 16 dark frames taken over the September 2001 run with median-value combination.

- Dome flats are taken using the inside of the telescope dome, illuminated by a bright continuum source such as a tungsten light. Although it is more convenient to get dome images than twilight flats, they can be subject to vignetting and fringing.

- Twilight flat field frames are taken from the sky immediately after sunset and before sunrise. To get a twilight flat frame careful attention is required because the time available to acquire the image is quite short (the sky should be much brighter than any stars which happen to be in the field of view, although not bright enough to saturate the chip). Nevertheless, twilight flats are the best for the flat-fielding, and generally 'flat frame' means twilight flat frame in this study.

- Some authors use sky flats to mean twilight flat frames. However, in this study we refer to sky flat frames as those made by combining dithered astronomical frames with different pointings, without overlapping objects. As Valdes (2002) pointed out, the twilight flat frame seems adequate but his experience shows that the colour of the sky and brightness gradients across the generally larger field of view of a mosaic array do not provide completely satisfactory flat fielding so the sky flat frame correction is an important reduction step in mosaic CCD data reduction.

- When very accurate photometry is required, Gullixson (1992) suggested that super flat field, combined many blank sky images, can be used as secondary flat fielding. However, a CCD mosaic usually has a large field of view and it is very hard to get void areas in the sky. Super sky flat frames are similar to sky flat frames in the view that they use the night sky itself.

In this study we first flat field with master twilight flat frames, for all object frames; then make sky flat frames with the resulting frames and do secondary flat fielding with the sky flat frame for all science images. As for the master bias and dark frames, we made master flat frames using all flat frames for each filter taken each in run and applied then to the astronomical frames taken in the same run. Figures 2.15, 2.16 and 2.17 show examples of B, V, and R master flat frames taken during October 2001. In these frames, there are small doughnut shapes in CCD #2, #3, #5, and #6 due to dust in the filters, and there is a discontinuity at the upper few rows in CCD #8.

For the purpose of examination of similarity of quantum efficiency in each CCD chip, we define a flatness index (Sung, 1995):

$$\text{Flatness } (\%) = \frac{\text{Standard Deviation}}{\text{Mean}} \times 100 \tag{2.8}$$

Figures 2.18, 2.19, and 2.20 show the flatness for each filter using frames taken in November 2002. In Figures 2.18 – 2.20, the x-axis is logarithmic mean value in ADU unit and the y-axis is the flatness defined in Equation 2.8. Open and filled rectangles represent November 2002*b* and 2002*a* flat frames, respectively. The flatness of the *B* filter shows the most constant values and *R* most variable. Because we separately applied master bias and dark frames in November 2002 data, there appears to be no difference between data sets. Except CCD #7 in the *B* flat frames, the flatness is around 5 percent in most filters and in all CCD chips.

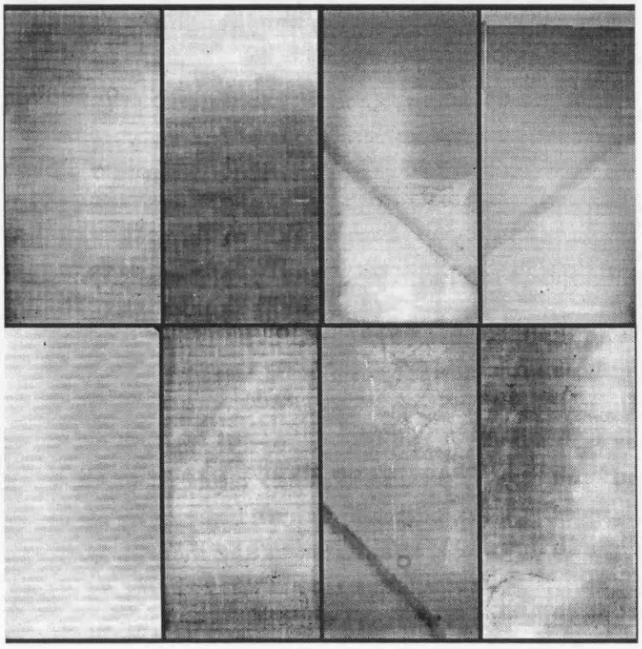

Figure 2.15: A master *B* flat frame – This is an example of master *B* flat frame made from 25 frames taken over September 2001 run with median combination.

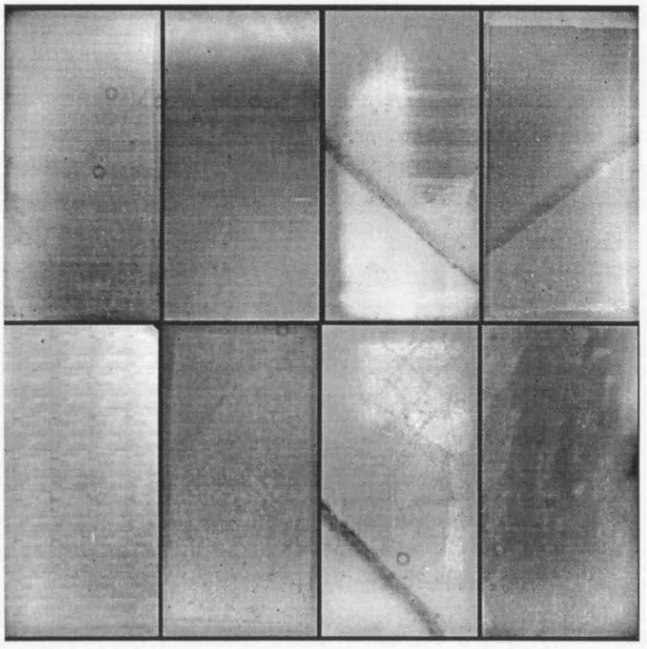

Figure 2.16: A master V flat frame – The same as Figure 2.15 except that the V master flat is made from 24 frames.

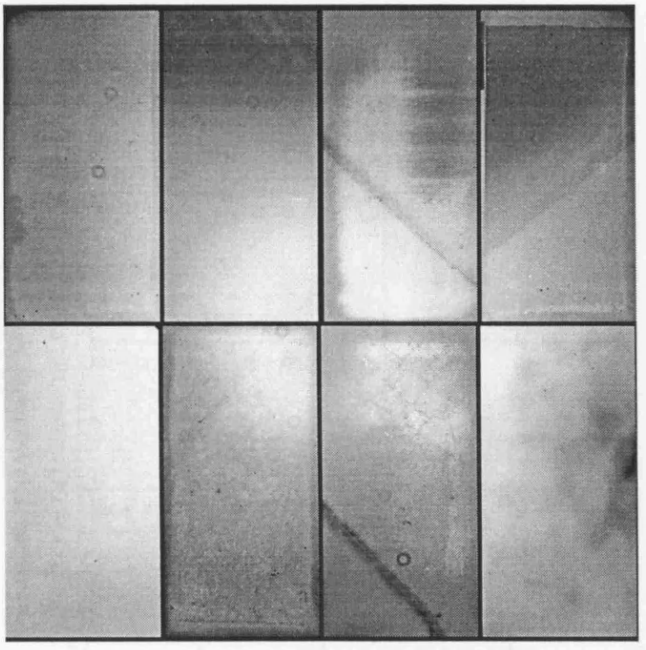

Figure 2.17: A master R flat frame – The same as Figure 2.15 except that the R master flat is made from 24 frames.

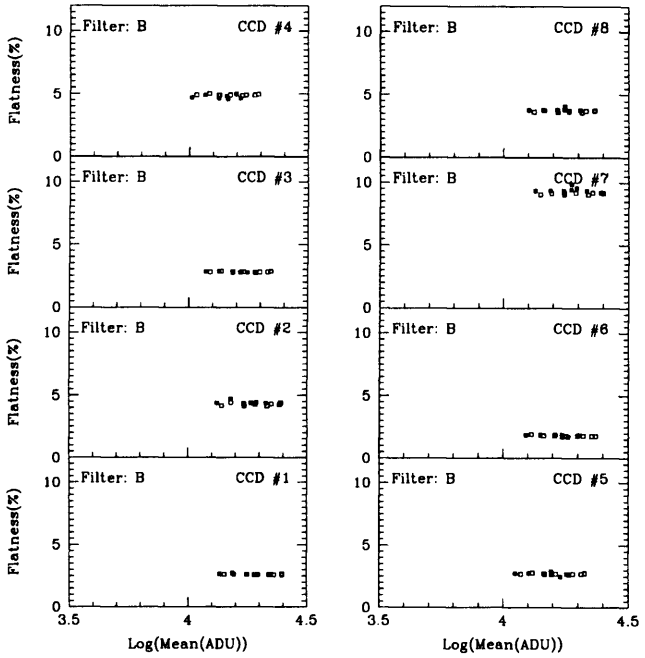

Figure 2.18: Flatness for the B flat for the November 2002 run. The open and filled rectangles represent November 2002*b* (9 frames) and 2002*a* (7 frames) data, respectively.

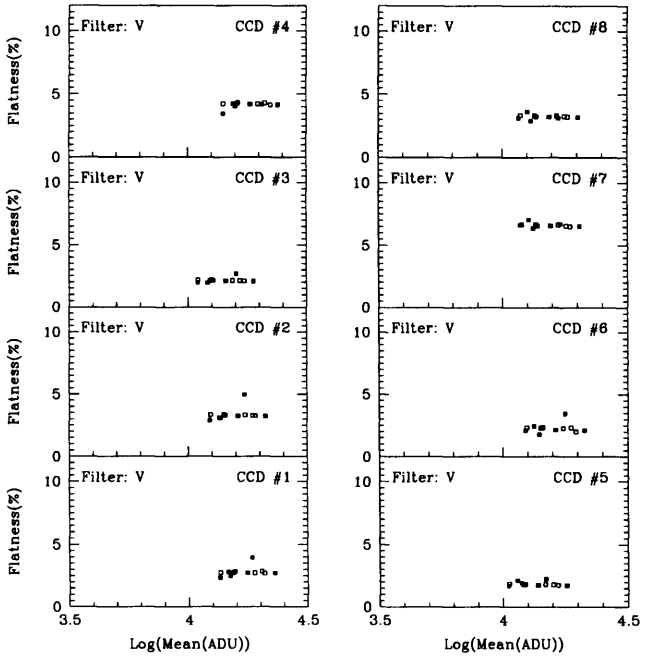

Figure 2.19: Flatness for the V flat, symbols as in Figure 2.18.

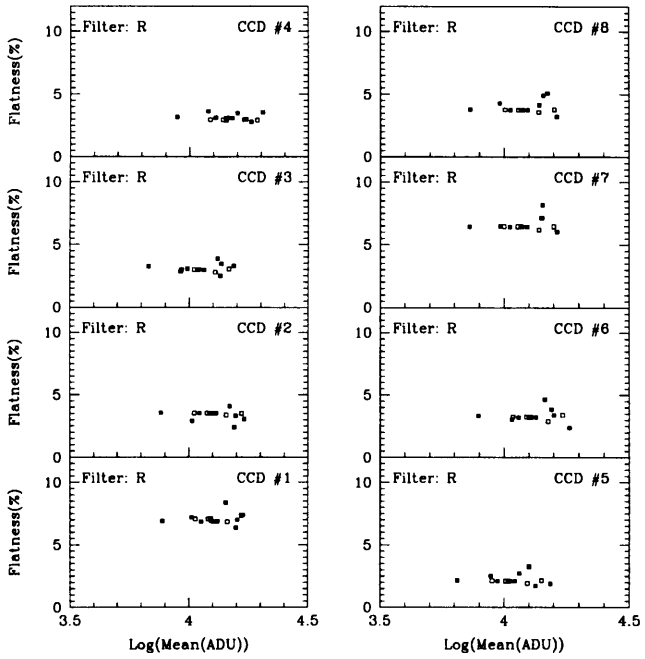

Figure 2.20: Flatness for R flat, symbols as in Figure 2.18.

2.4 Conclusion

We have acquired a very large photometric dataset using a mosaic system, WFI, covering three observational runs. Each CCD in the mosaic has a characteristic cosmetics, bias level, non-linear response, dark-current, and flat-field properties. Those features are also showed variations with respect to runs. So we have investigated each aspect, and conclude that each can be satisfactory accounted for or corrected.

CHAPTER 3

Data reduction and Photometry

The reduction procedure for mosaic and single CCDs is essentially identical provided the former is treated independently for each chip. However, excellent reduction tools exist, such as the Image Reduction and Analysis Facility (IRAF) package **MSCRED**, which allows for each chip to be dealt with simultaneously. Documentation detailing the reduction procedures can be found on-line at the National Optical Astronomy Observatories (NOAO) (http://www.noao.edu/noao/noaodeep/ReductionOpt/frames.html) and Local Group Survey: Mosaic Reduction Notes (http://www.lowell.edu/users/massey/lgsurvey/splog2.html) webpages, and also 'A User's Guide to CCD Reductions with IRAF' (Massey, 1997) for a basic guide to CCD data reduction. Here we give an overview of the reduction procedures in section 3.1. In section 3.2, we describe the models of standardisation and test completeness for the survey area and photometry in section 3.3. The method of combining frames is explained in section 3.4, with internal and external calibration. In section 3.5, we compare our results with published catalogues in terms of astrometry and photometry. Lastly we briefly mention how to make a three-colour composite image, in section 3.6.

3.1 Preprocessing

The following is a brief summary of data and computing facilities that were available to us. A list of the main reduction procedures is also given for quick reference.

- Data : Wide Field Imager (WFI) mosaic (#8 $\times$ 2k $\times$ 4k).

- Hardware : A linux PC running Redhat v7.2/9.1 with 1 GB Memory and a 200 GB hard drive.
- Software : **IRAF** v2.11.3, **MSCRED** v4.5 and **FIGARO** v5.6 and the image display tools ds9 and GAIA.

The main preprocessing reduction steps are

- Creating an initial bad pixel mask
- Overscan and bias correction
- Linearity correction
- Dark frame correction
- Flat field correction
- Updating bad pixel mask
- Setting world coordinate system

3.1.1 Creating an initial bad pixel mask

As detailed in section 2.1, the WFI mosaic CCD chips suffer from 'hot' and 'cold' pixels, especially chips #1 and #4. In order to allow for this we identified bad columns and rows by examining each individual chip. An initial 'Bad Pixel Mask' (BPM) was then constructed for each chip using the **imreplace** task in IRAF; we then examined the mosaic image for all the frames obtained using the **mscdisplay** task and searched each frame for 1) vignetting effect, 2) crosstalk caused by sharing the same control box, and 3) bad focusing and other defects. The first is potentially a serious problem in wide field imaging. Vignetting, which is caused by various out-of-focus obstructions in the light path, can result in the dimming of objects towards the edge of the telescope field of view. Fortunately, our WFI data did not appear to show any significant vignetting effects and any slight effects that were present could be removed easily enough by flat fielding.

The second effect can also cause problems. Often, in mosaic systems, pairs of CCD chips share the same controller box which can give rise to an artifact known as crosstalk between the two chips (Valdes, 2002). This is best seen as a 'reflection' of heavily saturated stars from one chip to the next. Again, we are rather fortunate in that the crosstalk signals were not strong in the WFI mosaic case where each of the two controllers is used to read 4 chips so we did not need to apply any corrections for this. In the cases where frames were incorrectly focused we simply rejected them as they are of limited scientific use.

In addition to visually examining each frame, we checked image header files for all object frames using the **imheader** task to make sure all the necessary information such

as gain, readout noise, saturation level, and airmass for example, were present. (These are accessed directly by some of the data reduction procedure.) We found it was necessary to insert values for the gain, readout noise, and saturation levels, using the information from the instrument documentation (refer to Table 2.1). Note that the saturation levels in Table 2.1 are those above bias levels. In some frames the airmass information was also missing so we calculated and inserted these values as explained in section 2.

3.1.2 Overscan and bias correction

We do not use the standard technique when overscan and bias correcting our data. Firstly we prefer to use the median value rather than mean, for the purpose of eliminating the influence of cosmic rays and cosmetic features when correcting our overscan and bias. Secondly, we choose not to fit the overscan region with a low order spline fit along each column or row. Instead, we adopt a single value with which to overscan correct our data by taking the median of the entire overscan region: typically, a median value for each line or row of the overscan region is used to correct data. In order to obtain this median value we split the mosaic into its separate CCDs and used the **ISTAT** routine in the starlink software, **FIGARO**, to get a median value for whole overscan area. We then reform the mosaic image. As a pipeline, we made **IRAF** script files (Anderson, 1989) using the starlink softwares and **IRAF** packages.

To create our master bias (or zero image) frame, we combined every (overscan corrected) bias frame taken during an entire each observing run using the **zerocombine** task, with a median filter to reject spurious pixels. We then subtracted the zero image frame from every science frame within that observing run.

3.1.3 Linearity correction

After application of the master bias frame, it is necessary to apply a polynomial linearity correction to the WFI data. The recommended polynomial relation is given by Equation 3.1 and coefficients are present in Table 3.1 (see http://www.aao.gov.au/wfi/commission_plan.html).

$$N_c = \mathrm{A0} \cdot N_m + \mathrm{A1} \cdot N_m^2 + \mathrm{A2} \cdot N_m^3 + \mathrm{A3} \cdot N_m^4, \tag{3.1}$$

where N_c is the corrected count and N_m is the observed count in each pixel. Unfortunately, the **MSCRED** package does not support a linearity correction task so we have to split

Table 3.1: Recommended polynomial linearity correction coefficients for the WFI data.

CCD	A0	A1	A2	A3	Residuals (%)
#1	1	0	3.86e-12	0	0.4
#2	1	0	3.18e-12	0	1.0
#3	1	0	8.43e-12	0	0.9
#4	1.02753	-1.6455e-6	1.7791e-11	0	0.8
#5	1	0	4.26e-12	0	1.3
#6	1	0	4.26e-12	0	1.3
#7	1	0	-5.50975e-12	2.39334	0.6
#8	1	0	5.37e-12	0	0.4

each Multiple Extension FITS (MEF) image into individual CCDs again, insert coefficient values in each image header, calculate linearity corrections using the **imexpr** task, and then join the images back together.

3.1.4 Dark correction

We again choose to use a median filter when constructing master dark frames. We create them according to the exposure times of our astronomical frames (*e.g.* 60s and 600s). We find that the dark current rate level in 60s astronomical images is negligible (see section 2.3) but we apply the correction nonetheless for completeness and consistency.

3.1.5 Flat field correction

Master twilight flat frames are created using by the **flatcombine** task. For each colour, we combine all the twilight flat frames acquired each run and apply the master frame to all object frames. Next we generate master sky flat frames with the **sflatcombine** task, using twilight flat field corrected object frames from the same day, and apply them to all the object frames to give secondary flat fielding corrections. The **flatcombine** and **sflatcombine** tasks are clever enough to process frames with respect to filter sets.

3.1.6 Updating bad pixel mask

Besides the basic cosmetics of CCD chips, the saturated pixels in general, and the bleed trails from saturated stars in particular, contain no useful information and give rise to noise and errors in the image when we generate the world coordinate system and do photometry. We masked and fixed those bad pixels during master bias correction using the **ccdproc** task with the setting 'saturate', 'bleed', and 'fixpix' parameters set to yes. Cosmic-rays will cause further problems as their positions on the frame are random. We therefore have to add such pixels to our updated bad pixel masks for each frame individually in order to remove them. We do these by using the **craverage** task to detect the cosmic rays and the **fixpix** task to replace by the average of their neighbouring pixels.

After creating the cosmic ray mask, we combine it with our previously created bad pixel mask and set all bad pixels to a value of 60000 (*i.e.* above saturation level) according to Massey's (basically, Valdes') note. This is because the photometry routines will know to reject such high values from our data. We insert 'SETBPM' keyword into header file to keep information from this reduction step.

3.1.7 Setting world coordinate system

Unfortunately, WFI data have no World Coordinate System (WCS) information for our observation runs; moreover, the right ascension (RA) and declination (DEC) information in header file is inaccurate because the telescope pointing is relatively poor. We therefore have to create a WCS for all our object frames manually, using **IRAF** and other software. Valdes' 'Creating a Mosaic World Coordinate System' is an excellent guide; however, the disadvantages of his method is that we have to do this process by hand, which is very time consuming when many frames are involved. Therefore, we choose to use the **WCStools** software (Mink, 1996, 1997, 1999). It is a semi-automatic method in our case because we have to create an initial WCS data file (see below), based on the coordinates of least three stars for each frame. However, because of the poor pointing and inaccurate RA and DEC information, the initial WCS data file is only valid for the same grid of frames taken on the same day. That is, it does not work for dithered frames (even for the same grid taken on different days).

The WCS setting procedures used in this study are as follows.

- Firstly we edit each CCD chip's initial WCS data file having physical coordinates (X

and Y) and matching celestial coordinates (RA and DEC) for each grid, including at least three stars. Although there are many ways to make an initial WCS data file, we choose to display the image in a display tool (*e.g.* ds9) and get digitised sky images for the same area in **gaia**. Then we search for and identify stars that are located towards the corners of each image so that we can produce a coarse WCS reference grid for the entire frame.

- The next step is to create an initial WCS using the **ccmap** task using the default parameters except the 'project' parameter which we set to 'tan' because **WCStools** program can only support the 'tan' option at the moment.

- To extract positions and magnitudes from the image, the **SExtractor** software (Bertin and Arnouts, 1996) was used.

- Lastly, the **imwcs** task in **Wcstools** program makes precise WCS using the USNO-A2.0 star catalogue (Urban *et al.*, 1997).

After doing these steps, it is strongly recommended that one should check the accuracy of WCS using the **msctpeak** task included in **MSCRED** package. Now it is time to take into account several effects such as differential atmospheric refraction, scale change, and axis rotation in order to transform mosaic data into a uniform plate scale. The **msccmatch** task is used to correct these effects. The further steps are required if one wants to do photometry in combined images. However, as we were planning to do photometry for individual CCD chips to get a better photometry, we did up to this step as preprocessing.

3.2 Standardization

The next step in the reduction procedure is to get instrumental magnitudes using the point spread function (PSF) in the DAOPHOT package of IRAF, and performed in the usual manner. For the philosophical and technical methods and algorithms of DAOPHOT, see Stetson (1987); for a cookbook of stellar CCD photometry, refer to Massey and Davis (1992) and Wells (1994). The Starlink cookbook by Palmer and Davenhall (1999) is also an excellent source of background material.

The final stage is to transform the data into the standard system using aperture photometry of standard stars. In our study we used the Massey (2002) catalogue stars with $\sigma \leq 0.02^{\mathrm{m}}$ in each filter as standards, rather than Landolt (1983, 1992) or E-region

(Kilkenny *et al.*, 1998) standard stars, because they are inappropriate to mosaic CCDs with large FOVs.

The Massey (2002) survey area includes pointing #7, 9, 14, 18 and partially #2, 3, 4, 5, 6, 8, 10, 11, 12, 13, 15, 16, 17, 19, 20, 21, 28 in our fields (see Figure 2.3). Basically the transformation into the standard system uses a least square fitting technique such as Alcaino *et al.* (2003). However in our study, we made three reduction models and selected the best model. Before explaining each model, we suppose that, for each chip in the mosaic, there is a simple linear colour transformation between the standard and instrumental systems, of the form

$$V = v_0 + \epsilon(B - V). \tag{3.2}$$

Here v_0 is the instrumental V magnitude, and ϵ is colour term which varies from chip to chip. For the validity of this assumption we plot the cumulative ratio of $(V - v_0)$ values against $(B-V)$ in Figure 3.1 for the three observations. The solid, dotted, and long dashed lines represent the September, October 2001 and November 2002 data respectively. The vertical and horizontal lines are mean and 1σ values in each observation.

In principle, we can write

$$v_0 = -2.5 \log_{10} N_v + \alpha_v - k_v X \tag{3.3}$$

where

- N_v is the number of counts per second from the star (after all preliminary data processing steps, including background subtraction, have been concluded; *i.e.*, N_v is the net stellar signal)
- α_v is a normalising 'constant' term (and is constant only if conditions are photometric, otherwise it is variable); and
- k_v is the extinction coefficient, and X is the airmass

Of course, equivalent equations can be applied to other passbands. In general – and certainly for the WFI data discussed here – it is not safe to assume that α is constant, so this normalising constant has to be determined for every exposure. In that case, if $k_v X$ is approximately constant across a CCD frame, it can be absorbed into this normalizing constant (that is, we may write $\alpha_v - k_v X \simeq c$). For $z \simeq 60°$ and $k \simeq 0.1$ we have

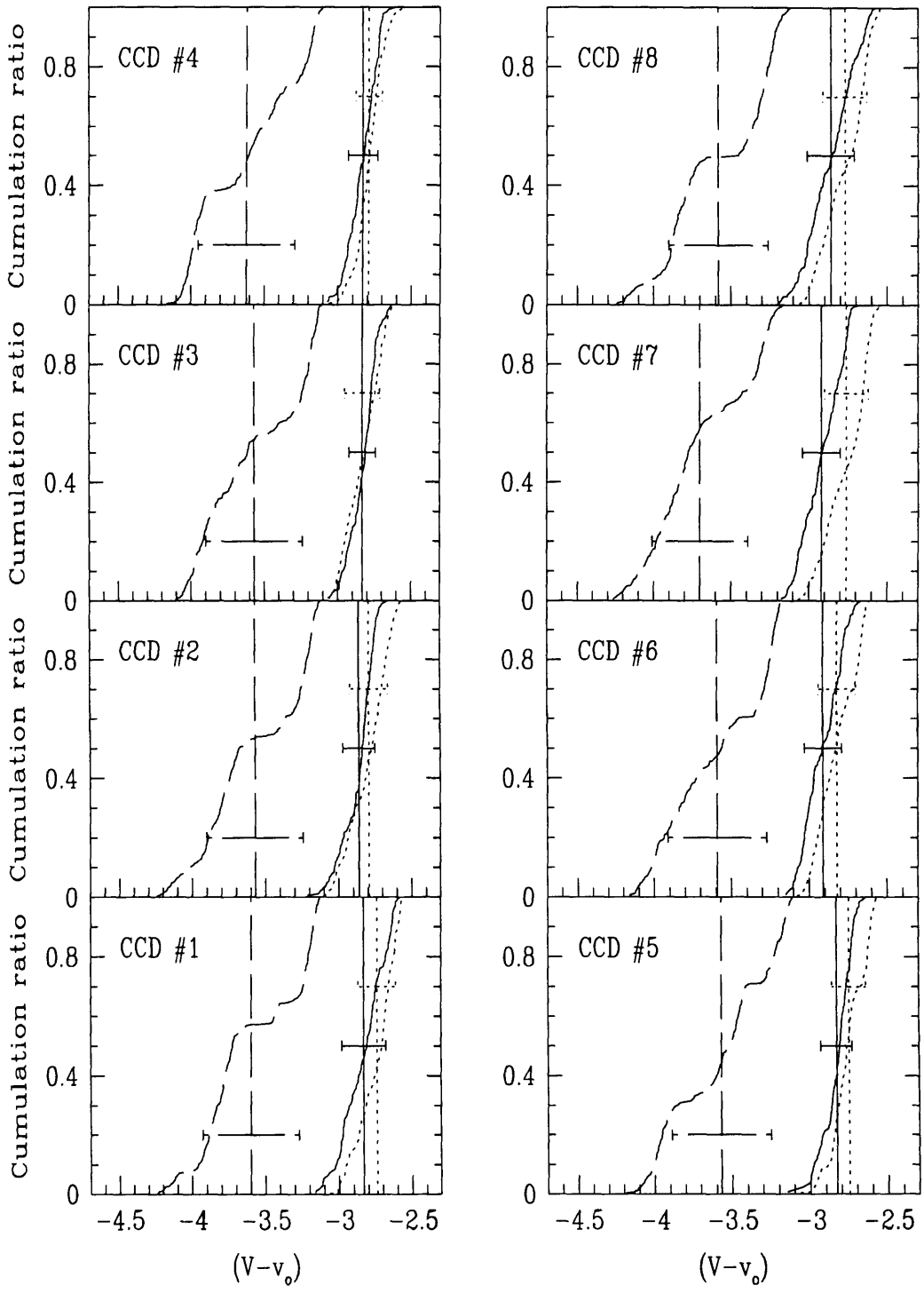

Figure 3.1: The cumulative ratio plot of $(V - v_0)$ for three observations. Solid, dotted, and long dashed lines are September, October 2001 and November 2002 data respectively. The vertical and horizontal lines represent mean and 1σ values in each observation.

$\partial kX/\partial z < 0.01\text{m}/^\circ$, which suggests that this is acceptable. (One could, in principle, reduce this error further by assuming a reasonable value for k, and applying differential corrections across the frame, by writing $c = c_0 + k\Delta X$, where ΔX is the difference in airmass with respect to the centre of the CCD.)

3.2.1 Model 1

Model 1 assumes that each CCD on the mosaic is to be reduced in isolation (*i.e.*, without any knowledge of the other chips). We already have

$$V = -2.5\log_{10} N_v + \alpha_v - k_v X + \epsilon(B - V), \tag{3.4}$$

and, from the previous discussion, we combine α and kX into a single term. Putting $-2.5\log_{10} N_v \equiv v$ and $\alpha_v - k_v X \equiv c_V$, then our adopted model relating the observed and true magnitudes is

$$V = v + c_V + \epsilon_V(B - V) \tag{3.5}$$

In a similar manner, when we assume that there is a simple linear transformation between colour indices and their net signals,

$$(B - V) = c_{BV} + \epsilon_{BV}(b - v) \tag{3.6}$$

and

$$(V - R)_J = c^J_{VR} + \epsilon^J_{VR}(v - r)_J \tag{3.7}$$

$$(V - R)_C = c^C_{VR} + \epsilon^C_{VR}(v - r)_C \tag{3.8}$$

where $b \equiv -2.5\log_{10} N_b$ and $r \equiv -2.5\log_{10} N_r$ in each filter system. From equation 1.6 (Bessell, 1983), we can rewrite equation 3.8 as the following:

$$(V - R)_J = c_{VR} + \epsilon_{VR}(v - r)_C \tag{3.9}$$

where we assume that c's vary from one exposure to another because of changes in atmospheric transmission, but that ϵ's are constant for a given chip. Equations 3.5, 3.6, and 3.9 are the basic formulae of our standardisation transformation equations.

In order to estimate c's and ϵ's, suppose we have $j = 1, M$ different exposures. Say, we will use all the exposures in a given colour system, regardless of exposure time or field

centre. For each exposure, the frame contains $i = 1, N(j)$ standard stars. The residual, or difference, between observed and modelled magnitudes for star i in frame j is

$$r_{i(j)} = (v - V)_{i(j)} + c_{Vj} + \epsilon_V (B - V)_{i(j)} \tag{3.10}$$

from equation 3.5. The best (least-squares) estimates of ϵ's and of the set of M different c_j's values, is obtained by minimizing χ^2, the weighted sum of the squares of the residuals;

$$\chi^2 \equiv \sum_{j=1}^{M} \sum_{i=1}^{N(j)} \left[\frac{r_{i,j}^2}{\sigma_{i,j}^2} \right].$$

$$\begin{aligned}
\chi^2 &= \sum_{i(1)=1}^{N(1)} \frac{1}{\sigma_{i(1)}^2} \left[(v - V)_{i(1)} + c_{V1} + \epsilon_V (B - V)_{i(1)} \right]^2 \\
\ldots &+ \sum_{i(j)=1}^{N(j)} \frac{1}{\sigma_{i(j)}^2} \left[(v - V)_{i(j)} + c_{Vj} + \epsilon_V (B - V)_{i(j)} \right]^2 \\
\ldots &+ \sum_{i(M)=1}^{N(M)} \frac{1}{\sigma_{i(M)}^2} \left[(v - V)_{i(M)} + c_{VM} + \epsilon_V (B - V)_{i(M)} \right]^2,
\end{aligned} \tag{3.11}$$

i.e.,

$$\chi^2 = \sum_{j=1}^{M} \left\{ \sum_{i(j)=1}^{N(j)} \frac{1}{\sigma_{i(j)}^2} \left[(v - V)_{i(j)} + c_{Vj} + \epsilon_V (B - V)_{i(j)} \right]^2 \right\}, \tag{3.12}$$

where the weights, $1/\sigma^2$, might reasonably be computed by assuming $\sigma = \sqrt{N_v}$.

The condition of minimizing the sum of the squares of the residuals requires

$$\begin{aligned}
\frac{\partial \chi^2}{\partial \epsilon_V} &= 0, \\
\frac{\partial \chi^2}{\partial c_{Vj}} &= 0, \qquad j = 1, M;
\end{aligned} \tag{3.13}$$

that is,

$$\begin{aligned}
\frac{\partial \chi^2}{\partial \epsilon_V} &= \sum_{j=1}^{M} \left\{ \sum_{i(j)=1}^{N(j)} \frac{2}{\sigma_{i(j)}^2} (v - V)_{i(j)} (B - V)_{i(j)} \right\} \\
&+ \sum_{j=1}^{M} \left\{ c_{Vj} \sum_{i(j)=1}^{N(j)} \frac{2}{\sigma_{i(j)}^2} (B - V)_{i(j)} \right\} \\
&+ \sum_{j=1}^{M} \left\{ \epsilon_V \sum_{i(j)=1}^{N(j)} \frac{2}{\sigma_{i(j)}^2} (B - V)_{i(j)}^2 \right\}, \qquad \text{and} \\
\frac{\partial \chi^2}{\partial c_{Vj}} &= \sum_{i(j)=1}^{N(j)} \frac{2}{\sigma_{i(j)}^2} (v - V)_{i(j)} + c_{Vj} \sum_{i(j)=1}^{N(j)} \frac{2}{\sigma_{i(j)}^2} + \epsilon_V \sum_{i(j)=1}^{N(j)} \frac{2}{\sigma_{i(j)}^2} (B - V)_{i(j)}
\end{aligned} \tag{3.14}$$

To clarify the summations, we write these equations as

$$\begin{aligned}\frac{\partial\chi^2}{\partial\epsilon_V} &= A_{1,1} + c_{V1}A_{1,2} + \epsilon_V A_{1,3} \\ &+ A_{2,1} + c_{V2}A_{2,2} + \epsilon_V A_{2,3} \\ &+ A_{3,1} + c_{V3}A_{3,2} + \epsilon_V A_{3,3} \\ \ldots &+ A_{M,1} + c_{VM}A_{M,2} + \epsilon_V A_{M,3} \end{aligned} \tag{3.15}$$

i.e.,

$$\begin{aligned}\frac{\partial\chi^2}{\partial\epsilon_V} &= \sum_{k=1}^{M} A_{k,1} + \sum_{k=1}^{M} c_{Vk}A_{k,2} + \epsilon_V \sum_{k=1}^{M} A_{k,3} = 0; \\ \frac{\partial\chi^2}{\partial c_{Vj}} &= B_{j,1} + c_{Vj}B_{j,2} + \epsilon_V B_{j,3} = 0, \qquad j = 1, M \end{aligned} \tag{3.16}$$

So, we have $M + 1$ simultaneous equations with $M + 1$ unknowns (ϵ_V, together with $c_{Vj}, j = 1, M$), which can be solved by standard techniques. In order to get a solution by Gauss-Jordan elimination method, we express those equations in matrix form given by

$$\begin{bmatrix} A_{11} & A_{22} & \cdots & A_{M2} & (A_{11} + A_{22} + \cdots + A_{M3}) \\ B_{12} & 0 & \cdots & 0 & B_{13} \\ 0 & B_{22} & \cdots & 0 & B_{23} \\ \ldots & \ldots & \ldots & \ldots & \ldots\ldots\ldots\ldots \\ 0 & 0 & \cdots & B_{M2} & B_{M3} \end{bmatrix} \begin{bmatrix} c_{V1} \\ c_{V2} \\ \cdot \\ c_{VM} \\ \epsilon_V \end{bmatrix} = \begin{bmatrix} -(A_{11} + A_{21} + \cdots A_{M1}) \\ -B_{11} \\ -B_{21} \\ \cdot \\ -B_{M1} \end{bmatrix}$$

The solution of this set of simultaneous equations is a simple matrix inversion which we solve using the *gaussj* subroutine in Numerical Recipes (Press *et al.*, 1992). As well, it can also be quite straightforwardly extended to allow calculation of formal errors on ϵ_V and the c_{Vj} values.

We can calculate the values of the ϵ_{BV}, c_{BVj} and ϵ_{VR}, c_{VRj} using the same method as V. In Table 3.2, we summarise the values of ϵ's and the average values of c's ($\bar{c}$'s) using Model 1 for the three observations with respect to exposure time (*e.g.* 60s and 600s).

3.2.2 Model 2

Model 2 takes the same basic assumption of a simple linear colour transformation being applicable to each chip. We also assume that each chip has a different sensitivity to every other chip in the mosaic, but we now make the additional assumption that the ratios of chip sensitivities is constant *e.g.* if chip #1 is twice as efficient as chip #2 for one exposure, it is twice as efficient for all exposures.

For this model, we need to determine:

Table 3.2: The ϵ's and $\bar{c}$'s values for the three observations using Model 1 with respect to exposure time in equations 3.5, 3.6, and 3.9.

	Sep. 2001		Oct. 2001		Nov. 2002	
	60s frames	600s frames	60s frames	600s frames	60s frames	600s frames
$\bar{c}_V$	26.595	29.017	26.697	29.172	25.778	28.245
$\sigma_{\bar{c}_V}$	0.149	0.160	0.108	0.100	0.319	0.336
ϵ_V	0.035		0.028		0.052	
$\bar{c}_{BV}$	-0.616	-0.584	-0.649	-0.615	-0.671	-0.731
$\sigma_{\bar{c}_{BV}}$	0.107	0.060	0.060	0.053	0.103	0.080
ϵ_{BV}	0.912		0.989		0.935	
$\bar{c}_{VR}$	-0.026	0.001	0.045	0.005	-0.042	-0.049
$\sigma_{\bar{c}_{VR}}$	0.083	0.081	0.042	0.031	0.075	0.086
ϵ_{VR}	0.885		0.931		0.916	

- ϵ for each chip;
- the relative sensitivity of each chip. We make an arbitrary choice, say CCD #1 is the reference chip, which by definition has relative sensitivity of 1.0;
- a normalising constant for the entire mosaic, for each exposure.

The advantage of this model is that the relative sensitivities of the chips are determined from observations of all the standard stars in all exposures and that the overall normalisation for a given exposure is determined by all the standard stars on the entire mosaic, not just those on a single chip. That means that these normalisations should be determined with much greater precision.

One of the disadvantages of this model is that it does make an additional assumption – which may or may not be correct. Another is that it can only be used for the mosaic frames containing standard stars in every chip. Therefore this model can determine precise normalisation but based on low statistics.

As before, we have $j = 1, M$ different exposures of the mosaic and also have $k = 1, K$ CCD chips on the mosaic. For the jth exposure we have $i = 1, N(j,k)$ standard stars for

the kth chip. Our basic model relating observed counts to standard magnitudes is then

$$V_{i(j,k)} = -2.5\log_{10}(N_{i(j,k)} \times f_k) + c_{Vj} + \epsilon_{Vk}(B-V)_{i(j,k)} \tag{3.17}$$

where f_k is the relative sensitivity of chip k, which has colour term ϵ_k, and c_j is the (mosaic-wide) normalisation for exposure j. For convenience, we again rewrite this as

$$V_{i(j,k)} = v_{i(j,k)} + g_{Vk} + c_{Vj} + \epsilon_{Vk}(B-V)_{i(j,k)} \tag{3.18}$$

As for Model 1, the transformation equations of Model 2 are

$$\begin{aligned} V &= v + g_{Vk} + c_{Vj} + \epsilon_{Vk}(B-V) \\ (B-V) &= g_{BVk} + c_{BVj} + \epsilon_{BVk}(b-v) \\ (V-R) &= g_{VRk} + c_{VRj} + \epsilon_{VRk}(v-r)_C \end{aligned} \tag{3.19}$$

The residuals which we wish to minimise in order to obtain best estimates of the coefficients of V in equation 3.19 are

$$r_{i(j,k)} = (v-V)_{i(j,k)} + g_{Vk} + c_{Vj} + \epsilon_{Vk}(B-V)_{i(j,k)} \tag{3.20}$$

For exposure j of chip k, the weighted sum of the squares of the residuals is

$$\chi^2_{j,k} = \sum_{i(j,k)=1}^{N(j,k)} \frac{1}{\sigma^2_{i(j,k)}} \left[(v-V)_{i(j,k)} + g_{Vk} + c_{Vj} + \epsilon_{Vk}(B-V)_{i(j,k)}\right]^2 \tag{3.21}$$

We want to minimize the total χ^2, summed over all chips, and all exposures:

$$\chi^2 = \sum_{k=1}^{K} \left\{ \sum_{j=1}^{M} \left\{ \sum_{i(j,k)=1}^{N(j,k)} \frac{1}{\sigma^2_{i(j,k)}} \left[(v-V)_{i(j,k)} + g_{Vk} + c_{Vj} + \epsilon_{Vk}(B-V)_{i(j,k)}\right]^2 \right\} \right\} \tag{3.22}$$

Once again, we want to minimize the sum of the squares of the residuals, by setting

$$\begin{aligned} \frac{\partial\chi^2}{\partial\epsilon_{Vk}} &= 0, \qquad k = 1, K \\ \frac{\partial\chi^2}{\partial g_{Vk}} &= 0, \qquad k = 2, K \\ \frac{\partial\chi^2}{\partial c_{Vj}} &= 0, \qquad j = 1, J \end{aligned} \tag{3.23}$$

(where we have chosen $g_{V1} \equiv 1$), where

$$\begin{aligned} \frac{\partial\chi^2}{\partial\epsilon_{Vk}} &= \sum_{j=1}^{M} \left\{ \sum_{i(j,k)}^{N(j,k)} \frac{2}{\sigma^2_{i(j,k)}} \left[(v-V)_{i(j,k)} + g_{Vk} + c_{Vj} + \epsilon_{Vk}(B-V)_{i(j,k)}\right](B-V)_{i(j,k)} \right\} \\ \frac{\partial\chi^2}{\partial g_{Vk}} &= \sum_{j=1}^{M} \left\{ \sum_{i(j,k)}^{N(j,k)} \frac{2}{\sigma^2_{i(j,k)}} \left[(v-V)_{i(j,k)} + g_{Vk} + c_{Vj} + \epsilon_{Vk}(B-V)_{i(j,k)}\right] \right\} \\ \frac{\partial\chi^2}{\partial c_{Vj}} &= \sum_{j=1}^{M} \left\{ \sum_{i(j,k)}^{N(j,k)} \frac{2}{\sigma^2_{i(j,k)}} \left[(v-V)_{i(j,k)} + g_{Vk} + c_{Vj} + \epsilon_{Vk}(B-V)_{i(j,k)}\right] \right\} \end{aligned} \tag{3.24}$$

i.e.,

$$\frac{\partial\chi^2}{\partial\epsilon_{Vk}} = \sum_j \sum_{i(j,k)} \frac{(v-V)_{i(j,k)}}{\sigma^2_{i(j,k)}}(B-V)_{i(j,k)} + g_{Vk}\sum_j \sum_{i(j,k)} \frac{1}{\sigma^2_{i(j,k)}}(B-V)_{i(j,k)} + \sum_j c_{Vj} \sum_{i(j,k)} \frac{1}{\sigma^2_{i(j,k)}}(B-V)_{i(j,k)} + \epsilon_{Vk}\sum_j \sum_{i(j,k)} \frac{(B-V)^2_{i(j,k)}}{\sigma^2_{i(j,k)}} = 0 \tag{3.25}$$

$$\frac{\partial\chi^2}{\partial g_{Vk}} = \sum_j \sum_{i(j,k)} \frac{(v-V)_{i(j,k)}}{\sigma^2_{i(j,k)}} + g_{Vk}\sum_j \sum_{i(j,k)} \frac{1}{\sigma^2_{i(j,k)}} + \sum_j c_{Vj} \sum_{i(j,k)} \frac{1}{\sigma^2_{i(j,k)}} + \epsilon_{Vk}\sum_j \sum_{i(j,k)} \frac{(B-V)_{i(j,k)}}{\sigma^2_{i(j,k)}} = 0 \tag{3.26}$$

$$\frac{\partial\chi^2}{\partial c_{Vj}} = \sum_k \sum_{i(j,k)} \frac{(v-V)_{i(j,k)}}{\sigma^2_{i(j,k)}} + \sum_k g_{Vk} \sum_{i(j,k)} \frac{1}{\sigma^2_{i(j,k)}} + c_{Vj}\sum_k \sum_{i(j,k)} \frac{1}{\sigma^2_{i(j,k)}} + \sum_k \epsilon_{Vk} \sum_{i(j,k)} \frac{(B-V)_{i(j,k)}}{\sigma^2_{i(j,k)}} = 0 \tag{3.27}$$

There are $k = 1, K$ in equation 3.25, each with $3 + M$ terms; $k = 2, K$ in equation 3.26, each with $3 + M$ terms; and $j = 1, M$ in equation 3.27, each with $2 + 2K$ terms. That is, there are $2K - 1 + M$ equations.

There are K unknown colour terms, ϵ_{Vk}; $K - 1$ unknown relative sensitivities, g_{Vk}; and M unknown exposure normalisations – *i.e.*, $2K - 1 + M$ unknowns.

The system of simultaneous equations can therefore be solved, as before. Table 3.3 gives the values of ϵ_k's , $\bar{c}$'s and g_k's using Model 2 with respect to exposure time.

Table 3.3: ϵ_k's, $\bar{c}$'s, and g_k's values for the three observations using Model 2 with respect to exposure time.

			g_1	g_2	g_3	g_4	g_5	g_6	g_7	g_8	ϵ_1	ϵ_2	ϵ_3	ϵ_4	ϵ_5	ϵ_6	ϵ_7	ϵ_8	$\bar{c}$
Sep. 2001	V	60s	1.000	0.996	0.991	1.058	0.984	0.947	0.984	0.999	0.015	0.018	0.023	0.032	0.083	0.100	-0.022	-0.009	25.537
		600s																	27.984
	(B-V)	60s	1.000	1.014	1.023	0.888	1.083	0.994	0.986	0.983	0.902	0.884	0.909	1.011	0.852	0.908	0.908	0.906	-1.635
		600s																	-1.551
	(V-R)	60s	1.000	1.003	1.007	0.998	1.024	1.021	1.017	1.022	0.866	0.885	0.889	0.913	0.879	0.865	0.841	0.861	-1.007
		600s																	-1.032
Oct. 2001	V	60s	1.000	1.002	0.993	1.023	1.014	1.008	1.004	1.072	0.063	-0.003	0.059	0.074	0.041	0.007	0.023	-0.066	25.631
		600s																	28.094
	(B-V)	60s	1.000	0.917	0.940	0.877	0.940	0.975	0.914	0.928	0.946	0.996	0.983	1.048	0.992	0.955	0.994	0.992	-1.583
		600s																	-1.593
	(V-R)	60s	1.000	0.983	0.995	1.019	1.027	1.003	1.013	1.056	0.942	0.976	0.949	0.941	0.879	0.935	0.919	0.859	-0.975
		600s																	-0.955
Nov. 2002	V	60s	1.000	0.994	0.967	1.006	1.011	0.955	0.961	0.970	0.008	-0.014	0.128	0.048	0.039	0.077	0.019	0.059	25.236
		600s																	27.387
	(B-V)	60s	1.000	1.012	0.982	0.922	0.999	0.988	1.028	1.006	0.895	0.893	0.945	0.996	0.927	0.898	0.867	0.907	-1.566
		600s																	-1.680
	(V-R)	60s	1.000	1.022	1.056	1.011	1.048	1.048	1.047	1.018	0.933	0.893	0.837	0.979	0.912	0.843	0.821	0.914	-1.048
		600s																	-1.087

3.2.3 Model 3

Model 3 generally follows the assumptions of Model 2. However, instead of assuming that the relative chip sensitivities are constant across the entire mosaic, we now make the more general assumption that the relative sensitivities of chips read out through a single controller are constant. In the WFI system, two San Diego State University second generation CCD controllers (Leach *et al.*, 1998) are mounted to read out the CCDs and transfer the data.

So while Model 2 assumed $g_1 \equiv 1$ and $g_2 - g_8$ to be constant, Model 3 assumes $g_1 \equiv 1$, $g_5 \equiv 1$, and that there is an offset $\Delta_{(j)}$ between controllers 1 and 2. Our model is thus

$$V_{i(jk)} = -2.5\log_{10}(N_{i(jk)} \times f_{Vk}) + c_{Vj} + \epsilon_{Vk}(B-V)_{i(jk)} + \Delta_{Vj(k)} \tag{3.28}$$

We have to adopt one controller as the reference, so we set $\Delta_{Vj(k=1,4)} \equiv 0$.

$$V_{i(jk)} = v_{i(jk)} + g_{Vk} + c_{Vj} + \epsilon_{Vk}(B-V)_{i(jk)} + \Delta_{Vj(k)} \tag{3.29}$$

The standardisation transformations are

$$\begin{aligned} V &= v + g_{Vk} + c_{Vj} + \epsilon_{Vk}(B-V) + \Delta_{Vj(k)} \\ (B-V) &= g_{BVk} + c_{BVj} + \epsilon_{BVk}(b-v) + \Delta_{BVj(k)} \\ (V-R) &= g_{VRk} + c_{VRj} + \epsilon_{VRk}(B-V) + \Delta_{VRj(k)} \end{aligned} \tag{3.30}$$

The residual in V is

$$r_{i(jk)} = (v-V)_{i(jk)} + g_{Vk} + c_{Vj} + \epsilon_{Vk}(B-V)_{i(jk)} + \Delta_{Vj(k)} \tag{3.31}$$

$$\chi^2 = \sum_{k=1}^{K}\sum_{j=1}^{M}\sum_{i(j,k)=1}^{N(j,k)} \left\{\frac{r_{i(jk)}}{\sigma_{i(jk)}}\right\}^2 \tag{3.32}$$

as before in Model 2. Our equations of condition are now

$$\frac{\partial\chi^2}{\partial\epsilon_{Vk}} = 0 \quad k = 1, K \tag{3.33}$$

$$\frac{\partial\chi^2}{\partial g_{Vk}} = 0 \quad k = 2,3,4,6,7,8 \quad [g_{V1} \equiv 1, \quad g_{V5} \equiv 1] \tag{3.34}$$

$$\frac{\partial\chi^2}{\partial c_{Vj}} = 0 \quad j = 1, M \tag{3.35}$$

$$\begin{aligned} \frac{\partial\chi^2}{\partial\Delta_{Vj}} &= 0 \quad j = 2, M \\ &\Delta_{V1} \equiv 0 \quad \text{for} \quad k = 5-8 \\ &\Delta_{Vj} \equiv 0 \quad \text{for} \quad k = 1-4, \quad \text{all} \quad j \end{aligned} \tag{3.36}$$

Table 3.4: ϵ_k's, g_k's, $\bar{c}$'s and $\bar{\Delta}$'s values for the three observations using Model 3 with respect exposure time.

			g_1	g_2	g_3	g_4	g_5	g_6	g_7	g_8	ϵ_1	ϵ_2	ϵ_3	ϵ_4	ϵ_5	ϵ_6	ϵ_7	ϵ_8	$\bar{c}$	$\bar{\Delta}_j$
Sep. 2001	V	60s	1.000	0.998	0.992	1.060	1.000	0.949	0.986	1.001	0.017	0.018	0.023	0.032	0.063	0.100	-0.022	-0.009	25.535	0.000
		600s																	27.983	
	(B-V)	60s	1.000	1.003	1.011	0.876	1.000	0.982	0.974	0.971	0.891	0.884	0.910	1.011	0.904	0.908	0.908	0.906	-1.623	0.000
		600s																	-1.538	
	(V-R)	60s	1.000	1.000	1.004	0.995	1.000	1.018	1.014	1.020	0.860	0.885	0.889	0.913	0.925	0.865	0.841	0.861	-1.004	0.000
		600s																	-1.029	
Oct. 2001	V	60s	1.000	0.990	0.981	1.010	1.000	0.995	0.992	1.060	0.046	-0.003	0.059	0.074	0.044	0.007	0.023	-0.066	25.642	0.000
		600s																	28.106	
	(B-V)	60s	1.000	0.967	0.990	0.928	1.000	1.025	0.964	0.978	0.983	0.996	0.983	1.048	0.984	0.955	0.994	0.992	-1.633	0.000
		600s																	-1.643	
	(V-R)	60s	1.000	0.958	0.970	0.994	1.000	0.978	0.989	1.031	0.883	0.976	0.949	0.941	0.884	0.935	0.919	0.859	-0.950	0.000
		600s																	-0.930	
Nov. 2002	V	60s	1.000	0.990	0.964	1.002	1.000	0.951	0.958	0.966	0.002	-0.014	0.128	0.048	0.051	0.078	0.019	0.058	25.240	0.000
		600s																	27.390	
	(B-V)	60s	1.000	1.012	0.982	0.923	1.000	0.989	1.029	1.006	0.896	0.893	0.945	0.996	0.927	0.898	0.867	0.907	-1.567	0.000
		600s																	-1.681	
	(V-R)	60s	1.000	1.005	1.039	0.993	1.000	1.031	1.029	1.000	0.888	0.892	0.837	0.980	0.996	0.843	0.821	0.912	-1.030	0.000
		600s																	-1.070	

There are K in equation 3.33, $K-2$ in 3.34, M in 3.35, and $M-1$ in 3.36, *i.e.*, $2(K+M)-3$ equations. There are K unknowns in ϵ_k, $K-2$ in g_k, M in c_j, and $M-1$ in Δ_{Vj}, *i.e.*, $2(K+M)-3$ unknowns.

As we increase the number of unknown parameters, the *gaussj* subroutine used in Models 1 and 2 does not work as well, so the *LU* decomposition method (See details in Press *et al.*, 1992) is used to solve the linear set of equations with a double precision option. The solutions for Model 3 are summarised in Table 3.4.

3.2.4 Model test

We first check for the seasonal variations in 600s exposure frames of grid element #02*a* – the element for which we have observations covering the same area of the sky for the three runs with good photometry. We choose the October 2001 data as our reference because they are in the middle of the seasonal sequence and have the best FWHM amongst the element #02*a* data (refer to Table 2.3). Figures 3.2 and 3.3 show the difference in magnitudes in each filter for the September 2001 (S) and November 2002 data (N) with respect to the October 2001 data (O). The average and standard deviations of the magnitude differences plotted in those figures are summarised in Table 3.5. According to the Table 3.5, model 1 has slightly higher errors, however, it shows consistency in the difference throughout the seasons and lower standard deviations compare to models 2 and 3. When the relative chip sensitivity is considered, say in model 2 and 3, we can see an increase in the accuracies, except in $\Delta B(N-O)$, but basically there are no differences between model 2 and model 3, which uses different control boxes.

As an external check for the models, we compared them with a published catalogue. In this case, we calculate weighted magnitudes, as explained in section 3.4.2, with respect to the models and compare them with Zaritsky *et al.* (2002) catalogue in Figure 3.4. This figure also shows that model 2 and 3 have slightly better results.

In conclusion, the complicated models seem to slightly increase the accuracy, however, they require more assumptions and lower statistics. Therefore, we adopt model 1 as the standardisation equations not only because it is a relatively simple model that gives consistency but also because the differences in the errors amongst the models are negligible.

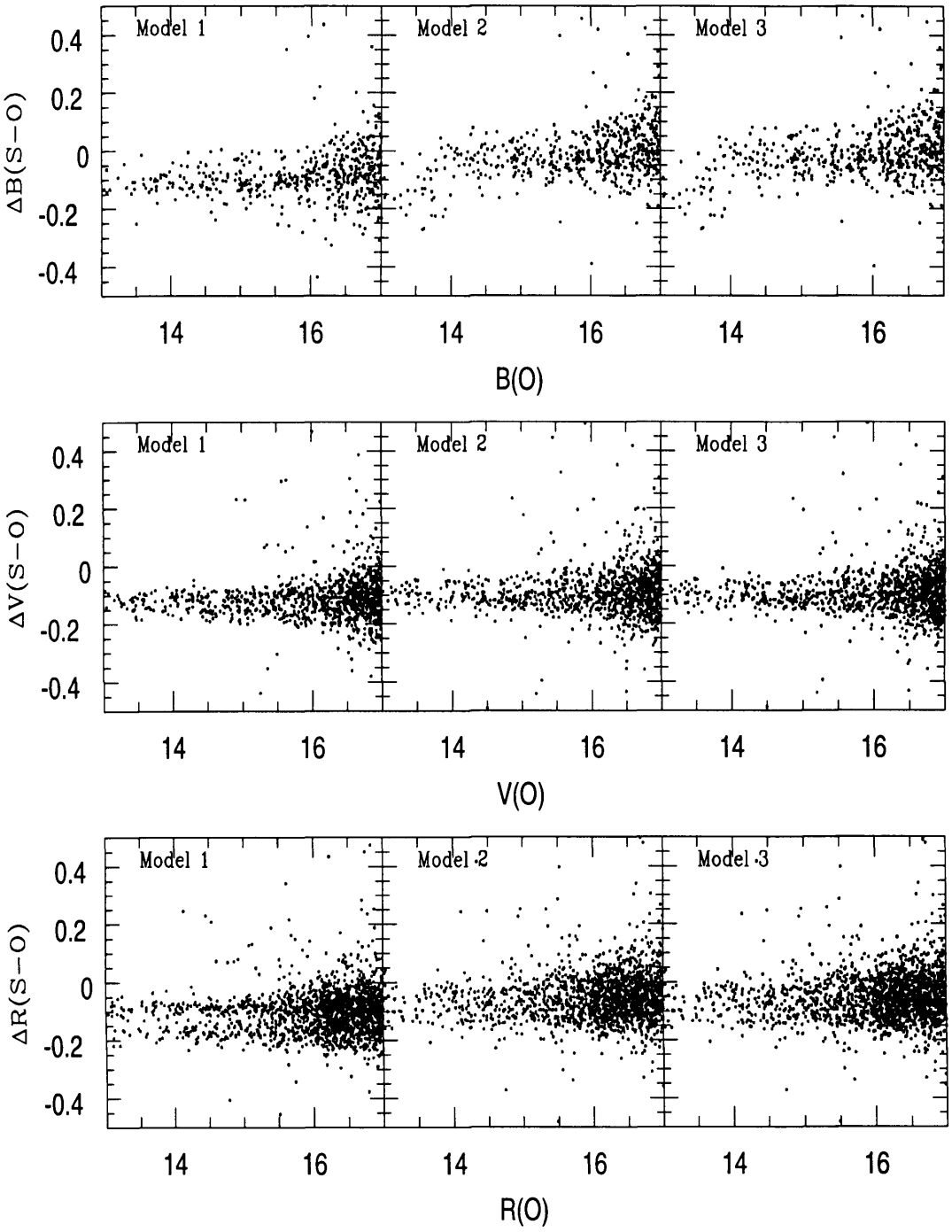

Figure 3.2: The seasonal magnitude variations of B, V,and R using the three models for grid #02a. The x-axis shows the October (O) data and y-axis shows magnitude difference between September and October (S-O).

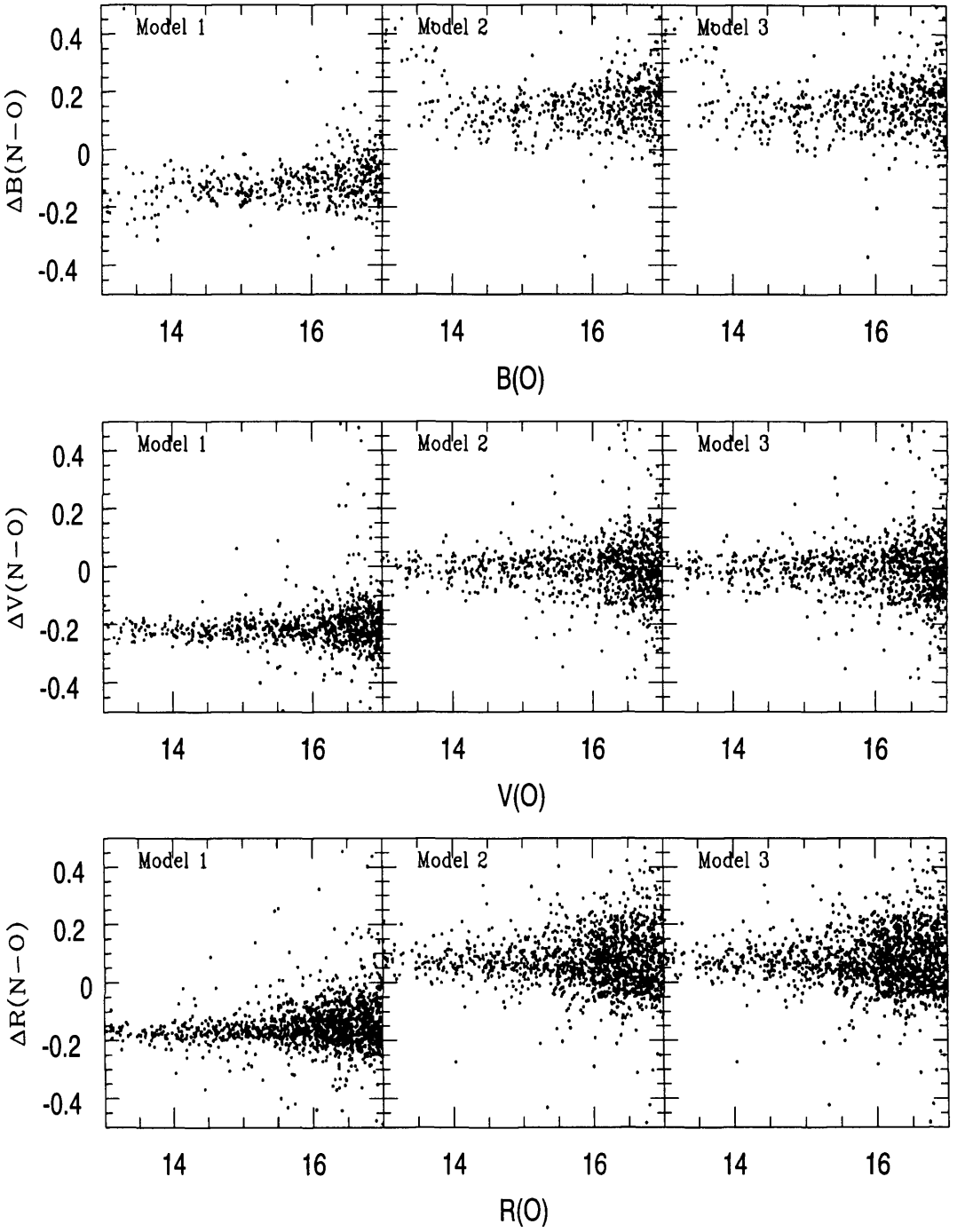

Figure 3.3: The same as Figure 3.2 except the magnitude difference is now between November and October (N-O).

Table 3.5: The averages and standard deviations of the magnitude differences plotted in the Figure 3.2 and 3.3.

		Model 1	Model 2	Model 3
SEP. – OCT.	$\overline{\Delta B}$	-0.090	-0.021	-0.019
	$\sigma_{\Delta B}$	0.081	0.090	0.091
	$\overline{\Delta V}$	-0.117	-0.098	-0.098
	$\sigma_{\Delta V}$	0.058	0.065	0.063
	$\overline{\Delta R}$	-0.110	-0.071	-0.069
	$\sigma_{\Delta R}$	0.073	0.071	0.071
NOV. – OCT.	$\overline{\Delta B}$	-0.112	0.159	0.160
	$\sigma_{\Delta B}$	0.099	0.118	0.120
	$\overline{\Delta V}$	-0.206	0.014	0.013
	$\sigma_{\Delta V}$	0.076	0.127	0.127
	$\overline{\Delta R}$	-0.173	0.076	0.077
	$\sigma_{\Delta R}$	0.084	0.093	0.093

3.3 Completeness tests

Although we performed a photometric survey for the whole SMC area, our data are incomplete in terms of survey area and photometry mainly due to the malfunction of filter systems, weather conditions, binarity, and so on. For the reasons, we discuss the completeness of the survey area in subsection 3.3.1 and of photometry in subsection 3.3.2.

3.3.1 Survey completeness

During the data reduction process, we found that a malfunction in the filter wheel system had caused colour filter to be mis-identified. The result of this is incomplete BVR data sets, such that, for example, in the case of grid #07*b* there is no 60s B filter exposure frame; this is actually V filter image, thus giving a VVR data set. Such data sets were rejected from our catalogue. We also reject non-photometric frames or chips. As a results of these, we estimate the survey completeness ($S.C$) based on the following definition. We assume an 100% survey completeness for a given grid if there are two exposures of 60 and 600s, in photometric conditions, for that grid and its dithered counterparts ($i = 1, 2$) for

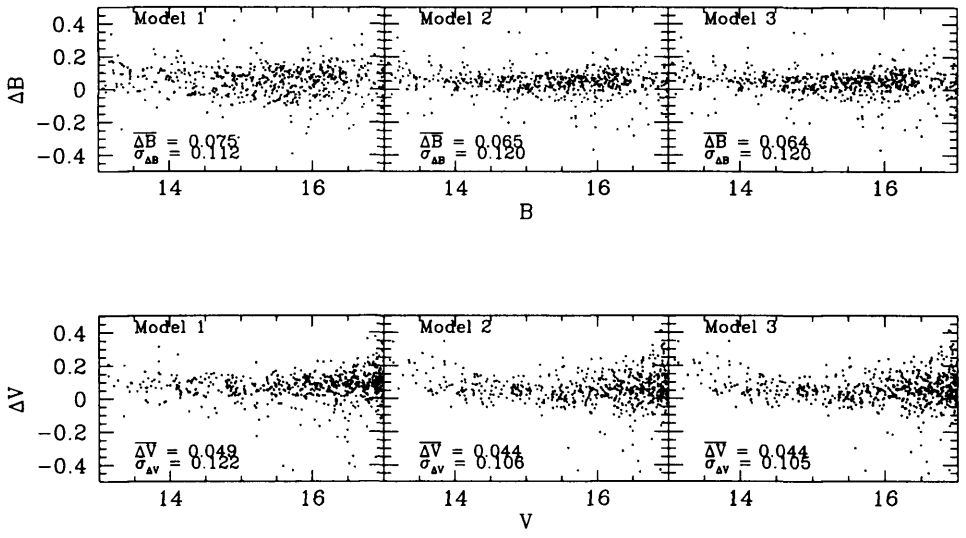

Figure 3.4: The magnitude differences between Zaritsky *et al.* (2002) catalogue and the grid #02*a* stars with respect to standardisation models.

the all chips ($k = 1, 8$). Say,

$$S.C = \frac{\sum_{i=1}^{2}\sum_{k=1}^{8}(N_o^{60}(k) + N_o^{600}(k) - M_o(60,600)(k))_i}{\sum_{i=1}^{2}\sum_{k=1}^{8}(N^{60}(k) + N^{600}(k) - M(60,600)(k))_i} \times 100\ (\%) \tag{3.37}$$

where $N^{60}(k)$ and $N^{600}(k)$ are the (estimated) total number of stars in the kth chip for the 60 and 600s exposure frames, respectively. $M(60,600)(k)$ is the number of matched stars in the 60s and 600s frames in kth chip. If there are chips with no photometric stars in one exposure frame, we estimate the number by multiplying the other exposure frame and the average ratio calculated from its chips having photometric stars in both exposure frames. On the other hand, $N_o^{60}(k)$, $N_o^{600}(k)$ and $M_o(60,600)(k)$ represent the actual number of observed stars in the 60 and 600s frames and matched stars in kth chip, respectively. If there are chips with no photometric stars in both exposure frames, for example, the 3rd and 8th chip in grid #04*a*1 (see Appendix B.1), we estimated the ratio using dithered frames. Lastly, if better dithered frames are available we choose them in our calculation. Through those procedures we find an average 95.1% survey completeness for our SMC survey. Of course, this is (slightly) higher than the actual completeness

Table 3.6: The instrumental magnitude classes used for the artificial star test.

Magnitude ranges	# of artificial stars	Magnitude ranges	# of artificial stars
16.5 - 17.5	12	21.5 - 22.5	357
17.5 - 18.5	56	22.5 - 23.5	484
18.5 - 19.5	114	23.5 - 24.5	516
19.5 - 20.5	147	24.5 -	271
20.5 - 21.5	220		

because one dithered frame can not cover the gaps between each chip and some of the frames are not perfect photometric frames. The photometric frames used to construct the SMC catalogue for the three observations and the survey completeness for each grid are given Appendix B.1.

3.3.2 Photometric completeness

In order to estimate the accuracy of the photometry and to test the sampling completeness, the artificial star technique (Stetson and Harris, 1988; Stetson, 1991) was used in this study. Because our data sets have the two exposure times for each filter frame, the limit of magnitude completeness depends on the 600 second frame in each field. Amongst dithered frames for a given field, we performed the artificial star test for the first dithered frames suffixed as *b*, because not only all fields have them but also they corresponding to mean area for grids having over two ditherings. After fixing the number of artificial stars with respect to the instrumental magnitude ranges given in Table 3.6, we randomly generated positions and magnitudes by random number function, *ran2* (Press *et al.*, 1992). We constrain the positions to an area of [21:2024, 21:4074] to avoid placing stars near the edges on each chip. The results for all fields in B are summarised in Table 3.7. Two example fields in V and R are given in Table 3.8. The full details with respect to each CCD can be found in Appendix B.2. In Table 3.7 and 3.8, the values are the average percentage for the eight CCDs. Because stars brighter than 12 magnitude are saturated in our 600 second B frames, we exclude stars above these magnitudes in our artificial star study. In general, the photometric completeness in B magnitude beginning to decline at $\sim$ 18.5, although B is $\sim$ 17.5 in crowded fields such as # 06*b*, 07*b*, 08*b*, and $\sim$ 19.5 in

Table 3.7: The results of the artificial star test in B for each field. The values in each magnitude range are the average percentage for a mosaic (eight CCDs) image.

Fields	B magnitude ranges								
	13 – 14	14 – 15	15 – 16	16 – 17	17 – 18	18 – 19	19 – 20	20 – 21	21 –
# 01*b*	100.00	98.66	98.25	96.26	92.95	80.99	41.50	4.34	0.46
# 02*b*	100.00	99.55	97.26	94.13	85.85	65.30	29.34	3.37	0.42
# 03*b*	100.00	98.88	99.23	98.98	98.18	96.95	84.48	19.48	1.80
# 04*b*	98.96	97.77	96.05	93.88	88.58	77.07	41.76	8.38	1.01
# 05*b*	100.00	100.00	99.67	99.40	98.64	96.99	82.41	15.70	1.61
# 06*b*	100.00	99.55	97.48	94.81	89.20	72.90	37.35	7.99	2.40
# 07*b*	97.92	99.11	97.81	94.05	87.27	65.65	27.74	7.12	2.31
# 08*b*	98.96	99.55	97.81	96.26	89.60	68.28	28.15	5.72	1.71
# 09*b*	100.00	100.00	99.01	98.47	95.91	88.24	69.63	37.33	12.59
# 10*b*	100.00	100.00	99.78	99.15	97.90	94.26	82.28	55.16	16.42
# 11*b*	100.00	99.55	98.46	98.21	94.94	88.90	65.06	15.84	2.54
# 12*b*	100.00	99.55	99.45	99.23	98.64	96.11	86.83	54.48	12.13
# 13*b*	100.00	100.00	99.56	99.74	99.03	97.58	95.17	88.44	50.46
# 14*b*	100.00	99.33	98.90	98.04	96.19	88.52	64.05	13.15	1.61
# 15*b*	100.00	99.33	98.25	98.55	96.25	90.79	68.44	15.43	1.66
# 16*b*	98.96	97.32	97.59	97.70	97.67	97.37	92.77	65.29	12.68
# 17*b*	100.00	99.33	98.14	97.70	96.14	91.81	79.73	31.64	2.21
# 18*b*	100.00	98.44	96.82	94.13	91.25	85.01	70.17	39.37	7.24

continued

Fields	B magnitude ranges								
	13 – 14	14 – 15	15 – 16	16 – 17	17 – 18	18 – 19	19 – 20	20 – 21	21 –
# 19*b*	100.00	100.00	99.67	99.91	99.38	98.91	93.39	32.03	1.85
# 20*b*	100.00	99.78	99.78	99.40	98.86	97.83	91.30	31.56	1.98
# 21*b*	100.00	99.78	99.56	99.49	99.26	97.90	87.53	22.70	1.20
# 22*b*	100.00	99.78	99.67	98.72	97.90	95.06	74.20	12.19	1.52
# 23*b*	100.00	99.78	99.01	98.64	97.56	93.77	85.20	47.97	5.03
# 24*b*	100.00	99.78	98.79	98.98	98.18	93.21	63.38	6.73	0.46
# 25*b*	100.00	99.78	99.56	99.74	99.49	98.35	86.91	15.94	1.01
# 26*b*	100.00	100.00	99.56	99.57	99.03	96.57	71.93	8.36	0.88
# 27*b*	100.00	100.00	99.67	98.98	98.24	95.06	61.18	4.89	0.69
# 28*b*	100.00	100.00	99.67	99.57	98.86	96.22	65.26	5.67	0.74
# 29*b*	98.96	99.33	99.67	99.83	99.60	98.46	86.13	14.80	1.43
# 30*b*	100.00	99.78	99.45	99.40	98.24	94.36	61.23	5.40	0.78
# 31*b*	100.00	99.33	99.45	99.40	98.01	94.01	50.59	3.22	0.46
# 32*b*	100.00	99.11	98.68	97.79	96.76	85.78	30.40	1.60	0.23
# 33*b*	100.00	98.88	97.92	97.36	95.80	89.22	58.55	8.79	0.69
# 34*b*	100.00	99.11	98.90	98.81	98.30	95.38	86.16	29.48	1.75
Average	99.82	99.42	98.78	98.07	96.11	90.08	67.65	21.75	4.47

Table 3.8: The same as Table 3.7 except for the two example fields in V and R.

		Magnitude ranges								
		13.5	14.5	15.5	16.5	17.5	18.5	19.5	20.5	21.5
Fields	Filter	– 14.5	– 15.5	– 16.5	– 17.5	–18.5	– 19.5	– 20.5	– 21.5	–
#07*b*	*V*	97.92	97.99	94.74	87.41	68.69	38.31	10.82	3.66	2.40
	R	100.00	99.33	94.85	89.46	77.61	47.06	17.02	5.21	3.51
#30*b*	*V*	100.00	99.78	99.67	98.47	97.27	94.36	51.47	3.63	1.01
	R	100.00	100.00	99.45	98.72	96.99	94.54	62.22	5.33	1.29
Average[a]	*V*	99.70	99.44	98.56	97.33	93.64	83.57	50.74	9.46	2.11
	R	99.81	99.45	98.46	96.86	92.67	82.27	49.45	8.55	2.28

[a] Average values for the total fields

sparse regions, for example, # 25*b*, 26*b*, 27*b*. The abnormally lower completeness in # 01*b* field seems to be caused by the poor quality of data (see subsection 2.2.1). Combining with to 95.1% survey completeness in the previous section and the 90% photometric completeness at 18 magnitude of B in this section, our SMC catalogue has an 85.6 % completeness up to 18 magnitude in B.

3.4 Combining frames

A problem of mosaic survey data is that a given star is observed several times in dithered frames to fill gaps in the mosaic CCD and in slightly overlapped adjacent fields frames. In order to match those stars we used the starlink programme, **TOPCAT** (version 1.1) with the 'sky' algorithm and 0.000025 radians ($\sim$ 5 arcsec) errors in RA and DEC. In this section we will describe how we estimate their 'best' magnitude in terms of both internal and external calibrations.

3.4.1 Internal calibration

We suppose that there are $j = 1, J$ exposures of the CCD mosaic and that the mosaic has $k = 1, K$ chips. We choose some reference exposure (say, $j \equiv 1$) and a reference chip (say, $k \equiv 1$). This CCD frame has $i = 1, I(j,k)$ stars. The net counts (*i.e.*, after flat-fielding etc) for star i are $C(i,j,k)$ ($C(i,1,1)$ is for the reference frame by our definition).

In general, assuming accurate linearity correction and background subtraction we can write $C(i,j,k) = C(i,1,1) \times G(j,k)$ where $G(j,k)$ is the gain for frame (j,k). This gain depends on both the sensitivity of chip k with respect to reference chip ($k = 1$), and the effectiveness of exposure j with respect to the reference exposure ($j = 1$), which in turn depends on the exposure time, transparency, seeing and so on.

Therefore the estimate of $G(j,k)$ is just

$$G(j,k) = \frac{\sum_{i=1}^{I} C(i,j,k)}{\sum_{i=1}^{I} C(i,1,1)} \tag{3.38}$$

where the summation is over all stars in common to frames (j,k) and $(1,1)$.

After evaluating $G(j,k)$ for every frame which has any stars in common with frame $(1,1)$, the normalized count (*i.e.*, normalized to the gain of frame $(1,1)$, which is defined as $G(1,1) \equiv 1$) for each star i is

$$C'(i,j,k) = \frac{C(i,j,k)}{G(j,k)} \qquad [cf: \quad C'(i,1,1) \equiv \frac{C(i,1,1)}{1.0}] \tag{3.39}$$

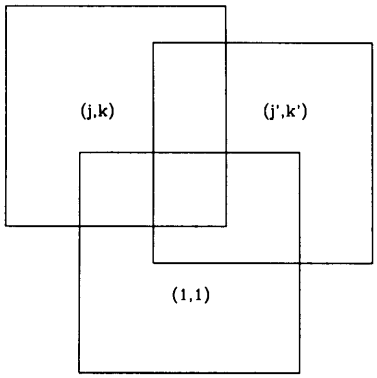

Figure 3.5: An illustration showing frames overlapped each other.

The statistical weight of this estimate can be assumed to be proportional to the number of counts; $\sigma(i,j,k) \simeq \sqrt{C(i,j,k)}$. So the best estimate of the weighted mean normalised counts for star i is

$$\begin{aligned} \bar{C}(i) &= \frac{\sum_{(j,k)} \frac{C(i,j,k)}{G(j,k)} \cdot \frac{1}{\sigma^2(i,j,k)}}{\sum_{(j,k)} \frac{1}{\sigma^2(i,j,k)}} \\ &= \frac{\sum_{(j,k)} \frac{1}{G(j,k)}}{\sum_{(j,k)} \frac{1}{C(i,j,k)}} \qquad [N.B. :\neq \frac{\sum_{(j,k)} C(i,j,k)}{\sum_{(j,k)} G(i,j,k)}, \quad \text{which is unweighted}] \end{aligned} \tag{3.40}$$

where the summations are over all frames (j,k) in which star i appears and $G(j,k)$ are nearly constant values, $\sim$ 1.75 e/ADU, across the chips in WFI system (see Table 2.1).

However, suppose that there are two frames which overlap frame (1,1) and they also overlap each other (see Figure 3.5). Then we can determine not only their relative gains compared to (1,1) but also their gains relative to each other.

We now have stars $i = 1, I'$ where I' is the total number of stars observed in all frames; and frames $j = 1, J$.

In frame j, the counts for star i (if observed) are $C(i,j)$. The gain (relative sensitivity) for frame j is $G(j)$. As in equation (3.40), the weighted mean normalised counts for star i are given by

$$\bar{C}(i) = \frac{\sum_{j=1}^{J} \frac{1}{G(j)}}{\sum_{j=1}^{J} \frac{1}{C(i,j)}} \tag{3.41}$$

where the summations are over frames j which include star i. The $O-C$ residual for each observation of star i is therefore

$$r(i,j) = C(i,j) - \bar{C}(i) \tag{3.42}$$

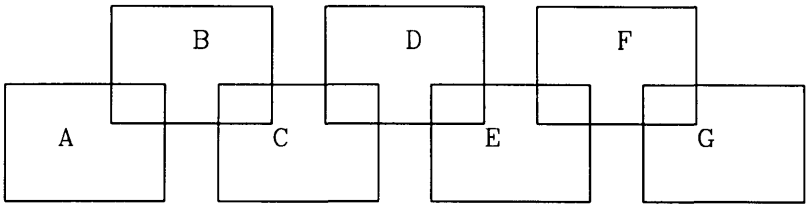

Figure 3.6: An illustration showing frames schematically overlapped.

$$\text{with weight } w_{ij} = \frac{1}{\sigma_{ij}^2} \simeq \frac{1}{C_{ij}} \tag{3.43}$$

From equations in 3.41, 3.42, and 3.43, the weighted sum of the squares of residuals for star i is then

$$\begin{aligned} \chi^2(i) &= \sum_{j=1}^{J} \left\{ \left[C(i,j) - \frac{\sum_{l=1}^{J} 1/G(l)}{\sum_{l=1}^{J} 1/C(i,l)} \right] / C(i,j) \right\}^2 \\ &= \sum_{j=1}^{J} \left\{ 1 - \frac{\sum_{l=1}^{J} [1/G(l)]}{C(i,j) \sum_{l=1}^{J} [1/C(i,l)]} \right\}^2 \end{aligned} \tag{3.44}$$

and the weighted sum of the squares of the residuals over all stars is

$$\chi^2 = \sum_{i=1}^{I'} \chi^2(i) \tag{3.45}$$

We need to determine $G(j)$, $j = 1, J$ by minimizing the sum of the squares of the residuals; *i.e.*, we set

$$\frac{\partial \chi^2}{\partial G(j)} = 0 \quad \text{for} \quad j = 2, J \tag{3.46}$$

Once the $G(j)$ values are determined we can evaluate the $\bar{C}(i)$ values.

3.4.2 External calibration

Internal calibrations determine relative normalisations for each frame, and then combine results from different frames for each star. However, this approach suffers from two weaknesses.

(i) In effect, the normalisations are basically incremental. Suppose the overlapping exposures are schematical, like Figure 3.6. Chip B's sensitivity is calculated against chip A, C from B, D from C and so forth (at least schematically). Chip 'G' is many processing steps from chip A, and errors accumulate (random walk effect)

(ii) The relative normalizations have been implicitly assumed to be colour independent. This is probably very wrong in practice.

Therefore, rather than attempting an internally consistent calibration of each frame with respect to all other frames, we consider external calibration (*e.g.*, with respect to Massey standards), which should in any case enforce internal consistency without the problem of accumulating errors. Because, in practice, the overlaps between exposures/frames are small, this is a reasonable method.

In order to take into account the different numbers of counts recorded in different frames, we combined them with a weighted mean to obtain a final magnitude and its standard deviation. In calculating the weight, we require gross plus net counts:

gross counts (star + sky) $= g_i$

sky counts $= s_i$

star counts $= n_i \quad (g_i = n_i + s_i)$

When some star i has a measured magnitude m_i in frame j,

$$m_i = C_j - 2.5 \log n_i = C_j - 2.5 \log e \cdot \ln n_i \tag{3.47}$$

$$\sigma^2_{m_i} = (\frac{\partial m_i}{\partial n_i})^2 \sigma^2_{n_i} \tag{3.48}$$

where

$$\frac{\partial m_i}{\partial n_i} = \frac{-2.5 \log e}{n_i}, \qquad \sigma^2_n \approx \sigma^2_g + \sigma^2_s \approx g_i + s_i \quad \text{(Poisson statistics)}$$

$$\begin{aligned} \sigma^2_{m_i} &= (\frac{-2.5 \log e}{n_i})^2 (g_i + s_i) \\ &= 1.179 \frac{(g_i + s_i)}{(g_i - s_i)^2} \end{aligned}$$

For the matched stars, we find the median value and only select stars having equal and less than 0.1 difference for their median value. Then the adopted magnitude and standard deviation of a given star is the weighted average of individual measurements. Say,

$$\bar{m}_i = \frac{\sum_i^{I'} w_i m_i}{\sum_i^{I'} w_i} \qquad \bar{\sigma}_i = \frac{\sum_i^{I'} w_i \sigma_i}{\sum_i^{I'} w_i} \tag{3.49}$$

where $w_i = \dfrac{1}{\sigma^2_{m_i}} = \dfrac{(g_i - s_i)^2}{1.179(g_i + s_i)}$

3.4.3 Results

In summary, therefore, we reduce each CCD exposure according to 'model 1' (see subsection 3.2.1), and combine results for the same star observed in different frames according to the external calibration described in subsection 3.4.2. This gives our final photometric catalogue.

Table 3.9 shows a portion of our whole SMC catalogue in B, V, and R sorted in order of RA. Column 1 is a sequential identifier. Column 2 and 3 are the RA (degrees) and DEC (degrees) in J2000 epoch. Columns 4, 7, and 10 represent the magnitudes in B, V, and R. Columns 5, 8, and 11 are the photometric errors, and columns 6, 9, and 12 are the number of frames which used to derive the weighted mean magnitude. If magnitudes of all stars used in the calibration of a weighted magnitude (of course, except for median star) show a spread greater than 0.1 compare to their median, we flag as '99' in these columns and simply use a median value as the magnitude. This catalogue contains $\sim$ 1.3 million stars across the 26 deg^2 of the SMC. We put data brighter than 19.0 magnitude in B ($\sim$ 700,000 stars) and machine readable programme (read_smc.f) onto a CD-ROM attached at the end of this thesis. In the near future we will make our SMC catalogue publicly available online to the astronomical community.

3.5 Comparison results with published catalogues

As a check on the accuracy of our data in terms of astrometry and photometry, we compare our results with published catalogues; astrometry in section 3.5.1 and photometry in section 3.5.2. The catalogues used for the comparison with our data are the OGLE, MCPS, and Massey surveys.

The Optical Gravitational Lensing Experiment (OGLE, Udalski *et al.*, 1998) group published BVI maps containing precise photometric and astrometric data for the central regions of the SMC bar. Their data are claimed to be complete to $B \sim 20.0$, $V \sim 20.5$, and $I \sim 20.0$ and the accuracy of the photometry is about 0.01 magnitude. The estimated accuracy of the astrometry is 0.15 arcsec with possible systematic errors of up to 0.7 arcsec.

The Magellanic Clouds Photometric Survey (MCPS), performed by Zaritsky *et al.* (2002) contains $UBVI$ photometry for the central 18 deg^2 area of the SMC and an extinction map across the SMC. Except in the dense region of the SMC, their photometry is complete to at least $V \sim 20$. Let us now consider the astrometric accuracy.

Table 3.9: A portion of the full SMC catalogue.

ID	RA[1]	DEC[2]	B	σ_B	Flag[3]	V	σ_V	Flag	R	σ_R	Flag
0000001	3.54173708	-74.68917084	17.670	0.022	1	17.996	0.033	1	17.517	0.025	1
0000002	3.54325533	-74.51149750	18.068	0.124	1	17.080	0.038	1	16.478	0.023	1
0000003	3.54563284	-74.56498337	18.550	0.042	99	17.536	0.015	99	16.710	0.009	99
0000004	3.55048180	-74.42867279	18.553	0.041	1	17.587	0.015	1	16.999	0.011	1
0000005	3.55086756	-74.34977722	18.149	0.133	1	17.314	0.044	1	16.670	0.028	1
0000006	3.55229902	-74.43345642	17.914	0.024	1	16.725	0.007	1	16.021	0.005	1
0000007	3.55510116	-74.50046539	18.416	0.036	1	17.444	0.014	1	16.870	0.010	1
0000008	3.55535913	-74.61768341	18.314	0.031	1	17.263	0.012	1	16.564	0.007	1
0000009	3.55825067	-74.28086853	18.147	0.028	1	17.534	0.015	1	17.135	0.012	1
0000010	3.56249487	-74.40327454	15.422	0.005	2	14.612	0.002	2	14.106	0.001	2
.....	.....	.....	.....	.....	.	.....	.....	.	.....	.....	.

[1]RA : Degrees in 2000 epoch

[2]DEC : Degrees in 2000 epoch

[3]Flag : Number of matched stars. The '99' value represent that there are no stars satisfying our selection criteria.

Zaritsky *et al.* (2002) compared their catalogue with that of Massey for stars brighter than $V = 15$ and find that the offset is less than $1''$ with distribution peak at $0.3''$. Massey (2002) present a $UBVR$ CCD photometric survey for 7.2 deg^2 of the SMC. In particular, because he was interested in brighter stars in the SMC, the photometric completeness of his catalogue is limited to $U \sim B \sim V \sim 15.7$ and $R \sim 15.2$. For celestial coordinates, he used the Space Telescope Guide Star Coordinate (GSC) solutions. However he gives no comments about the astrometric accuracy of his catalogue stars.

3.5.1 Astrometry

The estimation of the internal astrometric error in our survey data can be regarded as 0.5 arcsec because we fitted the astrometric solution using **MSCCMATCH** task in **mscred** package for each image within 0.5 arcsec root mean square.

As a consistency check of our external errors, we compared our data (hereafter WFI astrometry) with OGLE, MCPS, and Massey's survey (hereafter MASS). For the matching procedures, we again used the starlink program, **TOPCAT** with the maximum error less than 7 arcsec in RA and DEC, which is somewhat larger than our catalogue matching limit (5 arcsec). The results are shown in Figure 3.7 with grid comparisons. In the figure, the left panel represents the comparison fields – the narrow lines show our frames and the bold ones those of OGLE, MCPS, and the MASS survey – and the right panel shows the number distribution of astrometric solution differences between our data and the other catalogues. Although we used somewhat larger search radius, the peak of matching radius for all the comparison catalogues are within 1 arcsec. The peak radius is 0.6, 0.7 and 0.6 for the OGLE, MCPS, and MASS data respectively. It seems that there is no significant positional difference, although the external accuracy of astrometric solutions show a tendency to extend about 2 arcsec in the distribution diagrams. These results are broadly in agreement with what one might expect given our plate scale, and the seeing during our observations.

3.5.2 Photometry

To test our photometric accuracy, we compared with the same stars matched in astrometry solutions. We compared only B and V with OGLE and MCPS (because they have no R data), and B, V, and R with MASS. In Figure 3.8, we present magnitude difference with respect to these three catalogues. The top, middle and bottom panels are magnitude

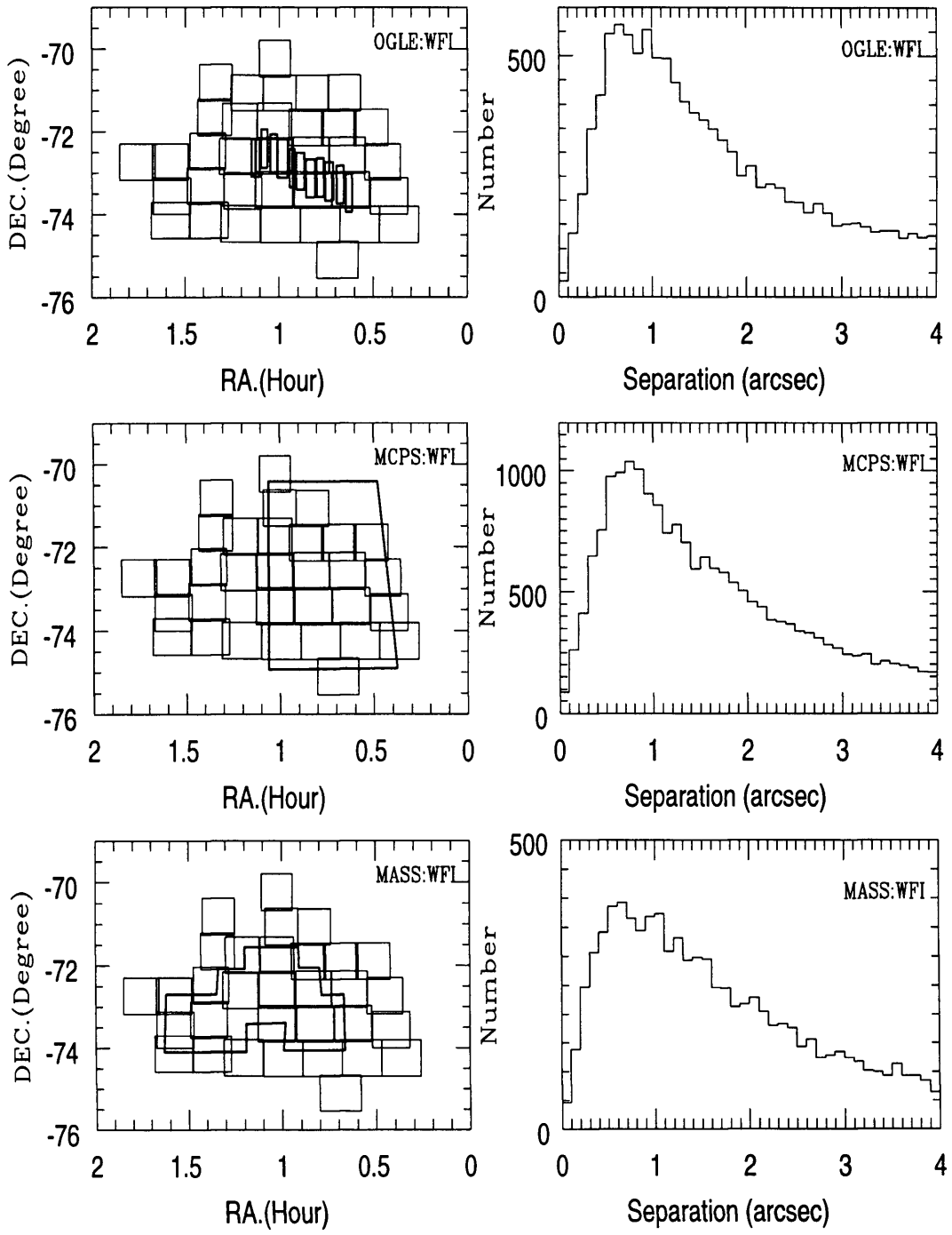

Figure 3.7: The left panels are the comparison of grids and the right are the number distribution of astrometric solutions between our work and the comparison catalogues – OGLE, MCPS, and MASS. In the left panels the narrow lines present our fields and the bold lines are others.

differences with respect to WFI in B, V, and R respectively.

The OGLE database has many stars ($\sim$ 2.2 million) despite its small survey area compared to the other catalogues. However, because the main aim of the OGLE project is to find gravitational lensing events it gives more attention to faint stars so there are fewer bright ones. However, Massey (2002) was particularly interested in brighter stars, so we only compared stars brighter than 15 magnitudes of the Massey's catalogue in BVR. For the remaining catalogues, we extend comparison to 16 magnitude stars in each filter.

The average magnitude differences with respect to magnitude bins are summarised in Table 3.10: 0.077, 0.065, and -0.120 in B, 0.105 , 0.054, -0.137 in V for the OGLE, MCPS, and MASS respectively and the ΔR between WFI and MASS is -0.163 (The differences with MASS are non-zero because here we compare all astrometrically matched stars, and not merely the high-accuracy MASS subset used in the photometric calibration). However, our catalogue stars well match with MASS for brighter stars than 15 magnitude, while with OGLE for the fainter ones than 16 magnitude. This feature seems to be caused by the different scientific purpose of each comparison catalogue: the main concern of OGLE was to find gravitational lensing events, paying much attention toward fainter stars. On the other hand, Massey was particularly interested in the study of hot stars (remember that the photometric completeness of OGLE is $B \sim V \sim 20.0$ and that of MASS is $B \sim V \sim 15.7$ and $R \sim 15.2$). On average, our catalogue shows agreement with MCPS throughout the comparison magnitude ranges within ~ 0.06 magnitude error in B and V.

3.6 Stacking

Although we performed photometry for the individual chips in a mosaic image, it can also be done for the stacked mosaic image (with less accuracy). However the main purpose of the stacking images here is the visual presentation. In this section, we will briefly describe how to make a deep single giant image from the frames taken in a different areas with slight overlap in each field. Before stacking all frames, we need some further processes in each frame.

- **MSCIMAGE:** The first step is running the **mscimage** task to make a single image for the reference image or reference coordinate from a mosaic image. In accordance with authors' suggestion of webpages introduced in the beginning of this chapter,

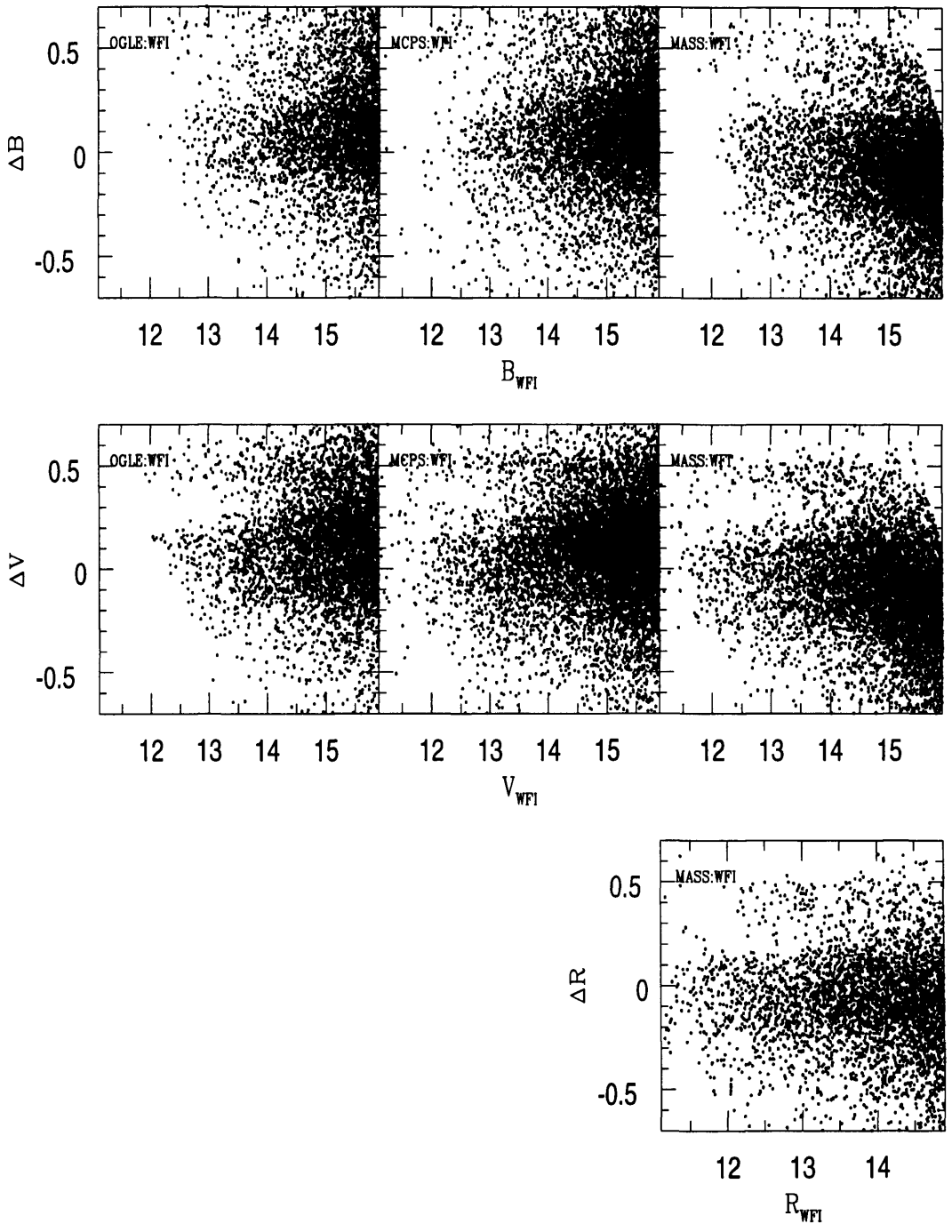

Figure 3.8: Comparison of the photometric results with the OGLE, MCPS, and MASS catalogues for the brighter stars than 16 magnitude in B and V and 15 magnitude in R. The x-axis is our photometric magnitude and the y-axis illustrates the magnitude difference with respect to our data (WFI). For the comparison of survey areas in the SMC, see also Figure 3.7.

Table 3.10: The averages and standard devations of the magnitude differences plotted in the Figure 3.8.

		Magnitude ranges					
		12 ~ 13	13 ~ 14	14 ~ 15	15 ~ 16	16 ~ 17	Ave.
OGLE - WFI	$\overline{\Delta B}$	0.194	0.076	0.095	0.130	0.048	0.077
	$\sigma_{\Delta B}$	0.079	0.068	0.080	0.093	0.081	0.085
	$\overline{\Delta V}$	0.166	0.084	0.120	0.135	0.083	0.105
	$\sigma_{\Delta V}$	0.054	0.061	0.072	0.092	0.096	0.091
MCPS - WFI	$\overline{\Delta B}$	-0.004	0.061	0.077	0.116	0.039	0.065
	$\sigma_{\Delta B}$	0.158	0.082	0.070	0.082	0.068	0.075
	$\overline{\Delta V}$	0.002	0.039	0.094	0.085	0.019	0.054
	$\sigma_{\Delta V}$	0.087	0.063	0.064	0.076	0.085	0.079
MASS - WFI	$\overline{\Delta B}$	0.049	-0.037	-0.073	-0.158	-	-0.120
	$\sigma_{\Delta B}$	0.071	0.073	0.067	0.065	-	0.069
	$\overline{\Delta V}$	-0.018	-0.038	-0.074	-0.205	-	-0.137
	$\sigma_{\Delta V}$	0.053	0.055	0.057	0.063	-	0.065
	$\overline{\Delta R}$	-0.088	-0.065	-0.111	-0.241	-	-0.163
	$\sigma_{\Delta R}$	0.057	0.054	0.067	0.087	-	0.079

the 'sinc17' in the interpolation method parameter seems to give the better result. Although it consumes much time, it is worth to use that parameter. As well in order to keep bad pixel information from each chip and to assign gaps amongst chips to it, it is recommended to use pixel mask creation option.

- **MSCSKYSUB:** Because each chip in a mosaic image has different character such as quantum efficiency, it is necessary to match sky background levels for the whole image area using the **mscskysub** task. For the 'mask' parameter, we use the bad pixel mask (BPM) generated from the result of the **mscimage** task.

- **MSCIMATCH:** After processing the above two steps for the all images, it it time to determine the scale and zero level offset for the ensemble of images which will be combined with the **mscstack** task. In **mscimatch**, we used **mscgetcat** to obtain a coordinate list of positions used in determining the proper scaling, run interactively

in order to check for inappropriate regions. The first frame in the list of input files becomes the reference frame: say, scale is 1 and zero level offset is 0. If the data were taken under photometric conditions, the relative scale should be equal to the ratio of the exposure to that of the reference image.

- **Montage:** Although the **MSCRED** package has a task, **mscstack**, to combine all frames, in our case the current version can stack only four region frames at the same time due to the large frame size. So in order to combine all 33 fields' data, we use another program, **Montage**[1]. This software does not impose any limit on the data file size; however, it does not recognise the bad pixel mask file, so causing some dark spots in the final stacked image.

- **EXPORT:** The **export** task is used to convert the final 'fits' file into a greyscale 'gif' file with appropriate contrast and brightness settings. Then we perform three colour composition with B, V, R images using a commercial software package (photoshop in our case).

Figure 3.9 is the final stacked mosaic image of the SMC using B, V, and R frames. The high resolution image also can be found in an attached CD-ROM ($\sim$ 30 MB).

[1]This research made partly use of Montage, funded by the National Aeronautics and Space Administration's Earth Science Technology Office, Computational Technologies Project, under Cooperative Agreement Number NCC5-626 between NASA and the California Institute of Technology

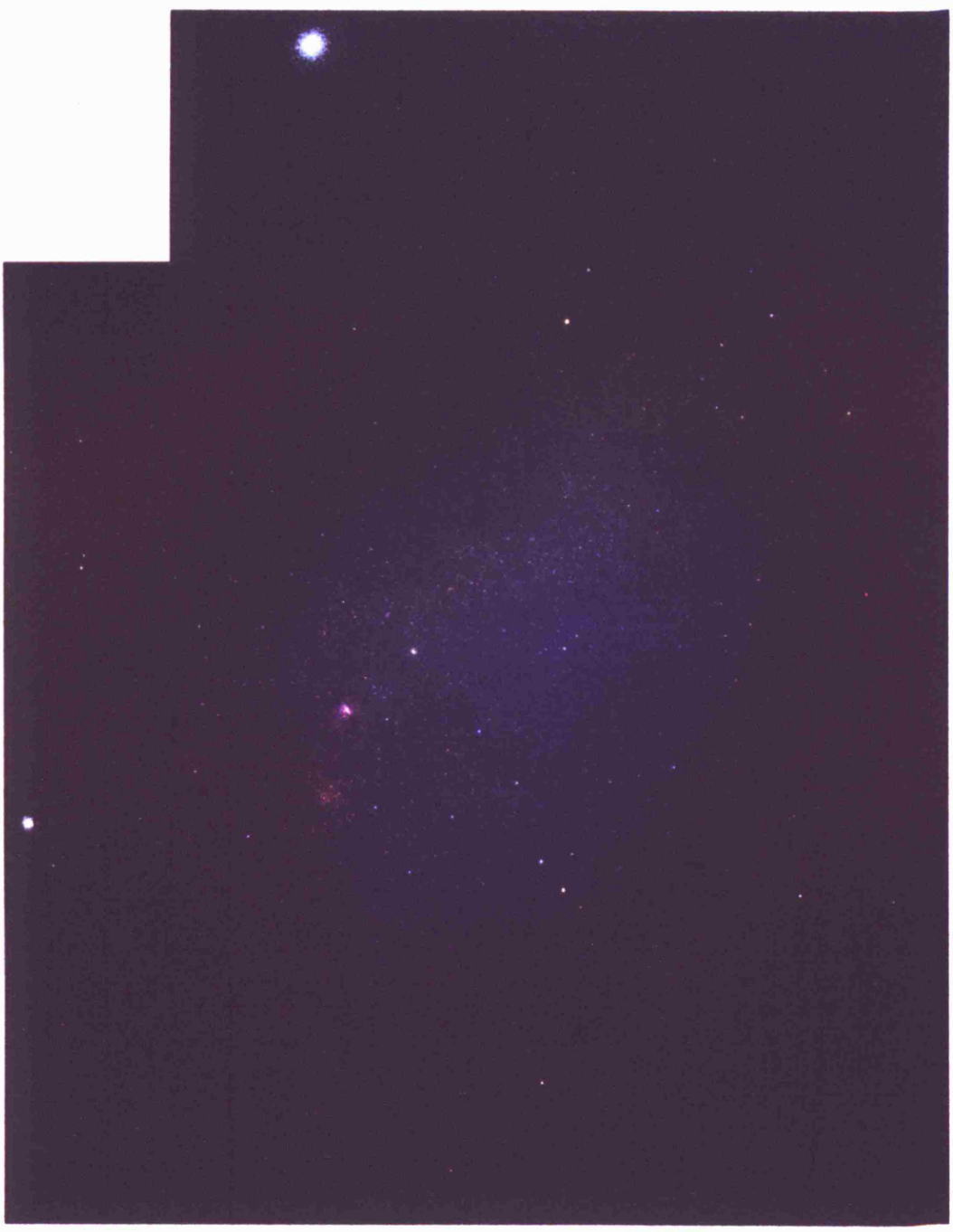

Figure 3.9: The three-colour composition mosaic image of the SMC using the B, V, and R frames.

CHAPTER 4

The Hertzsprung-Russell diagram of the SMC

The Hertzsprung-Russell (H-R) diagram is a basic tool for the studies of stellar populations so we have constructed a theoretical H-R diagram for the Evans *et al.* (2004) 2dF spectroscopic sample using our photometric data. Prior to constructing the H-R diagram, we review the basic concepts, estimate the extinction and distance modulus to the SMC, and construct a Colour-Magnitude diagram (CMD) of the SMC, together with a number distribution diagram using the photometric data presented in the previous chapter.

4.1 The magnitude scale

The magnitude system has been used since ancient times. Around late 2 BC, a Greek astronomer, Hipparchos, divided the brightness of stars into six classes, the brightest was first class and the faintest was sixth class, based upon naked-eye observations. In 1856, Norman Pogson found that this magnitude system is well expressed as a logarithmic scale, a brightness difference of one class corresponds to about 2.5 times in flux. For example, a class two star is $\sim$ 2.5 times brighter than a class three, and fainter than class one and so on. So based on the definition that first class star is one hundred times brighter than sixth, the following equation is now used to express a magnitude system;

$$m_1 - m_2 = -2.5 \log_{10} \left(\frac{I_1}{I_2} \right) \tag{4.1}$$

where m_1 and m_2 are the magnitudes of stars 1 and 2, and I_1 and I_2 are their intensities. The right side of the equation is negative so as to assign smaller numerical values to brighter

stars in accordance with historical custom. However the magnitudes defined in equation 4.1 are apparent magnitudes so do not represent intrinsic brightness. In order to describe their true brightness, the absolute magnitude is defined, as 'the apparent magnitude of an astronomical object if it were unreddened and at a distance of ten parsecs from the Earth. From equation 4.1,

$$M - m = -2.5 \log_{10} \left(\frac{I(10)}{I(r)} \right) \tag{4.2}$$

where M and m represent absolute and apparent magnitude, and $I(10)$ and $I(r)$ denote intensities at 10 pc and actual distance (r) in parsecs for a given star, while the intensity (I) is defined as;

$$I \equiv 4\pi r^2 f \tag{4.3}$$

where f is the flux. Combining equations 4.2 and 4.3

$$\begin{aligned} M - m &= -2.5 \log_{10} \left(\frac{I(10)}{I(r)} \right) \\ &= -2.5 \log_{10} \left(\frac{4\pi f \cdot 10^2}{4\pi f \cdot r^2} \right) \\ &= -2.5 \log_{10} \left(\frac{10}{r} \right)^2 \end{aligned} \tag{4.4}$$

recovering the expected 'inverse square' law. Therefore, the absolute magnitude, M, is given by

$$M = m + 5 - 5 \log_{10} r \tag{4.5}$$

The difference between apparent and absolute magnitude is called the *distance modulus* (DM) which is often quoted instead of the physical distance of an object:

$$DM \equiv m - M = 5 \log_{10} r - 5 \tag{4.6}$$

However equations 4.2, 4.5 and 4.6 are only valid if there is no intervening matter between the observer and the object. The light observed from a star has usually passed through interstellar gas and/or dust so the absorption and scattering of photons causes it to appear dimmer. Considering this effect, the absolute magnitude is rewritten as:

$$M = m + 5 - 5 \log_{10} r - A(\lambda) \tag{4.7}$$

where $A(\lambda)$ is the interstellar extinction measured in magnitudes, which is a function of wavelength in the sense that it generally decreases toward longer wavelengths. The

distance modulus is also then generalised as:

$$DM \equiv m - M - A(\lambda) = 5 \log_{10} r - 5 \tag{4.8}$$

4.2 Colour indices

In principle we would like to observe a star at all wavelengths, to determine its exact luminosity. However this is not practical and a system based on a definite wavelength interval is used. For this, many filter systems have been developed, the details of which are summarised in section 1.4.

The colour index is the magnitude difference of a star in two different filters. For example, in the UBV system, an often used colour index is $(B-V)$, where B and V are simply the magnitudes through the B and V filters respectively. One of the benefits of using a well defined colour index is that they can be closely related to astrophysical parameters. For example, the $(B-V)$ colour index has a well-defined relationship with spectral type or temperature of main sequence stars (*e.g.* details Kitchin, 2003). Observations in other filters *e.g.* U and R (I, J, and so on) can often provide further constraints on physical properties.

The dimming and reddening of a star due to the absorption or scattering by interstellar dust is termed extinction, defined as the difference between the observed (m) and the unreddened (m_0) magnitudes at wavelength λ:

$$A_\lambda \equiv (m - m_0)_\lambda \tag{4.9}$$

While the degree of reddening is defined as the colour excess $E(X-Y)$, where

$$E(X-Y) \equiv [m(X) - m(Y)] - [m(X) - m(Y)]_0 \tag{4.10}$$

From equations 4.9 and 4.10, the colour excess for the $(B-V)$ colour index in UBV system is

$$\begin{aligned} E(B-V) &\equiv (B-V) - (B-V)_0 \\ &= (B - B_0) - (V - V_0) \\ &= A_B - A_V \end{aligned} \tag{4.11}$$

with the unreddened quantity $(B-V)_0$ is called the *intrinsic colour index.* Although we can define interstellar extinction in any waveband, the most commonly used is A_V, the

extinction in the V band with the physical quantity, R_V defined as:

$$R_V \equiv \frac{A_V}{A_B - A_V} = \frac{A_V}{E(B-V)}, \tag{4.12}$$

the ratio of selective extinction to reddening from *e.g.* Schultz and Wiemer (1975) and Sneden *et al.* (1978) studies, this is approximately constant ($\sim$ 3.1) if there is no dense matter along the line of sight.

Although it is practically impossible to measure the total energy emitted by an object at all wavelengths, we can define the bolometric system, reflecting the energy output at all wavelengths, or rather bolometric magnitude by model calculations based on the photometric system. The bolometric correction ($B.C$) is the difference between the bolometric magnitude and an observed magnitude. Basically any photometric systems could be chosen as the observational basis, but the V filter in standard UBV system is normally used:

$$\begin{aligned} B.C &= m_{bol} - V \\ &= M_{bol} - M_V, \end{aligned} \tag{4.13}$$

with the bolometric magnitude for the Sun, $M_{bol} = +4.75$ (Allen, 1973). Hence, by design, $B.C_\odot \simeq 0$.

4.3 The CMD of the SMC

The CMD is an observational analogue of the HRD. The CMD, a plot of an observed magnitude versus a colour index, is useful to study the stellar population.

Based on our BVR photometric data of the SMC, we constructed composite colour magnitude diagrams for the whole SMC grid. However for clarity of presentation we have randomly selected 5% of the stars from the total of 1.3 million, and Figure 4.1 shows V against $(B-V)$ and V against $(V-R)$, together with their number distributions. In the number distribution diagram, the solid line represents the 5% sample stars and the dotted shows total number distribution of our whole SMC stars. The number distribution of randomly selected 5% samples with respect to magnitudes is sufficient to represent the distribution of the whole SMC stars. As a check of validity for that assumption, the numerical test is given in next chapter using the Bayesian statistic. As mentioned before, our photometric data are complete to around 18 magnitude and this also can be

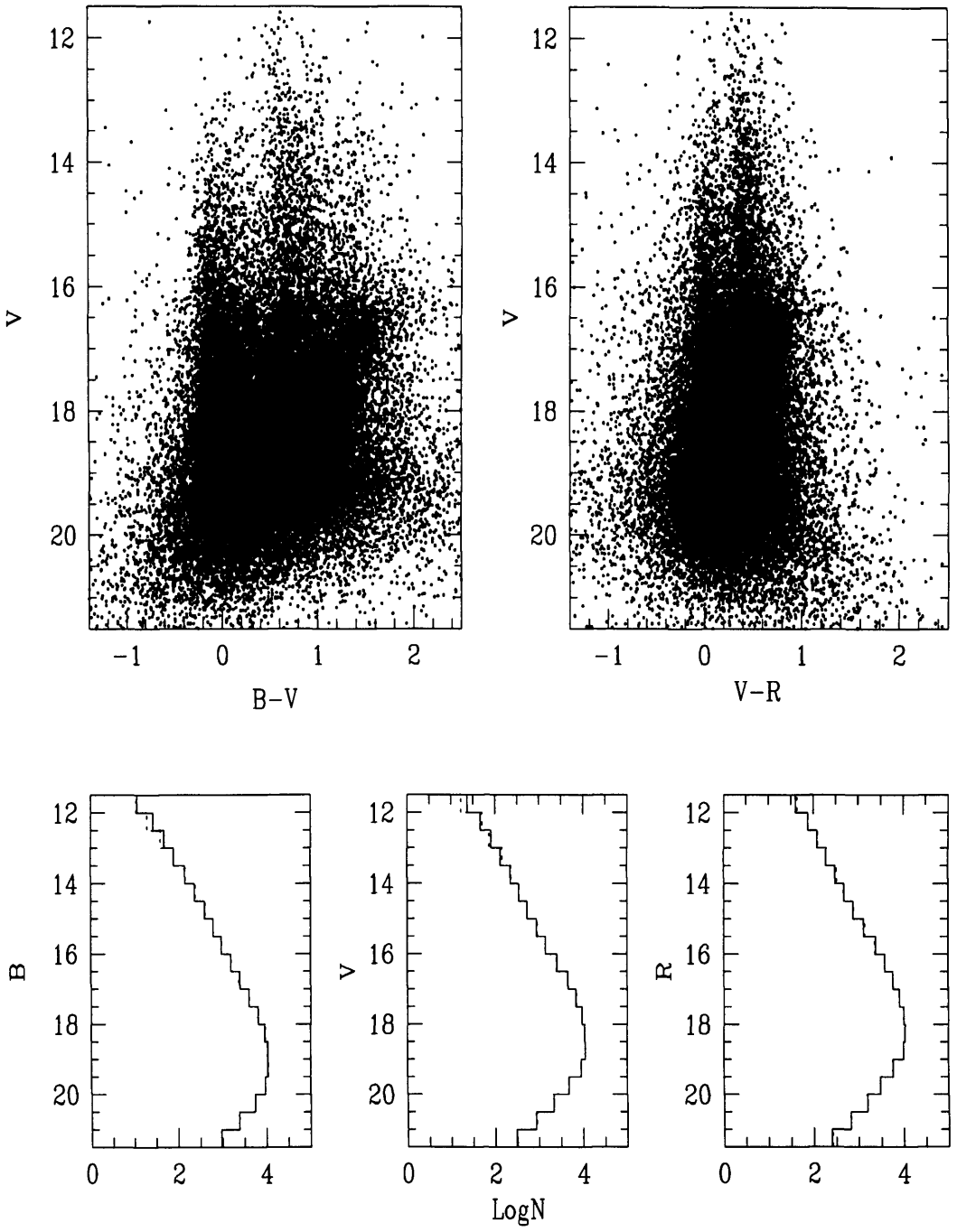

Figure 4.1: The upper panels shows the V versus $(B-V)$ and $(V-R)$ CMDs of our SMC stars. Only about 5% of the sample is plotted to aid clarity. In the lower panel, the solid lines represent the number distribution for the stars used to construct the CMDs with the dashed lines for the total SMC stars. For the comparison, the dotted lines are normalised in 18 magnitude.

confirmed from the number distribution diagrams, the peak values are around $B \sim 19.0$, $V \sim 18.5$, and $R \sim 18.0$. So considering stars brighter than 18 magnitude, we see three branches in V against $(B-V)$; $(B-V) \sim 0$, between $(B-V) = 0.6$ and 1.2, and lastly a diagonal branch starting of around $V = 16.5$ and $(B-V) \sim 1.8$. These features are less clear in the V versus $(V-R)$ plot. Stars located vertically along of $(B-V) \sim 0$ are primarily unreddened massive main-sequence stars burning Hydrogen in their cores. To account for the broad clump (ranging from $B-V = 0.6$ to 1.2), Massey (2002) argued that they are contaminated by foreground Galactic disc stars. He studied quantitively the degree of domination using Bahcall and Soneira (1980) model with the expected foreground contamination percentage shown in his figure 7. The third feature is the red supergiant (RSG) branch, in which stars are burning helium. Because massive stars evolve to RSGs and Wolf-Rayet (W-R) stars according to their mass and abundances, the number ratio of RSGs and W-Rs to blue stars in the SMC is an important feature to understand the effects of metallicity.

4.4 Spectral classification

In order to investigate IMF of a system, we have to convert observational quantities into theoretical ones for the comparison with theoretical models, or vice versa. In the case of photometric study, the colour excesses, extinctions and distance modulus values are needed in the transformation. Especially in the calculation of bolometric corrections for early-type stars, they only can be obtained from spectroscopic data. Although there are known values of all these parameters for the SMC, we will also derive them and compare our results with published values in next section. In this section, we briefly introduce the spectral system in order to give a background for the spectral classification of a star although the main subject of this thesis is the photometry study.

4.4.1 The Harvard system

As in other sciences, notably biology, a fundamental and easy way of studying objects is to group them into classes in accordance with observable properties, in this case, their spectra.

A. Secchi in the 1860s found that stars can be grouped into four classes according to spectral appearance. Following this, the more detailed Harvard scheme of spectral clas-

sification was developed by A. J. Cannon and her colleagues at the Harvard Observatory at the beginning of the last century and they published Henry Draper (HD) catalogue containing about 225,000 stars. The main standard of the Harvard system was the hydrogen Balmer absorption lines that were alphabetically ordered (A through P) according to their strengths, in the sense that A-type has the strongest Balmer lines, and P has the weakest. Some letters were dropped later on, the remaining types were rearranged, and subdivisions within each class were introduced. Finally the modern spectral sequence is;

$$O - B - A - F - G - K - M \tag{4.14}$$

Nowadays, R, N and S types are added to distinguish surface-chemistry effects in the K – M temperature range, and the sequence has been extended to types L, T,and Y to encompass brown dwarfs. Additional types, W and Q are used for Wolf-Rayet stars and novae.

In terms of temperature, O class spectra are the hottest and M the coolest. So stars with O and early B type are commonly called 'hot stars' or 'early type' with stars closer to M termed 'late type'.

4.4.2 The MK system

The Harvard system is based on a one-dimensional criterion, namely temperature. Following the work of E. Hertzsprung and H. N Russell, however, it was clear that there were stars at a given temperature showing different luminosities. This required a new parameter to better discriminate stars and W.W. Morgan, and P.C. Keenan at the Yerkes Observatory introduced a two-dimensional system usually called the MK system after their initials, considering both temperature and luminosity. Sometimes, this is also called the Yerkes system.

In the MK system, in addition to spectral type, one of five luminosity classes is assigned, labelled by Roman numerals. Table 4.1 shows the luminosity classes in the MK system. The luminosity classes in the MK scheme have three subclasses, a, ab, c, which decrease luminosity in a given class. In the MK system, a 'dwarf' star generally corresponds to a main sequence star (core hydrogen burning), with the Sun classified as a G2 V. Through revisions and extensions, the MK system is now used as the standard classification system.

Table 4.1: Luminosity classes in the MK system.

Class	Subclasses	Name
I	Ia, Iab, Ib	Supergiant
II	IIa, IIab, IIb	Bright giant
III	IIIa, IIIab, IIIb	Giant
IV	IVa, IVab, IVb	Subgiant
V	Va, Vab, Vb	Dwarf

4.5 HRD of the SMC

Before constructing the Hertzsprung-Russell diagram of the SMC, we first investigate the colour excesses, $E(B-V)$ and $E(V-R)$, interstellar extinctions, A_V and A_R, and distance modulus. So as mentioned above, we choose a subset of our catalogue with spectral classifications, and hence 'known' intrinsic colours. The SMC spectroscopic data are taken from the Evans *et al.* (2004) 2dF survey catalogue, which contains over 4000 stars. However, from a total of 4161 2dF spectra, 323 stars have only spectral type without luminosity class, 79 are noted as showing an ambiguous spectral type by the authors, 2223 are only roughly classified such as 'B0-5 (V)', and 22 are peculiar stars including two Wolf-Rayets. We remove those stars and use the remaining 1514 stars, which comprise 194 supergiants, 863 bright giants, 211 giants, 77 subgiants, and 169 dwarfs. Considering the photometric data, we use stars observed twice or more for the accuracy of magnitudes.

4.5.1 The colour excess and reddening

There have been many studies on the relationship between intrinsic colour and spectral type. Johnson (1966) presented intrinsic colours with respect to the MK system in many colour indices for supergiants/giants and main sequence stars. We derive $E(V-R)$ from Johnson (1966) because it is the only available calibration in this colour although the intrinsic colours are studied only for the late type stars, from G5 to M6 in giants, contrary to most of 2dF stars which are mostly O, B and A types.

In evaluating $E(B-V)$, we adopted $(B-V)_0$ from Fitzgerald (1970) because it contains data for the all luminosity classes, especially the bright giant stars which contribute the largest group in the 2dF catalogue. In order to estimate intrinsic colours between each

spectral type bin, we perform a high-order polynomial fit. In the Evans *et al.* (2004) catalogue, the latest spectral type is G8, so we choose that as the lower limit to the fits. Because sometimes extrapolation shows spurious results, especially in high-order fitting, we restrict the spectroscopic data to lie between the upper and the lower limits in luminosity class.

Figure 4.2 shows the adopted data points and high-order fits for each data set; the closed circles are Fitzgerald (1970) in $(B-V)_0$ and Johnson (1966) in $(V-R)_0$ and the solid lines the fits.[1] We present 2dF stars from Evans *et al.* (2004) used for the $E(B-V)$ calculation in Appendix C; the sequential ID, right ascension and declination in equinox of J2000, and spectral types are from Evans *et al.* (2004), and our photometric data are in the 5, 6 and 7th columns. In celestial coordinates, it shows a good match with ours so we adopt their values. We found the mean value of $E(B-V)$ is 0.086 from 653 stars and of $E(V-R)$ is 0.065 from 147 stars, with a suggestion of a trend from low values for supergiants ($E(B-V) = 0.062$, $E(V-R) = 0.040$) to a larger one for dwarfs ($E(B-V) = 0.131$, $E(V-R) = 0.090$). In Table 4.2, the resulting values, averages and standard deviations, with respect to luminosity class are summarised, together with the number of stars used in each class. The number of stars used in deriving $E(V-R)$ is slightly different to those for $E(B-V)$, due to the differences in the upper limits of the fits. As a double check, we adopted relations from Flower (1977) or Schmidt-Kaler (1982) in calculation of $E(B-V)$ and there were no significant differences.

It is generally accepted that the SMC has small and relatively uniform foreground reddening, $E(B-V) \sim 0.019$ (*e.g.* McNamara and Feltz, 1980). Grieve and Madore (1986) studied the total reddening of the SMC, with 46 supergiants from the Azzopardi and Vigneau (1975) and Feast *et al.* (1960) catalogues and found $E(B-V)$ ranging from 0.09 up to 0.2. Massey *et al.* (1995*b*) found the same result using the reddening-free 'Q' parameter with 179 SMC stars. More recently Larsen *et al.* (2000) reinforced this result from the study of B-type field stars and suggested 0.07 ± 0.02 for the $(B-V)$ colour excess. However our mean value of $E(B-V)$ is a slightly higher and shows a larger scatter compared to those previous studies. This maybe because we sample fainter stars (which may be more reddened).

After calculation of the colour excesses, we derived the interstellar extinctions using

[1] The used relationships between spectral types and instrinsic colours are for the Galactic metallicity so they could feasibly be slightly different for the SMC one.

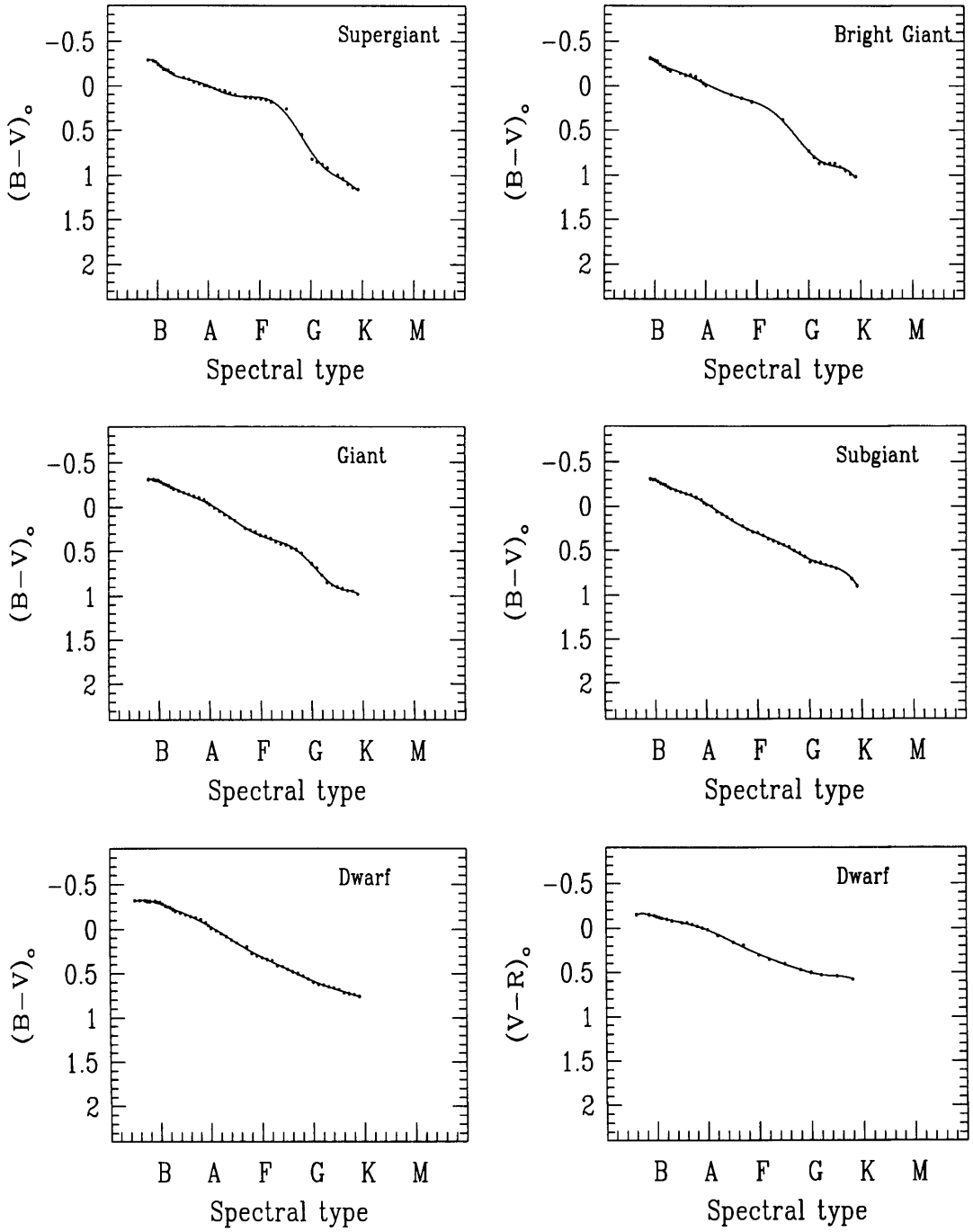

Figure 4.2: The relations between the MK system and intrinsic colour indices. The values from Johnson (1966) were adopted in $(V-R)_0$ for the main sequences while we used Fitzgerald (1970) in $(B-V)_0$ for all luminosity classes. The solid lines represent high-order polynomial fits to the data for the interpolation of intrinsic colours.

Table 4.2: The colour excess values with respect to luminosity classes.

Class	$E(B-V)$	$E(V-R)$
Supergiant (I)	0.062 ± 0.147 (74)	0.040 ± 0.130 (74)
Bright giant (II)	0.070 ± 0.164 (378)	
Giant (III)	0.103 ± 0.150 (91)	
Subgiant (IV)	0.156 ± 0.137 (36)	
Dwarf (V)	0.131 ± 0.120 (74)	0.090 ± 0.084 (73)
Total	0.086 ± 0.156 (653)	0.065 ± 0.112 (147)

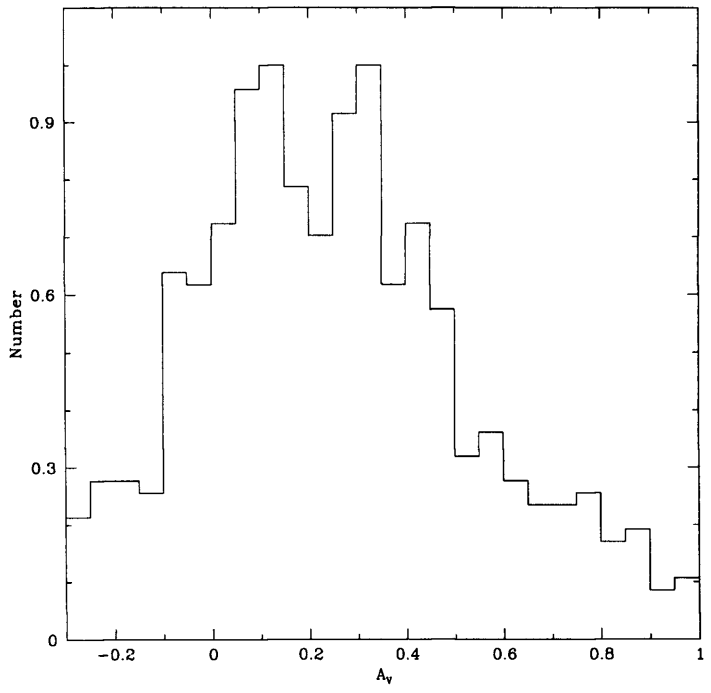

Figure 4.3: The normalised number distribution of interstellar extinction values for $-0.3 \leq A_V \leq 0.9$.

Equation 4.12, and the same value of R_V, 3.1, as mentioned section 4.1. We plot the normalised number distribution for the $-0.3 \leq A_V \leq 0.9$ range[2] in Figure 4.3, in which the mean value of interstellar extinction is ~ 0.225, taken between two peak values, corre-

[2]Note that we allow negative reddenings here; although unphysical, this is necessary in order to avoid biassed statistics.

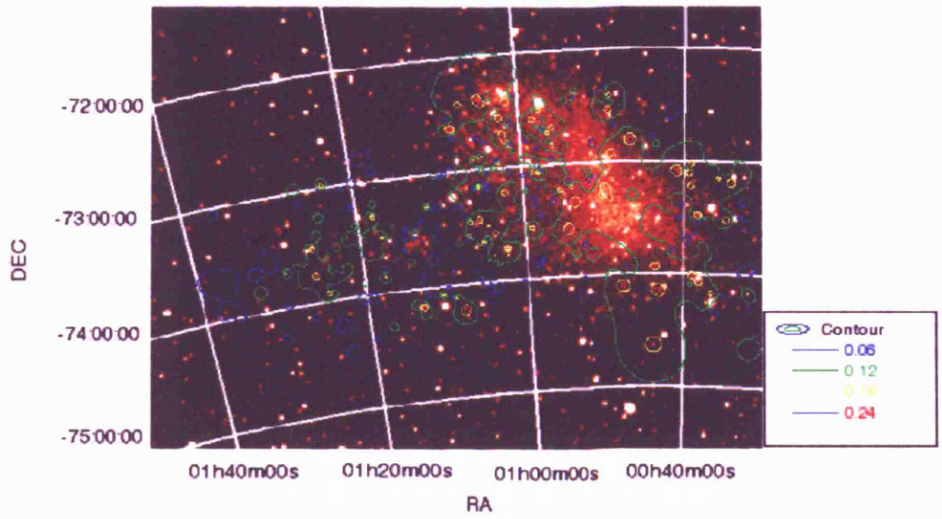

Figure 4.4: The contour map of colour excess in $(B-V)$ using the 484 stars from Table C.1. The legend is presented in bottom of right of the figure; blue shows $>$ 0.06, green $>$ 0.12, yellow $>$ 0.18 and red $>$ 0.24 in $E(B-V)$. Overall, the main body region of the SMC has $E(B-V)$ $>$ 0.12 and the field region is 0.06. However it seems that there are no particular optical counterpart regions for the high colour excess.

sponding to $E(B-V) = 0.076$. This is reasonable agreement with our mean value (0.086), however it shows strong tails after the peak values.

Meanwhile, using the stars in Table C.1 we draw the contour map of colour excess in Figure 4.4, and check the distribution of colour excess, in particular whether there are counterparts in the optical image for the regions having large $E(B-V)$. Overall the main body of the SMC has slightly higher value, ~ 0.12 (green colour), than the field area, ~ 0.06 (blue colour) in $E(B-V)$. However there are no optical counterparts in the $E(B-V) \geq 0.2$ regions (red circle) so it seems that the high colour excess values come from particular stars not specific regions.

In deriving A_R, we simply used the relation between A_V and $E(V-R)$; that is, from Equation 4.9 and 4.10

$$\begin{aligned} A_R &= [R - R_0] \\ &= [(V - V_0) - (V - R) + (V - R)_0] \\ &= A_V - E(V - R) \\ &= 0.160 \end{aligned} \tag{4.15}$$

where $E(V - R) = 0.065$. When we consider the uncertainties in the photometry this value approximately matches the value of $A_R = 0.194$ calculated from Howarth (1983) formula:

$$A_R = 2.25E(B - V) \tag{4.16}$$

where $E(B - V) = 0.086$.

4.5.2 Absolute magnitude and distance modulus

Schmidt-Kaler (1982) gave a tabulation of the relationship between spectral type and absolute magnitude for each luminosity class. Conti *et al.* (1983) presented a more detailed relation of M_V to spectral type for O-type supergiants, giants, and dwarfs. Humphreys and McElroy (1984) also compiled results for all luminosity classes, but it is limited to only at the type later than B5 except dwarfs. Therefore we mainly adopt the Schmidt-Kaler (1982) values, supplemented with Conti *et al.* (1983) for the O stars. In the same way that we calculated the spectral type-instrinsic colour relations, we performed high-order polynomial fits in order to interpolate between each spectral type bin. Also we constrainted the lower limit, as G8. Figure 4.5 shows the relations between the absolute magnitudes and the MK system. In the figure, the open symbols are from Conti *et al.* (1983), closed are from Schmidt-Kaler (1982), and the solid lines are the adopted fits for our calculation. After calculating the absolute magnitudes, we find a mean distance modulus to the SMC from Equation 4.8 and assumed A_V;

$$DM = V - M_V - A_V \tag{4.17}$$

Adopting the $E(B - V) = 0.086$ (so $A_V = 0.267$) value, we get a 18.55 ± 1.05 as the mean distance modulus. van den Bergh (2000) summarised the various methods of distance determination and suggested the true distance modulus of the SMC is 18.85, (58.9 kpc), with $\sim$ 0.1 uncertainty. Recently Harries *et al.* (2003) and Hilditch *et al.* (2005) studied the eclipsing binaries in the SMC and gave the distance modulus as 18.91 ± 0.03

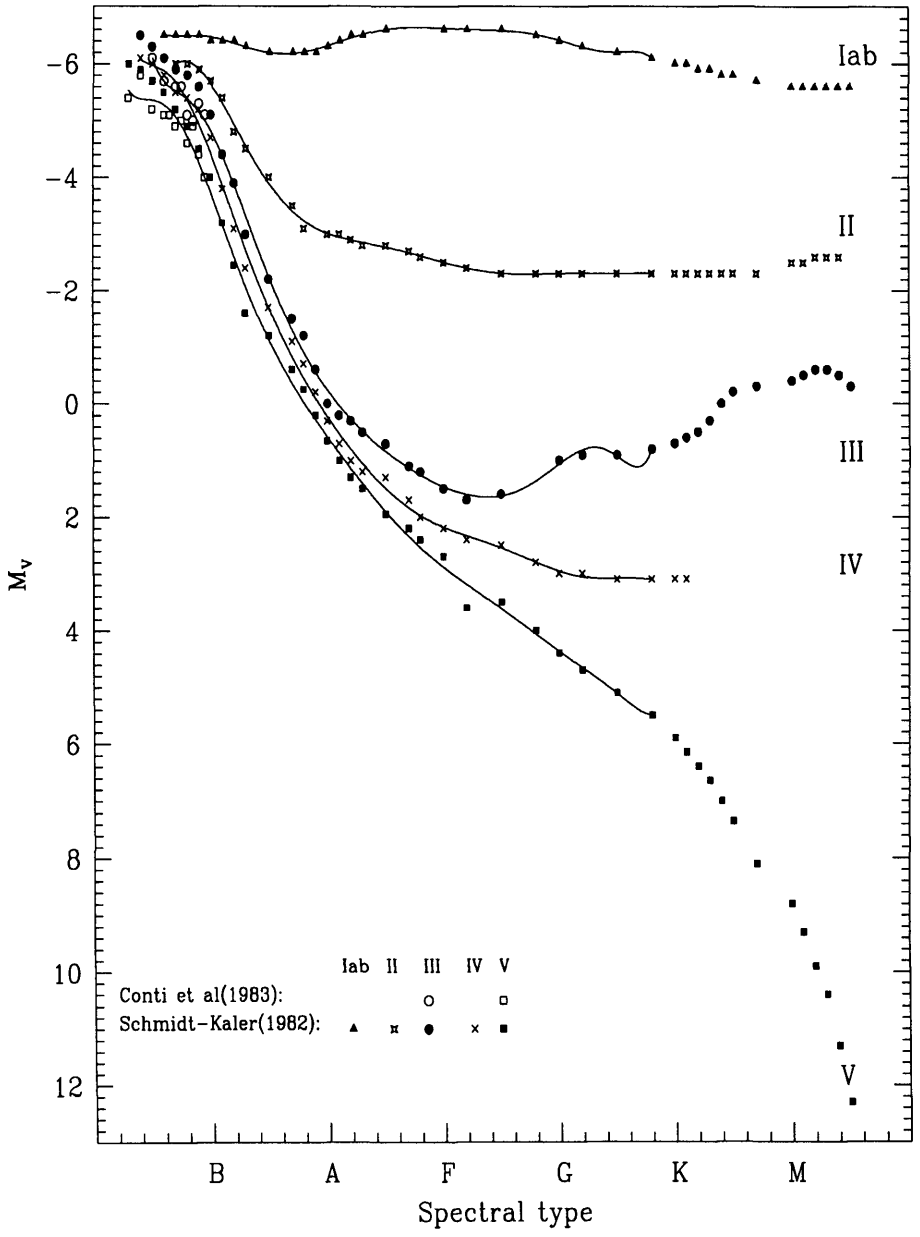

Figure 4.5: The relationship between absolute magnitude and spectral types, as a function of luminosity class. The open symbols are from Conti *et al.* (1983), filled are from Schmidt-Kaler (1982), and the solid lines are the adopted fits.

(statistical) ±0.10 (systematic), one the most precise determinations to date. Therefore our determination is a little bit smaller than the published results although it matches within uncertainty.

4.5.3 Effective temperature and bolometric magnitude

With parameters derived from previous subsections, we can construct a theoretical H-R diagram from a subset of the Evans *et al.* (2004) catalogue and estimate the IMF of the SMC in the next section. In the following chapter, we will compare this result with ones from photometric study and discuss the effect of spectral data in the IMF study of hot stars. So as a final step of the transformation into theoretical H-R diagram, we explain the relationship between effective temperature and bolometric correction here, in order to get a bolometric magnitude or luminosity.

As mentioned in section 4.2, there is a well defined relationship between $(B-V)$ and the temperature of stars. However it is degenerate for hot stars (O and early B types), while the effective temperature varies from 15 kK to 50 kK, the $(B-V)$ changes by only ~ 0.3 mag. Because of this degeneracy in the photometry, the most useful discriminant of temperature for O-type stars is from spectroscopy (Massey *et al.*, 1995*c*). Following the calibrations of stellar temperature, the other parameter needed to construct a theoretical HR diagram is the bolometric magnitude or luminosity, which can be obtained by bolometric correction of the absolute magnitude. With Equation 4.13, the bolometric magnitude (M_{bol}) is found from:

$$M_{bol} = M_V - B.C. \tag{4.18}$$

which $B.C$ is given by a function of the effective temperature. Alternatively the luminosity for each star is found from Equation 4.1;

$$M_{bol} = M_{bol}(\odot) - 2.5\log(L/L_\odot) \tag{4.19}$$

To convert observational quantities into a theoretical HR diagram (from which it is possible to undertake comparisons with theoretical results), there have been many studies of the relationship between colour indices/spectral type and effective temperature, together with bolometric corrections. Johnson (1966) investigated this relation for the main sequence and supergiants/giants, however it was limited for types later than the O stars. Flower (1977, 1996) later revised the $T_{eff} : (B-V) : B.C.$ scales for the luminosity

classes I, III, and V. For O stars, Howarth and Prinja (1989) investigated temperatures and bolometric corrections using 203 Galactic stars observed with *IUE*, and Chlebowski and Garmany (1991) constructed a new conversion table for O types using X-ray data. Recently, Balona (1994) determined effective temperature and bolometric corrections for O - F stars using Strömgren indices, and Vacca *et al.* (1996) studied calibrations of effective temperature, bolometric correction, and gravity for O and early B-type stars using revised stellar atmospheric models (Castelli and Kurucz, 1994). More recently Martins *et al.* (2002, 2005) reported that the inclusion of line blanking cause to lower effective temperature and presented new effective temperature calibration scale for O stars at solar metallicity.

Although there are many studies of transformations from colour indices to effective temperatures, these incur larger errors than conversions from spectral type to effective temperature. So here we use only the 2dF spectroscopic data to constructing a theoretical H-R diagram. Regarding to our photometric data, we will convert theoretical quantities into colour indices in order to investigate the IMF of the SMC and will compare the result with that gets from here in the next chapter.

Because the effective temperature calibration from Balona (1994) is based on Strömgren indices and that from Vacca *et al.* (1996) is the hottest at all spectral types as pointed out by Harries *et al.* (2003), we adopt the Martins *et al.* (2005) scales, the most recent result, for O type stars and Schmidt-Kaler (1982) for later types in the T_{eff} calibrations. In *B.C.* calibration, we use relation from Lanz and Hubeny (2003), who used comprehensive stellar atmosphere models and considered the metallicity, and from Balona (1994), derived from the Strömgren system, a more useful system than the *UBV*.

Martins *et al.* (2005) investigated two types of effective temperature scales, theoretical and observational, and suggested linear fits to observed Galactic O stars as function of spectral type with respect to luminosity class. Regarding the effects of metallicity on T_{eff}, Mokiem *et al.* (2004) show that the spectral type may be changed by up to one subtype when Z is decreased from 2 to 0.1 $Z_{\odot}$. Therefore we use a $(SP - 0.5)$ term instead of SP in the Martins *et al.* (2005) relation for our SMC stars, whence;

$$T_{eff} = \begin{cases} 50838 - 1995 \times (SP - 0.5) & (V) \\ 50882 - 2115 \times (SP - 0.5) & (III) \\ 47666 - 1881 \times (SP - 0.5) & (I) \end{cases} \tag{4.20}$$

where SP is spectral type defined as numerical value (refer to Martins *et al.*, 2005).

However there are no relations for luminosity classes II and IV in Martins *et al.* (2005) and Schmidt-Kaler (1982), so we simply interpolated values using the neighbouring luminosity classes.

For the bolometric correction, Lanz and Hubeny (2003) derived it as a first order function of $\log T_{eff}$ with consideration of the metallicity effect and gave:

$$B.C = 27.43 - 6.78 \log T_{eff} + 0.06 \frac{Z}{Z_{\odot}}. \tag{4.21}$$

On the other hand, Balona (1994) used a 3rd order function of T_{eff} for all stars with $T_{eff} > 5500K$, given by:

$$B.C = -5.5647 + 18.9446\theta - 19.8827\theta^2 + 6.1302\theta^3, \tag{4.22}$$

where $\theta = 5040.0/T_{eff}$. Based on the two bolometric calibrations, we found the point at which the two relations smoothly overlapped, which is $\log T_{eff} = 4.47K$ (around B0 spectral type). So we use the Lanz and Hubeny (2003) relationship for $\log T_{eff} \geq 4.47K$, and Balona (1994) for $\log T_{eff} < 4.47K$. Figure 4.6 shows the adopted effective temperature calibrations for I, III, and V luminosity classes and bolometric correction calibrations.

4.5.4 HRD

The theoretical H-R diagram using the parameters calculated in the previous sections is presented in Figure 4.7 for 3806 of the 2dF stars; we take the average spectral type for those broadly classified. The solid lines are 1, 3, and 5 Myr isochrones and the dotted lines are stellar evolutionary tracks for the masses noted in the figure. Because the spectral types have minimum intervals of 0.5, the data points in figure are discretely spaced and they each represent more than one star.

In order to estimate the IMF of the SMC, we assume a continuous star formation rate and count the number of stars in each mass bin, listed in Table 4.3. Figure 4.8 shows the slope of IMF for massive stars in the SMC, $\Gamma = -2.4$. This result agrees with $\Gamma = -2.5 \pm 0.3$ found provisionally for non-field SMC stars (Evans, 2001) derived in a different way; converting theoretical quantities into observable ones. However, it must be considered as only a rough value, as it takes no account of selection effects/completeness. We will discuss more details for the IMF of SMC, using our photometric data, in the next chapter.

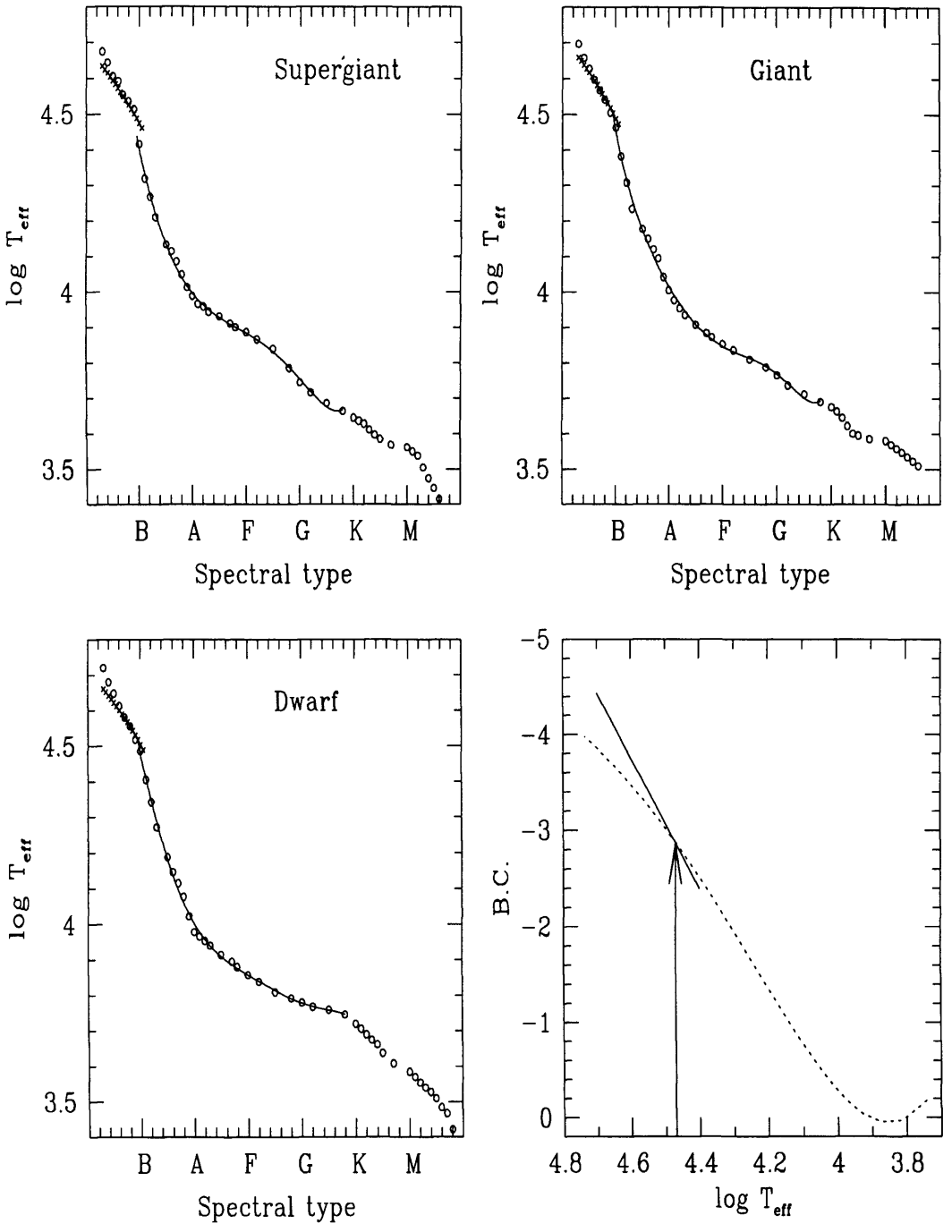

Figure 4.6: The adopted calibrations of effective temperature for supergiant, giant, and dwarf spectral ranges; cross symbols are from the Martins *et al.* (2005) relations (see Equation 4.20) and open circles from the Schmidt-Kaler (1982) data, with their high order fits shown as solid lines. The bolometric corrections are from Lanz and Hubeny (2003), dotted line, and from Balona (1994), solid line, in the $B.C.$ vs $\log T_{eff}$ diagram.

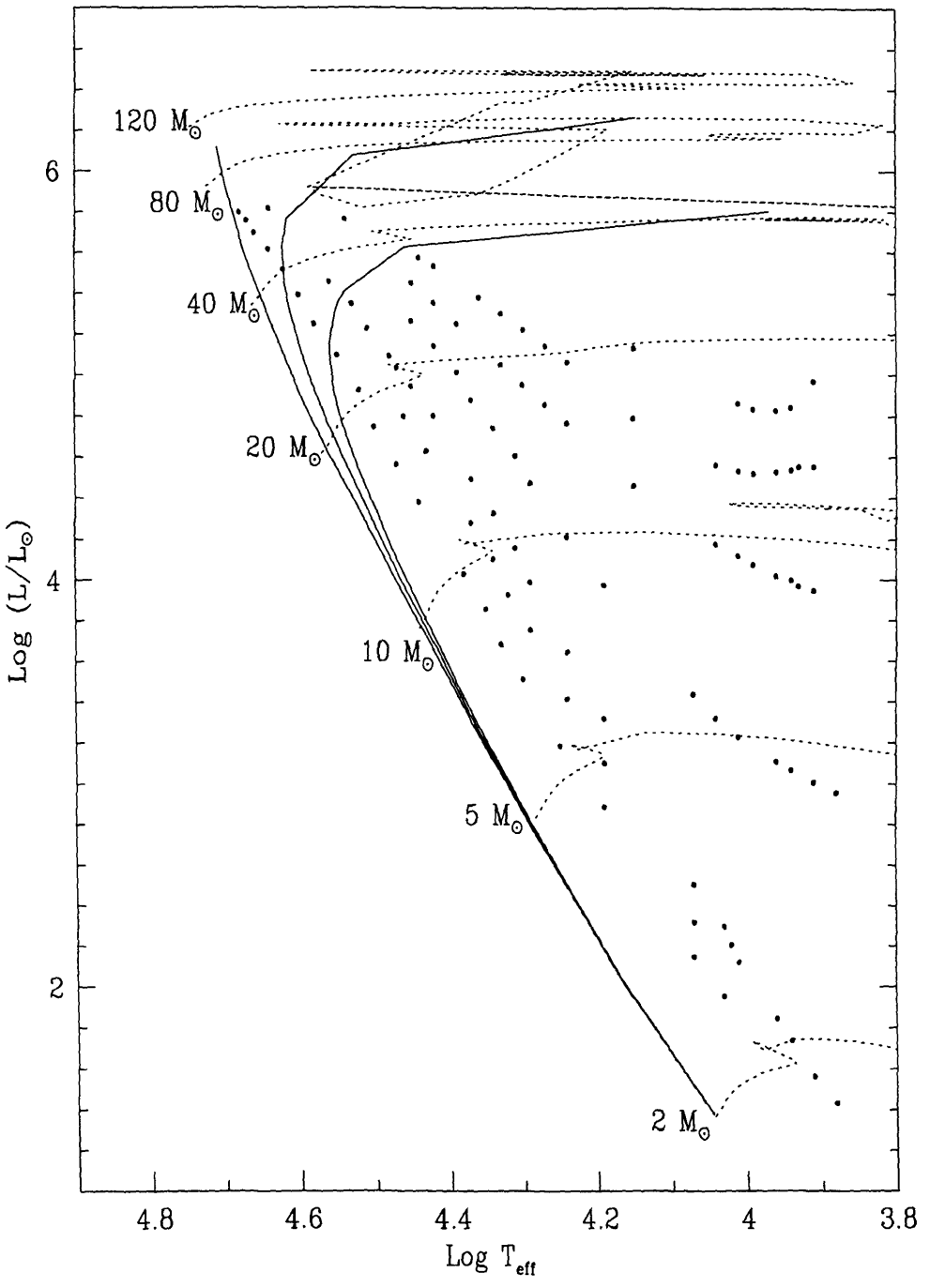

Figure 4.7: The theoretical H-R diagram of the SMC using parameters described in text for 3806 stars from the 2dF survey (filled circles). The solid lines are 1, 3, 5 Myr isochrones and the dotted lines are evolutionary tracks from Charbonnel *et al.* (1993).

Table 4.3: The initial mass function of the SMC derived from the Evans (2001) 2dF survey.

	Mass bin ($M_\odot$)			
	2 – 8	8 – 12	12 – 20	20 – 32
No. of stars	1810	1506	471	14
Γ		−2.40		

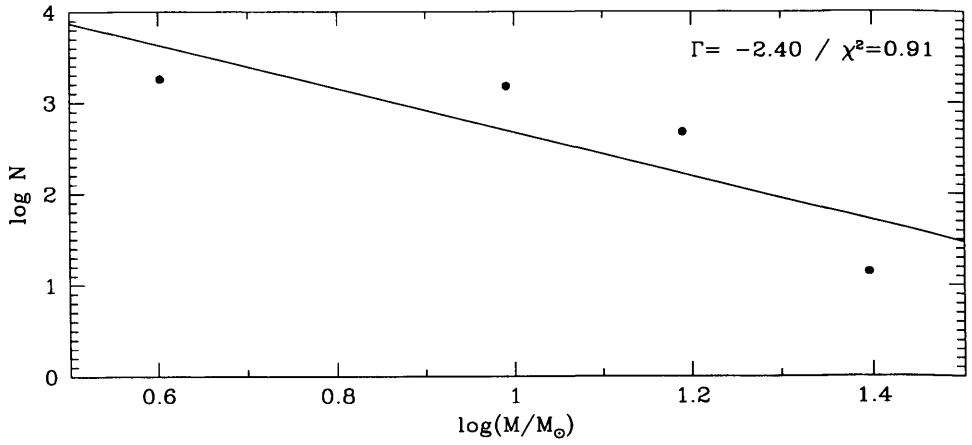

Figure 4.8: The slope of the stellar initial mass function for massive stars in the SMC using 3806 2dF samples. We assume that the star formation rate is continuous.

CHAPTER 5

The IMF of the SMC

It has been shown that population synthesis methods are a powerful tool for the study of stellar systems, clusters or galaxies, connected with evolutionary models. In order to investigate the IMF of the SMC in terms of the star formation history and the effects of metallicity, we now employ the stellar population synthesis technique. The synthesis code used for our samples is called *PSYNTH*, written by Howarth (2004). It requires the following as input parameters:

- Stellar-evolution models, characterised by metallicity. The adopted evolutionary models are from the Geneva group (Schaller *et al.*, 1992) so the allowed values are $Z = 0.001$, 0.004, 0.008, 0.02 and 0.04 (cf. $Z_{\odot} = 0.02$ and $Z_{SMC} = 0.004$).

- Minimum and maximum masses to be calculated (in solar units). For the 0.004 metallicity grid, the minimum and maximum masses are 1 and 120 $m_{\odot}$ respectively. (If the input minimum mass is equal to the input maximum mass, *PSYNTH* generates an evolutionary track at that mass, rather than a population.)

- Age of synthetic population in years. A positive value is used to generate a starburst (instantaneous) model, whilst a negative value generates a continuous star formation model. In order to approximate a discrete star formation history, it includes 'time span' option taking two arguments, in years.

- IMF slope. The Salpeter value is $\Gamma = -1.3$.

- Desired number of stars. By default, the number of stars is that of surviving stars in the synthesized population, which is generally less than the number of stars generated.

There are two types of output from the synthesized population; the theoretical quantities and the observable ones. For photometric data, observables are based on transformation relations from Bessell *et al.* (1998). For each synthesized star, the theoretical quantities, determined by the evolutionary models, are

- Zero age mass (in $m_{\odot}$)
- Age (years)
- Current mass (in $m_{\odot}$)
- Luminosity ($\log L/L_{\odot}$)
- Effective temperature ($\log T_{eff}$)
- Radius (in $R_{\odot}$)
- Gravity ($\log g$, cgs);

while the observable parameters, obtained from transformations of the theoretical ones, are absolute B and V magnitudes, the $(B-V)$ and $(V-R)$ colour indices, $\log L/L_{\odot}$, and the bolometric correction. By statistical (Bayesian) comparison of the model observable quantities with our samples, we will investigate the IMF and star formation history of the SMC. We first discuss the basic concepts and recent studies that have used the population synthesis method.

5.1 Stellar evolution models

The development of computers opened a new field in astronomy, numerical astronomy, that enables calculations of the interior structure in a star with respect to time, *i.e.*, stellar evolution. Schönberg and Chandrasekhar (1942) proposed the inhomogeneous model of the stellar evolution of main sequence stars and later Iben (*e.g.* Iben, 1965) published a series of stellar evolution models. The advances of computing in the mid 1980s were sufficient to predict stellar lifetimes, luminosity, and even surface abundances from nucleosynthesis. Stellar evolution models now have a wide range of applications in astrophysics,

from the study of individual stars to clusters to galaxies. The most widely used stellar evolutionary models are from the Geneva and Padova groups. Both calculate evolutionary tracks for various metal abundances and masses; however, we use the Geneva models in our population synthesis code because they calculated a $Z = 0.004$ grid (Charbonnel *et al.*, 1993), corresponding to SMC metalicity. Full descriptions of their calculations and grids for $Z = 0.020$, solar metalicity and $Z = 0.001$ are presented by Schaller *et al.* (1992). Schaerer *et al.* (1993*a*,*b*) published further model grids with $Z = 0.008$, suitable for the study of the LMC, and $Z = 0.040$. In order to consider the high mass-loss rates found in massive star evolution, Meynet *et al.* (1994) enhanced the grids over the 12 to 120 $m_{\odot}$ mass range, at each of the previous published metallicities. Also they constructed grids of models with rotation in the range of 9 to 120 $m_{\odot}$ at solar metallicity (Meynet and Maeder, 1997), and more recently, calculated a grid of models with rotation (from 9 to 60 $m_{\odot}$), at $Z = 0.004$, appropriate for the SMC. Maeder and Meynet (2001) found that the effect of rotation caused the evolutionary tracks to move toward lower effective temperatures, to extend the main sequence band width, and that the use of non-rotating tracks would overestimate the mass at lower metalicity. However the evolutionary model containing rotational effects are not considered here because we have no information about the rotational velocities of the SMC stars. Even if we know them, it is practically impossible to consider the individual speeds together.

Basically the evolutionary tracks are discrete grids for a given masses so the physical parameters from population synthesis model, *PSYNTH* are interpolated quantities between near masses tracks following the advice in Maeder and Meynet (1988);

'the interpolation between evolutionary tracks must be properly based on points of corresponding evolutionary status'.

5.2 The Initial Mass Function

If a stellar mass is given, we can basically determine all parameters of a star for a given time, *i.e*, the mass governs its characteristics (modulo metallicity and rotation). Therefore the key point for the study of clusters or galaxies is the mass distribution of their constituent stars. In particular, the study of the initial mass function of a system is very important to its mechanical and chemical evolution.

In a seminal work, Salpeter (1955) investigated the IMF for main-sequence stars in the

solar neighborhood from the observed luminosity function and mass-luminosity relation, correcting for evolved stars. The slope of his luminosity function ($\Gamma = -1.3$, Γ defined in Equation 5.8) is now referred as a 'Salpeter slope'. Motivated by his work, there have been many studies of the IMF during last half century. Miller and Scalo (1979) examined both observational and theoretical evidence relating to the IMF and star formation history in the solar neighborhood. They found that the IMF was independent of time and that the theoretical models were consistent with a constant stellar birth rate. Scalo (1986) gave a thorough review of the subject and highlighted remaining problems of IMF studies for a wide range of systems, *i.e.* field stars, star clusters, and nearby galaxies. Recently Gilmore and Howell (1998) edited new results provided by the 38th Herstmonceux conference, on the stellar initial mass function. Overall, there is no strong evidence for the IMF variations, with most results following the Salpeter slope, within observational errors, regardless of mass-ranges and/or targets, *i.e.*, they confirm the 'universal IMF'.

We introduced the definition of the IMF and summarise some relevant studies according to mass ranges in Chapter one. In this section, we will explain how the IMF slope is used to generate stellar populations in *PSYNTH*.

From Equation 1.1, the IMF is,

$$\phi = \phi_0 m^{\gamma} \tag{5.1}$$

So the number of stars between masses m and $m + dm$ is given by

$$dN(m) = \phi(m)dm = \phi_0 m^{\gamma} dm \tag{5.2}$$

Because Equation 5.2 has an analytical integral solution, we can use the inversion method in a Monte Carlo simulation to populate N stars following an IMF slope for a given minimum and maximum mass-interval. The inversion method consists in introducing the cumulative probability

$$f = N(m) = \int_{m_{min}}^{m} \phi(m)dm \tag{5.3}$$

that takes random values in the interval [0,1], and the inversion function $m = N^{-1}(f)$. Of course, the $\phi(m)$ should be normalised, so that

$$\int_{m_{min}}^{m_{max}} \phi(m)dm = 1. \tag{5.4}$$

From Equation 5.1 and 5.4, and from $\Gamma = \gamma + 1$ relation, The normalized constant is

$$\phi_0 = \begin{cases} \frac{\Gamma}{m_{max}^{\Gamma} - m_{min}^{\Gamma}}, & \Gamma \neq 0 \\ \ln^{-1}\left(\frac{m_{max}}{m_{min}}\right), & \Gamma = 0 \end{cases} \tag{5.5}$$

For the case that $\Gamma = 0$, it can be numerically approximated with the value very close to zero so we will not consider this case here. Substituting Equation 5.1 and 5.5 into Equation 5.3, the cumulative probability is

$$f = N(m) = \frac{m^{\Gamma} - m_{min}^{\Gamma}}{m_{max}^{\Gamma} - m_{min}^{\Gamma}} \propto m^{\Gamma} \tag{5.6}$$

$$m_{ZAMS} = [m_{min}^{\Gamma} + f(m_{max}^{\Gamma} - m_{min}^{\Gamma})]^{1/\Gamma}$$

or taking logarithm scale,

$$\log m_{ZAMS} = \frac{\log[m_{min}^{\Gamma} + f(m_{max}^{\Gamma} - m_{min}^{\Gamma})]}{\Gamma} \tag{5.7}$$

Therefore by generating random numbers (f) between 0 and 1, we can generate a population of stars with mass m in Equation 5.7 for a given minimum and maximum masses range and for the given IMF slope (Γ). Here the IMF slope (Γ) is expressed in the following by taking the logarithm and then differentiating in Equation 1.3;

$$\begin{aligned} d\log\xi(\log m) &= \Gamma \cdot d\log m \\ \Gamma &\equiv \frac{d\log\xi(\log m)}{d\log m} \end{aligned} \tag{5.8}$$

So the Γ defined as the above and used in our study is the logarithmic slope of the IMF evaluated at logarithmic (base ten) mass, $\log m$.

Hence with zero age main sequence masses from Equation 5.7, the theoretical quantities of model stars formed at $t = T_0$ (*i.e.* with one burst) can be obtained by evolving them until $t = T_0$ on the evolutionary grid. The method for the model stars following continuous star formation between T_1 and T_2 ($T_2 > T_1$) is the same as the burst case except that we have to determine the age (or time) by another random number, g, between 0 and 1. Say, $t = (T_2 - T_1)g + T_1$ in this case. More complex star formation histories can be approximated by concatenating series of continuous star formation for the suitably-defined time intervals and burst formations.

On the observational side, we only know the present day mass function (PDMF), the actual numbers as function of mass from the result of a star formation history. So the

Equation 5.3 becomes:

$$N(m,t) = \int_{m_{min}}^{m} \int_{0}^{t} \phi(m) b(t) dm dt \tag{5.9}$$

where $b(t)$ is the star formation rate. One extreme of the star formation history is to suppose that stars are born at the same time, $t = T_0$. Then the star-formation rate is a delta-function and so from Equation 5.9,

$$N(m,t) \propto m^{\Gamma}|_{m_{min}}^{m_0} \tag{5.10}$$

where m_0 is the mass which the main sequence lifetime (τ) is T_0. For this case, the PDMF is the same as the IMF except that higher mass stars than m_0 are dead. In the case of continuous star formation, $b(t)$ is constant and situation becomes steady-state, *i.e.* the number of star births and deaths is equal. For the time t greater than τ of the lowest mass,

$$N(m,t) \propto m^{\Gamma} \times \tau(m)|_{m_{min}}^{m_{max}} \tag{5.11}$$

Therefore in order to estimate the IMF of a system which has undergone continous star formation, the observed mass bins have to be divided by the appropriate lifetime, $\tau(m)$.

5.3 Age and star formation history

The study of the star formation in the SMC is very interesting due to its low metalicity, high gas-to-total mass fraction and irregular shape. In particular, it can give a clue to the role of external dynamical interactions (with LMC and/or Milky Way) in triggering the star formation process.

One method to determine a star-formation history of the SMC would be to measure the main sequence turnoff ages for all clusters. However it is impractical at present; the SMC contains around 2000 clusters (Hodge, 1986) and only some of the SMC clusters have age estimates, from the various techniques. For example, Stryker *et al.* (1985) studied the age of the NGC 121 from the main sequence turnoff and found it is 12 ± 2 Gyr old, the oldest cluster known to date.

Gardiner and Hatzidimitriou (1992) concluded from their stellar population study that the star formation rate in the SMC has decreased over the past 2 Gyr, with exceptions of active star formation regions in the core and in the wing.

Also there have been many studies of the star formation history in the SMC in connection with chemical evolution. Most of these showed an agreement in the sense that the SMC has markedly different features compare to those of our Galaxy. Olszewski *et al.* (1996) and Westerlund (1997) reviewed the details of the star formation history in both Magellanic Clouds and concluded that majority of the stars are under 4 Gyr old. However in contrast with the LMC, the star formation rate in the SMC appears to more uniform (van den Bergh, 2000; Olszewski *et al.*, 1996). Pagel and Tautvaišienė (1998) made two analytical models of the star formation history in the SMC based on chemical evolution: a bursting and a smooth model. According to their bursting model, there were two starbursts around 10 Gyr and 1.3 Gyr ago, before the formation of the current massive stars. So their burst models are not useful for our study of the massive star population. The smooth model can be approximated by continuous star formation within 2 Gyr.

Hernandez *et al.* (1999) introduced a different method for deriving star formation histories based on Bayes's theorem (which we will explain later), and used it to study the star formation history of the solar neighbourhood (Hernandez *et al.*, 2000*a*) using the Hipparcos catalogue; and of four local Group dwarf galaxies (Hernandez *et al.*, 2000*b*), using HST data. However their method requires an IMF value as a prior condition, and they adopted Kroupa *et al.* (1993)'s result for their studies. Because our main driver is to study the IMF slope rather than the star formation history, we do not consider their approach[1].

Very recently, Harris and Zaritsky (2004) investigated the star formation and chemical enrichment history of the SMC using their photometric survey (Zaritsky *et al.*, 2002). Although there are $\sim$ 2 Gyr systematic differences, their results show good overall agreement with burst model from Pagel and Tautvaišienė (1998). They divided the SMC star formation history into three epochs;

- An early epoch ($t > 8.4$ Gyr) : About 50% of the SMC stars were formed.
- An intermediate epoch ($3 < t < 8.4$ Gyr) : The SMC has a long quiescent period.
- An active epoch ($t < 3$ Gyr) : There has been active star formation caused by bursts at 2.5 Gyr, 400 Myr, and 60 Myr. They pointed out that the older two bursts are in accordance with past perigalactic passages between the SMC and the Milky

[1]Our interest is primarily in the massive-star population, which does not encode the star-formation history because of the short lifetime.

Way. However according to Geneva evolutionary model, stars massive than only $\sim$ 6 $m_{\odot}$ left main sequence stage after 400 Myr so it is inappropriate to our study for hot stars. For the reason, we choose 10 and 60 Myr epochs for the test of burst star formation history of the SMC.

In our IMF study of the SMC using a population synthesis method, we assume three types of star-formation models: 1) Continuous, 2) Starbust, and 3) a more complex Hybrid model.

- Continuous star-formation model. Although it is known that the oldest cluster in the SMC is 12 Gyr old (Stryker *et al.*, 1985), the lifetime of a $2m_{\odot}$ star is only 1.08 Gyr according to the Geneva evolutionary library ($Z = 0.004$). So we use '-2 Gyr' (negative), sufficiently larger than the lifetime of our minimum mass, as an input of age. This model well matches the Pagel and Tautvaišienė (1998) models, which give good explanations of the chemical evolution in the SMC, because they can be approximated as continuous models for the recent 2 Gyr.

- Burst star-formation models. To simulate a starburst history, we assume single bursts at '+10' Myr and '+60' Myr (positive) epochs. With equal contributions from each single burst, we also test a double burst model. So the burst models are subdivided into three models: two single bursts and one double-burst model.

- Complex star formation model. To consider the complex star formation histories in the SMC, we also test a simple 'complex' model made by 50%, 25% and 25% number contributions from the continuous model and the bursts models at $t = 10$ and 60 Myr, respectively.

In total, we therefore consider five star-formation models: continuous, two single-burst, double-burst, and complex model.

5.4 Stellar atmosphere models

In our population synthesis code, *PSYNTH*, two key libraries are implemented: the stellar evolutionary tracks from Geneva group and transformations from Bessell *et al.* (1998): which are tied in to stellar-atmosphere models. Although we simply use interpolated stellar parameters from the grids, it is worthwhile reviewing the model atmospheres, to understand their strengths and limitations.

Model atmospheres calculate the fiow of energy transportation in the photosphere of a star. In classical works, the stellar atmosphere was approximated by plane-parallel geometry and Local Thermodynamic Equilibrium (LTE), mainly to simplify the computations, in which the state of gas was described with the hydrostatic equations and Saha-Boltzman equations.

Plane-parallel geometry is modelled as a one-dimensional calculation, assuming a series of slabs of atmosphere at an adequate distance interval, a valid assumption for stars whose atmospheres are thin compared to the radius. However it is known that some stars have extended atmospheres, *e.g.*, due to stellar winds, most often found in supergiants. In this case, a spherically extended atmosphere should be considered in order to take account of the gradient of physical parameters between the inner and outermost parts.

LTE is a state with the following assumptions (Mihalas, 1970);

'the occupation numbers of the atoms, the opacity, the emission, and indeed all thermodyamic properties of a small volume of the material in the atmosphere are the same as their thermodynamic equilibrium values at the local values of the temperature T and the electron density N_e' at the radius r.

This means that the distribution of particles and their possible states of excitation and ionization can be completely described by the Maxwellian, Boltzman distribution and Saha equations, at the local temperature. In general the LTE assumption is useful and valid where collisions dominate. However as the role of radiation becomes important in a hot star, for example up to 40% of the total pressure (Philips, 1999), the state of the gas is increasingly dependent not only on T and N_e but also the radiation field. In practice, the LTE assumption breaks down under the condition that the temperature is high, $T > 10kK$ (*e.g.* Auer and Mihalas, 1972); and also in the case that surface gravity (hence particle densities) is low, even at cool temperatures (Kurucz, 1979). Therefore in order to more accurately describe the stellar atmosphere, it should be treated in non-LTE.

The other assumptions in the early studies of model atmosphere are hydrostatic and radiative equilibria. Hydrostatic equilibrium is the state that the pressure stratification is balanced with the gravitational field, *i.e.*, that all velocity fields are ignored. In reality, a stellar atmosphere is nearer to hydrodynamic equilibrium rather than hydrostatic. Lastly, although the radiative equilibrium is a good approximation for most stars, it also neglects other processes in energy transport, such as convection and overshooting.

So far, we have discussed the problems in classical model atmospheres related to pro-

cesses at the macroscopic level. However the purpose of model atmospheres is to calculate occupation numbers for each atomic level, allowing the computation of pressure, densities, and opacities of a star, at a microscopic level. In practice, the difficulty comes from the fact that it is impossible to consider all possible transitions for all species in a stellar atmosphere. Actually there are $10^4 \sim 10^5$ energy levels and the similar number of permitted transitions for each level in the case of iron. However, only hundreds of transitions are usually included in the model atmosphere calculations due to the lack of atomic data. In non-LTE, the radiation field and state of gas are coupled, so the situation is more complicated because the radiation field, in turn, depends on the occupation numbers. This means they should be solved simultaneously, which is not directly possible, so an iterative method is used. To address this, Auer and Mihalas (1969) introduced the *'complete linearisation* (CL)' technique, coupling physical quantities such as level populations, radiation field, and temperature. Another option is *'accelerated lambda iteration* (ALI)', taking the radiation intensity as a lambda operator acting on the source function with a correction term found from the previous iteration.

In observational data, one of the most prominent features in UV spectroscopy is that there are many weak metal absorption lines giving rise to line blanketing. This is the process in which metal lines absorb radiation and then re-emit it, to longer wavelengths, with the result that opacities are increased and so the temperature structure is changed. As mentioned before, the number of cases of allowed transition increases on the heavier elements and peaks on iron-group elements. One method includes these opacities into the model using Opacity Distribution Functions (ODF), which represent a resampled total opacity in a given frequency interval. Kurucz (1979, 1992) published LTE line-blanketed model atmospheres using this technique, with a grid covering 5500 to 50,000 K at one, one-tenth, and one-hundredth solar metallicity, from the main sequence down to the radiation pressure limit in surface gravities. For each model he tabulated the temperature structures, fiuxes, UBV and *uvby* colours, bolometric corrections, and Balmer line profiles.

As an alternative, Anderson (1989) conceived a statistical method, called 'superlevels' and 'superlines', grouping several energy levels together. Based on this idea and a hybrid CL/ALI technique, Hubeny and Lanz (1995) presented stellar parameters for hot stars using non-LTE line-blanketed model atmosphere calculations (see also Lanz and Hubeny, 2003).

Recently Bessell *et al.* (1998) studied wide band colours, bolometric corrections and

temperature calibrations for O – M stars using various model atmospheres (references therein). According to their results, most colours show good agreement with empirical relations except $B - V$ colour for K giants, M dwarfs and M giants. In this thesis, we adopt their grid and note that the minor disagreement in $B - V$ for cool stars has minimal influence on our study, which deals mostly with hot stars.

5.5 Transformation into observable parameters

The outputs of theoretical stellar evolutionary model calculation for a given age and ZAMS mass generated using Equation 5.7 are (interpolated) current mass, luminosity, and effective temperature. We then transform those parameters into colour indices calculated by Bessell *et al.* (1998) in order to compare them with our photometric data. Bessell *et al.* (1998) constructed grids of bolometric corrections in terms of K and V magnitudes and eight intrinsic colour indices with respect to effective temperature (T_{eff}) and surface gravity ($\log g$) from contemporary model atmospheres. In order to estimate the colour indices from the output of the evolutionary models, we first have to calculate the surface gravity. The radius of a star is given by the relation between luminosity and effective temperature,

$$\frac{R}{R_\odot} = \left(\frac{L}{L_\odot}\right)^{1/2} \left(\frac{T_{\odot\ eff}}{T_{eff}}\right)^2 \tag{5.12}$$

where $T_{\odot\ eff} = 5770K$. Then the surface gravity is

$$g = \frac{GM}{R^2} = g_\odot \left(\frac{M}{M_\odot}\right) \left(\frac{R_\odot}{R}\right)^2 \tag{5.13}$$

After interpolating parameters given by Bessell *et al.* (1998) using the effective temperature from output of evolutionary model and the surface gravity from Equation 5.13, we can then transform them into the model observable quantities. The absolute bolometric magnitude for a star is

$$M_{bol} = M_{bol}(\odot) - 2.5 \log(L/L_\odot) \tag{5.14}$$

where $M_{bol}(\odot) = 4.74$ (Bessell *et al.*, 1998). So the absolute V magnitude is

$$M_V = M_{bol} - B.C \tag{5.15}$$

Because Bessell *et al.* (1998) only constructed grids for the range from 3500 to 50 kK in effective temperature, we extend their $B.C$ using the Howarth and Prinja (1989) relation for temperatures higher than 50 kK, which affects only a few synthesized stars.

$$B.C = B.C_{50kK} - 0.08\left(\frac{T - T(50kK)}{1000.0}\right) \tag{5.16}$$

Then the V magnitude in the SMC is

$$V = M_V + DM \tag{5.17}$$

where DM is apparent distance modulus, 18.86[2], which is derived from section 4.5.2 and comparable to recent absolute values.

Lastly the $(B-V)$ and $(V-R)$ are

$$\begin{aligned}(B-V) &= E(B-V) + (B-V)_0 \\ (V-R) &= E(V-R) + (V-R)_0\end{aligned} \tag{5.18}$$

where $E(B-V) = 0.107$ and $E(V-R) = 0.094$ (see also footnote 2).

We summarise the procedures of the transformation from theoretical outputs into model observable quantities in Figure 5.1.

5.6 Selection effects

Before comparing the photometric samples with synthesised populations, we have to consider the selection effects and incompleteness in our observations. One of the advantages of transforming theoretical data into observable parameters is that corrections are more easily, accurately and transparently applied than the reverse process.

As pointed out in section 4.3, our SMC catalogue also contains foreground Galactic stars. In order to remove those stars in comparisons (*i.e.*, to compare observational quantities of pure SMC stars with model ones), we select stars with $(B-V) < +0.6$ (*i.e.*, main sequence stars) in both observational and models. Some evolved SMC stars, *e.g.*, $(B-V) > 1.2$, are thereby excluded.

In addition, our photometric data are incomplete as mentioned in section 3.3:

[2] At the time of model calculations, we had obtained different values for the distance modulus and colour excesses to the final values presented in Chapter Four. Because the values used in model calculations are only slightly different, and because the model calculations require large amounts of computer time, we did not re-calculate using new values. However, we believe that this has negligible affect on our results.

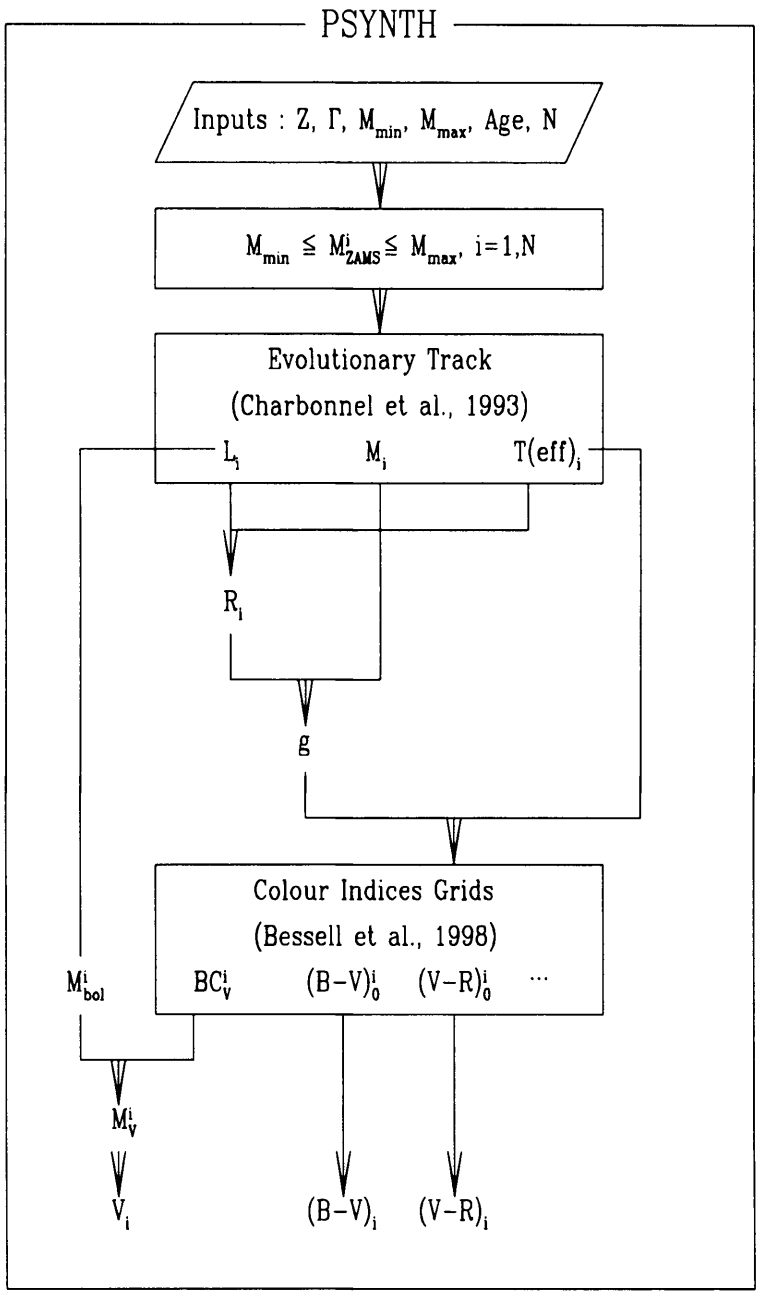

Figure 5.1: Summary of the transformation from theoretical outputs into model observable quantities using the population synthesis program, *PSYNTH*.

- Incompleteness in the survey area. Due to the weather conditions and instrument faults, there were some non-photometric frames. Based on our definition, we estimated that the survey is $\sim 95.1\%$ complete (see subsection 3.3.1).

- Photometric incompleteness caused by binarity, crowding and the faint limiting magnitude. By the artificial star method, we tested the completeness in B, V and R and found $\sim 90\%$ at $B \sim 18.0$ (see subsection 3.3.2).

In consideration of the selection effects, the main principles are 1) there is a true parent population that actually exists in the SMC and 2) the same selection effects in the observational data must be applied to the synthetic theoretical populations in order to lead to a comparable synthetic observed populations.

The number distribution of stars with respect to magnitude is different from region to region so we have no way to correct it. That is, it is impossible to correct for the incompleteness in survey area. However we can assume that the incompleteness in each survey area has an influence on only the total number of stars, not on the individual magnitude bins. Because the important thing in the comparison is not the absolute number of stars but the relative numbers (per unit interval in colour and magnitude), so we do not need to correct the effect of incompleteness in each survey area.

For the second selection effect, we use the results of the artificial star test for each grid discussed in subsection 3.3.2. As shown in Tables 3.7 and 3.8 (see details in Appendix B.2), the photometric completeness as a function of magnitude in each filter shows different features with respect to each grid. Of course, those are results from the combination of many factors, mainly crowding and the magnitude limits. For example, in Figure 5.2 we show the relative photometric completeness, normalised to 1, to illustrate the dense and sparse regions as a function of magnitude. In order to select synthetic stars to represent our catalogue stars, we consider the whole available photometric completeness results. From Figure 5.2, the relative completeness, P, of each filter is $P(B) \sim P(V) \sim P(R)$ in the dense region (upper panel) and is $P(B) < P(R) < P(V)$ in the sparse region (bottom panel). It is a natural result because the the crowding limits the photometric completeness in the dense area, whilst the magnitude is the sole limitation in the sparse area.

Suppose that the probability of observing star i of magnitudes B_i, V_i, and R_i in a grid are $P(B_i)$, $P(V_i)$ and $P(R_i)$, as determined in the study of photometric completeness. How then to define P_{obs}, the probability that the synthetic star will be selected ? Firstly,

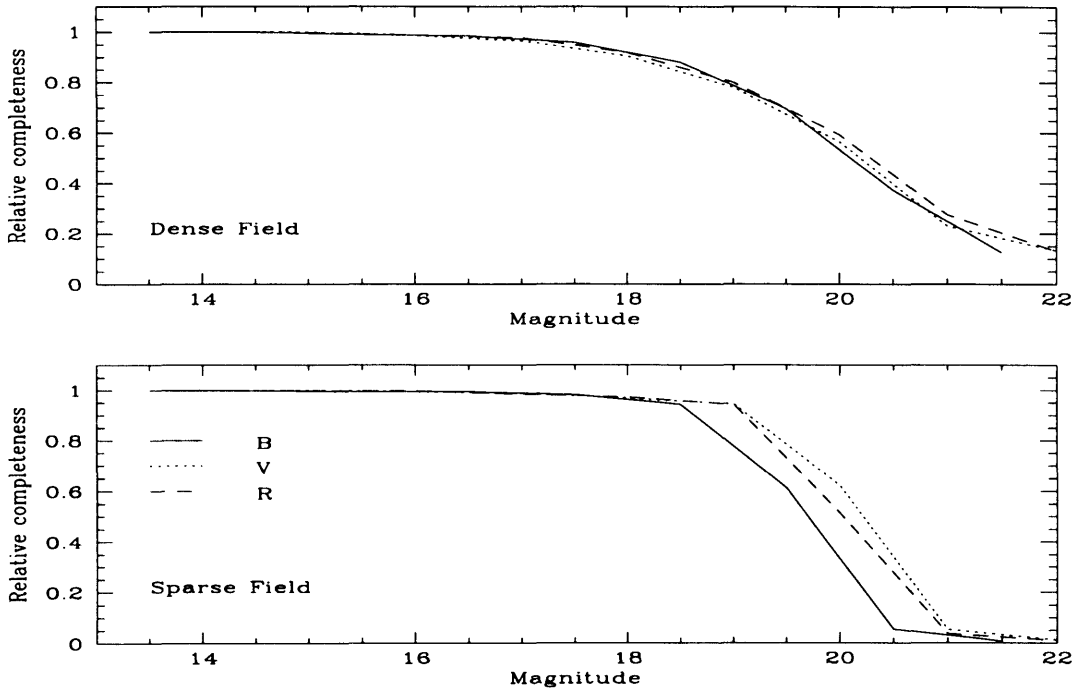

Figure 5.2: The relative photometric completeness as a function of magnitude in the dense (upper panel) and in the sparse region (bottom panel). The values are normalised to 1.

let's consider two extreme cases;

- If a field is sparse, *i.e.*, magnitude-limited, then we consider that the probability in each filter is independent so P_{obs} is just

$$P_{obs} = P(B_i) \times P(V_i) \times P(R_i) \tag{5.19}$$

- As found in Figure 5.2, if a field is dense, *i.e* crowding limited, the photometric completeness shows the similar feature regardless of filter. Say, $P(B_i) \simeq P(V_i) \simeq P(R_i)$. In this case, detection of a star depends mainly on position, not on magnitude. This means that $P(B_i)_j$, $P(V_i)_j$, and $P(R_i)_j$ are not independent so we choose P_{obs} as the minimum probability.

$$P_{obs} = \min\{P(B_i), P(V_i), P(R_i)\} \tag{5.20}$$

Of course, there will be locally dense regions in a sparse field and also cavities in a

Table 5.1: The star number ratio for each field relative to the total catalogue with $(B-V) < 0.6$.

Grid	#01	#02	#03	#04	#05	#06	#07	#08	#09	#10
Ratio(%)	1.39	1.55	3.52	2.07	0.79	4.07	6.16	3.56	13.87	20.88
Grid	#11	#12	#13	#14	#15	#16	#17	#18	#19	#20
Ratio(%)	5.57	1.26	5.85	4.92	2.97	4.15	1.21	1.63	1.05	0.41
Grid	#21	#22	#23	#24	#25	#26	#27	#28	#29	#30
Ratio(%)	0.78	1.89	1.29	0.63	0.76	1.84	1.20	0.50	1.26	2.02
Grid	#31	#32	#33	#34					Total	
Ratio(%)	0.33	0.25	0.19	0.20					100.	

dense field. However if we use field-by-field probabilities identifying fields as corresponding to one of these extremes, it is a reasonable approach in practical terms.

Based on both the ratio of the star numbers in each field to that in all fields (see Table 5.1) and visual examination of the photometric completeness for each grid, we classify twelve as crowded - #01, #06, #07, #08, #09, #10, #13, #14, #15, #17, #23, and #24, and the others as magnitude-limited fields.

For a given synthetic star, firstly we decide which observed field it 'belongs' to with random number generation between 0 and 100. If random number is greater than the cumulative ratio value of i field and less equal than that of $i+1$ field from Table 5.1, which is also normalised to 100, we regard it as the $i+1$ field star. This ensures proper weighting of sparse and dense fields (*i.e.*, for equal numbers of sparse and dense fields, there are nonetheless more stars in the dense fields). For example, if the generated random number for a given synthetic star is 7.5, it is considered as a #04 field star because the cumulative ratio value for #03 field is 6.46 (=1.39+1.55+3.52) and for #04 is 8.53 (=6.46+2.07) (see Table 5.1). After determining the field, we use Equation 5.19 or 5.20 to calculate P_{obs}, depending on whether it is crowding or magnitude limited. With another random number, we decide whether a synthetic star is observed or not, according to the P_{obs} value calculated using $P(B)$, $P(V)$, and $P(R)$ from the results of photometric completeness for that field (see Table 3.7 and 3.8).

Through the above steps, we can apply the same selection effects ('filtering') to the

synthesised population sets having various IMF slopes and star formation histories as in the observational data. For the population stars brighter than the upper magnitude range used for the artificial star tests, we assume the 100 % completeness up to 9.6 magnitude, the brightest B magnitude in our sample. We cut off the data fainter than 19 magnitude, not only because the incompleteness becomes severe below this magnitude but also in order to reduce the computational load; more stars are generated by the population synthesis code toward fainter magnitudes (because the IMF slope is negative), whence we have to reject more synthetic stars because the observational data have fewer stars toward that magnitude (due to the larger photometric incompleteness toward faint magnitudes). So the selection criteria applied to our sample is $9.5 < B < 19.0$ and $(B - V) < 0.6$.

For the statistical analysis described in section 5.8, the synthetic population should be significantly larger than the observed one. In practice, it therefore is impossible to compare all the photometric data ($\sim$ 1.3 million) with a synthesised population at once so we randomly collect subsamples containing about 5% of the stars satisfying our selection criteria ($\sim$ 0.46 million). Although we select the subsample at random, it may also have the possibility to be biased so we extract three observational subsamples and compare them with synthetic population models having the input parameters explained in the next section. Figure 5.3 represents the number distribution of the three subsamples, labelled as A, B, and C. In the first three pictures, the solid lines are the actual number distributions of subsamples, the dotted lines are the totals of our selected photometric data ($\sim$ 0.46 million) normalised to the subsamples. The distributions show good agreement with total distribution for the stars fainter than 13 magnitude. The slight mis-match in the regions of brighter than 13 magnitude is caused by the scarcity of brighter stars (*i.e.* small number statistics). So those features also support the fact that the subsamples are well selected without bias; the number distributions of subsamples in magnitude ranges brighter than $\sim$ 13 (*i.e.* in low statistic ranges) show small fluctuations (*i.e.*, no systematic trends), while those in fainter magnitudes (*i.e.* in high statistic ranges) represent good agreement with total photometric data. The last picture is plotted in order to compare together the number distribution of each subsample.

Lastly, because Bessell *et al.* (1998) computed model atmospheres based on the Cousins system in R, we again used Equation 1.5 for the selected three samples in order to convert these into the same system.

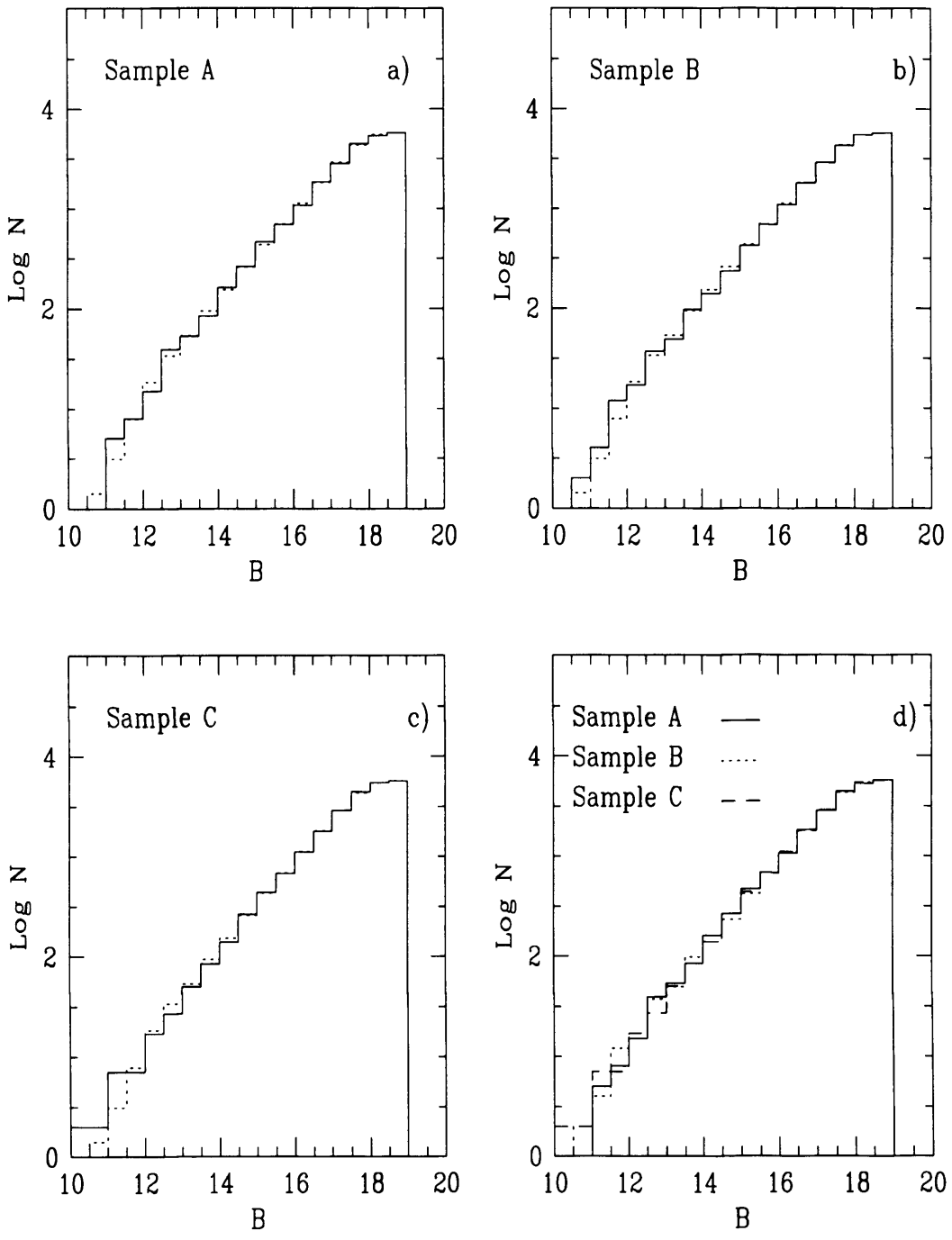

Figure 5.3: The number distributions of three observational subsamples used for comparison with the models. In Figure a), b), and c), the solid lines are the number distribution of subsamples, the dotted lines are that of total photometry data normalised to each subsample. Figure d) shows the comparison of each subsample.

5.7 Population models

In constructing the synthetic population models, we use the following input parameters.

- We fix the metal abundance for all models to $Z = 0.004$ (Lequeux *et al.*, 1979), *i.e.*, $Z_{SMC} = 0.2Z_{\odot}$.
- $m_{min} = 2.0m_{\odot}$, and $m_{max} = 120m_{\odot}$. From the evolutionary models, a $3m_{\odot}$ star corresponds to $B \simeq 19.0$, the lower magnitude limit of our samples. To be cautious, we choose $2m_{\odot}$ as the minimum mass. The selection of maximum mass is somewhat arbitrary. Kahn (1974) suggested that the upper mass limit for star formation is smaller in high metalicity regions, $\sim 40m_{\odot}$ in our Galaxy. Shields and Tinsley (1976) assumed $L \propto m^3$ for massive stars and predicted $m_{max} \propto Z^{-1/2}$ scale relations. However Massey *et al.* (1995*a*) found that the masses of the most massive stars are nearly equal in Milky Way and Magellanic Cloud associations, where the metalicity differs by a factor of 5. Later Massey and Hunter (1998) identified a large number of O3 stars in the R136 cluster of 30 Doradus and concluded that the upper mass limit is a matter of scarcity in a system. Therefore we choose $120m_{\odot}$, the highest mass for which evolutionary tracks are available, as the maximum mass although Figer (2005) suggested $\sim 150m_{\odot}$ as the upper mass limit for massive stars.
- We generated a synthetic population with 100 times more stars than in our subsamples in order to improve in statistical analysis, explained in next section.
- We test IMF slopes in the range of -1.1 to -3.5 at steps of 0.1.
- To consider the effect of star formation histories, we test five star formation history models (see section 5.3).

So the total number of population models considered in our study is 125 – five types of the star formation histories for the twenty five different IMF slopes – compared with each of three independent photometric samples, as described in the next section.

5.8 Statistical analysis

Visual inspection of the number distributions between the observed subsamples and synthetic models provides a qualitative insight of the results. To obtain quantitative results,

we employ the statistical analysis developed by Tolstoy and Saha (1996). They adopted Bayesian inference to estimate the likelihood between model Magnitude-Magnitude Diagram (MMD) and observational MMD, but their analysis is easily generalised to other parameter spaces (*e.g.*, CMD).

5.8.1 Bayesian inference

The method to determine the model which gives the best representation (relative probability or likelihood) of the observation is based on Bayesian inference.

The probabilities of events A and B are $P(A)$ and $P(B)$, where $\int P(A)dA = \int P(B)dB$ =1 (normalisation). Then the probability that A *or* B will happen is

$$P(A+B) = P(A) + P(B) - P(A,B) \tag{5.21}$$

where $P(A,B)$, the probability that A *and* B will happen, called the *joint probability* and given by

$$\begin{aligned} P(A,B) &= P(A)P(B|A) \\ &= P(B)P(A|B) \end{aligned} \tag{5.22}$$

where $P(B|A)$, the probability of B given A, and $P(A|B)$, the probability of A given B, called the *conditional probability*. If $P(A,B) = P(A)P(B)$, then A and B are said to be independent. From Equation 5.22,

$$P(B|A) = \frac{P(B)P(A|B)}{P(A)} \tag{5.23}$$

which is conventionally known as Bayes' theorem, published by a Presbyterian minister, the Reverend Thomas Bayes, in 1793. In Bayes' theorem, $P(B|A)$ is know as the *posterior* probability, $P(B)$ is as the *prior* or independent probability, and $P(A|B)$ is the *likelihood* function. As for other probabilities, $P(B|A)$ has to be normalised, so Bayes' theorem (Equation 5.23) is

$$P(B|A) = \frac{P(B)P(A|B)}{\int P(B)P(A|B)dB} \tag{5.24}$$

where $P(A) = \int P(B)P(A|B)dB$.

Now consider an observed data set composed of n points, $D = (D_1, \cdots, D_n)$ and the models describing the data set, $M = (M_1, \cdots, M_i, \cdots)$. From Bayes' theorem, the probability of a model M_i given the observed data set D, is:

$$P(M_i|D) = \frac{P(M_i)P(D|M_i)}{P(D)} \tag{5.25}$$

In practical cases as well in observational data, the probability is not continuous but discrete, so the normalisation can be replaced by the summation.

$$P(D) = \sum_i P(M_i)P(D|M_i) \tag{5.26}$$

However because it is impossible to consider every possible model, say, $\sum_{i=1}^{\infty} P(M_i)$, Bayes' theorem is rewritten as a relative possibility, or as the proportional relation:

$$\begin{aligned} P(M_i|D) &\propto P(M_i)P(D|M_i) \quad \text{or} \\ \textit{posterior} &\propto \textit{prior} \times \textit{likelihood} \end{aligned} \tag{5.27}$$

From Bayes' theorem, (Equation 5.27), we can *infer* as the following;

'The model that has the highest probability of describing the observed data set, $P(M_i|D)$, is that having the maximum likelihood, $max.[P(D/M_i)]$.'

5.8.2 Likelihood method

Again suppose that there is an observational data set $\boldsymbol{D}$ consisting of N pairs of points in two-dimensional coordinates, $\boldsymbol{X} = \boldsymbol{X}(x, y)$, with uncertainties $\boldsymbol{\sigma}$:

$$\begin{aligned} \boldsymbol{D} &= \boldsymbol{D}(D_x(n), D_y(n)) \\ \boldsymbol{\sigma} &= \boldsymbol{\sigma}(\sigma_x(n), \sigma_y(n)), \qquad \text{where} \quad n = 1, \cdots, N. \end{aligned} \tag{5.28}$$

and a model in the same dimensions with I pairs of points,

$$\boldsymbol{M} = \boldsymbol{M}(M_x(i), M_y(i)), \qquad i = 1, \cdots, I. \tag{5.29}$$

In our case, the x-dimension is the colour index and y is the magnitude on a CMD plane. Then for the many models, which one looks *'most likely'* to match the data set? To answer the question, we use the relative likelihood method derived from Tolstoy and Saha (1996).

The normalised probability density distribution of the ith model point with discrete distribution in the $\boldsymbol{X}$ plane, $\boldsymbol{\rho}(\boldsymbol{X})$, is given by delta function;

$$\boldsymbol{\rho}(\boldsymbol{X}) = \sum_{i=1}^{I} \frac{\delta(\boldsymbol{M}(i) - \boldsymbol{X})}{I}. \tag{5.30}$$

As I approaches ∞, $\boldsymbol{\rho}(\boldsymbol{X})$ becomes a continuous function, thus it is important to generate as many model points as possible in order that $\boldsymbol{\rho}(\boldsymbol{X})$ can be defined more accurately, that is, to get a more reliable statistic.

The (unnormalised) probability which a data point n, assuming a Gaussian distribution in its positional uncertainty, is matched to entire ensemble of model points, $\boldsymbol{S}_n(\boldsymbol{D})$, is then;

$$\boldsymbol{S}_n(\boldsymbol{D}) = \frac{1}{I}\frac{1}{2\pi\sigma_x(n)\sigma_y(n)}\sum_{i=1}^{I}\exp\left\{-\frac{(\boldsymbol{M}(\mathrm{i})-\boldsymbol{D}(\mathrm{n}))^2}{2\sigma(n)^2}\right\} \tag{5.31}$$

The likelihood taking natural logarithm, $\ln L$, is the Nth products of the probabilities of each point for all data points,

$$\ln L = \ln\left[\prod_{n=1}^{N}\boldsymbol{S}_n(\boldsymbol{D})\right] \tag{5.32}$$

As emphasized by Tolstoy and Saha (1996), the likelihood is only a relative probability so they defined a *'perfect'* likelihood ($\ln L_d$) from the model using data points themselves, and then used it as the zero point for each model such as $\ln(L_j/L_d)$ is the relative likelihood for jth model.

5.9 Results

Although synthetic datasets are relatively quickly generated, evaluation of the likelihood function is quite time-consuming (about one and half hours for one model with computing facilities described in section 3.1, so 1,125 hours in total), and varies with $\sim (Nn)^2$, where N and n are the numbers of synthetic and actual stars involved. It is therefore important to use the smallest numbers consistent with statistical accuracy.

Before performing the model calculations, we therefore check two points to test our assumptions. Firstly we investigate the variation of likelihood (*i.e.*, $\ln L/L_d$) with respect to the sampling percentage of catalogue stars in order to numerically check whether the adopted 5% sample is adequate to represent the characteristics of the whole photometry. Figure 5.4 shows the standard deviations divided by the mean value of likelihoods from ten different dataset for a given percentage. (The synthetic stars used in this calculation are generated by a continuous model with $\Gamma = -3.1$.) Although the figure shows a trend of continuous decrease after 5% in sampling percentage, the variations become stable from $\sim$ 1%, so a sample size of 5% is numerically reasonable (refer to Figures 4.1 and 5.3 for qualitative analysis by the number distribution).

Next we test how many model stars are needed to give a reliable statistic. The synthetic stars were taken from the same model as in Figure 5.4 and the results for a 5% data sample are presented in Figure 5.5 with respect to continuous models with $\Gamma = -1.1$, -2.1, and

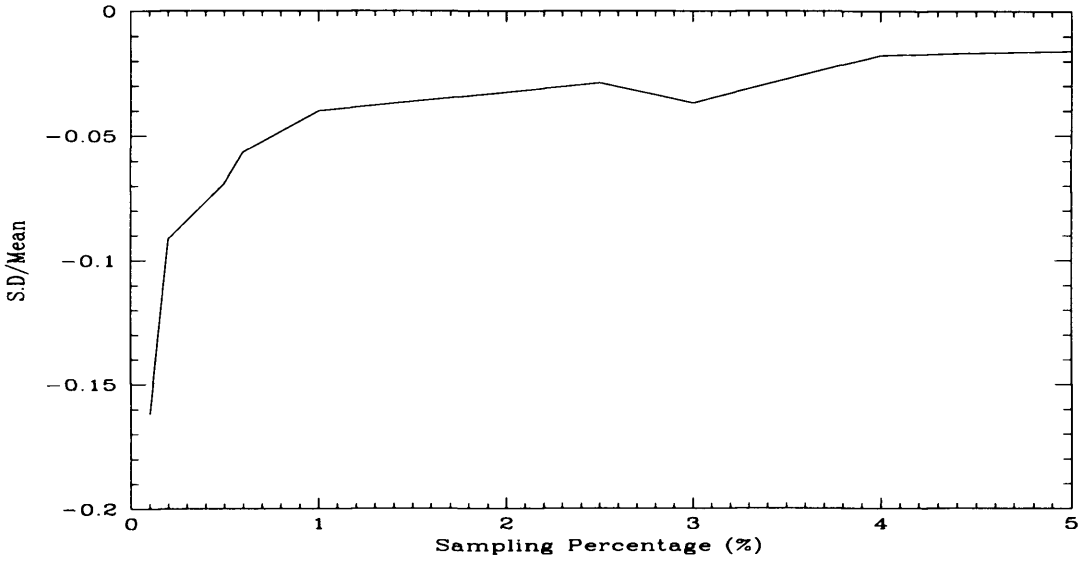

Figure 5.4: The variation of likelihood values with respect to sampling percentages using a continuous model with $\Gamma = -3.1$. The values are standard deviations (S.D) divided by mean from the ten different data sets for a given percentage. This figure shows a near constant value, -0.04, after 1% sampling.

-3.1. From Figure 5.5, the statistic becomes quite stable once the synthetic population is 20 times the number of observed stars (*i.e.*, the 5% sample). From the result in Figure 5.5, consideration of computational efficiency and general conservatism, we chose one hundred times the observed subsample as the number of the model stars.

In calculations of the likelihood statistic based on Bayesian inference, we use an average value of the standard deviations in each coordinate. Although ideally we have to use individual standard deviation values (see Equation 5.28), this would represent a substantially additional computation overhead. Because our photometric data are catalogued by independent magnitudes for each filter system, B, V, and R, the standard deviation in a colour index is calculated from the error propagation relation:

$$\sigma^2(A - B) = \sigma^2(A) + \sigma^2(B), \tag{5.33}$$

where A and B are magnitudes in each filter. From the average of each standard deviation

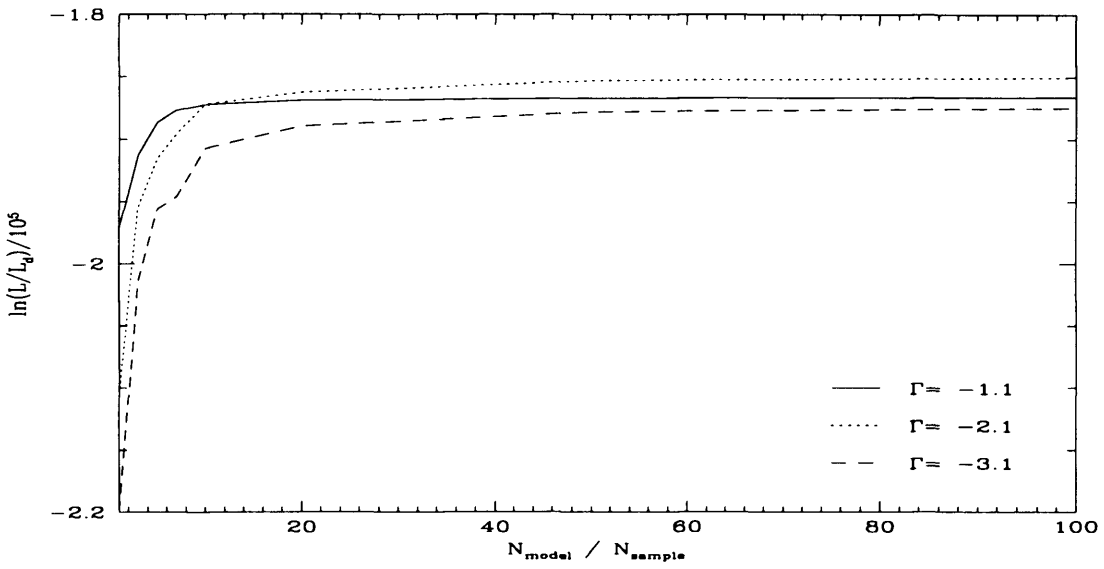

Figure 5.5: The variation of the likelihood statistic according to model size. The values are for $\Gamma = -1.1$, -2.1, and -3.1 as shown from a continuous star-formation model.

in our photometry data, we adopt $\sigma(V) = 0.028$, with $\sigma = 0.055$ and 0.042 in $(B - V)$ and $(V - R)$. If we assume that $\sigma(B) \sim \sigma(V)$, then $\sigma(B - V) \sim 1.4\ \sigma(V) \sim 0.039$ from Equation 5.33. So the adopted values in colour indices suggest that the photometric errors in B and R are statistically larger than V.

5.9.1 Continuous model

First we consider a continuous star formation model for the SMC. In the Geneva evolutionary models, the maximum age for a $2m_\odot$ with $Z = 0.004$ is 1.08 Gyr. Hence in this model, we assume that stars were continuously born from 2 Gyr ago. Although the smooth model from Pagel and Tautvaišienė (1998) for the star formation history in the SMC shows a small continuous decrease within recent 2 Gyr (see their Figure 2), it can be approximated as a constant continuous model, giving a theoretical base for the validity of this model.

With model sets containing one hundred times the population of observed stars for

a randomly selected 5% sample (say 2,300,000 synthetic stars) and having different IMF slope from -1.1 to -3.5, we calculate maximum likelihood values and present the results in Figure 5.6. The upper panel shows likelihood from the $(B-V)$ versus V plane, with the lower showing $(V-R)$ versus V for the three samples (A, B, and C), as shown with different lines. In general they show a very similar pattern in all three samples for a given coordinate set: a slow increase up to $\Gamma = -1.6$ in $(B-V)$ coordinate and rather steep decrease after $\Gamma = -2.1$, while continuous decrease in $(V-R)$ plane. In the comparison between coordinates, the values in $(B-V)$ vs V are higher 1.5 times than those in $(V-R)$ vs V differently with other star formation models. The maximum difference amongst sample sets is $\sim$ 5.7 % (*e.g.* $\sim -1.48 \times 10^5$ in sample A and $\sim -1.56 \times 10^5$ in Sample B at $\Gamma = -1.6$) in $(B-V)$ vs V. This difference is smaller in $(V-R)$ vs V, $\sim$ 0.45 %. Another fact considering the comparison with different colour indices is that the sample showing high values in one colour index does not give the same result in the other. For example, on average the sample B has lowest values in $(B-V)$ vs V coordinate; however, sample C shows lowest in $(V-R)$ vs V.

Although the likelihood statistic shows a small fluctuation in this model, the maximum is at $\Gamma = -1.6$ in $(B-V)$, however there is no peak in $(V-R)$ for a given IMF slope ranges. Meanwhile because likelihood is a relative possibility (see Equation 5.27) and $(B-V)$ and $(V-R)$ are independent, we can consider a combined likelihood;

$$[\ln(L/L_d)]_C \propto [\ln(L/L_d)]_{(B-V)} + [\ln(L/L_d)]_{(V-R)}. \tag{5.34}$$

Figure 5.7 shows combined likelihood, which $[\ln(L/L_d)]_{(V-R)}$ values are normalised to value at $\Gamma = -1.6$ in $(B-V)$ against V phase. Therefore $\Gamma = -1.6$, maximum from the combined likelihood calculation, well represents our SMC photometric data when continuous star formation is assumed, although larger (less negative) values are also acceptable.

5.9.2 Burst model

In this model, we investigate burst star formation history at two different epochs; a burst at 10 and at 60 Myr (see section 5.3). The results are presented in Figure 5.8 for the burst at $t = 10$ Myr and in Figure 5.9 for $t = 60$ Myr. All notations are the same as the Figure 5.6. On the whole, the burst model at 10 Myr shows smooth variations compare to other models and maxima at $\Gamma = -1.3$, the traditional IMF slope, in both coordinates. The fact that single burst model at an relevant epoch gives maximum value at traditional IMF

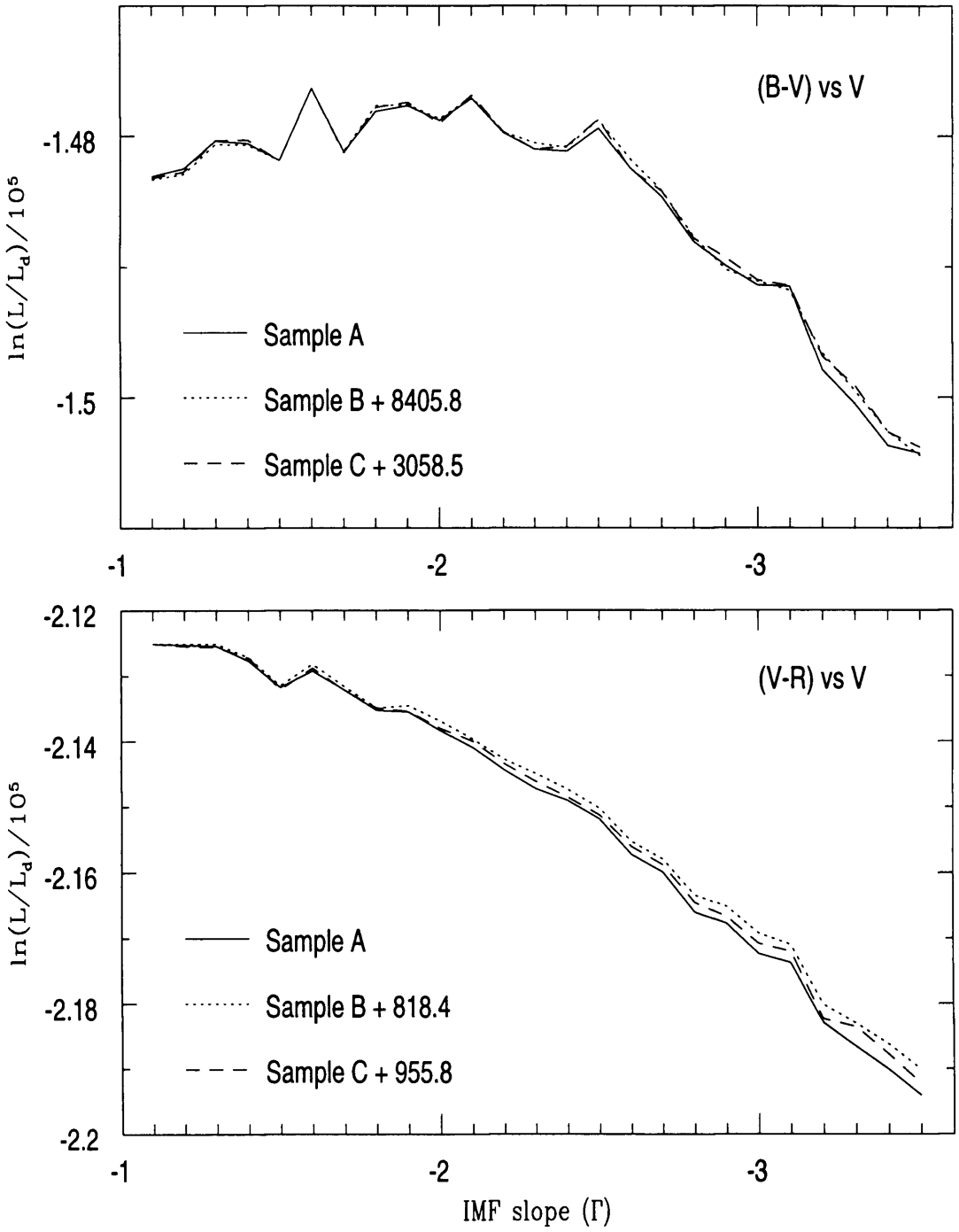

Figure 5.6: Likelihood results for the continuous model. The upper panel is result from $(B - V)$ versus V and the lower is from $(V - R)$ versus V for the three different sample sets.

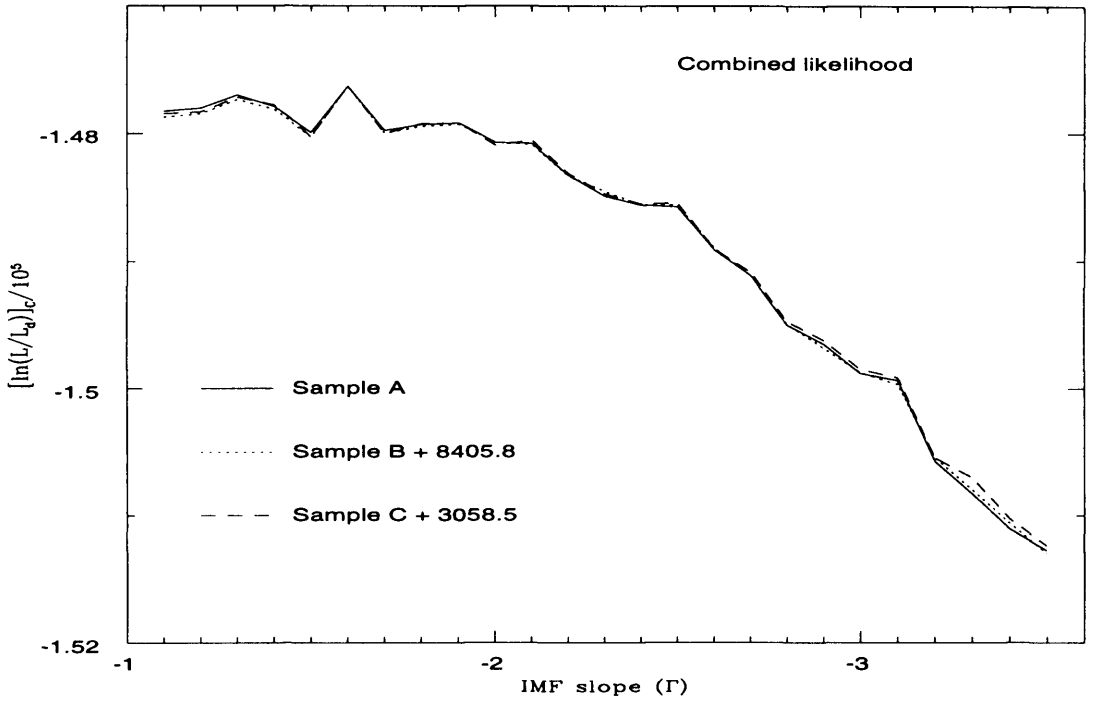

Figure 5.7: The combined likelihood calculations for continuous model.

slope is interesting because most of IMF studies are for the clusters/associations which are assumed to have the same ages and most of them show universal IMF slope at $\Gamma = -1.3$. On the other hand, the burst model at 60 Myr represents a continuous decrease as the IMF becomes steeper so does not have maximum within our IMF slope ranges. This is natural consequence because, as mentioned before, stars massive than $\sim 6\ m_{\odot}$ are already dead after 60 Myr (according to Genova evolutionary model), while our catalogue stars are mostly massive. Even if we perform the model calculations for the extended IMF ranges, the maximum value seems does not approach that of the continuous model.

Considering the fact that the SMC is a galaxy, consisting of different age stars, and hot stars are born quite recently, the bad results of burst models are not an unexpected, especially for a burst at an old epoch.

5.9.3 Double burst model

As another type of burst model, we assume two bursts, with equal proportions from each single burst, say 50% at $t = 10$ and 50% at $t = 60$ Myr. An interesting result is that

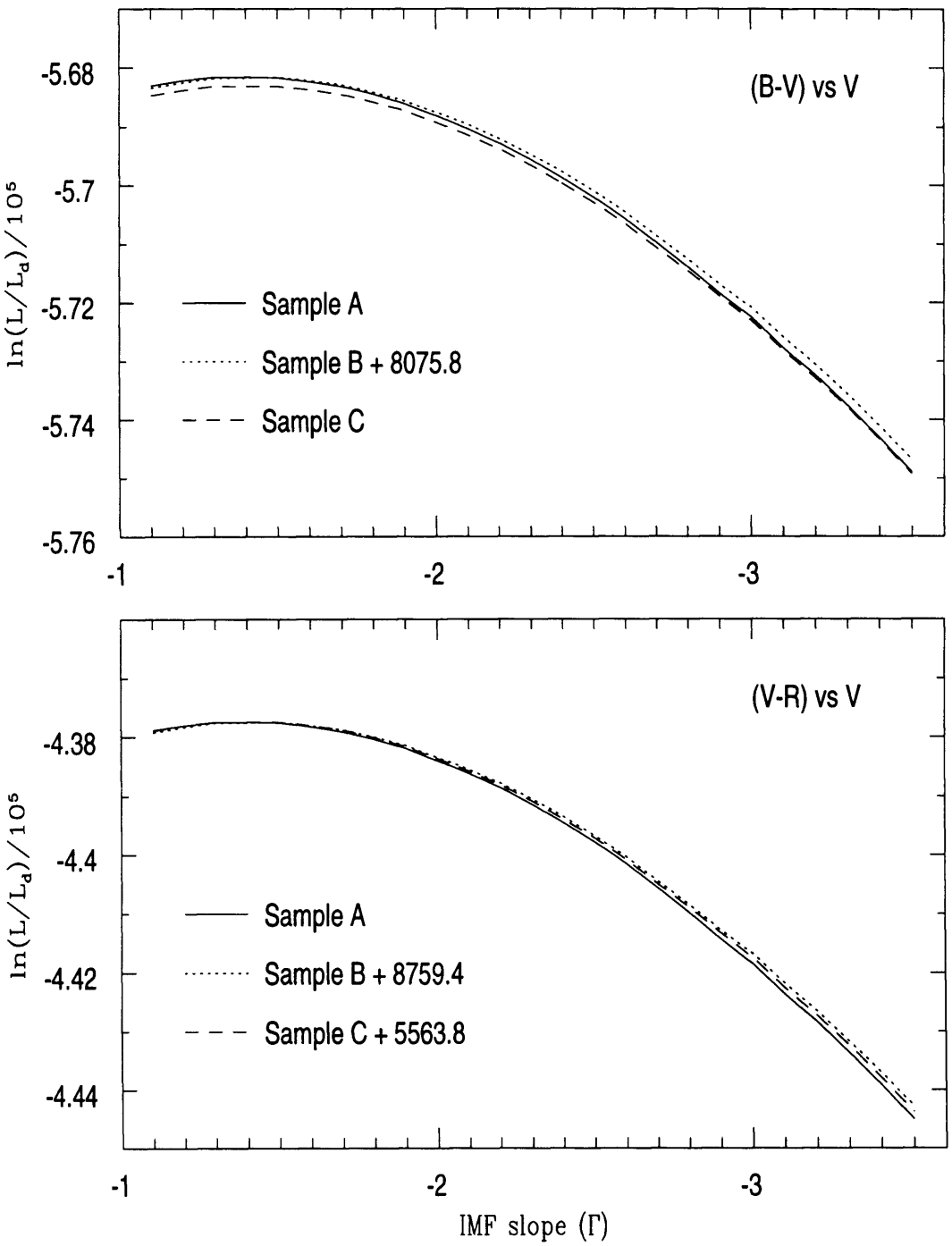

Figure 5.8: The same as Figure 5.6 except for single burst at 10 Myr.

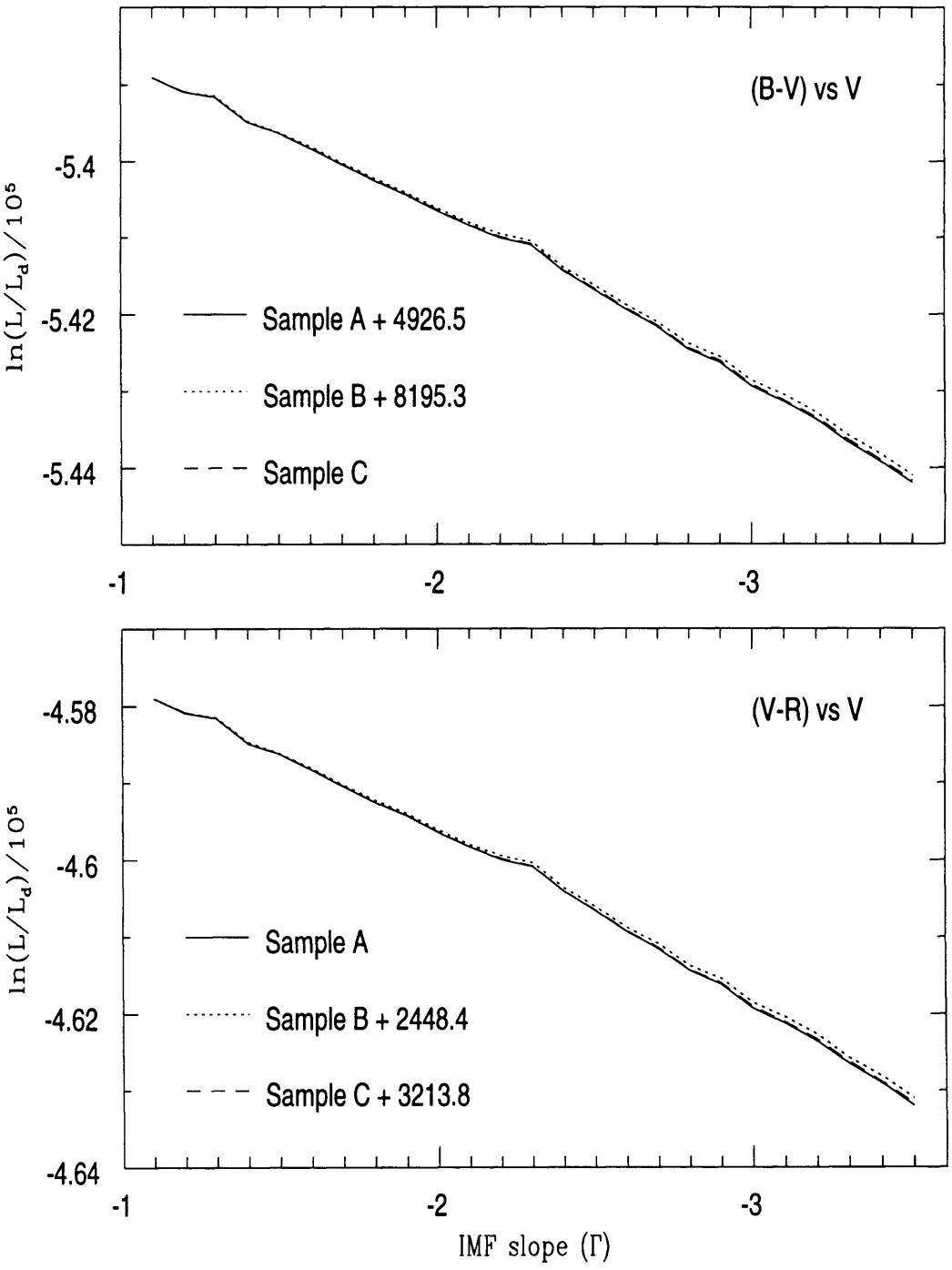

Figure 5.9: The same as Figure 5.6 except for single burst at 60 Myr.

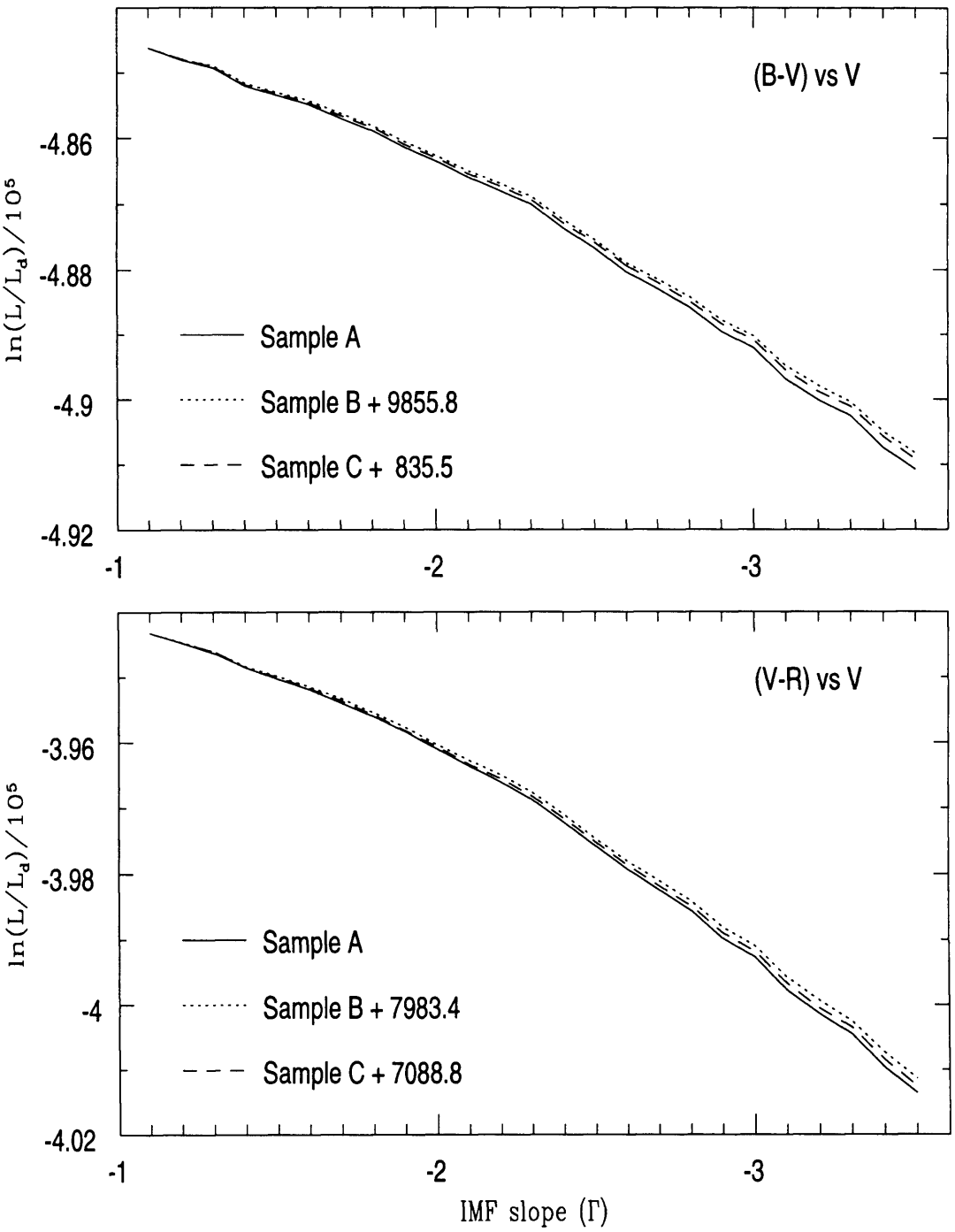

Figure 5.10: The same as Figure 5.6 except for a bursts at 10 and at 60 Myr with half of the synthetic sample from both.

it shows averagely higher maximum likelihood values than those of each single burst, although this model still gives lower values than the continuous one (see Figure 5.10). As the reason mentioned above, the double burst model is more ideally realistic than a single burst model for the SMC, a galaxy composed of stars born at different eras. In general, this model follows the tendency of the burst model at t =60 Myr in the pattern and has slightly higher values than those of single models in maximum likelihood statistic calculations. This model also has no maximum peak within our IMF slope ranges in both coordinates. However the likelihood values in the $(V - R)$ vs V plane are higher than in $(B - V)$ vs V coordinates (reflecting difference in photometric errors), like other burst models. Therefore, all our burst models seem to less realistic than continuous star formation scenario.

5.9.4 Complex model

Lastly, we test a complex model based on the previous model data sets: consisting of 50%, 25%, and 25% contributions from the continuous and burst models at 10 and 60 Myr, respectively. One impressive feature of this model is that all our complex models show only slightly lower likelihood values compared to the continuous model and a steep IMF (see Figure 5.11). The maximum peaks of the three samples in $(B - V)$ vs V plane occur at $\Gamma = -2.5$, with -1.6, the same value in the continuous model, in the $(V - R)$ vs V plane. Also as for the continuous model, we calculate a combined likelihood statistic normalised to a maximum value at $\Gamma = -1.6$ in $(B - V)$ vs V space and present in Figure 5.12. In this case, the combined likelihood values give a maximum at $\Gamma = -2.3$; still a steep IMF, and similar to the result from spectroscopic data in the previous chapter. The thing which one should bear in mind with this model is the possibility that the more delicate complex model can give better results than the continuous model. Of course, we also know that any arbitrary well-tuned complex model can give better results. In any case, the differences between the maximum values between this and the continuous model are quite small; for example, only $-6,609$ at $\Gamma = -1.6$ in $(B - V)$ vs V space (see Table 5.2), corresponding to 4.5% variation in the continuous model.

5.9.5 Summary of results

In this chapter, we have described how to generate and select model stars, and then compared them with our SMC photometric data, based on a Bayesian statistical study,

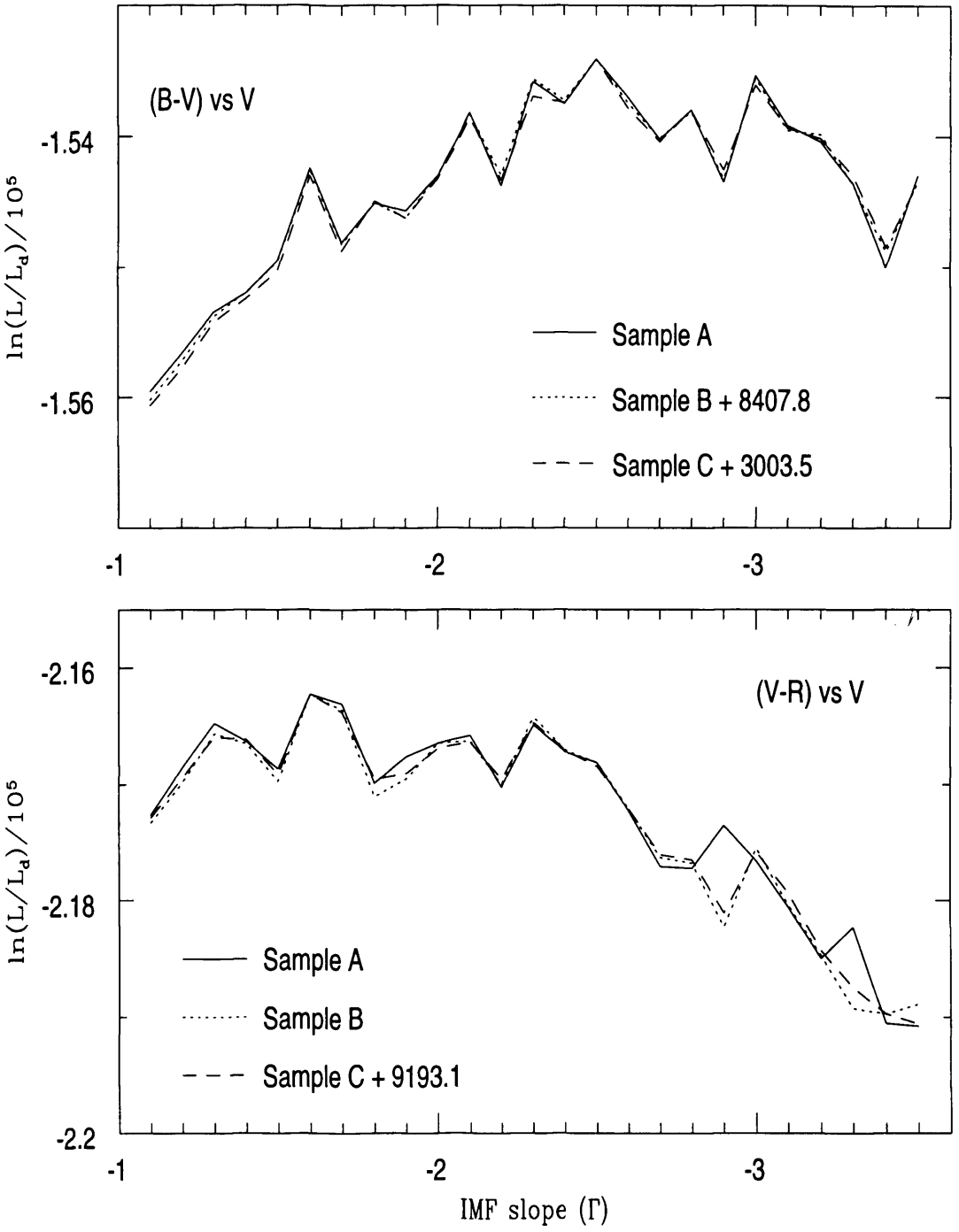

Figure 5.11: Likelihood results for the complex model composed of 50%, 25%, and 25% contributions from the continuous model and burst models at 10 and 60 Myr, respectively.

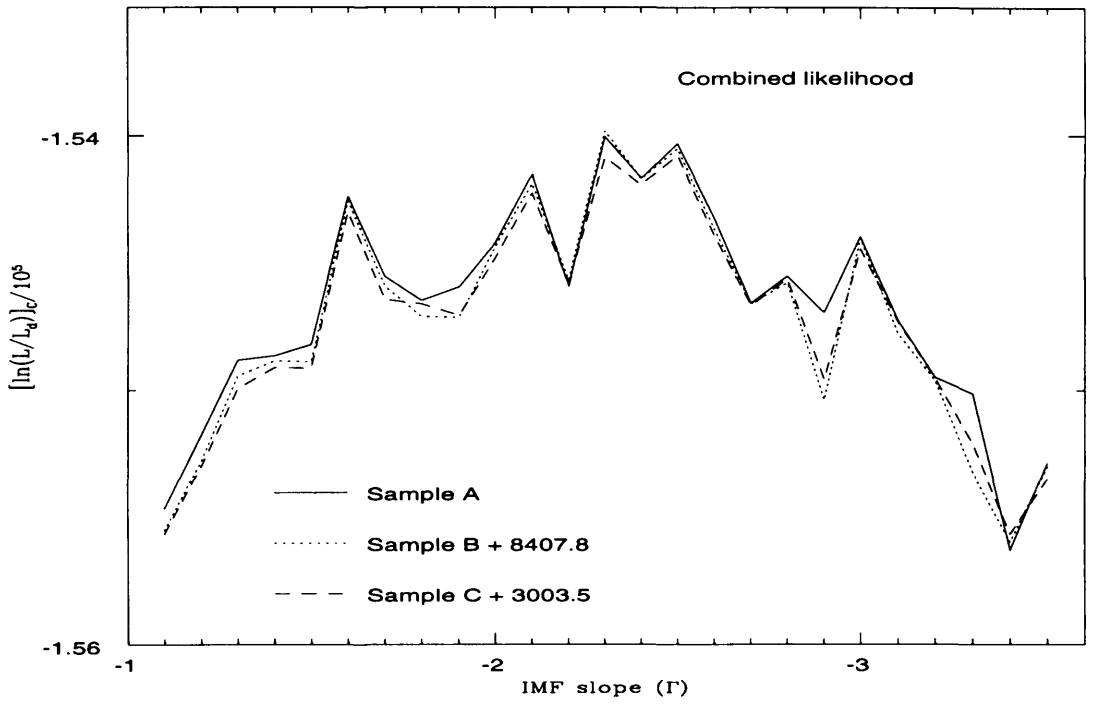

Figure 5.12: The combined likelihood calcuations for complex model.

with various IMF slopes and star formation histories. We used five models: 1) continuous star formation from 2 Gyr ago to present; 2) single burst star formation at 10 and 3) at 60 Myr epoch; 4) double bursts at both epochs with the same contribution in number; and lastly 5) complex model with 50%, 25%, and 25% contributions of continuous and burst models in the two epochs, with the IMF slopes in the range from -1.1 to -3.5. For numerical comparison, the results of the maximum likelihood calculations in each model for sample A are summarised in Table 5.2.

From the study of model calculations, we find, as one would expect, that the IMF of the SMC depends upon the adopted star formation history and summarise the main results in the following:

- The different subsample sets of all photometric data show a similar pattern in each model supporting the fact that a sample of 5% of the total is enough to represent the characteristic of our selected catalogue stars.

- The maximum likelihood values in $(V-R)$ vs V space is larger than those in $(B-V)$ vs V in all burst models, however it becomes reverse in other models.

Table 5.2: The summary of the maximum likelihood calculation for the each model in sample A.

	Maximum likelihood: $\ln(L/L_d)$									
	$(B-V)$ vs V					$(V-R)$ vs V				
IMF Slope	Continuous model	Single burst model[1]	Single burst model[2]	Double model[3]	Complex model[4]	Continuous model	Single burst model[1]	Single burst model[2]	Double model[3]	Complex model[4]
−1.1	−148305.7	−568302.7	−543833.7	−484618.7	−155953.7	−212512.1	−437881.1	−457907.1	−394321.1	−217261.1
−1.2	−148247.7	−568219.7	−544027.7	−484798.7	−155662.7	−212526.1	−437799.1	−458090.1	−394472.1	−216854.1
−1.3	−148036.7	**−568163.7**	−544092.7	−484918.7	−155342.7	−212540.1	**−437744.1**	−458164.1	−394627.1	−216479.1
−1.4	−148052.7	−568165.7	−544420.7	−485191.7	−155198.7	−212771.1	−437748.1	−458490.1	−394857.1	−216634.1
−1.5	−148183.7	−568172.7	−544560.7	−485340.7	−154948.7	−213167.1	−437757.1	−458628.1	−395024.1	−216865.1
−1.6	**−147630.7**	−568238.7	−544762.7	−485479.7	−154239.7	−212923.1	−437823.1	−458828.1	−395192.1	**−216229.1**
−1.7	−148116.7	−568319.7	−544975.7	−485691.7	−154808.7	−213211.1	−437905.1	−459046.1	−395395.1	−216307.1
−1.8	−147808.7	−568446.7	−545179.7	−485881.7	−154509.7	−213524.1	−438033.1	−459252.1	−395603.1	−216993.1
−1.9	−147765.7	−568601.7	−545364.7	−486133.7	−154567.7	−213548.1	−438189.1	−459423.1	−395838.1	−216760.1
−2.0	−147877.7	−568811.7	−545573.7	−486347.7	−154297.7	−213832.1	−438401.1	−459641.1	−396103.1	−216648.1
−2.1	−147711.7	−569027.7	−545766.7	−486591.7	−153812.7	−214095.1	−438617.1	−459834.1	−396360.1	−216580.1
−2.2	−147973.7	−569270.7	−545929.7	−486793.7	−154377.7	−214436.1	−438860.1	−459995.1	−396606.1	−217026.1
−2.3	−148097.7	−569553.7	−546019.7	−487004.7	−153581.7	−214722.1	−439144.1	−460087.1	−396871.1	−216491.1
−2.4	−148114.7	−569863.7	−546352.7	−487361.7	−153746.7	−214903.1	−439455.1	−460414.1	−397217.1	−216721.1
−2.5	−147938.7	−570197.7	−546596.7	−487673.7	**−153407.7**	−215188.1	−439788.1	−460662.1	−397583.1	−216810.1
−2.6	−148242.7	−570561.7	−546856.7	−488034.7	−153695.7	−215729.1	−440154.1	−460929.1	−397932.1	−217227.1

continued

	Maximum likelihood: $\ln(L/L_d)$									
	$(B-V)$ vs V					$(V-R)$ vs V				
IMF Slope	Continuous model	Single burst model[1]	Single burst model[2]	Double model[3]	Complex model	Continuous model	Single burst model[1]	Single burst model[2]	Double model[3]	Complex model
−2.7	−148460.7	−570969.7	−547083.7	−488292.7	−154020.7	−215993.1	−440561.1	−461154.1	−398239.1	−217709.1
−2.8	−148802.7	−571382.7	−547372.7	−488578.7	−153796.7	−216604.1	−440977.1	−461434.1	−398556.1	−217721.1
−2.9	−148988.7	−571834.7	−547549.7	−488955.7	−154345.7	−216775.1	−441431.1	−461618.1	−398982.1	−217356.1
−3.0	−149136.7	−572249.7	−547856.7	−489206.7	−153533.7	−217229.1	−441845.1	−461921.1	−399266.1	−217657.1
−3.1	−149146.7	−572764.7	−548059.7	−489683.7	−153913.7	−217372.1	−442362.1	−462121.1	−399770.1	−218050.1
−3.2	−149786.7	−573235.7	−548286.7	−490001.7	−154037.7	−218290.1	−442827.1	−462352.1	−400137.1	−218496.1
−3.3	−150050.7	−573756.7	−548584.7	−490251.7	−154356.7	−218652.1	−443355.1	−462650.1	−400444.1	−218229.1
−3.4	−150367.7	−574310.7	−548843.7	−490741.7	−154998.7	−219000.1	−443908.1	−462905.1	−400960.1	−219055.1
−3.5	−150426.7	−574899.7	−549124.7	−491077.7	−154294.7	−219403.1	−444499.1	−463194.1	−401360.1	−219077.1

[1] at $t = 10$ Myr.

[2] at $t = 60$ Myr.

[3] 50% at $t = 10$ + 50% at $t = 60$ Myr.

[4] 50%, 25%, and 25% from continuous and burst models at $t = 10$ and $t = 60$ Myr, respectively.

- The continuous model gives the best likelihood statistic. From this model, the IMF of the SMC is -1.6 in combined likelihood calculations, which is slightly steeper than Salpter's IMF slope of -1.3. That value is less steep than the result from the previous chapter ($\Gamma = -2.4$), which obtained using both spectroscopic and photometric data, but without attention to selection effects. However, this model also shows local maxima, with values at -2.1, slightly lower than -1.6, and -2.5, seem to caused by noise-like variations in the statistics.

- A single burst model at 10 Myr epoch gives the Salpeter's IMF slope, $\Gamma = -1.3$, with lower likelihood values than for the continuous model. The burst model at $t = 60$ Myr shows a continuous decrease as the IMF slope becomes steep. Overall, single burst models offer the least likely result, with the lowest likelihood of any models. The double burst model, equally drawn from $t = 10$ and 60 Myr bursts, has higher likelihood statistic values than for a single burst.

- The complex model yields a somewhat steeper IMF slope, $\Gamma = -2.5$ (-2.3) in $B-V$ vs V phase (in combined likelihood). In general, the values of maximum likelihood in this model are similar to those of continuous one, but with steeper IMFs.

In conclusion, we suggest that the continuous star formation history, consistent with Pagel and Tautvaišienė (1998), is the best model in representing the SMC; and that the IMF of hot stars in the SMC is -1.6, less steep than found in previous studies.

5.9.6 Discussion

Although our study shows a slightly steeper IMF slope than that of Salpeter (and so the variation of the IMF), it also has some weaknesses should be addressed.

Binarity. One of the main weaknesses in our study is that we did not consider the effects caused by the binarity, *i.e.*, we treated all stars as single. According to Binney and Merrifield (1998), a maximum 50% of Galactic stars are binaries in the field region, although it is not well known whether or not the fraction in a field is similar in different environments. No matter what the binarity fraction in the SMC is, it is true that some of our catalogue stars are actually binaries composed of unresolved less bright ones.

Even neglecting the effects of binarity on evolution, this fact alone causes the overestimation in the number of brighter stars, so the real IMF slope must be steeper than our results. Scalo (1998) suggests $\Delta\Gamma \sim -0.3$, the steeper IMF slope, if the binary fraction is

Table 5.3: Likelihood results for the some further considered burst models at t = 1, 30, and 100 Myr in $(B-V)$ versus V plane.

	Maximum likelihood: $\ln(L/L_d)$ for the bursts model		
	t = 1 Myr	t = 30 Myr	t = 100 Myr
$\Gamma = -1.3$	−611056.7	−552774.7	−667595.7
$\Gamma = -2.3$	−611959.7	−554980.7	−669194.7
$\Gamma = -3.3$	−618976.7	−558233.7	−670875.7

greater than 40%. However, since nearly all other studies also neglect binarity, our results can still be directly compared to values in the literature.

Star formation histories. Evidently, and as confirmed in our results, the inferred IMF of a system depends on its assumed star formation history. Therefore in the SMC, consisting of sub-systems having different formation histories such as clusters and associations, the IMF investigation relies upon the adopted star formation history. Even if all sub-systems of the SMC followed the same pattern of a star formation history, they maybe started at different epochs. Although the continuous star formation history model of the SMC gives the highest maximum likelihood values in our models, the complex model implies a probability that a more 'tuned' combination of star formation histories could give better results. However it is beyond the remit of our study to consider more complex models (and in practice it is impossible to test every star formation history).

Instead, we tested other burst models for three assumed IMF slopes. In Table 5.3, we summarise maximum likelihood values for sample A using the burst models at 1, 30, and 100 Myr epochs with respect to $\Gamma = -1.3$, -2.3, and -3.3 in $(B-V)$ against V plane. As can be seen in Table 5.3, the resulting values for the additional burst models show still lower likelihoods than that for the continuous model, and decrease as the IMF slope becomes steep.

Field/Dense regions. Our results for the IMF are from the whole SMC region, not individual ones. Massey *et al.* (1995*c*) investigated the IMF of hot stars in the field and in associations of the Magellanic Clouds. They found the IMF slopes of the field stars is much steeper, $\Gamma = -4.1 \pm 0.2$ in the LMC and -3.7 ± 0.5 in the SMC, compared to the associations in the MCs, $\Gamma = -1.3 \pm 0.3$, the classical Salpeter IMF. Recently Evans (2001)

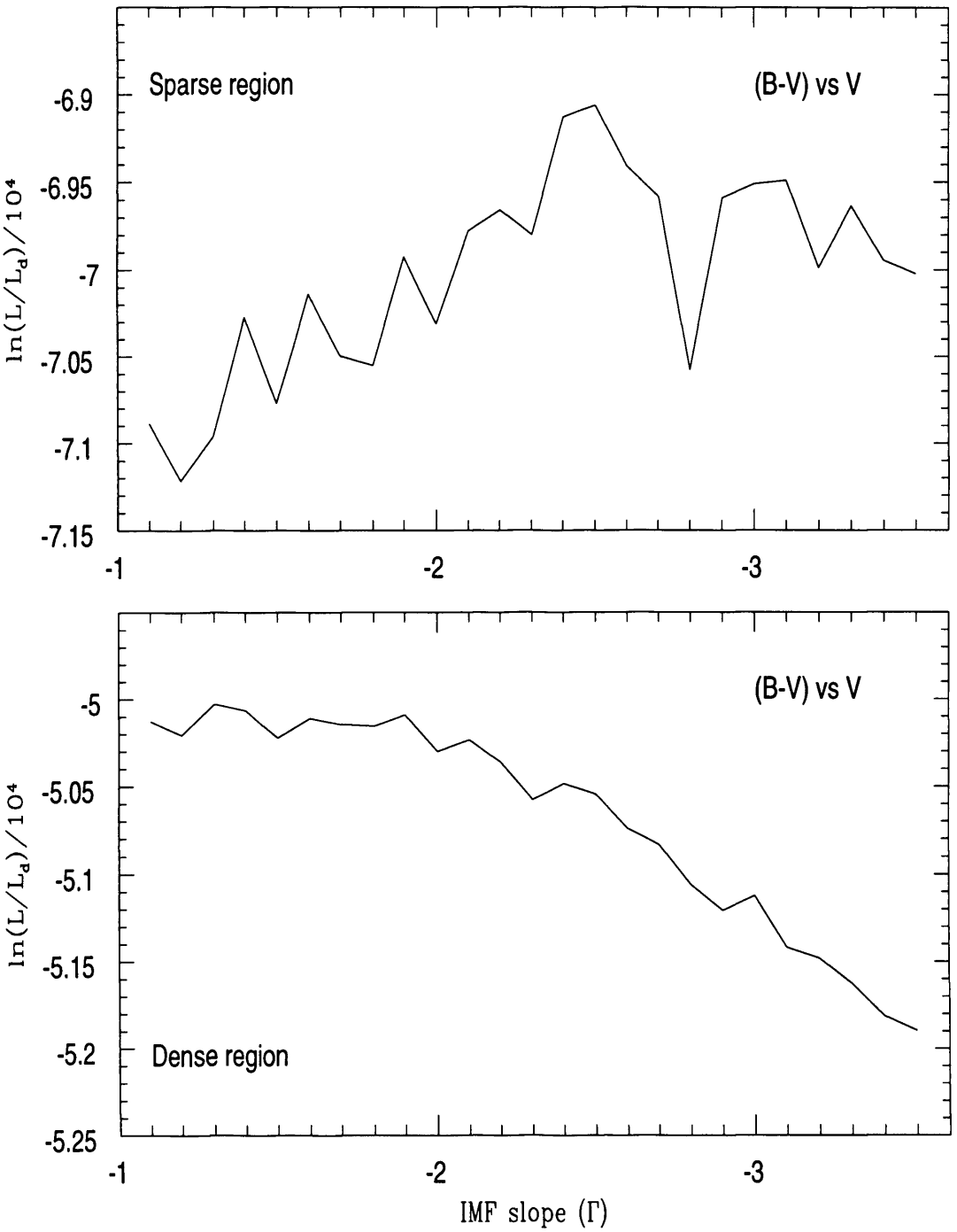

Figure 5.13: Likelihood results for the field (upper panel) and dense (lower panel) region stars using the continuous model in $(B-V)$ versus V coordinate.

also presented a steeper IMF for field stars in the SMC ($\Gamma = -3.8 \pm 0.4$) based on the 2dF spectroscopic study. However, his result for the non-field stars showed slightly steeper IMF slope ($\Gamma = -2.5 \pm 0.3$) than the Massey *et al.* (1995*c*) result for the associations.

In the classification of the field stars, Massey *et al.* (1995*c*) assumed the 30 pc distance, approximately $1'45''$ angular distance, criterion from a clusters/associations. Because practically it it impossible to apply this criterion to all our survey stars, we coarsely test regional differences on the IMF for the stars belonging to the areas presented in Figure 5.2, used the examples of the photometric incompleteness in dense and sparse regions. Figure 5.13 shows likelihood results for sparse and dense regional stars using continuous model in $(B - V)$ vs V coordinate. For the sparse region, we found that the maximum value occurs at $\Gamma = -2.5$, which steeper than other results. While the likelihood for the dense regional stars represents maximum value at $\Gamma = -1.3$, shallower than the results for the whole area SMC. Therefore, this result well agrees with previous studies in terms that shallow IMF slope in the field and steep one in the dense regions and suggests that $\Gamma = -1.6$ for the whole SMC area is caused by the influences of both regional stars.

Photometric errors. One weakness in our study is that the astrometry and photometry are less accurate than other studies as the penalty for cataloguing huge amounts of stars ($\sim$ 1.3 million stars) using unoptimised instrumentation. Because of the numbers of stars, it is impossible to do eye-examination for all data reduction steps. For example, the matching procedure of stars found in overlapped and dithered frames was done by a numerical program (*i.e.* TOPCAP) so there maybe some mis-matched stars (especially faint ones). Another source relating to inaccuracy in photometry is that we used a catalogue stars (Massey, 2002) as standards, not well-studied primary standard stars such as Landolt (1983, 1992), because it is hard to obtain standard stars in mosaic CCD observation requiring a couple of standards in every chip (eight chips in WFI) and because we observed in generally non-photometric conditions. What is worse, there are no available catalogues observed with Cousins R filter for the whole area of the SMC at the time when we reduced data. For this reason, we used Cousins (1980) relations in transformation between Johnson and Cousins Rs to use Massey (2002) catalogue stars. That seems to be one of reasons for lower likelihood values in $(V - R)$ against V than in $(B - V)$ vs V plane such as in the continuous model.

CHAPTER 6

Summary and future work

In this Chapter, we summarise the main points of our work that have been reached and describe the future work that should be done in order to confirm and develop the results of this thesis.

6.1 Summary

Stars are the basic component in astronomical objects and mass is the main parameter characterising them. Once the mass of a star is known, theoretically we can calculate its physical parameters at a given time, through the evolutionary models. So the study of the initial mass function of a system gives clues for the understanding of its evolution. In order to investigate of the IMF of hot stars, and the effect of the metallicity, we performed a B, V, and R photometric survey for the Small Magellanic Cloud, selected for its proximity and low metallicity.

6.1.1 Introduction

In the introduction, we reviewed related literature and the basic concepts regarding to the definition of the IMF and recent results with respect to different mass ranges. Although recently there are some suggestions of variations in the IMF, most studies follow the result derive from Salpeter (1955), $\Gamma = -1.3$, regardless of systems, metallicities, and mass ranges. We summarise the results of its recent studies in Table 1.1. Subsequently, we briefly described the features of the SMC, the wide-spread photometric systems, and the Hertzsprung-Russell diagram.

6.1.2 Observations

We used the wide field imager (WFI), composed of eight CCDs, each 2k by 4k pixels, mounted on the 40 inch telescope at Siding Spring Observatory in Australia. To cover the whole area of the SMC, we divided it into 35 fields and performed observations in three runs, 5 – 11 September & 26 – 31 October 2001, and 9 – 17 November 2002. Throughout the observations, we took two exposures in each filter, 60s and 600s, to include bright and faint stars. The characteristics of the instrument, filter system, and observational log are listed in Tables 2.1, 2.2, and 2.3 respectively.

One of the important features of the WFI system is the dark current. In order to reduce readout time of charges on CCDs, the WFI has warm operating temperature causing high dark current levels. For this reason, we obtained dark frames according to exposure times of object ones in each run. As another feature, some frames had no the necessary information, such as exposure time and airmass in data head file so we corrected them manually.

6.1.3 Data Reduction

In our mosaic data reduction, we followed the procedures of single CCDs using the **IRAF** package, except for a couple of steps described in Chapter Three in detail. For the overscan correction, we used Starlink software, **figaro**, to find the median value on the whole overscan areas for each CCD and applied it. As mentioned above, the dark frame correction is essential for our data so we made two master dark frames, 60s and 600s, by median combination of dark frames taken in each run. In addition, we applied linearity corrections using the coefficients and the procedures given in a technical note. The most different step, compared to usual procedures, was the standardisation. Because of large field of view, the Landolt or E-region standard stars are inappropriate to mosaic CCDs, so we used Massey's (2002) catalogue as standards. In transforming the instrumental magnitudes to the standard system, we tested three standardisation models and adopted model 1 based on the comparison with other catalogues. Lastly, we performed an artificial star test to estimate completeness for the all filters and fields. We obtained the SMC catalogue containing about 1.3 million stars, $\sim$ 91% complete in survey area and $\sim$ 90% complete around 18 magnitude in B. Based on comparsions with other catalogues, we found that the astrometric accuracy is 0.1 arcsecond and the photometric ones are 0.1 magnitude in

B and V and 0.2 magnitude in R.

6.1.4 HRD of the SMC

Using our photometric and Evans *et al.* (2004)'s 2dF spectroscopic data, we obtained $E(B-V) = 0.086$ and $E(V-R) = 0.065$ from Fitzgerald (1970) relationships between intrinsic colour indices and MK system. From Schultz and Wiemer (1975) and Sneden *et al.* (1978) studies, $R_V = 3.1$, we derived interstellar extinction in V, $A_V = 0.267$. Our result of colour excess in $(B-V)$ shows good agreement with commonly cited value of the SMC, $E(B-V) = 0.09$ (*e.g.* Massey *et al.*, 1995*b*). To estimate the distance modulus of the SMC, we adopted the relations between spectral type and absolute magnitude from Schmidt-Kaler (1982) with complementary results from Conti *et al.* (1983) for O stars. Together with our estimation of interstellar reddening value, we found $D.M = 18.55$, slightly less then the result from Harries *et al.* (2003), 18.89, derived using eclipsing binaries.

Lastly we constructed colour magnitude diagrams, V vs $(B-V)$ and vs $(V-R)$, from our photometry data (Figure 4.1), and a theoretical H-R diagram using solely 2dF spectroscopic data (Figure 4.7), because the relation between colour index and effective temperature is poor toward higher/cooler temperature stars. We used relation functions derived from Martins *et al.* (2005) for effective temperature calibration and from Lanz and Hubeny (2003) for $\log T_{eff} > 4.47K$ and Balona (1994) for $\log T_{eff} < 4.47K$ in bolometric correction. By counting the number of stars between the evolutionary tracks of selected mass ranges, we found the slope of the IMF for the massive stars on the SMC is $\Gamma = -2.4$, steeper than the Salpeter IMF, based on solely spectroscopic data.

6.1.5 IMF of the SMC

In Chapter Five, we studied the IMF and the star formation history for the SMC using our photometric data. Differently to previous studies, we transformed the theoretical quantities of synthetic population stars into the observable ones (rather then vice versa) using parameters obtained in this thesis. Because of huge number of stars in our catalogue, we randomly extracted three 5% samples and compared them with synthetic populations made assuming various IMF slopes, from $\Gamma = -1.1$ to -3.5 by 0.1 step, and various star formation histories: continuous, single bursts at 10 and 60 Myr, double burst at those eras, and a complex model based on continuous and double burst star formations. The

selection criteria applied to our catalogue stars are $9.5 < B < 19.0$ and $(B - V) < 0.6$.

We used the likelihood method from Tolstoy and Saha (1996) in the comparisons of observations and models, and the results are given in Figures 5.6, 5.8, 5.9, 5.10, and 5.11 for each model. As well, for the purpose of the numerical comparisons of the results, we summarise the maximum likelihood values in Table 5.2 for one sample. According to our study, continuous star formation with $\Gamma = -1.6$, slightly steeper than the Salpeter IMF, best represents the SMC data. On the other hand, the burst models give the worst results amongst assumed models although burst at $t = 10$ Myr shows maximum around traditional IMF slope. An interesting result is from the complex model. In this case, the maximum likelihood value occurs at $\Gamma = -2.3$ (from combined likelihood), and it shows slightly lower one compare to continuous model. In conclusion, we suggest that the SMC has suffered continuous star formation history and the IMF slope of the hot stars is -1.6, suggesting the non-universality of the IMF.

6.2 Future work

Since Salpeter's (1955) work, there have been many studies relating to IMF for the various targets, mass ranges, and metallicities. Although there are suggestions about variations of the IMF in recent publications, most results have shown the universality of it, within observational errors. Hence we believe that our study supplies some the strongest evidence for variations of the IMF, at least for hot stars in low metallicity. However our research is the results from only one target, the SMC, and the hot star mass range. Therefore we can not answer those questions: 'What is the Γ for the low mass range?', 'What is the dependence on the metallicity?', 'Is steep IMF still valid for other clusters or external galaxies?' and so on. In order to give answers for those questions, more studies are required, for the other systems, having different environments. Of course, the studies have to include a large number of stars, which can give reliable statistics, and both photometric and spectroscopic data in the case of hot stars. In addition, for the method, which we did, transforming theoretical quantities into observable ones is more the reliable and reasonable.

As for future work, we are planning to study the LMC, having different metallicity to the SMC, ($Z = 0.008$). The IMF study of LMC will give an opportunity to check or confirm our IMF slope for the hot stars in the SMC, and to provide further clues to understand the effects of metallicity.

Appendix A

Table discussed in Chapter 2

Table A.1: The 'a','b' and 'c' characters represent the dithered grids.

# Grid	$\alpha_{2000}(h,m,s)$	$\delta_{2000}(^\circ,','')$	# Grid	$\alpha_{2000}(h,m,s)$	$\delta_{2000}(^\circ,','')$	# Grid	$\alpha_{2000}(h,m,s)$	$\delta_{2000}(^\circ,','')$	# Grid	$\alpha_{2000}(h,m,s)$	$\delta_{2000}(^\circ,','')$
#01a	00 20 00	-74 20 02	#09a	00 47 48	-73 30 00	#16a	00 49 48	-71 50 00	#25b	00 48 57	-71 04 00
#01b	00 21 00	-74 15 40	#09b	00 48 44	-73 26 00	#16b	00 50 39	-71 54 00	#26a	00 23 24	-73 30 00
#01c	00 22 00	-74 12 00	#09c	00 50 50	-73 23 00	#16c	00 52 36	-71 57 00	#26b	00 24 20	-73 34 00
#02a	00 32 35	-74 20 00	#10a	00 48 22	-72 40 00	#17a	01 22 40	-72 25 00	#27a	00 39 36	-71 50 00
#02b	00 33 33	-74 16 00	#10b	00 49 16	-72 36 00	#17b	01 22 47	-72 29 00	#27b	00 40 27	-71 54 00
#02c	00 34 31	-74 12 00	#10c	00 51 15	-72 33 00	#18a	01 23 18	-73 15 00	#28a	01 34 38	-74 05 00
#03a	00 45 10	-74 20 00	#11a	00 35 36	-73 30 00	#18b	01 22 22	-73 19 00	#28b	01 33 40	-74 09 00
#03b	00 46 08	-74 16 00	#11b	00 36 32	-73 26 00	#18c	01 20 16	-73 22 00	#29a	00 25 32	-72 40 00
#04a	00 57 45	-74 20 00	#11c	00 38 38	-73 23 00	#19a	01 22 29	-74 05 00	#29b	00 26 26	-72 44 00
#04b	00 58 42	-74 16 00	#12a	00 36 44	-72 40 00	#19b	01 21 31	-74 09 00	#30a	00 29 24	-71 50 00
#05a	01 10 20	-74 20 00	#12b	00 37 38	-72 36 00	#20a	01 34 29	-72 40 00	#30b	00 30 15	-71 54 00
#05b	01 11 18	-74 16 00	#12c	00 39 37	-72 33 00	#20b	01 33 35	-72 44 00	#31a	00 39 32	-71 00 00
#06a	01 00 00	-71 50 00	#13a	01 11 07	-71 50 00	#21a	01 34 13	-73 30 00	#31b	00 38 41	-71 04 00
#06b	01 00 58	-71 46 00	#13b	01 11 58	-71 46 00	#21b	01 33 17	-73 34 00	#32a	01 20 20	-70 45 00
#06c	01 02 46	-71 41 00	#13c	01 13 53	-71 43 00	#22a	01 00 00	-71 00 00	#32b	01 19 31	-70 49 00
#07a	01 00 00	-72 40 00	#14a	01 11 38	-72 40 00	#22b	00 59 11	-71 04 00	#33a	01 00 25	-70 10 00
#07b	01 00 54	-72 36 00	#14b	01 12 32	-72 36 00	#23a	01 10 14	-71 00 00	#33b	01 01 10	-70 14 00
#07c	01 02 53	-72 33 00	#14c	01 14 31	-72 33 00	#23b	01 09 25	-71 04 00	#34a	01 45 40	-72 40 00
#08a	01 00 00	-73 30 00	#15a	01 11 44	-73 30 00	#24a	01 20 47	-71 35 00	#34b	01 44 48	-72 44 00
#08b	01 00 56	-73 26 00	#15b	01 10 48	-73 26 00	#24b	01 19 56	-71 39 00	#35a	00 40 40	-75 10 00
#08c	01 03 02	-73 23 00	#15c	01 08 42	-73 23 00	#25a	00 49 46	-71 00 00	#35b	00 41 01	-75 06 00

Appendix B

Tables and code discussed in Chapter 3

B.1 Photometric frames

Table B.1: The summary for the photometric frames used to catalogue the SMC and estimate survey completeness from three observations.

	# of photometric frames				
Grid	60s	600s	Flag	Obs.	S.C (%)
#01*a*1	8	8	1	Sep.	
#01*a*2	8	8	2	Oct.	
#01*a*3	7	8	2	Nov.	
#01*b*1	8	8	1	Sep.	
#01*b*2	7	8	2	Oct.	
#01*b*3	7	8	2	Nov.	
#01*c*1	0	8	2	Sep.	100.0
#02*a*1	8	8	2	Sep	
#02*a*2	8	8	1	Oct.	
#02*a*3	8	8	2	Nov.	
#02*b*1	2	8	2	Sep	
#02*b*2	8	8	2	Oct.	
#02*b*3	8	8	2	Nov.	
#02*c*1	4	7	2	Sep	100.0
#03*a*1	8	8	2	Sep.	
#03*b*1	8	8	2	Sep.	100.0
#04*a*1	3	3	2	Sep.	
#04*b*1	0	8	2	Sep.	
#04*b*2	7	8	2	Nov.	67.2
#05*a*1	8	8	2	Sep.	
#05*a*2	0	0	0	Nov.	
#05*b*1	0	0		Sep.	
#05*b*2	0	0	0	Nov.	50.0
#06*a*1	8	8	2	Sep.	

continued

	# of photometric frames				
Grid	60s	600s	Flag	Obs.	S.C (%)
#06*a*2	7	8	2	Nov.	
#06*a*3	8	8	2	Oct.	
#06*b*1	8	8	2	Sep.	
#06*c*1	8	8	2	Nov.	100.0
#07*a*1	8	8	2	Sep.	
#07*b*1	0	8	2	Sep.	
#07*c*1	8	8	2	Nov.	100.0
#08*a*1	0	8	2	Sep.	
#08*b*1	8	8	2	Sep.	
#08*c*1	6	7	2	Nov.	98.9
#09*a*1	8	8	1	Sep.	
#09*a*2	7	8	2	Nov.	
#09*b*1	8	8	2	Sep.	
#09*c*1	2	8	2	Nov.	100.0
#10*a*1	8	8	2	Sep.	
#10*b*1	7	8	2	Sep.	
#10*c*1	8	8	2	Nov.	100.0
#11*a*1	8	6	2	Sep.	
#11*b*1	8	7	2	Sep.	
#11*c*1	7	8	2	Nov.	92.2
#12*a*1	8	4	2	Sep.	
#12*b*1	5	4	2	Sep.	
#12*c*1	8	8	2	Nov.	78.3
#13*a*1	7	8	2	Sep.	
#13*b*1	6	8	2	Sep.	
#13*c*1	8	8	2	Nov.	99.6
#14*a*1	6	8	2	Sep.	
#14*b*1	7	5	1	Sep.	
#14*b*2	8	8	1	Oct.	

continued

	# of photometric frames				
Grid	60s	600s	Flag	Obs.	S.C (%)
#14*b*3	7	8	2	Nov.	
#14*c*1	4	5	2	Nov.	99.7
#15*a*1	8	8	2	Oct.	
#15*b*1	8	8	2	Oct.	
#15*c*1	3	4	2	Nov.	100.0
#16*a*1	8	8	2	Oct.	
#16*b*1	8	8	2	Oct.	
#16*c*1	6	8	2	Nov.	100.0
#17*a*1	8	8	2	Oct.	
#17*b*1	8	8	2	Oct.	100.0
#18*a*1	8	8	2	Oct.	
#18*b*1	8	8	2	Oct.	
#18*c*1	0	0	2	Nov.	100.0
#19*a*1	8	8	2	Oct.	
#19*b*1	8	8	2	Oct.	
#19*b*2	8	8	1	Oct.	
#19*b*3	7	8	2	Nov.	100.0
#20*a*1	0	0		Oct.	
#20*b*1	8	8	1	Oct.	50.0
#21*a*1	8	8	2	Oct.	
#21*b*1	8	8	2	Oct.	100.0
#22*a*1	8	8	2	Oct.	
#22*b*1	8	8	2	Oct.	100.0
#23*a*1	8	8	2	Oct.	
#23*b*1	7	8	2	Oct.	99.5
#24*a*1	8	8	2	Oct.	
#24*b*1	8	8	2	Oct.	100.0
#25*a*1	8	8	2	Oct.	
#25*b*1	8	8	2	Oct.	100.0

continued

	# of photometric frames				
Grid	60s	600s	Flag	Obs.	S.C (%)
#26*a*1	8	8	2	Oct.	
#26*b*1	8	8	2	Oct.	100.0
#27*a*1	8	8	2	Oct.	
#27*b*1	8	8	2	Oct.	100.0
#28*a*1	8	8	2	Oct.	
#28*b*1	8	8	2	Oct.	100.0
#29*a*1	8	8	2	Oct.	
#29*b*1	8	7	2	Oct.	94.5
#30*a*1	8	8	2	Oct.	
#30*b*1	8	8	2	Oct.	100.0
#31*a*1	8	8	2	Oct.	
#31*b*1	8	8	2	Oct.	100.0
#32*a*1	8	8	2	Oct.	
#32*b*1	8	8	2	Oct.	100.0
#33*a*1	7	8	2	Nov.	
#33*b*1	6	8	2	Nov.	99.6
#34*a*1	7	8	2	Nov.	
#34*b*1	7	8	2	Nov.	99.8
#35*a*1	6	8	2	Nov.	
#35*b*1	8	8	2	Nov.	99.9

Note. In first column, the alphabet and arabic numbers at the end of the grid number represent dithered grids and the sequential number of frames taken for that grid. The second and third ones are the number of chips having photometric stars in 60 second and 600 second frame respectively. The fourth column in this table is inserted in order to flag how many 600s B frame is used. The fifth column is denoted to identify the obervational seasons (Obs.), September (Sep), October 2001 (Oct), and November 2002 (Nov). The last column is the survey completeness (S.C) for each grid as explained and calculated in the text.

B.2 Artificial star test

Table B.2: The results of artificial star test for 600s B frames in each b field.

B	Magnitude ranges								
Fields	13 – 14	14 – 15	15 – 16	16 – 17	17 – 18	18 – 19	19 – 20	20 – 21	21 –
# 01b CCD #1	100.00	98.21	98.25	95.24	93.18	81.51	32.02	4.46	0.37
# 01b CCD #2	100.00	96.43	99.12	95.24	92.27	74.51	40.29	3.10	0.37
# 01b CCD #3	100.00	100.00	98.25	96.60	89.55	81.51	46.49	4.65	0.37
# 01b CCD #4	100.00	98.21	100.00	97.28	94.09	75.91	38.43	5.43	0.00
# 01b CCD #5	100.00	100.00	97.37	97.96	94.55	82.35	45.25	5.04	1.11
# 01b CCD #6	100.00	96.43	98.25	95.92	93.18	82.35	45.45	2.91	0.74
# 01b CCD #7	100.00	100.00	97.37	94.56	92.73	87.39	45.45	5.04	0.74
# 01b CCD #8	100.00	100.00	97.37	97.28	94.09	82.35	38.64	4.07	0.00
# 02b CCD #1	100.00	100.00	92.11	90.48	77.27	53.50	18.80	2.71	1.11
# 02b CCD #2	100.00	100.00	99.12	94.56	87.27	64.71	29.96	3.68	0.00
# 02b CCD #3	100.00	100.00	97.37	93.88	91.82	67.23	34.92	3.88	0.00
# 02b CCD #4	100.00	98.21	98.25	95.92	75.45	55.46	23.55	5.04	0.00
# 02b CCD #5	100.00	100.00	98.25	96.60	91.82	71.71	32.44	3.10	0.00

continued

B	Magnitude ranges								
Fields	13 – 14	14 – 15	15 – 16	16 – 17	17 – 18	18 – 19	19 – 20	20 – 21	21 –
# 02*b* CCD #6	100.00	100.00	98.25	93.88	88.18	73.67	33.88	4.07	1.85
# 02*b* CCD #7	100.00	98.21	99.12	93.88	88.18	72.83	36.16	2.13	0.37
# 02*b* CCD #8	100.00	100.00	95.61	93.88	86.82	63.31	25.00	2.33	0.00
# 03*b* CCD #1	100.00	92.86	98.25	97.96	97.27	98.04	78.31	14.73	1.85
# 03*b* CCD #2	100.00	100.00	100.00	98.64	95.00	96.08	80.79	16.09	1.85
# 03*b* CCD #3	100.00	100.00	99.12	99.32	99.09	96.64	89.05	20.74	0.37
# 03*b* CCD #4	100.00	98.21	99.12	99.32	98.18	97.48	88.43	25.97	1.48
# 03*b* CCD #5	100.00	100.00	100.00	100.00	99.55	96.92	87.60	27.71	1.11
# 03*b* CCD #6	100.00	100.00	99.12	98.64	98.18	96.92	85.12	16.28	2.95
# 03*b* CCD #7	100.00	100.00	99.12	98.64	98.18	97.20	87.19	20.54	1.85
# 03*b* CCD #8	100.00	100.00	99.12	99.32	100.00	96.36	79.34	13.76	2.95
# 04*b* CCD #1	100.00	100.00	93.86	93.20	87.73	71.71	33.26	7.17	0.74
# 04*b* CCD #2	100.00	100.00	97.37	95.24	90.45	76.75	41.53	7.56	1.11
# 04*b* CCD #3	100.00	98.21	94.74	93.88	92.73	79.27	45.66	9.50	0.74
# 04*b* CCD #4	100.00	94.64	98.25	96.60	90.45	81.79	50.62	12.40	1.48
# 04*b* CCD #5	91.67	98.21	97.37	95.92	85.00	82.91	50.21	9.88	1.48
# 04*b* CCD #6	100.00	98.21	97.37	93.88	87.27	73.95	40.70	7.95	0.37

continued

B	Magnitude ranges								
Fields	13 – 14	14 – 15	15 – 16	16 – 17	17 – 18	18 – 19	19 – 20	20 – 21	21 –
# 04*b* CCD #7	100.00	96.43	94.74	88.44	85.45	77.31	39.46	6.78	1.48
# 04*b* CCD #8	100.00	96.43	94.74	93.88	89.55	72.83	32.64	5.81	0.74
# 05*b* CCD #1	100.00	100.00	99.12	100.00	98.64	98.32	78.31	9.69	1.85
# 05*b* CCD #2	100.00	100.00	100.00	99.32	99.55	97.76	82.23	15.12	1.11
# 05*b* CCD #3	100.00	100.00	99.12	100.00	98.18	97.76	87.60	21.12	2.21
# 05*b* CCD #4	100.00	100.00	100.00	98.64	98.64	98.04	82.85	20.74	3.32
# 05*b* CCD #5	100.00	100.00	100.00	100.00	98.64	97.20	86.16	19.96	1.48
# 05*b* CCD #6	100.00	100.00	100.00	98.64	97.73	94.40	81.61	13.37	1.11
# 05*b* CCD #7	100.00	100.00	100.00	99.32	98.18	96.08	81.40	14.15	0.74
# 05*b* CCD #8	100.00	100.00	99.12	99.32	99.55	96.36	79.13	11.43	1.11
# 06*b* CCD #1	100.00	98.21	96.49	96.60	93.18	82.91	40.50	7.75	1.48
# 06*b* CCD #2	100.00	100.00	100.00	98.64	95.00	76.47	41.53	9.88	1.48
# 06*b* CCD #3	100.00	100.00	97.37	93.20	87.27	73.11	40.08	7.56	1.48
# 06*b* CCD #4	100.00	98.21	97.37	89.80	78.64	58.26	24.17	8.14	2.58
# 06*b* CCD #5	100.00	100.00	97.37	93.88	82.73	60.22	30.17	6.78	4.06
# 06*b* CCD #6	100.00	100.00	97.37	95.24	90.45	74.51	35.74	6.20	3.32
# 06*b* CCD #7	100.00	100.00	96.49	95.24	93.18	77.03	41.12	11.43	2.21

continued

B	Magnitude ranges								
Fields	13 – 14	14 – 15	15 – 16	16 – 17	17 – 18	18 – 19	19 – 20	20 – 21	21 –
# 06*b* CCD #8	100.00	100.00	97.37	95.92	93.18	80.67	45.45	6.20	2.58
# 07*b* CCD #1	100.00	100.00	95.61	94.56	86.36	64.15	28.10	8.72	2.21
# 07*b* CCD #2	91.67	98.21	99.12	96.60	86.36	69.19	29.34	7.36	1.85
# 07*b* CCD #3	100.00	98.21	97.37	89.12	90.00	63.03	28.93	5.43	2.95
# 07*b* CCD #4	100.00	96.43	99.12	96.60	89.55	68.91	26.86	6.78	2.21
# 07*b* CCD #5	100.00	100.00	97.37	94.56	89.55	71.43	31.20	6.20	4.43
# 07*b* CCD #6	100.00	100.00	99.12	94.56	87.73	61.06	28.51	7.17	1.11
# 07*b* CCD #7	100.00	100.00	97.37	95.92	84.09	68.91	28.10	8.91	2.58
# 07*b* CCD #8	91.67	100.00	97.37	90.48	84.55	58.54	20.87	6.40	1.11
# 08*b* CCD #1	100.00	98.21	95.61	93.88	86.36	66.95	25.83	4.26	2.95
# 08*b* CCD #2	100.00	100.00	100.00	95.24	92.73	69.19	24.17	6.59	0.74
# 08*b* CCD #3	100.00	100.00	96.49	96.60	90.45	69.19	30.17	7.17	1.48
# 08*b* CCD #4	100.00	98.21	100.00	95.92	93.64	71.15	30.17	5.23	0.74
# 08*b* CCD #5	100.00	100.00	98.25	99.32	90.00	72.83	34.50	4.84	2.21
# 08*b* CCD #6	91.67	100.00	98.25	95.24	90.00	67.51	32.23	6.20	1.11
# 08*b* CCD #7	100.00	100.00	97.37	95.92	85.00	66.67	25.41	6.59	1.85

continued

B	Magnitude ranges								
Fields	13 – 14	14 – 15	15 – 16	16 – 17	17 – 18	18 – 19	19 – 20	20 – 21	21 –
# 08*b* CCD #8	100.00	100.00	96.49	97.96	88.64	62.75	22.73	4.84	2.58
# 09*b* CCD #1	100.00	100.00	98.25	97.28	89.09	85.43	57.02	24.81	9.59
# 09*b* CCD #2	100.00	100.00	99.12	97.96	95.00	83.47	60.54	27.71	9.23
# 09*b* CCD #3	100.00	100.00	98.25	100.00	98.18	89.08	73.55	41.47	9.59
# 09*b* CCD #4	100.00	100.00	100.00	99.32	97.27	96.36	84.09	54.46	19.56
# 09*b* CCD #5	100.00	100.00	100.00	99.32	99.55	95.52	82.85	54.46	20.30
# 09*b* CCD #6	100.00	100.00	98.25	98.64	98.18	88.24	74.59	39.15	13.65
# 09*b* CCD #7	100.00	100.00	99.12	97.28	93.64	81.79	61.16	27.71	8.86
# 09*b* CCD #8	100.00	100.00	99.12	97.96	96.36	85.99	63.22	28.88	9.96
# 10*b* CCD #1	100.00	100.00	99.12	98.64	97.27	93.56	86.36	55.23	15.13
# 10*b* CCD #2	100.00	100.00	100.00	99.32	97.27	94.40	79.34	54.84	9.23
# 10*b* CCD #3	100.00	100.00	100.00	98.64	96.82	91.04	77.27	47.67	15.87
# 10*b* CCD #4	100.00	100.00	100.00	98.64	96.36	87.96	72.52	38.57	15.50
# 10*b* CCD #5	100.00	100.00	100.00	100.00	98.18	93.56	77.07	50.00	18.08
# 10*b* CCD #6	100.00	100.00	100.00	99.32	98.18	97.48	87.60	59.69	18.82
# 10*b* CCD #7	100.00	100.00	100.00	99.32	99.55	98.32	86.36	63.76	19.93

continued

B	Magnitude ranges								
Fields	13 – 14	14 – 15	15 – 16	16 – 17	17 – 18	18 – 19	19 – 20	20 – 21	21 –
# 10*b* CCD #8	100.00	100.00	99.12	99.32	99.55	97.76	91.74	71.51	18.82
# 11*b* CCD #1	100.00	100.00	97.37	99.32	97.73	91.88	72.93	12.40	2.58
# 11*b* CCD #2	100.00	100.00	99.12	99.32	96.36	88.24	65.08	15.50	2.58
# 11*b* CCD #3	100.00	98.21	98.25	95.24	93.64	84.03	61.57	15.89	2.95
# 11*b* CCD #4	100.00	98.21	100.00	99.96	85.91	77.31	40.08	10.85	4.43
# 11*b* CCD #5	100.00	100.00	100.00	97.96	97.73	88.80	63.64	18.02	3.32
# 11*b* CCD #6	100.00	100.00	97.37	98.64	91.82	93.28	68.39	15.89	1.48
# 11*b* CCD #7	100.00	100.00	98.25	97.96	98.18	92.16	74.59	19.57	1.48
# 11*b* CCD #8	100.00	100.00	97.37	99.32	98.18	95.52	74.17	18.60	1.48
# 12*b* CCD #1	100.00	98.21	99.12	100.00	97.73	93.28	79.75	43.80	9.96
# 12*b* CCD #2	100.00	100.00	100.00	100.00	98.18	93.28	77.48	41.86	10.33
# 12*b* CCD #3	100.00	100.00	98.25	97.96	100.00	95.80	83.68	51.55	14.02
# 12*b* CCD #4	100.00	98.21	100.00	99.32	98.18	96.08	87.40	53.29	12.18
# 12*b* CCD #5	100.00	100.00	100.00	98.64	98.18	96.36	90.08	55.62	13.28
# 12*b* CCD #6	100.00	100.00	99.12	99.32	98.64	98.60	90.70	62.60	11.81
# 12*b* CCD #7	100.00	100.00	99.12	99.32	98.64	97.48	91.94	64.34	14.39

continued

B	Magnitude ranges								
Fields	13 – 14	14 – 15	15 – 16	16 – 17	17 – 18	18 – 19	19 – 20	20 – 21	21 –
# 12*b* CCD #8	100.00	100.00	100.00	99.32	99.55	98.04	93.60	62.79	11.07
# 13*b* CCD #1	100.00	100.00	99.12	99.32	98.18	98.04	96.07	89.73	42.44
# 13*b* CCD #2	100.00	100.00	99.12	100.00	98.18	98.32	95.25	89.73	48.34
# 13*b* CCD #3	100.00	100.00	100.00	100.00	100.00	97.48	96.07	90.12	57.56
# 13*b* CCD #4	100.00	100.00	99.12	100.00	98.64	98.32	96.07	88.57	47.60
# 13*b* CCD #5	100.00	100.00	100.00	100.00	100.00	96.92	96.28	88.95	57.20
# 13*b* CCD #6	100.00	100.00	100.00	100.00	99.55	96.92	92.98	84.11	43.91
# 13*b* CCD #7	100.00	100.00	100.00	100.00	99.09	97.76	94.01	89.34	57.93
# 13*b* CCD #8	100.00	100.00	99.12	98.64	98.64	96.92	94.63	87.02	48.71
# 14*b* CCD #1	100.00	100.00	97.37	97.28	96.82	91.88	72.93	10.66	1.11
# 14*b* CCD #2	100.00	100.00	100.00	98.64	95.45	90.48	70.04	15.89	0.74
# 14*b* CCD #3	100.00	100.00	98.25	99.32	96.36	89.36	73.35	20.54	0.37
# 14*b* CCD #4	100.00	98.21	100.00	98.64	96.82	90.48	63.43	13.37	2.58
# 14*b* CCD #5	100.00	100.00	99.12	98.64	97.27	88.52	58.47	12.79	1.85
# 14*b* CCD #6	100.00	100.00	100.00	97.96	95.00	84.03	55.37	9.50	1.85
# 14*b* CCD #7	100.00	98.21	99.12	97.96	96.36	86.55	59.71	13.18	1.85

continued

B	Magnitude ranges								
Fields	13 – 14	14 – 15	15 – 16	16 – 17	17 – 18	18 – 19	19 – 20	20 – 21	21 –
# 14*b* CCD #8	100.00	98.21	97.37	95.92	95.45	86.83	59.09	9.30	2.58
# 15*b* CCD #1	100.00	100.00	96.49	97.96	95.00	91.88	73.97	11.82	1.11
# 15*b* CCD #2	100.00	100.00	99.12	97.96	96.36	91.88	69.42	15.70	0.74
# 15*b* CCD #3	100.00	100.00	98.25	99.32	97.27	93.28	75.41	21.51	2.58
# 15*b* CCD #4	100.00	98.21	97.37	99.32	96.82	92.44	73.97	18.60	1.48
# 15*b* CCD #5	100.00	98.21	100.00	100.00	98.64	92.16	73.55	18.99	1.85
# 15*b* CCD #6	100.00	98.21	98.25	97.96	94.55	89.36	66.94	15.12	2.58
# 15*b* CCD #7	100.00	100.00	99.12	97.96	95.45	88.24	58.88	11.05	1.48
# 15*b* CCD #8	100.00	100.00	97.37	97.96	95.91	87.11	55.37	10.66	1.48
# 16*b* CCD #1	100.00	100.00	99.12	98.64	99.55	97.76	95.87	64.73	9.96
# 16*b* CCD #2	100.00	100.00	100.00	100.00	100.00	98.32	92.56	69.57	11.44
# 16*b* CCD #3	100.00	100.00	100.00	99.32	98.64	98.60	92.77	64.34	19.93
# 16*b* CCD #4	100.00	98.21	100.00	100.00	98.18	98.04	88.84	53.49	12.92
# 16*b* CCD #5	100.00	100.00	100.00	100.00	99.55	98.04	92.36	70.16	11.44
# 16*b* CCD #6	91.67	80.36	81.58	85.03	86.82	91.04	87.40	58.72	12.55
# 16*b* CCD #7	100.00	100.00	100.00	99.32	99.09	98.32	96.28	70.54	11.44

continued

B	Magnitude ranges								
Fields	13 – 14	14 – 15	15 – 16	16 – 17	17 – 18	18 – 19	19 – 20	20 – 21	21 –
# 16*b* CCD #8	100.00	100.00	100.00	99.32	99.55	98.88	96.07	70.74	11.81
# 17*b* CCD #1	100.00	100.00	97.37	97.96	95.00	92.16	81.40	29.65	1.11
# 17*b* CCD #2	100.00	100.00	98.25	98.64	96.36	93.56	82.44	33.14	2.58
# 17*b* CCD #3	100.00	98.21	98.25	97.96	97.27	91.88	81.61	38.76	2.58
# 17*b* CCD #4	100.00	98.21	99.12	98.64	95.45	89.92	76.03	26.74	1.48
# 17*b* CCD #5	100.00	100.00	98.25	97.96	96.82	90.48	75.83	30.62	2.95
# 17*b* CCD #6	100.00	100.00	99.12	95.24	95.91	92.44	78.31	32.36	2.58
# 17*b* CCD #7	100.00	100.00	97.37	97.96	95.00	91.60	82.02	31.40	3.32
# 17*b* CCD #8	100.00	98.21	97.37	97.28	97.27	92.44	80.17	30.43	1.11
# 18*b* CCD #1	100.00	98.21	92.98	91.16	91.36	84.87	74.59	43.80	4.06
# 18*b* CCD #2	100.00	100.00	98.25	92.52	90.91	82.63	66.32	36.24	5.17
# 18*b* CCD #3	100.00	98.21	94.74	91.84	91.82	84.59	73.35	40.89	9.23
# 18*b* CCD #4	100.00	96.43	97.37	96.60	91.36	87.68	75.83	42.05	7.75
# 16*b* CCD #5	100.00	98.21	98.25	97.96	95.45	89.36	71.49	37.40	7.75
# 18*b* CCD #6	100.00	96.43	99.12	93.88	86.82	80.95	66.12	34.30	7.75
# 18*b* CCD #7	100.00	100.00	96.49	93.20	90.45	84.59	66.32	40.31	9.59

continued

B	Magnitude ranges								
Fields	13 – 14	14 – 15	15 – 16	16 – 17	17 – 18	18 – 19	19 – 20	20 – 21	21 –
# 18*b* CCD #8	100.00	100.00	97.37	95.92	91.82	85.43	67.36	39.92	6.64
# 19*b* CCD #1	100.00	100.00	100.00	100.00	98.64	99.16	91.74	19.96	1.85
# 19*b* CCD #2	100.00	100.00	100.00	100.00	100.00	98.60	93.60	33.72	2.58
# 19*b* CCD #3	100.00	100.00	99.12	100.00	100.00	99.16	97.52	40.12	2.21
# 19*b* CCD #4	100.00	100.00	99.12	100.00	99.09	98.88	91.32	37.60	2.21
# 19*b* CCD #5	100.00	100.00	100.00	100.00	100.00	97.48	95.45	43.02	2.21
# 19*b* CCD #6	100.00	100.00	100.00	100.00	98.64	98.88	93.80	31.78	1.48
# 19*b* CCD #7	100.00	100.00	100.00	99.32	99.55	99.44	94.42	29.46	1.48
# 19*b* CCD #8	100.00	100.00	99.12	100.00	99.09	99.72	89.26	20.54	0.74
# 20*b* CCD #1	100.00	100.00	100.00	99.32	99.55	98.60	91.74	23.64	0.74
# 20*b* CCD #2	100.00	100.00	100.00	100.00	100.00	98.04	90.29	31.59	1.48
# 20*b* CCD #3	100.00	100.00	99.12	100.00	98.18	97.76	93.60	36.43	1.48
# 20*b* CCD #4	100.00	98.21	100.00	98.64	98.64	96.64	90.50	35.47	4.43
# 20*b* CCD #5	100.00	100.00	100.00	100.00	98.64	98.60	91.53	35.47	2.58
# 20*b* CCD #6	100.00	100.00	100.00	98.64	97.73	97.48	89.67	33.33	1.85
# 20*b* CCD #7	100.00	100.00	100.00	99.32	99.09	97.76	92.77	33.33	2.58

continued

B	Magnitude ranges								
Fields	13 – 14	14 – 15	15 – 16	16 – 17	17 – 18	18 – 19	19 – 20	20 – 21	21 –
# 20*b* CCD #8	100.00	100.00	99.12	99.32	99.09	97.76	90.29	23.26	0.74
# 21*b* CCD #1	100.00	100.00	98.25	100.00	99.09	98.88	88.43	15.89	0.00
# 21*b* CCD #2	100.00	100.00	100.00	100.00	100.00	98.32	86.16	19.19	1.85
# 21*b* CCD #3	100.00	100.00	99.12	100.00	99.09	97.48	92.15	29.46	0.37
# 21*b* CCD #4	100.00	98.21	100.00	99.32	98.64	97.20	88.84	27.91	2.95
# 21*b* CCD #5	100.00	100.00	100.00	99.32	99.55	98.32	88.22	30.23	1.11
# 21*b* CCD #6	100.00	100.00	100.00	99.32	99.55	97.76	85.74	20.93	0.00
# 21*b* CCD #7	100.00	100.00	100.00	98.64	98.64	96.92	86.36	21.71	1.85
# 21*b* CCD #8	100.00	100.00	99.12	99.32	99.55	98.32	84.30	16.28	1.48
# 22*b* CCD #1	100.00	100.00	100.00	97.96	97.27	93.56	66.74	6.20	2.58
# 22*b* CCD #2	100.00	100.00	100.00	98.64	99.09	94.96	71.69	10.47	1.48
# 22*b* CCD #3	100.00	100.00	99.12	100.00	98.18	96.64	77.27	17.64	0.74
# 22*b* CCD #4	100.00	100.00	100.00	99.32	96.82	93.84	69.83	13.18	1.11
# 22*b* CCD #5	100.00	100.00	100.00	100.00	97.27	94.68	75.62	15.70	2.58
# 22*b* CCD #6	100.00	100.00	100.00	96.60	96.82	95.24	77.07	13.37	1.11
# 22*b* CCD #7	100.00	100.00	100.00	99.32	98.64	94.68	77.69	11.43	1.85

continued

B	Magnitude ranges								
Fields	13 – 14	14 – 15	15 – 16	16 – 17	17 – 18	18 – 19	19 – 20	20 – 21	21 –
# 22*b* CCD #8	100.00	98.21	98.25	97.96	99.09	96.92	77.69	9.50	0.74
# 23*b* CCD #1	100.00	100.00	100.00	99.32	97.27	96.92	90.91	54.46	6.27
# 23*b* CCD #2	100.00	100.00	100.00	99.32	98.18	94.40	87.81	47.48	4.06
# 23*b* CCD #3	100.00	100.00	99.12	97.96	97.27	94.96	86.98	48.06	8.86
# 23*b* CCD #4	100.00	98.21	100.00	100.00	95.45	89.36	79.34	41.86	5.90
# 23*b* CCD #5	100.00	100.00	98.25	99.32	99.55	93.56	80.37	42.83	5.17
# 23*b* CCD #6	100.00	100.00	99.12	97.28	96.36	92.44	83.47	47.87	2.21
# 23*b* CCD #7	100.00	100.00	98.25	98.64	98.18	93.00	87.60	51.16	4.06
# 23*b* CCD #8	100.00	100.00	97.37	97.28	98.18	95.52	85.12	50.00	3.69
# 24*b* CCD #1	100.00	100.00	97.37	98.64	98.64	95.24	64.46	3.49	0.00
# 24*b* CCD #2	100.00	100.00	99.12	100.00	98.18	94.12	61.16	5.43	0.00
# 24*b* CCD #3	100.00	100.00	98.25	99.32	98.18	93.56	65.50	7.75	0.00
# 24*b* CCD #4	100.00	98.21	100.00	99.32	96.36	93.28	64.05	6.98	0.37
# 24*b* CCD #5	100.00	100.00	99.12	100.00	99.09	92.44	64.26	10.27	0.74
# 24*b* CCD #6	100.00	100.00	100.00	96.60	97.27	91.32	58.68	7.75	1.11
# 24*b* CCD #7	100.00	100.00	99.12	99.32	98.64	92.16	67.77	6.78	0.74

continued

B	Magnitude ranges								
Fields	13 – 14	14 – 15	15 – 16	16 – 17	17 – 18	18 – 19	19 – 20	20 – 21	21 –
# 24*b* CCD #8	100.00	100.00	97.37	98.64	99.09	93.56	61.16	5.43	0.74
# 25*b* CCD #1	100.00	100.00	100.00	100.00	99.55	99.44	84.09	8.72	0.37
# 25*b* CCD #2	100.00	100.00	100.00	100.00	100.00	98.60	87.19	14.73	0.37
# 25*b* CCD #3	100.00	100.00	99.12	100.00	100.00	98.04	90.08	20.16	0.74
# 25*b* CCD #4	100.00	98.21	99.12	100.00	98.18	96.64	82.64	18.02	1.48
# 25*b* CCD #5	100.00	100.00	100.00	99.32	100.00	97.20	87.40	19.38	2.21
# 25*b* CCD #6	100.00	100.00	99.12	100.00	98.64	99.16	84.09	14.15	1.85
# 25*b* CCD #7	100.00	100.00	100.00	99.32	100.00	98.88	89.46	17.05	0.37
# 25*b* CCD #8	100.00	100.00	99.12	99.32	99.55	98.88	90.29	15.31	0.74
# 26*b* CCD #1	100.00	100.00	99.12	100.00	99.09	97.20	64.88	3.68	1.48
# 26*b* CCD #2	100.00	100.00	100.00	99.32	99.55	96.64	68.39	8.91	0.37
# 26*b* CCD #3	100.00	100.00	99.12	100.00	99.09	95.52	78.10	10.08	1.11
# 26*b* CCD #4	100.00	100.00	100.00	100.00	98.64	96.64	68.80	11.63	0.74
# 26*b* CCD #5	100.00	100.00	100.00	100.00	98.64	97.48	74.79	12.21	1.85
# 26*b* CCD #6	100.00	100.00	100.00	98.64	98.64	95.52	72.73	6.40	0.74
# 26*b* CCD #7	100.00	100.00	99.12	99.32	99.09	96.92	77.69	7.17	0.00

continued

B	Magnitude ranges								
Fields	13 – 14	14 – 15	15 – 16	16 – 17	17 – 18	18 – 19	19 – 20	20 – 21	21 –
# 26*b* CCD #8	100.00	100.00	99.12	99.32	99.55	96.64	70.04	6.78	0.74
# 27*b* CCD #1	100.00	100.00	100.00	99.32	97.73	95.52	48.14	2.13	0.37
# 27*b* CCD #2	100.00	100.00	100.00	98.64	98.64	95.24	56.20	3.68	0.74
# 27*b* CCD #3	100.00	100.00	99.12	99.32	98.18	94.96	68.60	5.62	1.11
# 27*b* CCD #4	100.00	100.00	100.00	97.96	97.27	93.00	57.23	6.59	1.48
# 27*b* CCD #5	100.00	100.00	100.00	100.00	99.09	95.52	64.67	8.14	0.37
# 27*b* CCD #6	100.00	100.00	100.00	98.64	97.27	95.24	63.43	4.65	0.37
# 27*b* CCD #7	100.00	100.00	100.00	99.32	98.18	96.36	68.60	3.29	0.37
# 27*b* CCD #8	100.00	100.00	98.25	98.64	99.55	94.68	62.60	5.04	0.74
# 28*b* CCD #1	100.00	100.00	100.00	100.00	98.64	98.32	59.71	2.13	0.37
# 28*b* CCD #2	100.00	100.00	100.00	99.32	99.55	97.20	71.07	6.40	0.00
# 28*b* CCD #3	100.00	100.00	99.12	100.00	100.00	96.36	76.24	11.05	1.48
# 28*b* CCD #4	100.00	100.00	100.00	100.00	98.64	95.80	68.39	7.75	1.11
# 28*b* CCD #5	100.00	100.00	100.00	100.00	98.64	96.92	75.41	7.36	0.74
# 28*b* CCD #6	100.00	100.00	100.00	99.32	97.73	97.20	68.60	5.43	1.48
# 28*b* CCD #7	100.00	100.00	99.12	99.32	99.09	94.96	54.96	2.52	0.00

continued

B	Magnitude ranges								
Fields	13 – 14	14 – 15	15 – 16	16 – 17	17 – 18	18 – 19	19 – 20	20 – 21	21 –
# 28*b* CCD #8	100.00	100.00	99.12	98.64	98.64	93.00	47.73	2.71	0.74
# 29*b* CCD #1	100.00	98.21	99.12	99.32	99.55	98.32	87.81	9.30	0.37
# 29*b* CCD #2	100.00	98.21	100.00	100.00	100.00	98.04	86.16	12.98	0.74
# 29*b* CCD #3	100.00	100.00	100.00	100.00	100.00	98.88	89.46	23.06	1.85
# 29*b* CCD #4	91.67	98.21	99.12	100.00	98.64	98.04	79.96	15.89	1.85
# 29*b* CCD #5	100.00	100.00	99.12	100.00	100.00	98.32	87.19	18.02	1.48
# 29*b* CCD #6	100.00	100.00	100.00	100.00	99.09	98.60	83.68	10.47	2.21
# 29*b* CCD #7	100.00	100.00	100.00	99.32	99.55	99.44	88.64	15.89	0.37
# 29*b* CCD #8	100.00	100.00	100.00	100.00	100.00	98.04	86.16	12.79	2.58
# 30*b* CCD #1	100.00	100.00	100.00	99.32	98.18	95.24	54.34	3.29	0.37
# 30*b* CCD #2	100.00	100.00	100.00	99.32	100.00	97.20	61.98	5.62	0.00
# 30*b* CCD #3	100.00	100.00	99.12	100.00	100.00	96.08	69.01	6.40	1.11
# 30*b* CCD #4	100.00	100.00	100.00	99.32	97.27	93.56	61.78	7.36	2.21
# 30*b* CCD #5	100.00	100.00	100.00	100.00	95.91	91.60	61.16	7.17	1.11
# 30*b* CCD #6	100.00	100.00	98.25	98.64	96.82	89.64	55.37	3.68	0.74
# 30*b* CCD #7	100.00	100.00	99.12	98.64	98.64	94.96	65.08	4.84	0.37

continued

B	Magnitude ranges								
Fields	13 – 14	14 – 15	15 – 16	16 – 17	17 – 18	18 – 19	19 – 20	20 – 21	21 –
# 30*b* CCD #8	100.00	98.21	99.12	100.00	99.09	96.64	61.16	4.84	0.37
# 31*b* CCD #1	100.00	98.21	99.12	99.32	98.18	94.40	44.21	1.55	0.00
# 31*b* CCD #2	100.00	98.21	100.00	100.00	99.55	95.24	48.97	1.55	0.37
# 31*b* CCD #3	100.00	100.00	99.12	100.00	98.18	92.72	56.82	4.07	0.74
# 31*b* CCD #4	100.00	100.00	99.12	100.00	97.73	93.28	49.59	4.07	0.37
# 31*b* CCD #5	100.00	100.00	100.00	99.32	98.18	95.52	54.75	4.46	0.00
# 31*b* CCD #6	100.00	100.00	100.00	98.64	97.27	93.84	49.59	4.46	1.11
# 31*b* CCD #7	100.00	100.00	100.00	99.32	98.64	94.12	51.24	2.52	0.00
# 31*b* CCD #8	100.00	98.21	98.25	98.64	96.36	93.00	49.59	3.10	1.11
# 32*b* CCD #1	100.00	100.00	97.37	98.64	96.82	90.20	25.21	0.58	0.37
# 32*b* CCD #2	100.00	100.00	100.00	97.96	97.27	84.59	28.72	1.16	0.00
# 32*b* CCD #3	100.00	100.00	98.25	95.92	96.36	87.68	33.26	2.13	0.37
# 32*b* CCD #4	100.00	96.43	100.00	98.64	96.36	82.07	28.93	1.16	0.00
# 32*b* CCD #5	100.00	100.00	98.25	99.32	98.64	86.55	30.99	2.71	0.74
# 32*b* CCD #6	100.00	98.21	99.12	97.28	95.45	81.79	33.06	0.78	0.00
# 32*b* CCD #7	100.00	98.21	99.12	95.92	95.91	86.55	36.36	2.52	0.00

continued

B	Magnitude ranges								
Fields	13 – 14	14 – 15	15 – 16	16 – 17	17 – 18	18 – 19	19 – 20	20 – 21	21 –
# 32*b* CCD #8	100.00	100.00	97.37	98.64	97.27	86.83	26.65	1.74	0.37
# 33*b* CCD #1	100.00	98.21	94.74	97.28	94.55	87.39	52.89	6.98	1.11
# 33*b* CCD #2	100.00	98.21	97.37	98.64	97.73	90.76	59.92	7.75	0.00
# 33*b* CCD #3	100.00	100.00	99.12	97.28	95.91	91.60	63.43	11.43	1.48
# 33*b* CCD #4	100.00	96.43	99.12	97.28	96.82	87.11	55.79	8.14	0.74
# 33*b* CCD #5	100.00	100.00	98.25	98.64	95.45	88.52	57.44	11.63	0.37
# 33*b* CCD #6	100.00	100.00	98.25	96.60	96.36	88.80	55.99	9.50	0.74
# 33*b* CCD #7	100.00	98.21	99.12	95.24	93.64	89.36	63.02	6.98	0.37
# 33*b* CCD #8	100.00	100.00	97.37	97.96	95.91	90.20	59.92	7.95	0.74
# 34*b* CCD #1	100.00	100.00	99.12	99.32	98.64	95.80	82.44	22.87	1.85
# 34*b* CCD #2	100.00	98.21	100.00	98.64	98.18	95.52	86.16	29.46	0.74
# 34*b* CCD #3	100.00	100.00	97.37	98.64	98.64	96.08	88.84	34.50	0.74
# 34*b* CCD #4	100.00	98.21	99.12	99.32	98.64	94.40	84.71	28.49	3.32
# 34*b* CCD #5	100.00	100.00	100.00	99.32	99.55	96.36	85.74	34.30	2.95
# 34*b* CCD #6	100.00	96.43	99.12	97.96	97.27	93.84	86.16	27.91	1.48
# 34*b* CCD #7	100.00	100.00	98.25	98.64	97.27	94.96	88.02	30.81	2.58

continued

B	Magnitude ranges								
Fields	13 – 14	14 – 15	15 – 16	16 – 17	17 – 18	18 – 19	19 – 20	20 – 21	21 –
# 34*b* CCD #8	100.00	100.00	98.25	98.64	98.18	96.08	87.19	27.52	0.37

Table B.3: The results of artificial star test for 600s V and R frames in each b field.

		Magnitude ranges								
Fields	Filter	13.5 – 14.5	14.5 – 15.5	15.5 – 16.5	16.5 – 17.5	17.5 –18.5	18.5 – 19.5	19.5 – 20.5	20.5 – 21.5	21.5 –
# 01*b* CCD #1	V	100.00	98.21	98.25	93.20	80.45	49.58	11.57	2.33	1.11
	R	100.00	98.21	98.25	92.52	76.82	47.90	11.57	1.94	0.74
# 01*b* CCD #2	V	100.00	96.43	98.25	93.88	84.09	56.02	17.98	1.16	0.74
	R	100.00	100.00	97.37	95.24	86.36	56.02	16.32	1.16	0.74
# 01*b* CCD #3	V	100.00	98.21	96.49	95.24	85.91	58.54	19.83	1.36	0.74
	R	100.00	100.00	95.61	92.52	86.36	61.62	16.53	1.74	0.00
# 01*b* CCD #4	V	100.00	98.21	96.49	94.56	89.09	69.19	23.14	1.55	0.00
	R	100.00	98.21	96.49	95.24	86.82	68.91	23.97	2.13	0.00
# 01*b* CCD #5	V	100.00	100.00	97.37	96.60	91.36	68.07	24.59	2.33	0.00
	R	100.00	100.00	96.49	95.24	89.09	64.71	25.21	2.91	0.37

continued

Fields	Filter	Magnitude ranges 13.5 – 14.5	14.5 – 15.5	15.5 – 16.5	16.5 – 17.5	17.5 –18.5	18.5 – 19.5	19.5 – 20.5	20.5 – 21.5	21.5 –
# 01*b* CCD #6	*V*	100.00	96.43	97.37	96.60	89.09	60.50	22.31	1.55	0.74
	R	100.00	98.21	95.61	97.28	86.82	66.95	23.35	2.13	1.11
# 01*b* CCD #7	*V*	100.00	100.00	92.98	92.52	85.00	62.18	19.21	1.55	0.74
	R	100.00	100.00	94.74	91.84	83.18	66.67	19.42	1.74	0.74
# 01*b* CCD #8	*V*	100.00	100.00	96.49	93.88	89.55	55.46	14.67	1.74	0.74
	R	100.00	100.00	97.37	93.20	86.36	58.26	12.81	1.36	0.37
# 02*b* CCD #1	*V*	100.00	100.00	95.61	95.24	90.91	68.07	17.98	2.52	1.48
	R	100.00	100.00	96.49	96.60	86.82	64.15	17.15	1.74	0.74
# 02*b* CCD #2	*V*	100.00	98.21	97.37	97.96	94.09	80.67	26.45	4.26	1.11
	R	100.00	100.00	98.25	97.28	91.82	72.55	23.97	2.13	0.00
# 02*b* CCD #3	*V*	100.00	96.43	98.25	99.32	95.00	83.47	35.12	3.10	1.85
	R	100.00	98.21	96.49	95.92	90.91	80.39	29.13	3.29	0.74
# 02*b* CCD #4	*V*	100.00	98.21	100.00	97.96	94.55	84.03	31.61	2.33	0.00
	R	100.00	98.21	100.00	97.96	91.82	80.95	25.83	0.97	0.37
# 02*b* CCD #5	*V*	100.00	100.00	99.12	98.64	96.82	85.43	34.71	2.33	0.37
	R	100.00	98.21	98.25	95.92	95.00	80.39	33.88	2.91	1.11
# 02*b* CCD #6	*V*	100.00	100.00	99.12	96.60	94.55	83.19	31.82	1.55	0.37
	R	100.00	100.00	99.12	95.24	93.64	80.67	29.55	0.97	1.11
# 02*b* CCD #7	*V*	100.00	100.00	98.25	97.28	92.73	80.39	28.93	1.36	1.11
	R	100.00	98.21	95.61	96.60	91.36	78.15	25.00	0.97	0.74
# 02*b* CCD #8	*V*	100.00	100.00	94.74	97.96	92.27	70.03	25.62	1.74	2.21

continued

Fields	Filter	Magnitude ranges 13.5 – 14.5	14.5 – 15.5	15.5 – 16.5	16.5 – 17.5	17.5 –18.5	18.5 – 19.5	19.5 – 20.5	20.5 – 21.5	21.5 –
	R	100.00	100.00	93.86	93.20	89.55	70.31	18.60	1.94	1.11
# 03*b* CCD #1	*V*	100.00	100.00	99.12	100.00	99.09	96.36	70.04	11.43	4.43
	R	100.00	100.00	100.00	100.00	98.18	94.96	77.69	17.25	2.95
# 03*b* CCD #2	*V*	100.00	100.00	100.00	98.64	96.82	95.52	72.93	12.02	2.21
	R	100.00	100.00	100.00	100.00	97.73	95.24	80.17	18.60	5.90
# 03*b* CCD #3	*V*	100.00	100.00	100.00	100.00	99.55	95.24	83.47	19.77	2.95
	R	100.00	100.00	100.00	100.00	99.55	98.88	91.94	32.95	6.27
# 03*b* CCD #4	*V*	100.00	98.21	100.00	100.00	97.73	95.52	71.49	10.08	1.11
	R	100.00	100.00	100.00	99.32	99.09	98.60	94.01	19.19	2.21
# 03*b* CCD #5	*V*	100.00	100.00	100.00	100.00	99.09	96.64	84.50	18.41	1.85
	R	100.00	100.00	100.00	100.00	100.00	99.44	94.42	33.14	3.32
# 03*b* CCD #6	*V*	100.00	100.00	100.00	100.00	99.09	95.52	69.83	8.33	0.74
	R	100.00	100.00	100.00	99.32	98.64	97.76	79.55	11.24	4.06
# 03*b* CCD #7	*V*	100.00	100.00	100.00	98.64	97.27	95.80	76.65	13.18	2.95
	R	91.67	91.07	92.11	86.39	80.91	70.03	42.98	7.75	2.95
# 03*b* CCD #8	*V*	100.00	100.00	99.12	99.32	98.64	92.72	69.42	13.37	4.80
	R	100.00	100.00	100.00	98.64	97.73	93.56	70.87	15.12	3.69
# 04*b* CCD #1	*V*	100.00	100.00	100.00	99.32	98.18	93.56	57.85	7.17	3.69
	R	100.00	100.00	100.00	99.32	97.27	94.40	69.63	14.53	4.06
# 04*b* CCD #2	*V*	100.00	100.00	100.00	100.00	99.55	96.08	76.65	17.05	2.95
	R	100.00	100.00	100.00	100.00	99.09	97.76	85.33	25.00	4.43

continued

Fields	Filter	Magnitude ranges 13.5 – 14.5	14.5 – 15.5	15.5 – 16.5	16.5 – 17.5	17.5 –18.5	18.5 – 19.5	19.5 – 20.5	20.5 – 21.5	21.5 –
# 04*b* CCD #3	*V*	100.00	100.00	99.12	100.00	98.64	95.24	81.20	22.48	4.06
	R	83.33	100.00	100.00	100.00	98.18	96.92	89.05	28.29	5.90
# 04*b* CCD #4	*V*	100.00	98.21	99.12	99.32	99.09	97.76	75.21	11.43	1.48
	R	100.00	98.21	99.12	99.32	98.18	95.80	86.36	21.51	2.58
# 04*b* CCD #5	*V*	100.00	100.00	100.00	100.00	99.55	97.48	83.06	24.03	5.17
	R	100.00	100.00	99.12	99.32	99.09	98.04	88.43	29.65	3.69
# 04*b* CCD #6	*V*	100.00	100.00	100.00	100.00	98.64	94.12	71.28	13.37	3.69
	R	100.00	100.00	99.12	100.00	97.27	94.40	76.03	14.92	2.95
# 04*b* CCD #7	*V*	100.00	100.00	100.00	99.32	98.18	90.48	63.22	11.05	2.21
	R	100.00	100.00	99.12	100.00	99.55	95.52	79.75	24.42	6.64
# 04*b* CCD #8	*V*	100.00	100.00	99.12	100.00	97.73	93.84	68.80	13.37	5.17
	R	100.00	100.00	99.12	98.64	94.55	90.20	69.63	14.92	6.64
# 06*b* CCD #1	*V*	100.00	96.43	95.61	91.84	81.82	49.86	12.60	3.49	0.37
	R	100.00	98.21	96.49	91.84	70.00	32.49	6.20	1.74	2.95
# 06*b* CCD #2	*V*	100.00	100.00	99.12	92.52	80.91	43.70	13.64	3.68	1.85
	R	100.00	100.00	100.00	92.52	74.55	35.29	8.68	1.55	2.21
# 06*b* CCD #3	*V*	100.00	100.00	93.86	87.76	71.82	36.69	10.33	3.49	2.21
	R	100.00	100.00	92.11	88.44	63.64	27.45	6.82	2.91	2.21
# 06*b* CCD #4	*V*	100.00	91.07	86.84	74.15	51.82	25.77	7.23	1.74	2.95
	R	100.00	91.07	89.47	70.07	46.36	15.97	4.13	2.13	2.95
# 06*b* CCD #5	*V*	100.00	98.21	95.61	81.63	54.09	23.53	8.47	3.88	2.21

continued

Fields	Filter	Magnitude ranges 13.5 – 14.5	14.5 – 15.5	15.5 – 16.5	16.5 – 17.5	17.5 –18.5	18.5 – 19.5	19.5 – 20.5	20.5 – 21.5	21.5 –
	R	100.00	96.43	97.37	80.95	55.45	16.53	6.61	2.52	1.11
# 06*b* CCD #6	*V*	100.00	98.21	96.49	91.84	69.55	38.10	9.09	2.52	1.85
	R	100.00	100.00	97.37	85.03	64.55	28.01	7.64	3.49	2.21
# 06*b* CCD #7	*V*	100.00	100.00	92.11	89.80	73.64	38.38	8.47	2.33	2.21
	R	100.00	98.21	94.74	85.03	61.36	25.21	5.17	3.29	1.85
# 06*b* CCD #8	*V*	100.00	100.00	96.49	95.92	80.00	40.62	12.19	2.13	1.48
	R	100.00	100.00	96.49	89.80	55.91	20.17	8.06	2.33	2.21
# 07*b* CCD #1	*V*	100.00	98.21	94.74	89.12	68.64	37.54	9.71	2.71	2.21
	R	100.00	100.00	94.74	89.12	79.55	52.94	16.53	6.20	3.32
# 07*b* CCD #2	*V*	100.00	100.00	97.37	87.76	73.64	40.06	11.16	4.07	2.58
	R	100.00	98.21	97.37	89.12	84.55	51.26	17.15	4.65	2.58
# 07*b* CCD #3	*V*	100.00	98.21	92.11	86.39	69.55	40.62	11.16	2.91	1.11
	R	100.00	100.00	94.74	87.76	77.73	48.46	16.53	6.78	3.32
# 07*b* CCD #4	*V*	100.00	92.86	98.25	89.80	73.18	43.98	14.26	3.10	4.43
	R	100.00	98.21	96.49	93.88	80.45	50.14	20.45	4.46	3.32
# 07*b* CCD #5	*V*	100.00	100.00	95.61	85.03	68.64	40.90	11.36	4.65	1.85
	R	100.00	100.00	94.74	87.07	76.82	44.26	17.36	4.84	2.58
# 07*b* CCD #6	*V*	100.00	96.43	92.11	92.52	68.64	35.01	11.16	4.46	3.32
	R	100.00	100.00	93.86	89.80	75.91	40.34	14.26	5.23	5.90
# 07*b* CCD #7	*V*	100.00	98.21	94.74	85.71	62.73	39.50	9.71	3.49	2.21
	R	100.00	98.21	94.74	91.84	73.18	48.18	18.39	4.84	4.06
# 07*b* CCD #8	*V*	83.33	100.00	92.98	82.99	64.55	28.85	8.06	3.88	1.48

continued

Fields	Filter	Magnitude ranges 13.5 – 14.5	14.5 – 15.5	15.5 – 16.5	16.5 – 17.5	17.5 –18.5	18.5 – 19.5	19.5 – 20.5	20.5 – 21.5	21.5 –
	R	100.00	100.00	92.11	87.07	72.73	40.90	15.50	4.65	2.95
# 08*b* CCD #1	*V*	100.00	98.21	95.61	86.39	81.36	42.86	9.09	4.07	1.85
	R	100.00	100.00	94.74	81.63	73.64	41.18	12.81	4.07	3.69
# 08*b* CCD #2	*V*	100.00	100.00	100.00	89.12	77.73	44.26	13.64	3.10	1.48
	R	100.00	100.00	96.49	88.44	77.73	39.50	16.74	4.26	1.85
# 08*b* CCD #3	*V*	100.00	100.00	95.61	93.88	80.45	46.50	13.84	4.46	0.74
	R	100.00	100.00	94.74	93.20	81.36	47.34	15.70	6.59	2.95
# 08*b* CCD #4	*V*	100.00	98.21	99.12	96.60	84.55	52.38	17.56	4.46	2.58
	R	100.00	92.86	99.12	93.20	85.45	56.02	20.66	5.04	3.69
# 08*b* CCD #5	*V*	100.00	100.00	97.37	93.20	85.45	45.94	18.39	4.46	1.85
	R	100.00	100.00	95.61	91.84	78.64	42.86	12.40	3.68	2.21
# 08*b* CCD #6	*V*	91.67	100.00	97.37	91.16	82.27	42.58	14.67	2.13	1.11
	R	91.67	100.00	99.12	88.44	71.82	36.97	14.26	4.26	2.58
# 08*b* CCD #7	*V*	100.00	100.00	98.25	95.24	72.27	43.14	10.12	3.10	1.48
	R	100.00	100.00	96.49	90.48	69.55	39.22	10.95	4.65	2.58
# 08*b* CCD #8	*V*	100.00	100.00	97.37	95.24	66.82	33.61	11.36	3.49	1.48
	R	100.00	100.00	90.35	87.76	64.55	30.25	9.92	5.81	2.21
# 09*b* CCD #1	*V*	100.00	100.00	95.61	97.96	86.36	72.83	43.18	18.41	11.44
	R	100.00	100.00	97.37	93.88	83.64	71.71	42.56	18.99	20.30
# 09*b* CCD #2	*V*	100.00	100.00	99.12	99.32	90.45	76.75	52.69	27.52	11.81
	R	100.00	100.00	100.00	94.56	91.82	72.83	47.52	19.19	10.33
# 09*b* CCD #3	*V*	100.00	100.00	99.12	96.60	95.45	79.27	61.57	30.43	17.34

continued

Fields	Filter	Magnitude ranges 13.5 – 14.5	14.5 – 15.5	15.5 – 16.5	16.5 – 17.5	17.5 –18.5	18.5 – 19.5	19.5 – 20.5	20.5 – 21.5	21.5 –
	R	100.00	100.00	99.12	97.96	92.27	81.23	67.77	27.13	12.92
# 09*b* CCD #4	*V*	100.00	100.00	100.00	100.00	95.91	94.68	75.62	37.40	16.61
	R	100.00	100.00	99.12	100.00	95.91	88.24	70.45	30.62	12.18
# 09*b* CCD #5	*V*	100.00	100.00	100.00	99.32	97.27	91.04	75.21	36.82	15.13
	R	100.00	100.00	100.00	99.32	97.73	87.11	68.18	27.33	11.44
# 09*b* CCD #6	*V*	100.00	100.00	100.00	97.96	94.09	82.63	68.80	28.49	8.12
	R	100.00	100.00	99.12	95.24	91.36	77.87	60.54	24.81	12.18
# 09*b* CCD #7	*V*	100.00	98.21	99.12	97.28	87.73	69.75	46.07	19.38	12.18
	R	100.00	100.00	99.12	93.88	85.91	73.39	45.66	19.57	11.44
# 09*b* CCD #8	*V*	100.00	100.00	97.37	93.88	88.18	74.23	51.65	21.32	11.81
	R	100.00	100.00	95.61	96.60	86.36	72.55	48.97	16.47	15.13
# 13*b* CCD #1	*V*	100.00	100.00	100.00	99.32	99.55	96.64	92.36	64.53	8.12
	R	100.00	100.00	100.00	98.64	96.82	96.64	85.95	39.53	4.80
# 13*b* CCD #2	*V*	100.00	100.00	100.00	100.00	96.36	97.48	91.32	71.71	11.07
	R	100.00	100.00	99.12	100.00	98.64	94.68	88.84	47.67	7.01
# 13*b* CCD #3	*V*	100.00	98.21	100.00	100.00	100.00	96.64	92.56	78.10	13.28
	R	100.00	100.00	99.12	97.96	99.09	95.24	90.70	57.56	9.23
# 13*b* CCD #4	*V*	100.00	100.00	99.12	98.64	99.09	97.76	92.56	73.06	10.70
	R	100.00	100.00	97.37	98.64	97.73	95.80	91.74	56.20	7.38
# 13*b* CCD #5	*V*	100.00	100.00	100.00	98.64	97.73	96.64	90.70	67.44	14.02
	R	100.00	100.00	100.00	98.64	98.18	93.28	86.57	47.87	8.86
# 13*b* CCD #6	*V*	100.00	100.00	100.00	100.00	99.55	96.36	90.29	58.72	9.59

continued

Fields	Filter	Magnitude ranges 13.5 – 14.5	14.5 – 15.5	15.5 – 16.5	16.5 – 17.5	17.5 –18.5	18.5 – 19.5	19.5 – 20.5	20.5 – 21.5	21.5 –
	R	100.00	100.00	100.00	100.00	97.73	94.68	83.47	48.06	11.07
# 13*b* CCD #7	*V*	100.00	100.00	100.00	99.32	98.18	96.92	91.94	68.99	14.39
	R	100.00	100.00	100.00	97.96	96.82	94.96	89.67	50.97	6.27
# 13*b* CCD #8	*V*	100.00	100.00	97.37	98.64	98.64	96.08	89.88	64.92	12.92
	R	100.00	100.00	99.12	99.32	97.27	94.12	87.40	49.03	7.75
# 14*b* CCD #1	*V*	100.00	100.00	95.61	95.92	95.00	85.43	58.68	10.47	1.48
	R	100.00	100.00	93.86	97.96	94.55	86.27	43.60	6.78	2.58
# 14*b* CCD #2	*V*	100.00	100.00	99.12	97.28	95.00	82.91	56.20	10.66	1.11
	R	100.00	98.21	97.37	96.60	94.09	81.79	47.73	8.72	2.95
# 14*b* CCD #3	*V*	100.00	100.00	97.37	94.56	94.55	84.59	60.95	13.37	2.95
	R	100.00	100.00	98.25	93.88	93.18	81.79	53.31	8.91	0.74
# 14*b* CCD #4	*V*	100.00	96.43	99.12	98.64	92.27	81.51	57.85	11.82	1.85
	R	100.00	98.21	99.12	99.32	90.00	81.51	49.79	9.30	2.21
# 14*b* CCD #5	*V*	100.00	100.00	98.25	95.24	87.27	68.91	38.22	8.33	1.11
	R	100.00	100.00	99.12	94.56	86.82	63.59	29.96	5.23	2.58
# 14*b* CCD #6	*V*	100.00	98.21	97.37	93.88	88.18	68.63	39.67	8.91	2.58
	R	100.00	100.00	98.25	96.60	89.09	71.99	33.06	5.43	2.21
# 14*b* CCD #7	*V*	100.00	100.00	98.25	96.60	88.64	75.91	42.98	11.43	1.11
	R	100.00	98.21	96.49	97.28	86.82	69.47	38.64	8.33	2.58
# 14*b* CCD #8	*V*	100.00	100.00	97.37	93.88	90.45	73.11	43.39	7.36	1.48
	R	100.00	100.00	94.74	90.48	87.73	71.43	32.44	5.62	3.32
# 16*b* CCD #1	*V*	100.00	100.00	99.12	98.64	93.64	86.83	56.20	6.59	1.48

continued

Fields	Filter	Magnitude ranges 13.5 – 14.5	14.5 – 15.5	15.5 – 16.5	16.5 – 17.5	17.5 –18.5	18.5 – 19.5	19.5 – 20.5	20.5 – 21.5	21.5 –
	R	100.00	100.00	98.25	97.96	92.73	84.03	49.38	8.53	2.58
# 16*b* CCD #2	*V*	100.00	100.00	99.12	98.64	95.91	79.83	51.45	8.53	3.69
	R	100.00	100.00	99.12	97.96	88.64	81.23	46.69	8.33	2.95
# 16*b* CCD #3	*V*	100.00	100.00	98.25	95.24	91.82	78.71	48.35	9.11	1.11
	R	100.00	100.00	98.25	90.48	85.45	73.11	38.84	8.14	5.54
# 16*b* CCD #4	*V*	100.00	100.00	99.12	94.56	86.36	67.23	28.93	7.36	2.58
	R	100.00	100.00	100.00	91.84	82.73	57.70	24.38	8.91	7.38
# 16*b* CCD #5	*V*	100.00	100.00	97.37	99.32	94.09	80.95	48.76	9.11	2.21
	R	100.00	100.00	97.37	97.96	89.09	70.87	38.02	11.24	2.95
# 16*b* CCD #6	*V*	100.00	100.00	98.25	96.60	94.09	87.39	50.62	7.17	2.58
	R	100.00	100.00	96.49	95.24	92.73	80.11	47.11	6.40	3.69
# 16*b* CCD #7	*V*	100.00	98.21	100.00	98.64	95.91	87.68	62.40	11.05	3.32
	R	100.00	100.00	100.00	98.64	95.91	85.99	47.73	6.59	1.85
# 16*b* CCD #8	*V*	100.00	100.00	98.25	97.96	97.27	91.32	61.98	9.69	1.11
	R	100.00	100.00	99.12	96.60	97.27	89.08	51.24	5.23	1.11
# 17*b* CCD #1	*V*	100.00	100.00	97.37	97.28	95.00	93.00	56.82	7.36	0.74
	R	100.00	100.00	97.37	97.96	95.45	86.55	47.52	3.29	1.11
# 17*b* CCD #2	*V*	100.00	100.00	100.00	99.32	96.82	89.64	55.17	9.88	0.37
	R	100.00	100.00	100.00	99.32	95.45	87.96	51.86	6.40	0.74
# 17*b* CCD #3	*V*	100.00	98.21	96.49	96.60	95.45	87.96	66.94	11.82	0.74
	R	100.00	98.21	97.37	97.96	95.91	87.96	57.23	6.59	0.74
# 17*b* CCD #4	*V*	100.00	98.21	100.00	97.96	93.64	88.80	64.88	11.43	0.37

continued

Fields	Filter	Magnitude ranges 13.5 – 14.5	14.5 – 15.5	15.5 – 16.5	16.5 – 17.5	17.5 –18.5	18.5 – 19.5	19.5 – 20.5	20.5 – 21.5	21.5 –
	R	100.00	98.21	99.12	98.64	94.09	86.27	53.10	6.20	0.74
# 17*b* CCD #5	*V*	100.00	100.00	96.49	97.28	96.36	86.83	56.82	10.47	1.48
	R	100.00	98.21	99.12	95.92	93.18	85.43	47.52	6.78	1.48
# 17*b* CCD #6	*V*	100.00	98.21	97.37	95.92	95.91	88.52	53.10	7.75	1.11
	R	100.00	100.00	99.12	95.24	91.36	83.75	49.38	6.01	0.74
# 17*b* CCD #7	*V*	100.00	98.21	98.25	97.96	95.00	86.55	59.92	9.11	0.74
	R	100.00	98.21	98.25	97.28	94.55	82.91	49.17	5.04	0.00
# 17*b* CCD #8	*V*	100.00	100.00	98.25	97.96	96.82	86.27	55.37	8.33	1.85
	R	100.00	100.00	96.49	96.60	93.18	85.43	43.39	4.07	1.11
# 18*b* CCD #1	*V*	100.00	96.43	92.98	87.76	90.00	79.83	50.62	8.14	1.11
	R	100.00	94.64	93.86	93.20	88.18	62.75	20.66	1.55	0.37
# 18*b* CCD #2	*V*	91.67	98.21	98.25	90.48	90.91	72.83	43.60	9.69	1.85
	R	100.00	98.21	96.49	91.84	89.55	66.39	20.04	2.71	0.00
# 18*b* CCD #3	*V*	100.00	96.43	92.98	92.52	89.55	77.87	48.35	12.60	1.48
	R	100.00	96.43	94.74	92.52	90.00	63.31	19.01	2.71	0.74
# 18*b* CCD #4	*V*	91.67	98.21	97.37	94.56	88.64	84.03	57.44	12.02	0.74
	R	100.00	96.43	99.12	94.56	86.82	68.07	25.00	2.71	0.37
# 18*b* CCD #5	*V*	100.00	100.00	97.37	95.24	92.27	78.71	48.35	11.05	1.48
	R	100.00	98.21	99.12	93.88	90.00	59.94	19.21	3.68	1.85
# 18*b* CCD #6	*V*	100.00	100.00	95.61	95.24	86.36	74.51	43.80	7.75	1.85
	R	100.00	98.21	96.49	93.20	87.73	52.66	16.32	2.33	1.11
# 18*b* CCD #7	*V*	100.00	100.00	96.49	91.84	88.18	75.63	46.69	11.05	1.48

continued

Fields	Filter	Magnitude ranges 13.5 – 14.5	14.5 – 15.5	15.5 – 16.5	16.5 – 17.5	17.5 –18.5	18.5 – 19.5	19.5 – 20.5	20.5 – 21.5	21.5 –
	R	100.00	100.00	98.25	95.24	81.82	58.82	18.18	2.33	1.48
# 18*b* CCD #8	*V*	91.67	98.21	96.49	94.56	86.36	75.07	41.53	9.30	1.85
	R	100.00	100.00	95.61	93.20	85.45	56.58	19.21	1.74	1.48
# 19*b* CCD #1	*V*	100.00	100.00	100.00	99.32	99.09	98.32	65.91	4.26	1.48
	R	100.00	100.00	100.00	99.32	98.64	98.32	72.52	8.72	1.85
# 19*b* CCD #2	*V*	100.00	100.00	100.00	99.32	99.55	97.20	72.52	8.72	0.00
	R	100.00	100.00	100.00	99.32	99.55	97.48	83.06	9.30	2.21
# 19*b* CCD #3	*V*	100.00	100.00	99.12	100.00	100.00	98.32	83.06	12.79	1.11
	R	100.00	100.00	99.12	100.00	98.64	98.88	86.78	19.38	1.85
# 19*b* CCD #4	*V*	100.00	100.00	99.12	100.00	98.64	98.32	70.45	6.20	1.11
	R	100.00	100.00	99.12	99.32	98.18	98.04	87.81	12.40	1.11
# 19*b* CCD #5	*V*	100.00	100.00	100.00	100.00	100.00	98.04	83.06	15.70	2.21
	R	100.00	100.00	100.00	99.32	100.00	97.48	90.70	22.29	2.58
# 19*b* CCD #6	*V*	100.00	100.00	100.00	100.00	99.09	98.32	74.17	6.20	0.37
	R	100.00	100.00	100.00	100.00	98.18	98.60	79.75	11.05	1.11
# 19*b* CCD #7	*V*	100.00	100.00	100.00	100.00	99.09	98.60	69.01	7.17	1.11
	R	100.00	100.00	100.00	100.00	98.64	97.76	85.74	15.70	0.74
# 19*b* CCD #8	*V*	100.00	100.00	100.00	100.00	100.00	98.32	71.49	5.81	0.74
	R	100.00	100.00	99.12	100.00	99.55	98.88	82.85	12.40	2.58
# 20*b* CCD #1	*V*	100.00	100.00	100.00	100.00	99.09	98.60	73.55	7.95	0.74
	R	100.00	100.00	100.00	100.00	97.73	98.04	70.25	7.17	0.37
# 20*b* CCD #2	*V*	100.00	100.00	99.12	100.00	98.64	98.04	77.69	10.27	0.74

continued

Fields	Filter	Magnitude ranges 13.5 – 14.5	14.5 – 15.5	15.5 – 16.5	16.5 – 17.5	17.5 –18.5	18.5 – 19.5	19.5 – 20.5	20.5 – 21.5	21.5 –
	R	100.00	100.00	99.12	100.00	98.18	98.04	75.83	8.72	0.74
# 20*b* CCD #3	*V*	100.00	100.00	100.00	100.00	99.55	97.76	84.50	14.15	2.21
	R	100.00	100.00	99.12	100.00	99.09	96.92	78.72	12.98	1.48
# 20*b* CCD #4	*V*	100.00	100.00	100.00	99.32	98.64	96.64	78.51	9.69	0.00
	R	100.00	96.43	100.00	98.64	97.73	95.80	72.11	6.78	1.48
# 20*b* CCD #5	*V*	100.00	100.00	100.00	100.00	99.09	95.80	82.44	14.53	2.21
	R	100.00	100.00	100.00	99.32	99.55	95.24	75.83	14.73	3.69
# 20*b* CCD #6	*V*	100.00	100.00	100.00	100.00	99.09	95.80	75.62	9.11	1.48
	R	100.00	100.00	100.00	100.00	98.18	96.08	72.93	7.17	1.48
# 20*b* CCD #7	*V*	100.00	100.00	100.00	100.00	99.09	98.88	83.68	10.27	1.11
	R	100.00	100.00	98.25	99.32	98.18	96.36	75.00	6.40	0.37
# 20*b* CCD #8	*V*	100.00	100.00	99.12	100.00	99.55	97.48	75.83	6.98	1.11
	R	100.00	98.21	99.12	98.64	98.64	95.24	78.10	9.69	1.48
# 21*b* CCD #1	*V*	100.00	100.00	99.12	100.00	99.55	98.60	71.28	6.40	0.37
	R	100.00	100.00	98.25	99.32	99.09	98.60	69.63	7.36	0.37
# 21*b* CCD #2	*V*	100.00	100.00	100.00	100.00	100.00	96.92	80.17	9.30	0.74
	R	100.00	98.21	100.00	100.00	98.18	97.48	74.38	7.95	1.11
# 21*b* CCD #3	*V*	100.00	100.00	100.00	100.00	99.09	96.92	84.30	13.37	1.48
	R	100.00	100.00	100.00	99.32	99.09	95.24	82.44	14.34	2.21
# 21*b* CCD #4	*V*	100.00	98.21	100.00	98.64	98.64	96.92	77.69	8.91	0.37
	R	100.00	98.21	99.12	99.32	98.18	98.04	78.31	10.08	0.37
# 21*b* CCD #5	*V*	100.00	100.00	100.00	100.00	99.55	96.92	83.47	14.73	1.85

continued

Fields	Filter	Magnitude ranges 13.5 – 14.5	14.5 – 15.5	15.5 – 16.5	16.5 – 17.5	17.5 –18.5	18.5 – 19.5	19.5 – 20.5	20.5 – 21.5	21.5 –
	R	100.00	100.00	100.00	100.00	99.09	96.36	78.31	13.57	2.21
# 21*b* CCD #6	*V*	100.00	100.00	100.00	99.32	99.55	98.04	81.61	11.43	0.74
	R	100.00	100.00	100.00	98.64	98.64	97.48	66.12	5.04	2.21
# 21*b* CCD #7	*V*	100.00	100.00	100.00	100.00	98.64	96.64	79.96	11.24	1.48
	R	100.00	100.00	100.00	98.64	99.55	95.52	67.98	4.26	0.37
# 21*b* CCD #8	*V*	100.00	100.00	99.12	100.00	99.09	97.20	69.01	6.20	1.11
	R	100.00	100.00	99.12	100.00	98.64	96.36	73.14	6.98	0.37
# 22*b* CCD #1	*V*	100.00	98.21	100.00	97.96	96.36	88.52	47.52	3.68	1.85
	R	100.00	98.21	100.00	97.28	95.00	87.68	40.29	4.84	1.85
# 22*b* CCD #2	*V*	100.00	100.00	99.12	97.96	98.18	89.36	56.20	5.81	1.11
	R	100.00	100.00	100.00	98.64	96.36	86.27	41.94	4.46	0.74
# 22*b* CCD #3	*V*	100.00	100.00	100.00	98.64	99.09	92.72	73.14	11.63	2.95
	R	100.00	100.00	99.12	99.32	96.82	91.60	62.40	6.98	0.74
# 22*b* CCD #4	*V*	100.00	100.00	99.12	98.64	95.45	89.92	55.99	5.23	1.85
	R	100.00	100.00	99.12	96.60	92.73	89.08	53.93	5.23	2.21
# 22*b* CCD #5	*V*	100.00	100.00	100.00	100.00	97.27	92.72	67.15	12.60	2.21
	R	100.00	100.00	99.12	98.64	93.18	87.96	52.48	7.56	2.95
# 22*b* CCD #6	*V*	100.00	100.00	100.00	98.64	95.45	96.64	64.88	5.04	1.11
	R	100.00	100.00	100.00	95.24	95.00	92.16	48.14	6.20	1.48
# 22*b* CCD #7	*V*	100.00	100.00	100.00	99.32	98.18	93.00	63.64	6.59	1.48
	R	100.00	100.00	100.00	97.96	95.91	92.72	58.06	4.84	0.37
# 22*b* CCD #8	*V*	100.00	98.21	98.25	97.96	97.73	96.92	60.74	4.07	0.74

continued

Fields	Filter	Magnitude ranges 13.5 – 14.5	14.5 – 15.5	15.5 – 16.5	16.5 – 17.5	17.5 –18.5	18.5 – 19.5	19.5 – 20.5	20.5 – 21.5	21.5 –
	R	100.00	98.21	98.25	99.32	97.73	91.88	53.72	4.46	0.37
# 23*b* CCD #1	*V*	100.00	100.00	99.12	98.64	97.27	96.92	78.72	11.43	0.74
	R	100.00	100.00	100.00	98.64	96.82	94.68	46.28	4.07	1.11
# 23*b* CCD #2	*V*	100.00	100.00	100.00	100.00	96.36	91.60	70.87	18.22	1.11
	R	100.00	100.00	100.00	99.32	97.27	90.76	51.24	3.49	0.74
# 23*b* CCD #3	*V*	100.00	100.00	97.37	97.96	95.00	92.72	79.96	22.09	3.32
	R	100.00	100.00	99.12	99.32	95.45	93.84	61.36	5.62	2.21
# 23*b* CCD #4	*V*	100.00	98.21	99.12	100.00	96.82	87.39	66.32	16.86	0.37
	R	100.00	96.43	99.12	97.96	94.09	85.71	44.42	5.04	1.11
# 23*b* CCD #5	*V*	100.00	100.00	100.00	97.96	95.00	86.83	65.08	16.47	2.58
	R	100.00	100.00	99.12	99.32	94.09	85.43	47.31	6.59	1.48
# 23*b* CCD #6	*V*	100.00	100.00	100.00	97.28	96.36	86.27	71.07	11.24	2.58
	R	100.00	100.00	100.00	97.28	95.91	88.24	50.62	2.52	1.85
# 23*b* CCD #7	*V*	100.00	100.00	99.12	97.28	95.45	92.16	74.17	15.50	2.58
	R	100.00	100.00	99.12	97.96	95.45	93.84	56.61	4.65	0.37
# 23*b* CCD #8	*V*	100.00	100.00	98.25	97.28	95.45	92.16	71.90	12.60	1.11
	R	100.00	100.00	97.37	97.28	96.36	91.60	55.37	3.10	0.37
# 24*b* CCD #1	*V*	100.00	100.00	97.37	97.96	95.45	87.11	29.75	1.74	0.00
	R	100.00	100.00	98.25	95.92	92.73	78.99	26.24	1.36	0.00
# 24*b* CCD #2	*V*	100.00	100.00	98.25	99.32	95.45	86.83	33.88	1.94	0.00
	R	100.00	98.21	100.00	98.64	95.45	83.75	25.00	1.55	0.00
# 24*b* CCD #3	*V*	100.00	96.43	97.37	97.28	96.82	84.03	37.19	1.94	0.37

continued

Fields	Filter	Magnitude ranges 13.5 – 14.5	14.5 – 15.5	15.5 – 16.5	16.5 – 17.5	17.5 –18.5	18.5 – 19.5	19.5 – 20.5	20.5 – 21.5	21.5 –
	R	100.00	98.21	95.61	96.60	93.64	79.83	29.13	2.52	0.37
# 24*b* CCD #4	*V*	100.00	98.21	99.12	99.32	94.09	84.87	34.09	1.55	0.74
	R	100.00	98.21	100.00	97.96	90.91	78.15	29.75	1.74	0.00
# 24*b* CCD #5	*V*	100.00	100.00	100.00	96.60	96.36	82.91	35.95	2.33	0.00
	R	100.00	100.00	95.61	95.92	90.91	75.07	26.45	1.74	0.37
# 24*b* CCD #6	*V*	100.00	100.00	100.00	97.96	95.45	78.15	27.27	3.29	0.00
	R	100.00	98.21	98.25	95.24	91.36	73.11	24.79	1.94	0.74
# 24*b* CCD #7	*V*	100.00	100.00	99.12	97.28	96.82	84.59	34.71	1.74	0.74
	R	100.00	100.00	98.25	97.28	93.64	75.35	23.35	2.91	0.74
# 24*b* CCD #8	*V*	100.00	100.00	98.25	96.60	93.64	86.55	30.58	1.36	0.37
	R	100.00	100.00	96.49	94.56	91.36	78.99	23.14	1.94	1.11
# 25*b* CCD #1	*V*	100.00	100.00	100.00	100.00	99.55	98.32	61.57	4.26	0.37
	R	100.00	100.00	100.00	100.00	100.00	97.76	66.32	6.01	0.00
# 25*b* CCD #2	*V*	100.00	100.00	99.12	100.00	99.55	97.48	60.54	4.26	0.74
	R	100.00	100.00	99.12	99.32	99.09	98.04	68.80	4.26	1.11
# 25*b* CCD #3	*V*	100.00	100.00	99.12	100.00	99.55	96.36	79.75	9.30	1.11
	R	100.00	100.00	99.12	100.00	98.64	96.08	76.24	8.72	1.11
# 25*b* CCD #4	*V*	100.00	98.21	100.00	99.32	97.73	96.08	55.58	5.23	1.48
	R	100.00	98.21	99.12	100.00	98.18	96.08	58.88	3.68	2.21
# 25*b* CCD #5	*V*	100.00	100.00	100.00	99.32	99.55	96.08	76.24	11.05	0.37
	R	100.00	100.00	100.00	99.32	98.64	96.64	73.35	11.05	1.48
# 25*b* CCD #6	*V*	100.00	100.00	100.00	100.00	98.18	96.92	67.77	5.62	1.11

continued

Fields	Filter	Magnitude ranges 13.5 – 14.5	14.5 – 15.5	15.5 – 16.5	16.5 – 17.5	17.5 –18.5	18.5 – 19.5	19.5 – 20.5	20.5 – 21.5	21.5 –
	R	100.00	100.00	100.00	100.00	97.73	96.08	60.12	4.07	1.11
# 25*b* CCD #7	*V*	100.00	100.00	100.00	99.32	100.00	97.48	72.11	8.91	1.48
	R	100.00	100.00	100.00	99.32	100.00	97.20	72.11	8.14	1.85
# 25*b* CCD #8	*V*	100.00	100.00	99.12	99.32	99.09	98.88	71.90	6.20	0.74
	R	100.00	100.00	99.12	99.32	98.64	96.64	71.49	4.84	0.37
# 26*b* CCD #1	*V*	100.00	100.00	100.00	100.00	99.09	92.72	49.79	4.46	1.11
	R	100.00	98.21	100.00	99.32	97.73	90.20	43.39	4.65	2.21
# 26*b* CCD #2	*V*	100.00	100.00	100.00	100.00	96.82	94.12	59.09	5.04	1.48
	R	100.00	100.00	100.00	100.00	97.73	91.88	57.02	6.59	1.85
# 26*b* CCD #3	*V*	100.00	100.00	100.00	100.00	98.64	94.40	62.19	9.11	1.85
	R	100.00	100.00	100.00	98.64	98.64	91.32	61.98	7.95	1.85
# 26*b* CCD #4	*V*	100.00	98.21	100.00	98.64	97.27	92.44	51.03	4.84	1.85
	R	100.00	98.21	99.12	98.64	92.27	91.88	41.12	2.71	1.48
# 26*b* CCD #5	*V*	100.00	100.00	100.00	99.32	98.18	96.08	64.88	8.14	1.85
	R	100.00	100.00	100.00	99.32	97.73	93.00	66.12	8.91	2.95
# 26*b* CCD #6	*V*	100.00	100.00	99.12	100.00	97.73	96.08	60.95	2.91	2.21
	R	100.00	100.00	99.12	100.00	97.73	93.56	56.82	5.23	0.74
# 26*b* CCD #7	*V*	100.00	100.00	98.25	98.64	98.18	95.52	55.99	5.81	0.00
	R	100.00	100.00	98.25	98.64	97.73	96.08	64.67	6.20	0.74
# 26*b* CCD #8	*V*	100.00	100.00	99.12	100.00	98.64	95.24	60.12	4.07	1.11
	R	100.00	100.00	99.12	99.32	98.64	94.40	64.88	5.81	1.48
# 27*b* CCD #1	*V*	100.00	100.00	99.12	97.28	97.27	90.20	30.79	2.52	0.37

continued

Fields	Filter	Magnitude ranges 13.5 – 14.5	14.5 – 15.5	15.5 – 16.5	16.5 – 17.5	17.5 –18.5	18.5 – 19.5	19.5 – 20.5	20.5 – 21.5	21.5 –
	R	100.00	100.00	100.00	99.32	96.36	95.24	53.72	5.23	1.85
# 27*b* CCD #2	*V*	100.00	98.21	99.12	98.64	98.18	89.64	36.57	2.91	0.00
	R	100.00	100.00	100.00	97.96	98.18	94.40	52.27	2.71	1.11
# 27*b* CCD #3	*V*	100.00	98.21	99.12	98.64	97.27	88.80	45.45	3.68	1.48
	R	100.00	100.00	100.00	98.64	95.45	93.00	64.46	7.36	2.58
# 27*b* CCD #4	*V*	91.67	98.21	100.00	95.24	97.27	85.43	41.53	3.88	0.37
	R	100.00	98.21	100.00	96.60	94.55	85.15	39.46	4.07	1.11
# 27*b* CCD #5	*V*	100.00	100.00	100.00	99.32	97.27	91.60	48.55	5.81	1.11
	R	100.00	100.00	100.00	99.32	97.27	91.60	59.71	10.27	0.74
# 27*b* CCD #6	*V*	100.00	100.00	100.00	98.64	97.27	91.04	42.36	1.36	0.74
	R	100.00	100.00	100.00	100.00	96.36	91.88	55.58	6.01	1.11
# 27*b* CCD #7	*V*	100.00	100.00	100.00	99.32	98.64	93.00	46.49	1.74	0.37
	R	100.00	100.00	100.00	99.32	97.73	94.12	62.81	4.84	1.11
# 27*b* CCD #8	*V*	100.00	100.00	99.12	99.32	98.64	90.76	44.21	2.52	0.37
	R	100.00	100.00	98.25	98.64	98.18	94.40	60.54	4.46	1.48
# 28*b* CCD #1	*V*	100.00	100.00	100.00	100.00	98.64	97.20	48.35	2.52	0.00
	R	100.00	100.00	99.12	100.00	99.09	94.12	44.63	2.52	0.00
# 28*b* CCD #2	*V*	100.00	100.00	100.00	98.64	99.09	96.36	53.72	3.88	0.37
	R	100.00	100.00	100.00	97.28	98.64	93.56	44.42	1.74	0.00
# 28*b* CCD #3	*V*	100.00	100.00	98.25	100.00	99.09	96.92	55.17	3.29	0.74
	R	100.00	100.00	99.12	100.00	98.64	97.48	56.20	5.81	1.48
# 28*b* CCD #4	*V*	100.00	100.00	100.00	100.00	97.73	94.96	51.45	2.33	0.74

continued

Fields	Filter	Magnitude ranges 13.5 – 14.5	14.5 – 15.5	15.5 – 16.5	16.5 – 17.5	17.5 –18.5	18.5 – 19.5	19.5 – 20.5	20.5 – 21.5	21.5 –
	R	100.00	100.00	100.00	100.00	98.18	94.68	50.62	5.04	1.11
# 28*b* CCD #5	*V*	100.00	100.00	100.00	100.00	98.18	96.08	59.50	5.23	0.74
	R	100.00	100.00	100.00	100.00	98.64	94.40	61.16	3.88	1.11
# 28*b* CCD #6	*V*	100.00	100.00	99.12	99.32	96.36	93.28	46.49	2.13	0.37
	R	100.00	100.00	100.00	100.00	94.55	95.52	51.86	2.71	1.48
# 28*b* CCD #7	*V*	100.00	100.00	99.12	99.32	96.82	97.20	57.64	4.26	0.00
	R	100.00	100.00	99.12	99.32	97.27	92.72	57.85	3.68	1.11
# 28*b* CCD #8	*V*	100.00	100.00	99.12	99.32	100.00	93.56	53.93	3.10	0.74
	R	100.00	100.00	99.12	97.96	98.64	92.72	46.07	3.49	1.11
# 29*b* CCD #1	*V*	100.00	100.00	99.12	99.32	98.18	96.08	60.95	3.88	0.00
	R	100.00	100.00	99.12	98.64	98.18	97.48	72.73	6.78	0.74
# 29*b* CCD #2	*V*	100.00	100.00	100.00	100.00	99.09	94.96	55.17	4.65	0.74
	R	100.00	100.00	100.00	99.32	100.00	97.48	73.76	7.17	0.74
# 29*b* CCD #3	*V*	100.00	100.00	99.12	100.00	99.55	97.48	70.66	8.72	1.48
	R	100.00	100.00	99.12	100.00	98.64	96.64	80.17	12.02	2.21
# 29*b* CCD #4	*V*	100.00	100.00	100.00	98.64	97.27	94.68	62.40	9.11	1.48
	R	100.00	100.00	99.12	97.96	98.64	96.92	72.31	8.72	1.85
# 29*b* CCD #5	*V*	100.00	100.00	100.00	100.00	99.55	95.24	71.07	6.78	2.58
	R	100.00	100.00	100.00	99.32	97.27	95.24	78.93	12.40	1.11
# 29*b* CCD #6	*V*	100.00	100.00	100.00	99.32	98.64	97.48	64.46	5.62	1.11
	R	100.00	100.00	100.00	100.00	99.09	97.48	74.38	6.59	0.74
# 29*b* CCD #7	*V*	100.00	100.00	100.00	99.32	100.00	96.92	69.63	7.17	0.74

continued

Fields	Filter	Magnitude ranges 13.5 – 14.5	14.5 – 15.5	15.5 – 16.5	16.5 – 17.5	17.5 –18.5	18.5 – 19.5	19.5 – 20.5	20.5 – 21.5	21.5 –
	R	100.00	100.00	100.00	99.32	99.55	97.48	76.24	8.53	1.85
# 29*b* CCD #8	*V*	100.00	100.00	99.12	99.32	96.36	92.72	64.67	5.62	3.32
	R	100.00	100.00	99.12	100.00	99.09	94.96	75.00	9.11	2.58
# 30*b* CCD #1	*V*	100.00	100.00	100.00	98.64	98.18	94.12	47.93	2.52	0.00
	R	100.00	100.00	99.12	98.64	97.73	96.08	58.26	4.46	1.11
# 30*b* CCD #2	*V*	100.00	100.00	100.00	99.32	99.09	96.08	50.62	4.07	0.74
	R	100.00	100.00	99.12	99.32	100.00	95.80	60.54	4.65	0.37
# 30*b* CCD #3	*V*	100.00	100.00	99.12	99.32	99.55	96.08	60.33	6.40	1.85
	R	100.00	100.00	99.12	99.32	97.27	98.04	74.79	5.81	1.48
# 30*b* CCD #4	*V*	100.00	98.21	100.00	98.64	97.73	95.52	52.07	3.88	0.37
	R	100.00	100.00	100.00	98.64	96.36	95.80	60.33	4.65	0.74
# 30*b* CCD #5	*V*	100.00	100.00	100.00	96.60	95.45	90.76	44.01	4.65	1.85
	R	100.00	100.00	100.00	98.64	95.91	91.32	67.98	7.56	3.32
# 30*b* CCD #6	*V*	100.00	100.00	99.12	98.64	92.27	89.92	47.52	4.07	2.21
	R	100.00	100.00	99.12	97.28	90.91	89.08	54.34	5.04	1.48
# 30*b* CCD #7	*V*	100.00	100.00	100.00	97.28	96.36	96.08	54.55	1.74	0.74
	R	100.00	100.00	99.12	98.64	99.55	96.08	64.05	6.20	1.11
# 30*b* CCD #8	*V*	100.00	100.00	99.12	99.32	99.55	96.36	54.75	1.74	0.37
	R	100.00	100.00	100.00	99.32	98.18	94.12	57.44	4.26	0.74
# 31*b* CCD #1	*V*	100.00	100.00	100.00	99.32	96.36	89.08	29.34	0.97	0.37
	R	100.00	100.00	99.12	100.00	97.73	92.72	34.50	2.71	0.74
# 31*b* CCD #2	*V*	100.00	100.00	100.00	98.64	99.09	94.12	32.02	1.36	0.37

continued

Fields	Filter	Magnitude ranges 13.5 – 14.5	14.5 – 15.5	15.5 – 16.5	16.5 – 17.5	17.5 –18.5	18.5 – 19.5	19.5 – 20.5	20.5 – 21.5	21.5 –
	R	100.00	100.00	100.00	97.96	99.09	95.24	44.63	2.52	0.00
# 31*b* CCD #3	*V*	100.00	100.00	99.12	98.64	97.27	93.84	42.77	1.36	0.74
	R	100.00	98.21	100.00	98.64	97.73	94.12	50.41	3.88	0.74
# 31*b* CCD #4	*V*	100.00	100.00	100.00	99.32	96.82	91.60	31.82	0.97	0.37
	R	100.00	100.00	100.00	99.32	95.91	94.96	43.60	2.71	0.00
# 31*b* CCD #5	*V*	100.00	100.00	100.00	100.00	96.82	89.64	40.29	1.94	0.74
	R	100.00	100.00	100.00	100.00	95.91	93.56	46.28	3.29	0.37
# 31*b* CCD #6	*V*	100.00	98.21	100.00	97.28	96.36	91.04	35.95	2.13	0.74
	R	100.00	100.00	100.00	98.64	94.55	93.56	44.63	2.33	0.74
# 31*b* CCD #7	*V*	100.00	100.00	99.12	99.32	98.64	94.12	38.43	2.91	0.00
	R	100.00	100.00	99.12	99.32	98.18	93.84	41.94	2.13	0.74
# 31*b* CCD #8	*V*	100.00	100.00	98.25	98.64	97.27	90.20	31.82	1.16	0.74
	R	100.00	98.21	98.25	98.64	98.18	91.60	38.22	1.74	1.11
# 32*b* CCD #1	*V*	100.00	100.00	98.25	98.64	95.00	81.23	13.02	0.39	0.37
	R	100.00	100.00	98.25	100.00	97.73	87.68	26.65	1.36	0.37
# 32*b* CCD #2	*V*	100.00	100.00	100.00	98.64	94.09	83.19	15.50	0.78	0.00
	R	100.00	100.00	100.00	97.28	98.18	90.48	30.58	1.55	0.37
# 32*b* CCD #3	*V*	100.00	100.00	97.37	97.96	94.55	81.23	20.66	0.78	1.11
	R	100.00	100.00	98.25	97.96	98.18	90.20	40.70	3.29	0.74
# 32*b* CCD #4	*V*	100.00	98.21	99.12	98.64	95.45	81.23	16.53	0.58	0.00
	R	100.00	100.00	99.12	97.28	97.73	92.44	31.20	1.55	0.37
# 32*b* CCD #5	*V*	91.67	100.00	99.12	98.64	95.45	75.91	17.56	2.33	0.00

continued

Fields	Filter	Magnitude ranges 13.5 – 14.5	14.5 – 15.5	15.5 – 16.5	16.5 – 17.5	17.5 –18.5	18.5 – 19.5	19.5 – 20.5	20.5 – 21.5	21.5 –
	R	91.67	98.21	100.00	98.64	97.73	89.08	37.19	2.13	0.37
# 32*b* CCD #6	*V*	100.00	100.00	99.12	96.60	94.55	71.15	13.43	1.16	0.37
	R	100.00	100.00	97.37	97.28	96.82	88.24	29.34	1.36	0.74
# 32*b* CCD #7	*V*	100.00	100.00	98.25	97.96	96.82	77.59	17.36	0.97	0.37
	R	100.00	100.00	100.00	97.28	96.82	89.36	33.88	1.36	0.74
# 32*b* CCD #8	*V*	100.00	100.00	97.37	97.96	96.82	76.19	15.91	0.97	0.37
	R	100.00	100.00	98.25	97.96	98.64	85.99	26.65	0.97	1.85
# 33*b* CCD #1	*V*	100.00	98.21	95.61	100.00	97.73	91.60	42.15	2.52	0.74
	R	100.00	98.21	98.25	98.64	97.27	90.76	34.71	1.74	0.37
# 33*b* CCD #2	*V*	100.00	100.00	98.25	99.32	98.18	92.16	46.69	2.71	0.00
	R	100.00	100.00	98.25	99.32	97.73	94.12	42.98	2.33	0.00
# 33*b* CCD #3	*V*	100.00	100.00	98.25	98.64	97.27	88.52	52.07	5.62	1.11
	R	100.00	100.00	98.25	97.96	96.82	89.64	44.01	3.29	1.11
# 33*b* CCD #4	*V*	100.00	98.21	99.12	99.32	96.82	91.60	46.28	0.97	0.00
	R	100.00	98.21	99.12	99.32	96.82	92.16	39.67	2.52	0.74
# 33*b* CCD #5	*V*	100.00	98.21	100.00	100.00	98.18	89.92	45.87	4.84	0.74
	R	100.00	100.00	100.00	99.32	98.18	87.11	38.84	2.52	0.74
# 33*b* CCD #6	*V*	100.00	98.21	99.12	97.28	96.36	87.96	43.60	2.71	0.37
	R	100.00	100.00	99.12	98.64	96.82	85.71	33.68	1.74	0.74
# 33*b* CCD #7	*V*	100.00	98.21	98.25	97.28	98.18	90.20	49.38	2.91	0.74
	R	100.00	98.21	99.12	99.32	95.91	90.20	40.08	1.55	0.00
# 33*b* CCD #8	*V*	100.00	100.00	97.37	97.28	99.09	88.24	44.42	2.71	1.48

continued

Fields	Filter	Magnitude ranges								
		13.5 – 14.5	14.5 – 15.5	15.5 – 16.5	16.5 – 17.5	17.5 –18.5	18.5 – 19.5	19.5 – 20.5	20.5 – 21.5	21.5 –
	R	100.00	100.00	97.37	98.64	99.09	85.43	32.23	2.71	1.48

B.3 READ_SMC.f

```
      PROGRAM READ_SMC
C nos : total Number Of SMC stars greater than 19 magnitude in B (733483 stars)
C nc : sequential Number of Catalogue (i6)
C ra : Right Ascension in degrees at 2000 epoch (f15.8)
C de : DEclination in degrees at 2000 epoch (f15.8)
C bm : Mangitude in B (f6.3), bme : Error in bm (f6.3)
C vm : Mangitude in V (f6.3), vme : Error in vm (f6.3)
C rm : Mangitude in R (f6.3), rme : Error in rm (f6.3)
C flagb, flagv, flagr : the number of frames in driving magnitude
C at B, V, and R. (f6.3). See more details in Chapter Three

      parameter(nos=733483)
      integer flagb,flagv,flagr
      open(11,file="smc19B.cat")
      open(12,file="result.cat")

      do i=1,nos
         read(11,20) nc,ra,de,bm,bme,flagb
     +           ,vm,vme,flagv,rm,rme,flagr
      IF (Condition Statement)
         write(12,20) nc,ra,de,bm,bme,flagb
     +           ,vm,vme,flagv,rm,rme,flagr
      ENDIF
10    enddo
20    format(i6,2x,2(f15.8,1x),2(f6.3,1x),i2,1x,2(f6.3,1x),i2,1x,
     +           2(f6.3,1x),i2)
      stop
      end
```

Appendix C

Table discussed in Chapter 4

Table C.1: The 2dF stars from Evans *et al.* (2004) used for the $E(B-V)$ calculation, together with our photometric data.

ID	α_{2000}	δ_{2000}	SP type	V	$(B-V)$	$(V-R)$
6	0:28:58.32	-73:28: 6.5	A2 II	16.320	0.068	0.088
15	0:30:25.78	-73:25:12.3	A0 (II)	17.008	-0.017	-0.002
19	0:30:49.51	-73:59:59.8	A0 (II)	16.059	-0.016	0.051
24	0:31: 7.21	-73:27: 9.6	B3 (IV)	16.799	0.072	0.092
35	0:31:58.79	-73:52: 7.3	A2 II	14.248	0.137	0.081
48	0:32:46.50	-73:41:43.8	A0 (II)	14.881	0.037	0.076
50	0:32:53.69	-73:48:31.6	B0.5 (V)	15.469	-0.207	-0.050
54	0:33:11.79	-74:20:45.1	A2 II	16.537	0.195	0.199
55	0:33:17.74	-73:39:46.0	B9 (II)	15.226	0.005	0.026
56	0:33:17.75	-73:55:24.4	B8 (IV)	17.937	0.062	-0.009
57	0:33:22.27	-74: 1:10.6	A0 (II)	16.822	0.021	0.040
59	0:33:31.81	-73:53: 0.2	B5 (IV)	17.373	0.029	-0.115
68	0:33:53.19	-73:41:37.2	A3 II	14.340	0.072	0.112
70	0:34: 0.86	-73:18: 7.0	A0 (II)	16.935	-0.012	-0.032
72	0:34: 9.73	-74:14: 1.2	B8 (II)	14.389	0.004	0.059
75	0:34:14.11	-73:58: 0.3	B2.5 (III)	15.668	-0.120	-0.016
78	0:34:19.48	-74: 2:34.2	A0 (II)	15.991	0.041	0.035
89	0:34:35.46	-73:17:31.8	B5 (III)	16.813	-0.116	-0.072
90	0:34:36.35	-73: 8:25.0	A5 II	16.400	0.209	0.159
92	0:34:37.05	-74: 9: 5.1	B2 (V)	17.076	-0.125	0.067
93	0:34:38.63	-73:41:53.5	B3 (IV)	16.751	-0.164	0.055
94	0:34:39.56	-73: 5:28.6	A2 II	14.943	0.047	-0.077
96	0:34:46.37	-73:23:56.4	B5 (III)	16.572	-0.062	0.093
105	0:35: 1.24	-73:12:40.2	A2 II	15.465	0.079	-0.050
125	0:35:37.11	-73:20:45.9	A3 II	16.142	0.149	0.162
132	0:35:58.83	-73:25:57.0	A5 II	16.043	0.190	0.180
134	0:36: 1.74	-73:58:55.0	B9 (II)	15.777	0.009	0.026
136	0:36:10.93	-72:54:23.7	B2 (V)	16.182	-0.015	-0.124
140	0:36:16.35	-73:57:31.4	B5 (II)	15.118	-0.080	0.057
146	0:36:29.92	-73:55: 6.8	A7 II	13.870	0.172	0.150
149	0:36:33.57	-73:14:15.1	B0.5 (V)	17.029	-0.041	-0.048
158	0:36:47.53	-73:45:29.1	B5 (II)	14.652	-0.087	0.003
162	0:36:57.28	-72:48:17.1	B2 (IV)	16.257	-0.154	0.061
164	0:36:59.26	-73:39:38.5	B5 (III)	16.751	-0.032	-0.009
169	0:37: 6.07	-73:41:31.9	B8 (II)	15.063	-0.025	0.014
170	0:37:10.83	-73:53:37.2	B5 (III)	17.246	-0.031	0.041

continued

ID	α_{2000}	δ_{2000}	SP type	V	$(B-V)$	$(V-R)$
188	0:37:38.07	-74: 3:16.4	A0 (II)	16.258	0.002	0.104
190	0:37:39.33	-72:52:17.9	B2 (III)	14.738	-0.046	-0.289
198	0:37:53.78	-73:42:29.9	A0 (II)	15.070	0.093	0.017
202	0:37:57.45	-72:55:46.8	B8 (II)	13.896	0.048	-0.213
204	0:38: 0.94	-73:39: 8.4	B9 (Ib)	13.091	0.040	0.059
208	0:38: 7.88	-73:53:27.9	B2.5 (V)	17.154	-0.018	-0.023
234	0:38:34.38	-72:40:37.5	A0 (II)	16.317	0.060	0.114
238	0:38:40.26	-73:58:37.4	A2 II	13.938	0.220	0.113
242	0:38:47.98	-73:34: 7.7	B3 (V)	17.317	-0.067	-0.194
264	0:39:23.04	-73:28:11.6	A7 II	14.886	0.282	0.241
277	0:39:42.20	-73:47:17.4	A3 II	15.542	0.297	0.134
280	0:39:46.59	-73:14:32.9	A0 (Ib)	14.335	0.037	0.043
286	0:39:55.49	-73:12:20.9	B3 (V)	17.070	0.061	0.007
288	0:39:57.77	-73:40:48.5	A7 II	17.276	0.297	0.288
312	0:40:23.33	-73:21:58.5	A2 II	14.278	0.080	0.101
316	0:40:24.95	-73:44:15.8	B5 (III)	16.003	0.107	-0.061
322	0:40:31.22	-73:22:29.6	B9 (II)	14.149	0.015	0.044
331	0:40:42.86	-73:48:31.9	A3 II	15.327	0.157	0.106
338	0:40:49.50	-72:56:27.7	A0 (Ib)	14.490	0.199	-0.167
342	0:40:54.30	-72:44:55.6	A7 II	15.794	0.336	0.081
343	0:40:55.36	-74: 2:49.2	A0 (II)	17.323	0.050	-0.138
349	0:41: 6.81	-72:48:54.8	A7 II	16.070	0.364	-0.018
353	0:41: 9.34	-73:25:17.8	A7 II	14.183	0.143	0.201
356	0:41:11.78	-72:10: 5.5	A3 II	16.504	0.153	0.118
369	0:41:28.15	-72:47: 5.0	A2 II	13.150	0.121	0.064
394	0:41:58.22	-73: 6:32.7	A5 II	15.671	0.132	0.162
404	0:42: 9.94	-73:13:55.9	O8.5 V	14.481	-0.273	-0.011
406	0:42:11.95	-73:29:52.5	A0 (II)	15.129	0.064	0.029
409	0:42:12.90	-73:23: 1.5	A0 (II)	15.549	0.059	0.147
423	0:42:30.79	-72:48:13.8	A0 (III)	17.004	0.229	-0.183
434	0:42:50.28	-73:30:27.6	A3 II	14.405	0.060	0.009
441	0:42:59.65	-73:39:37.3	B2 (III)	14.433	-0.063	-0.164
444	0:43: 9.33	-72:16: 5.0	A3 II	15.209	0.076	0.102
446	0:43:11.76	-73:36:17.7	B0.5 (V)	15.055	-0.131	-0.112
451	0:43:16.39	-72:19:53.8	B0.5 (V)	15.998	-0.228	-0.050
461	0:43:21.30	-73: 7:24.4	B8 (V)	13.345	0.062	0.021
463	0:43:23.60	-72:15:38.0	A3 II	15.899	0.106	0.115
471	0:43:30.83	-73:20:34.3	B2.5 (IV)	15.993	-0.130	-0.104
492	0:43:58.13	-73:30:30.4	B5 (II)	14.187	0.037	0.039
522	0:44:42.23	-72:14: 4.6	B2 (III)	15.612	-0.144	-0.047
524	0:44:43.95	-73:52:18.1	A2 II	15.730	0.307	0.152

continued

ID	α_{2000}	δ_{2000}	SP type	V	$(B-V)$	$(V-R)$
533	0:44:54.09	-74: 2:29.1	A5 II	15.573	0.247	0.187
542	0:45: 1.42	-72:33:20.2	A3 II	16.379	0.203	0.185
543	0:45: 2.15	-73:37:35.7	A0 (Ib)	15.275	0.098	0.076
544	0:45: 3.45	-73:38:31.8	B2 (II)	14.481	0.076	0.108
547	0:45:10.27	-74:20:60.0	A0 (II)	14.878	0.222	0.150
553	0:45:15.80	-72:30:48.3	A3 II	17.732	0.071	0.304
558	0:45:21.66	-72:42:40.8	A5 III	15.760	0.236	0.175
562	0:45:28.55	-73:56:35.7	B2 (II)	14.721	-0.094	0.042
573	0:45:42.67	-73:34:32.6	A0 (II)	16.077	0.142	0.111
627	0:46:56.59	-72:51:34.8	B8 (II)	15.922	0.061	0.026
642	0:47:22.80	-72:22:36.7	A0 (II)	16.211	0.055	0.018
669	0:47:58.60	-72:31:41.3	B0.5 (II)e	14.610	0.030	-0.179
679	0:48:14.46	-73:39:25.9	B2.5 (Ib)	13.658	-0.083	0.022
705	0:48:55.59	-73:49:44.8	O9.5 V	14.925	-0.036	0.078
730	0:49:29.00	-72:41:50.0	A2 II	13.990	0.165	0.121
744	0:49:57.35	-72:24:19.3	B9 (Ib)	13.750	0.020	-0.019
757	0:50:18.51	-72:38:56.1	B0.5 (V)	14.948	-0.033	-0.030
761	0:50:25.67	-72: 8: 3.0	O9.5 Ib	14.505	-0.052	-0.044
764	0:50:28.00	-73: 3:16.5	B0 (III)	13.870	-0.091	-0.015
766	0:50:30.19	-72:12: 2.8	A2 II	15.548	0.091	0.070
773	0:50:38.40	-72:15:27.4	B2 (IV)	16.136	0.050	-0.015
786	0:50:58.97	-72: 8:16.2	B0.5 (IV)	14.558	-0.174	-0.073
797	0:51:15.85	-72:15: 8.8	A5 II	14.509	0.225	0.080
812	0:51:40.28	-72: 6:10.4	B9 (Ib)	14.479	0.013	0.036
837	0:52: 3.96	-72:12:16.9	B0.5 (II)	13.456	-0.116	-0.130
848	0:52:12.06	-72: 6:38.5	O9.7 III	14.435	-0.252	-0.055
854	0:52:15.32	-72: 9:15.7	B0 (IV)	14.576	-0.163	-0.069
868	0:52:27.86	-72:45:35.0	A0 (II)	15.941	0.053	0.084
880	0:52:40.72	-72:50:19.2	A2 II	13.714	0.082	0.058
918	0:53:13.01	-72: 9: 3.0	B0 (V)	15.048	-0.171	-0.058
920	0:53:14.32	-72:48:26.5	A7 II	15.477	0.311	0.227
921	0:53:16.24	-73:31:28.0	A5 II	16.045	0.275	0.139
941	0:53:36.33	-72:25:27.1	O8 V	14.475	-0.249	-0.091
958	0:53:48.89	-73:27: 0.9	A2 III	16.953	0.067	0.200
966	0:53:56.95	-73:43:48.3	B8 (II)	15.019	-0.018	0.126
980	0:54:14.68	-73:53:54.2	A5 III	17.183	0.185	0.183
986	0:54:20.91	-73:34:45.4	A7 II	15.893	0.209	0.288
1023	0:54:52.15	-73:31:44.6	B9 (II)	15.319	0.093	-0.039
1024	0:54:52.89	-72: 5:44.9	A3 II	13.808	0.205	0.108
1033	0:54:57.98	-72: 8:31.7	A0 (Ib)	13.947	0.019	0.051
1042	0:55: 3.44	-73: 3:47.7	A3 II	15.563	0.340	0.116

continued

ID	α_{2000}	δ_{2000}	SP type	V	$(B-V)$	$(V-R)$
1045	0:55: 4.26	-72:39:28.6	A7 II	14.827	0.240	0.177
1052	0:55: 6.85	-72: 9:53.6	B3 (Ib)	13.599	0.017	-0.101
1060	0:55:14.61	-72:13:52.4	A0 (II)	14.845	0.069	0.041
1068	0:55:22.83	-72:55:29.0	A2 III	15.905	0.250	0.062
1084	0:55:41.59	-72:52:49.5	A3 II	15.056	0.062	0.203
1111	0:55:57.34	-73:18: 3.7	A2 III	17.863	0.315	0.205
1134	0:56:14.75	-72:10:16.0	A5 II	15.786	0.261	0.152
1139	0:56:17.64	-72:45:31.5	A5 II	14.757	0.203	0.141
1147	0:56:27.45	-72:49:10.6	A5 II	15.126	0.229	0.184
1173	0:56:49.35	-72:45:18.5	B0.5 (IV)	14.757	-0.099	-0.103
1174	0:56:50.55	-72:14:13.1	A0 (II)	15.494	0.047	0.096
1181	0:56:55.31	-72:57:19.2	A5 II	15.791	0.356	0.090
1187	0:57: 0.81	-72: 8:10.5	B0 (III)	14.761	-0.244	0.025
1188	0:57: 3.03	-72: 7:58.8	B0 (V)	15.867	-0.174	-0.128
1198	0:57: 9.13	-72:58: 4.4	A0 (II)	15.141	0.011	0.117
1200	0:57:11.79	-72:13: 8.1	B9 (V)	16.203	0.028	0.229
1201	0:57:12.62	-72:57:50.3	A0 (II)	16.600	0.161	-0.011
1205	0:57:14.82	-72:52:18.8	A3 II	15.733	0.234	0.092
1217	0:57:20.94	-72:27:39.6	B9 (Ib)	14.044	0.058	-0.009
1232	0:57:28.18	-72:31: 3.3	B3 (II)	14.237	-0.034	-0.013
1241	0:57:37.25	-72:23:55.5	B0 (V)	15.119	-0.052	-0.147
1246	0:57:38.16	-72:32:51.5	B2 (III)	15.598	-0.005	-0.047
1260	0:57:46.53	-73: 2:51.5	B8 (III)	16.618	-0.087	-0.091
1263	0:57:47.76	-72:17:18.1	O9.5 Ib	15.315	-0.113	-0.054
1264	0:57:48.83	-72:39:40.2	B9 (Ib)	14.527	-0.004	0.146
1266	0:57:51.22	-72:36:56.7	A3 II	16.207	0.176	0.129
1268	0:57:51.27	-72:30:29.9	B2 (II)	14.639	-0.168	-0.051
1281	0:58: 1.72	-72:41:58.8	B3 (II)	14.215	-0.025	0.060
1287	0:58: 6.02	-72:53:44.5	A7 II	16.765	0.284	0.218
1293	0:58:12.40	-72:26:11.6	B0 (V)	15.276	-0.025	-0.072
1312	0:58:28.77	-72:19:18.0	A5 II	15.019	0.210	0.232
1324	0:58:35.09	-72:24:56.5	B0.5 (IV)	14.482	-0.275	-0.073
1348	0:58:52.00	-72:43:40.4	B0.5 (IV)	14.526	-0.056	-0.038
1361	0:59: 3.82	-72:45:40.8	A5 II	15.598	0.137	0.188
1367	0:59:10.45	-72:24:46.0	B8 (II)	14.393	0.031	-0.009
1369	0:59:11.75	-72:14:24.3	O9 V	15.954	-0.015	-0.094
1370	0:59:12.75	-72:24:18.5	B0 (V)	15.761	-0.037	0.161
1372	0:59:13.88	-73:33:38.5	A5 II	16.888	0.153	0.295
1374	0:59:14.79	-72:44:30.0	B9 (II)	15.895	-0.012	0.071
1378	0:59:16.59	-72:23:17.7	A0 (II)	15.113	0.057	0.220
1382	0:59:20.73	-72:14:25.8	B0 (V)	15.919	-0.202	0.024

continued

ID	α_{2000}	δ_{2000}	SP type	V	$(B-V)$	$(V-R)$
1388	0:59:25.95	-73: 9:40.2	B8 (III)	17.229	-0.054	0.153
1395	0:59:29.38	-72:55:39.6	B5 (II)	14.540	-0.094	0.022
1396	0:59:29.65	-72:47:30.2	B0.5 (V)	16.464	-0.055	-0.236
1397	0:59:30.65	-72:34:13.6	B9 (II)	15.976	-0.012	0.147
1402	0:59:34.41	-72:22:54.0	A0 (Ib)	14.533	0.121	-0.043
1425	0:59:50.42	-72:13:56.4	A0 (Ib)	14.676	0.149	-0.395
1426	0:59:50.91	-73: 4:36.0	A7 II	15.300	0.172	0.240
1430	0:59:53.83	-72:41:15.0	B0.5 (V)	15.685	-0.130	0.049
1433	0:59:56.46	-73:36:22.8	A3 III	16.734	0.107	0.357
1440	1: 0: 6.85	-72:47:18.5	O6 V	13.888	-0.100	-0.239
1442	1: 0: 8.20	-73: 1:50.3	A7 II	15.764	0.154	0.301
1474	1: 0:28.84	-73:16:35.4	A0 (II)	15.354	0.199	0.066
1477	1: 0:31.85	-72:27:31.9	A0 (II)	14.795	0.104	-0.021
1488	1: 0:36.77	-73:46:27.0	A2 II	16.199	0.147	0.038
1491	1: 0:37.14	-72:45:36.5	A0 (II)	15.039	0.083	0.013
1496	1: 0:41.73	-72:14:45.6	B0.5 (V)e	15.959	-0.165	0.211
1497	1: 0:42.18	-72:30:28.8	B0 (IV)	14.835	-0.261	0.094
1506	1: 0:45.51	-72:59:17.0	B8 (II)	14.589	0.032	0.086
1512	1: 0:48.42	-72:54:28.5	B0.5 (V)	15.838	-0.254	-0.066
1519	1: 0:56.77	-72:47:55.5	A3 II	16.378	0.132	0.002
1520	1: 0:56.87	-72:56:38.4	A7 II	16.724	0.304	0.185
1532	1: 1: 2.85	-72:39:29.6	O9.7 Iab	12.965	-0.081	-0.073
1533	1: 1: 3.06	-72:48: 9.3	A0 (II)	15.376	-0.003	0.128
1550	1: 1:15.79	-72:12:42.8	B2 (Ib)	13.175	-0.072	-0.055
1559	1: 1:19.64	-72:48:16.8	A3 II	15.042	0.095	0.054
1561	1: 1:22.85	-72:37:17.0	B0.5 (IV)	14.500	-0.192	-0.025
1570	1: 1:29.34	-73: 7: 3.7	A5 II	16.074	0.158	0.395
1571	1: 1:29.53	-73:15:55.8	B5 (III)	16.505	-0.079	0.139
1593	1: 1:46.63	-72:41:28.7	A0 (II)	16.664	0.089	0.046
1595	1: 1:47.91	-73:45:56.2	A5 II	14.116	0.113	0.013
1597	1: 1:48.77	-73:47: 8.9	B8 (II)	15.829	0.001	0.064
1606	1: 1:52.68	-72: 6: 3.7	A3 II	15.473	0.094	-0.114
1635	1: 2: 9.90	-72:35: 3.5	O9.5 III	15.385	-0.159	-0.206
1641	1: 2:12.71	-72:20:23.5	A0 (II)	15.489	0.002	-0.113
1647	1: 2:16.02	-73: 5:47.5	A0 (Ib)	14.752	0.156	0.111
1649	1: 2:17.44	-73: 8:40.0	A5 II	16.477	0.266	0.185
1660	1: 2:24.23	-72:31:15.4	B5 (II)	15.176	-0.145	0.148
1667	1: 2:31.58	-73:39:50.0	A7 II	16.130	0.248	0.352
1673	1: 2:35.51	-72:53:10.4	A5 II	16.024	0.251	0.234
1680	1: 2:38.60	-73:47:16.0	A2 III	16.982	0.139	0.304
1695	1: 2:45.64	-72:12: 5.4	B0 (III)	13.655	-0.166	-0.178

continued

ID	α_{2000}	δ_{2000}	SP type	V	$(B-V)$	$(V-R)$
1700	1: 2:46.24	-72: 9:11.2	B2 (IV)	16.232	0.064	-0.124
1714	1: 2:54.74	-72:45:51.1	B9 (II)	15.325	-0.039	0.086
1735	1: 3: 5.72	-72:29:42.1	B5 (II)	14.616	0.105	0.069
1759	1: 3:19.89	-72:26:24.5	B0 (III)	13.804	-0.029	-0.033
1766	1: 3:26.84	-72:57: 2.4	O9.5 III	13.647	-0.025	-0.122
1786	1: 3:33.86	-73:26:42.6	A3 II	15.917	0.290	0.081
1787	1: 3:34.91	-73:30:26.6	B8 (II)	14.729	0.115	-0.066
1790	1: 3:35.89	-72:17: 0.5	A7 II	13.489	0.406	0.231
1794	1: 3:36.46	-73:21:37.2	A7 II	15.401	0.200	0.320
1801	1: 3:39.51	-72:44:51.0	B8 (II)	14.092	0.068	0.067
1806	1: 3:43.45	-72:11:59.2	B9 (II)	14.480	0.069	0.016
1818	1: 3:51.70	-73:43: 9.1	A7 II	16.107	0.220	0.251
1827	1: 3:56.55	-72:41:17.5	O9 V	15.711	-0.079	-0.022
1838	1: 4: 1.56	-72:39: 5.2	A5 II	14.808	0.163	0.130
1852	1: 4: 8.21	-72:39:18.0	A0 (II)	16.529	-0.010	0.009
1855	1: 4:10.41	-72:13:56.2	A0 (Ib)	14.575	0.062	0.022
1887	1: 4:25.28	-72:49:31.0	A3 II	15.578	0.159	0.134
1896	1: 4:30.24	-72:15:53.5	A5 II	15.546	0.190	0.067
1913	1: 4:38.78	-72:43:31.4	A0 (II)	15.508	0.121	0.019
1916	1: 4:40.38	-73:35: 5.0	B9 (Ib)	14.075	0.103	0.080
1921	1: 4:46.15	-72: 5:59.1	B8 (II)	14.291	-0.017	-0.165
1936	1: 4:52.36	-73:46:60.0	A3 II	16.060	0.072	0.150
1938	1: 4:52.84	-73:18:10.8	A5 II	16.714	0.322	0.315
1953	1: 5: 0.15	-72: 6:38.0	B0.5 (IV)	14.627	-0.143	-0.220
1971	1: 5: 7.48	-72:48:18.5	O5 V((f))	14.423	-0.185	-0.063
1976	1: 5:11.13	-72:32:23.2	A2 II	14.756	0.118	0.012
1978	1: 5:11.52	-72:43:27.8	B9 (Ib)	13.402	0.069	0.129
1979	1: 5:11.56	-73:29:48.0	A3 II	16.586	0.246	0.329
1993	1: 5:16.04	-72:45:22.4	B5 (II)	14.881	-0.148	-0.117
2001	1: 5:21.08	-73:42:15.7	A3 II	15.795	0.136	0.318
2004	1: 5:22.14	-72: 8:22.0	A7 IIe?	15.525	0.401	-0.082
2005	1: 5:22.17	-72:54:44.8	A3 II	16.180	0.058	0.260
2023	1: 5:28.76	-72:29:22.4	O9.5 III	14.843	-0.281	-0.028
2024	1: 5:29.76	-73:26:19.0	A0 (II)	15.633	0.142	0.101
2025	1: 5:29.83	-72:51:40.2	B2 (III)	15.350	-0.210	-0.168
2046	1: 5:38.63	-72:21:30.9	A3 II	15.610	0.170	0.051
2051	1: 5:40.24	-73:13:46.4	A5 II	16.218	0.297	0.324
2064	1: 5:46.39	-72: 6:50.5	B0 (IV)	14.603	-0.022	-0.191
2066	1: 5:47.17	-72:36:40.3	A5 II	15.256	0.287	0.209
2082	1: 5:54.34	-72:56:52.0	B8 (II)	15.400	0.040	-0.019
2088	1: 5:55.82	-72:44:54.4	A0 (III)	17.193	0.147	0.135

continued

ID	α_{2000}	δ_{2000}	SP type	V	$(B-V)$	$(V-R)$
2093	1: 5:58.41	-73:32:24.7	A2 III	16.701	0.159	0.100
2094	1: 6: 0.38	-73:24:53.3	A0 (II)	15.891	0.008	0.078
2096	1: 6: 0.89	-72:44:41.3	B8 (II)	14.851	0.063	0.089
2099	1: 6: 2.05	-72:53:14.0	B3 (II)	14.541	-0.064	-0.015
2101	1: 6: 3.23	-73:20:23.4	A3 II	16.110	0.106	0.138
2104	1: 6: 3.39	-73:52:17.0	B8 (III)	17.554	-0.081	0.043
2120	1: 6: 9.73	-72:38:23.4	A5 II	15.455	0.319	0.259
2122	1: 6:10.43	-72:50:23.7	B3 (II)	15.308	-0.172	-0.030
2131	1: 6:13.40	-73:38:34.1	A3 II	15.569	0.079	0.227
2135	1: 6:15.57	-72:32:55.9	O9 V	15.020	-0.199	-0.023
2138	1: 6:17.35	-72:26:48.8	B9 (II)	15.546	-0.028	0.274
2141	1: 6:17.47	-73:30:19.7	B9 (III)	16.953	0.038	0.108
2146	1: 6:19.70	-73:19: 5.8	A7 II	16.093	0.307	0.413
2155	1: 6:23.37	-73:22: 4.1	A3 II	15.055	0.271	0.381
2161	1: 6:25.53	-73:43:39.7	A3 II	16.300	0.082	0.259
2165	1: 6:27.18	-73:38:26.4	B8 (III)	16.901	-0.070	0.225
2168	1: 6:27.28	-72:38: 5.6	A3 II	14.953	0.227	0.181
2170	1: 6:27.77	-72:52:47.9	B5 (II)	15.460	0.078	0.051
2173	1: 6:29.37	-72:35:59.6	A0 (II)	16.302	0.025	0.119
2179	1: 6:31.24	-72:44:56.0	A2 II	16.676	0.060	0.058
2181	1: 6:32.29	-72:34: 8.0	A3 II	15.691	0.174	0.235
2200	1: 6:40.38	-72:37:39.5	B1.5 (Ib)	13.617	-0.044	0.046
2201	1: 6:40.46	-73:10:23.6	B0.5 (Ib)	13.343	0.046	0.180
2251	1: 7: 7.03	-73: 0:20.1	A2 II	15.716	0.118	-0.062
2253	1: 7: 7.42	-73:11:10.1	O7 V	15.000	-0.180	-0.027
2255	1: 7: 7.54	-72:54: 1.5	A7 II	15.560	0.152	0.012
2290	1: 7:26.64	-73:37:43.9	A0 (II)	15.695	0.016	0.105
2300	1: 7:33.55	-73:18:37.4	B8 (III)	16.661	0.047	-0.088
2315	1: 7:39.35	-73:27: 3.9	A3 II	15.875	0.139	0.036
2327	1: 7:44.75	-73:11:24.3	A3 Ib	16.823	0.327	0.343
2333	1: 7:47.61	-73:43:22.9	A0 (II)	16.516	0.051	0.150
2353	1: 7:57.83	-73:18:31.6	A3 II	16.741	0.305	0.263
2369	1: 8: 5.57	-72: 8:42.3	A3 II	12.991	0.260	0.145
2372	1: 8: 6.80	-73:19:58.8	A2 II	15.814	0.049	0.210
2387	1: 8:13.55	-72:24:58.6	B2 (III)	15.097	-0.149	-0.160
2389	1: 8:16.20	-73: 8:55.3	B8 (III)	16.702	-0.081	0.001
2396	1: 8:19.35	-72:46:50.0	A5 II	16.568	0.274	-0.459
2416	1: 8:26.11	-72:45:38.6	A5 II	16.070	0.250	0.144
2421	1: 8:27.33	-73:21: 3.4	A7 II	16.763	0.194	0.208
2424	1: 8:29.15	-73: 9:42.5	A5 II	16.260	0.162	0.212
2447	1: 8:40.03	-73: 3:44.2	A3 II	16.357	0.083	0.029

continued

ID	α_{2000}	δ_{2000}	SP type	V	$(B-V)$	$(V-R)$
2449	1: 8:40.85	-73:40:41.4	A7 II	15.946	0.218	0.271
2451	1: 8:41.10	-72:42:22.1	A0 (II)	16.030	0.136	-0.090
2454	1: 8:41.89	-72:59: 8.6	A5 II	15.493	0.283	0.108
2457	1: 8:42.83	-72:36:56.9	B8 (II)	14.161	0.075	-0.165
2463	1: 8:46.21	-72:37:30.7	B9 (Iab)	12.466	0.017	0.080
2486	1: 8:57.00	-73: 9:11.6	B8 (III)	16.573	-0.017	0.024
2487	1: 8:57.38	-72:26: 2.5	B1.5 (II)	13.292	-0.203	-0.041
2488	1: 8:57.56	-72: 9:20.4	A7 II	15.255	0.309	0.088
2502	1: 9: 1.56	-73:29:40.7	A3 III	16.746	0.125	0.189
2512	1: 9: 5.44	-72:49:26.4	A0 (Ib)	14.239	0.147	0.116
2527	1: 9:10.64	-72:21:16.4	B5 (II)	15.352	0.151	0.442
2529	1: 9:11.92	-72:56: 4.4	A0 (II)	15.550	0.144	-0.138
2531	1: 9:12.72	-73:57:42.1	A3 II	16.214	0.349	0.194
2550	1: 9:21.28	-73:22: 0.3	A7 Iab	15.677	0.274	0.335
2563	1: 9:26.83	-72:40:53.4	A3 II	16.008	0.072	0.076
2591	1: 9:43.78	-73: 3:35.4	A0 (II)	16.573	0.000	-0.005
2596	1: 9:45.22	-72:15:16.4	A7 II	16.019	0.155	0.144
2630	1:10: 5.93	-73:44: 5.4	A0 (II)	16.429	0.040	0.161
2634	1:10: 9.80	-73:42:48.6	A7 Ib	16.497	0.263	0.297
2639	1:10:12.19	-73:36:58.3	A3 II	16.303	0.112	0.153
2650	1:10:16.20	-73:50:56.3	A3 II	15.548	0.268	0.288
2658	1:10:19.80	-72:44:25.9	B3 (III)	16.095	-0.183	-0.200
2659	1:10:19.92	-73:29:43.5	A5 II	17.002	0.170	0.159
2667	1:10:24.95	-73: 7:15.1	A0 (II)	15.221	0.048	0.055
2668	1:10:25.85	-73:36:38.8	A2 II	16.403	0.087	0.140
2688	1:10:38.37	-73:50:20.3	A7 II	15.971	0.161	0.189
2718	1:10:56.29	-73:48:13.9	A7 II	15.929	0.236	0.221
2723	1:10:59.36	-73:12:57.0	A0 (II)	17.218	0.053	0.071
2726	1:11: 2.35	-72:45:32.1	B9 (II)	15.952	-0.031	0.061
2733	1:11: 5.36	-73:45: 2.8	A0 (III)	16.693	-0.007	0.114
2738	1:11: 7.42	-73:17:28.6	A3 II	16.827	0.121	0.128
2763	1:11:21.58	-73: 1:22.1	A0 (II)	16.594	-0.005	-0.294
2769	1:11:23.94	-72:45:12.4	A0 (II)	15.278	0.159	0.058
2787	1:11:39.26	-73:12:16.0	A2 II	16.397	0.062	0.093
2798	1:11:47.89	-73:48:23.0	A3 II	16.322	0.270	0.169
2808	1:11:57.24	-73:17:34.6	A7 II	16.339	0.144	0.245
2823	1:12: 8.30	-73:44:14.9	A3 II	15.649	0.156	0.192
2826	1:12: 9.59	-73: 9:24.7	A3 II	15.100	0.164	0.162
2830	1:12:13.11	-72:54:18.3	B8 (II)	15.709	0.005	-0.102
2844	1:12:21.86	-73: 1:48.2	B3 (II)	15.174	-0.190	-0.042
2851	1:12:26.54	-73:27:22.0	B0.5 (V)	15.833	-0.234	-0.074

continued

ID	α_{2000}	δ_{2000}	SP type	V	$(B-V)$	$(V-R)$
2856	1:12:30.23	-73:48:14.4	A0 (II)	16.488	0.019	0.122
2867	1:12:38.62	-73:30:21.2	A5 II	15.782	0.125	0.222
2868	1:12:38.82	-73: 0:57.8	B8 (II)	14.339	0.134	-0.077
2877	1:12:43.89	-73:18:45.9	B2 (III)	15.330	-0.134	-0.004
2883	1:12:46.70	-73:17:49.6	B2 (III)	15.343	-0.140	0.000
2931	1:13:19.18	-73:52:22.9	A2 III	16.830	0.115	0.144
2937	1:13:22.27	-73:24: 6.4	B3 (II)	15.041	-0.124	0.050
2947	1:13:30.21	-73: 8:33.2	A0 (II)	16.734	0.018	0.199
2956	1:13:39.74	-73:47:25.1	A0 (II)	16.305	0.012	0.079
2995	1:14:16.06	-73:11:53.0	B2.5 (III)	15.223	-0.213	0.027
2998	1:14:17.30	-73:13: 0.9	O9.5 III	15.428	-0.102	0.040
3002	1:14:21.02	-73:54:25.8	A0 (II)	16.121	0.256	0.111
3004	1:14:22.43	-73:38:34.8	A7 II	14.731	0.151	0.203
3023	1:14:34.77	-73:16:49.1	O9.5 III	16.183	-0.249	-0.007
3034	1:14:45.92	-73:13:38.2	B2.5 (IV)	16.415	-0.037	0.082
3060	1:14:59.82	-73:53:48.3	A0 (II)	15.872	0.174	0.131
3069	1:15: 5.80	-73:55:28.7	A0 (II)	15.662	0.034	0.089
3075	1:15:12.89	-73:24:41.9	B0 (IV)	14.842	-0.225	-0.022
3079	1:15:14.69	-73:28:45.8	B0 (III)e	14.169	-0.110	0.231
3083	1:15:16.89	-73: 9:48.9	B0.5 (V)	16.018	-0.239	-0.044
3097	1:15:30.09	-73:20:15.7	O8 V	14.607	-0.206	-0.024
3103	1:15:31.68	-73:14:59.4	B0 (V)	15.305	-0.271	-0.039
3106	1:15:33.77	-73:16:12.6	O9 V	15.425	-0.245	-0.030
3107	1:15:33.91	-73:11:36.2	B0 (IV)	14.550	-0.239	0.003
3120	1:15:40.50	-73:17:50.5	B0 (V)	15.045	-0.239	-0.019
3134	1:15:46.76	-73:21:44.9	B3 (II)	14.180	-0.144	0.003
3153	1:15:58.68	-73:22:45.9	B0 (V)	15.802	-0.236	-0.029
3158	1:16: 1.10	-73:20: 5.4	O9.5 V	15.254	-0.174	-0.098
3199	1:16:33.22	-73:20: 7.7	O9 V	13.881	-0.221	-0.028
3206	1:16:39.87	-73:40:25.1	A3 II	15.535	0.142	0.199
3210	1:16:42.97	-73:27: 6.3	A5 II	14.528	0.156	0.187
3213	1:16:44.14	-73:16:52.8	B2 (IV)	16.421	-0.179	-0.022
3220	1:16:52.20	-73:14:52.1	A0 (II)	15.255	0.067	0.132
3222	1:16:53.99	-73: 8:51.2	O9.5 V	15.812	-0.157	-0.064
3227	1:16:58.42	-73:16:36.5	B0.5 (V)	16.328	-0.219	-0.019
3241	1:17:13.04	-72:51:13.2	A0 (II)	15.626	0.091	0.021
3246	1:17:15.63	-74: 4:55.1	A0 (II)	15.447	0.098	-0.004
3258	1:17:23.72	-74: 0: 4.8	A0 (II)	16.401	0.041	0.020
3261	1:17:24.64	-73: 7:21.4	B2.5 (IV)	16.037	-0.121	0.031
3281	1:17:51.79	-72:31:21.8	A5 Ib	16.822	0.229	0.156
3302	1:18: 3.64	-72:58:50.5	B8 (III)	17.131	0.018	0.026

continued

ID	α_{2000}	δ_{2000}	SP type	V	$(B-V)$	$(V-R)$
3308	1:18: 7.50	-72:49: 3.5	A3 III	16.416	0.143	0.126
3309	1:18:10.79	-74: 1:53.2	B9 (II)	15.108	0.108	0.013
3328	1:18:23.42	-73:14:25.3	B2 (III)	15.177	-0.033	-0.088
3335	1:18:28.67	-72:47:11.4	A5 II	15.575	0.224	0.106
3337	1:18:29.60	-73:31:11.8	B9 (Iab)	12.908	0.005	0.164
3339	1:18:29.79	-73:35:25.5	B0.5 (V)	15.349	-0.070	0.021
3344	1:18:37.50	-72:38:38.5	B8 (II)e	16.446	-0.054	0.021
3349	1:18:47.11	-73: 0:23.2	A0 (II)	16.015	0.072	0.040
3351	1:18:49.15	-72:57:29.3	A2 II	16.569	0.147	0.095
3359	1:18:54.76	-72:56:23.8	A0 (II)	15.586	0.127	0.141
3363	1:18:59.12	-73:23:12.2	B3 (III)	16.551	-0.067	-0.007
3368	1:19: 3.47	-73:16:51.0	B2 (III)	15.588	-0.091	-0.013
3377	1:19:11.24	-73: 2:56.1	B2.5 (III)	15.357	0.005	-0.121
3378	1:19:11.27	-72:30:22.4	A0 (II)	16.144	-0.003	0.071
3392	1:19:22.53	-73:20:12.3	B5 (II)	14.885	0.016	0.046
3411	1:19:39.88	-73:14:49.9	O9 V	14.770	-0.136	-0.038
3413	1:19:41.09	-73:10:13.1	B5 (II)e	15.084	-0.027	0.060
3437	1:20: 6.21	-72:32: 7.8	B3 (Ib)	13.304	-0.094	-0.003
3443	1:20:11.84	-73:45:39.2	A3 II	15.489	0.072	0.063
3444	1:20:13.43	-73:22:13.7	A2 II	14.551	0.190	0.079
3451	1:20:19.87	-72:49:23.9	A0 (II)	15.575	0.070	0.076
3453	1:20:21.11	-73:14:20.9	B0.5 (V)	15.985	-0.161	-0.042
3456	1:20:25.05	-73: 6: 3.0	B5 (Ib)	13.315	0.035	-0.012
3458	1:20:30.47	-74: 7:36.2	A3 II	14.427	0.107	0.088
3477	1:20:45.91	-73: 1:33.3	A3 II	15.818	0.126	0.075
3489	1:20:57.18	-73:13:52.2	B2.5 (Ib)e	14.283	0.000	0.093
3496	1:21: 2.04	-72:43:36.9	B0.5 (V)	15.428	-0.251	-0.089
3502	1:21: 8.15	-73:38:48.3	B2 (IV)	16.115	-0.104	-0.020
3503	1:21: 9.43	-73:37:33.8	B5 (II)	14.763	-0.062	0.018
3507	1:21:15.59	-73: 6:17.1	B0 (V)	15.018	-0.149	-0.129
3512	1:21:24.84	-73:22:26.2	B3 (II)e	15.117	-0.094	0.012
3516	1:21:28.52	-73:49:42.9	A2 II	13.560	0.089	0.018
3522	1:21:31.67	-73:44:59.9	B9 (II)	14.956	-0.045	-0.016
3523	1:21:31.97	-72:56:48.8	A0 (Ib)	14.572	0.029	0.055
3526	1:21:36.64	-72:49:37.3	A3 II	15.102	0.142	0.150
3543	1:21:51.61	-73:33:40.8	A0 (II)	16.182	0.079	0.097
3545	1:21:53.60	-73: 2:18.3	A3 II	15.903	0.149	0.169
3554	1:22:15.14	-72:46:19.7	B0 (V)	15.101	-0.240	-0.090
3566	1:22:25.81	-73:11:57.1	B2 (IV)	16.306	-0.045	0.011
3594	1:22:53.12	-72:25:44.3	A3 II	14.805	0.133	0.142
3602	1:23: 1.71	-72:34:23.5	A3 II	13.200	0.165	0.161

continued

ID	α_{2000}	δ_{2000}	SP type	V	$(B-V)$	$(V-R)$
3603	1:23: 2.47	-73:28:50.2	B2 (IV)e?	16.197	-0.062	0.042
3612	1:23:13.94	-73:24: 9.4	B0.5 (V)	15.175	-0.164	-0.012
3613	1:23:14.31	-73: 8:56.8	B9 (II)	16.841	-0.003	0.061
3617	1:23:21.17	-73:49:51.2	O8 V	14.312	-0.217	-0.097
3622	1:23:26.78	-73:29:33.8	A7 II	15.434	0.273	0.201
3625	1:23:27.62	-74:12:59.8	A0 (II)	17.247	-0.005	0.029
3630	1:23:34.27	-73:44:18.5	B5 (II)	14.764	-0.045	-0.005
3632	1:23:36.96	-73:28:56.2	B2.5 (II)	14.657	-0.115	-0.016
3638	1:23:40.11	-72:56:58.0	B0 (V)	15.647	-0.198	-0.082
3650	1:23:49.55	-73:48:24.6	A7 II	16.687	0.202	0.139
3651	1:23:52.23	-73:15:38.2	A7 II	16.030	0.284	0.222
3652	1:23:53.09	-72:44:57.9	B3 (III)	16.058	-0.160	0.002
3660	1:24: 3.05	-73:26:33.0	B2.5 (III)	15.516	-0.109	-0.023
3661	1:24: 3.31	-73:12: 7.6	B0.5 (V)	15.650	-0.164	-0.047
3664	1:24: 7.12	-73:15:28.2	O9.5 III	14.566	-0.185	0.000
3668	1:24:10.10	-72:49:39.5	A7 II	14.600	0.246	0.099
3671	1:24:10.72	-73:30:43.6	A5 II	14.450	0.274	0.194
3675	1:24:14.20	-73:57:39.8	B3 (Ib)	13.425	-0.103	-0.039
3677	1:24:20.78	-73:58:11.9	A0 (Ib)	13.480	0.038	0.017
3681	1:24:22.87	-72:42:48.1	B0 (IV)e	14.818	-0.041	0.102
3693	1:24:34.45	-73:27:31.3	B3 (II)	14.571	-0.107	-0.011
3694	1:24:34.46	-73: 9: 8.8	B2 (II)	14.102	-0.122	-0.102
3700	1:24:42.75	-73: 9: 3.3	O9 V	15.336	-0.184	-0.050
3704	1:24:47.45	-72:44:28.0	B2.5 (V)	17.210	-0.194	-0.083
3709	1:24:50.51	-73:14:39.1	B0 (V)	15.730	-0.188	-0.059
3710	1:24:50.54	-73:19: 5.4	B0.5 (V)	15.882	-0.143	-0.113
3712	1:24:51.29	-73:27: 1.9	O9 III	14.573	-0.173	-0.042
3725	1:24:59.26	-73:26:47.7	B5 (III)e?	16.438	-0.041	0.117
3732	1:25:17.02	-73:38:29.2	B9 (Iab)	13.553	0.035	0.085
3734	1:25:18.72	-72:59:15.6	A0 (II)	16.709	0.125	0.118
3735	1:25:19.68	-73:17:11.6	O9 V	15.434	-0.209	-0.033
3738	1:25:24.39	-73:39:36.5	A0 (II)	14.149	0.239	0.265
3739	1:25:24.63	-73:15:17.1	B0.5 (V)	16.340	-0.212	-0.056
3742	1:25:28.53	-73:24:15.4	O9 V	15.349	-0.176	-0.023
3755	1:25:47.81	-73: 8:38.2	B9 (II)	15.904	0.100	-0.035
3767	1:26:13.37	-73:23:35.3	A5 II	13.927	0.228	0.185
3773	1:26:24.48	-72:42:28.1	A2 III	17.115	0.139	0.155
3780	1:26:35.34	-73:15:15.9	O9.5 III	14.542	-0.043	-0.004
3781	1:26:37.69	-73:29:33.0	B0 (IV)e	15.148	-0.035	0.065
3783	1:26:41.68	-73:11:52.6	A0 (Ib)	14.156	0.100	0.119
3813	1:27:27.88	-73:51:30.8	A3 II	13.985	0.102	0.115

continued

ID	α_{2000}	δ_{2000}	SP type	V	$(B-V)$	$(V-R)$
3814	1:27:28.61	-72:49:49.0	B9 (Ib)	14.634	0.013	0.004
3825	1:27:39.32	-72:42:46.6	B0 (IV)e	15.299	-0.116	0.042
3839	1:27:57.70	-73:10:14.3	B0.5 (V)	15.243	-0.170	-0.046
3842	1:28: 7.84	-73:30:53.3	B3 (III)	16.084	-0.043	-0.041
3843	1:28: 8.44	-73:40:12.3	B8 (II)	14.461	0.028	0.044
3850	1:28:15.43	-73:14:42.8	B9 (II)	15.870	0.050	0.082
3868	1:28:35.50	-72:36:38.8	B0.5 (V)	16.298	-0.213	-0.055
3877	1:28:47.71	-73:18:22.3	B0 (V)	14.859	-0.202	-0.080
3880	1:28:49.86	-73:22:54.7	B2 (III)	15.525	-0.112	-0.043
3906	1:29:24.17	-73:29:41.5	B2.5 (II)	14.435	-0.107	-0.014
3932	1:30:13.42	-73:25:45.2	B0.5 (IV)	14.709	-0.085	-0.086
3946	1:30:32.32	-73:43:21.5	B8 (II)	15.229	-0.034	0.017
3954	1:30:43.20	-73:25: 3.8	O7 V	15.096	-0.263	-0.086
3968	1:31:18.99	-74: 0:21.4	A5 II	14.139	0.147	0.138
3976	1:31:30.10	-73:21:37.3	O9.5 V	14.871	-0.262	-0.072
3982	1:31:42.49	-73:19: 9.8	A5 II	14.418	0.104	0.136
3987	1:31:57.73	-73:16:17.4	B0.5 (V)	16.188	-0.252	-0.072
4005	1:33:33.03	-73:33: 1.7	B0.5 (IV)	14.036	-0.102	0.048
4007	1:33:43.33	-73:24:34.3	B8 (II)	15.809	-0.059	0.039
4034	1:36:53.82	-73:42:51.2	B8 (II)	13.923	-0.070	0.029
4037	1:37:12.54	-72:48:26.5	B9 (II)	14.114	0.000	0.059
4039	1:37:13.32	-73:23:12.4	A0 (II)	16.381	0.001	0.080
4040	1:37:17.12	-73:26:40.3	B5 (II)	14.798	-0.130	0.033
4042	1:37:27.01	-73:45:46.5	B5 (II)	15.278	-0.060	0.044
4045	1:38: 1.61	-73:40:47.0	A0 (II)	15.537	0.015	0.067
4048	1:39:12.86	-73:22:56.3	A0 (II)	14.485	-0.001	0.083
5017	0:47:55.47	-73: 1:11.8	B8 (II)	14.279	0.031	0.038
5041	0:50:39.96	-72:59:43.1	O8 V	14.470	-0.116	0.039
5046	0:51: 8.72	-72:56:23.6	B0 (V)e?	15.076	-0.037	0.032
5048	0:51:28.04	-73: 1: 1.3	B5 (II)	13.829	0.053	0.072
5057	0:52:27.52	-72:33:11.1	B9 (Iab)	12.788	-0.015	0.060
5062	0:52:53.47	-72:55:31.7	O8.5 V	14.894	-0.219	0.035
5063	0:53: 4.96	-72:52:18.8	A0 (Ib)	13.137	0.014	0.025
5090	0:56:20.79	-72:28:33.8	B2.5 (Ib)	13.067	-0.037	0.008
5096	0:57:32.53	-72:28:50.9	B0 (IV)	14.346	-0.118	-0.163
5101	0:59:52.80	-72:19: 3.3	B9 (Ia)	12.640	0.259	0.213
5102	0:59:54.88	-72:13: 6.0	B9 (Ib)	13.365	0.015	0.122
5105	1: 2:13.18	-72: 5:48.5	B0 (V)	15.229	-0.142	-0.101

Bibliography

Alcaino, G., Alvarado, F., Borissova, J. and Kurtev, R., 2003, *A&A*, **400**, 917

Allen, C., 1973, *Astrophysical Quantities* (Athlone Press., London)

Anderson, E., 1989, *An Introductory User's Guide to IRAF Scripts*, Central Computer Services, NOAO, IRAF Manual

Arp, H., 1962, in McVittie, G. C. (ed.), *Problems of Extra-Galactic Research*, IAU Symposium 15, p. 42

Auer, L. H. and Mihalas, D., 1969, *ApJ*, **158**, 641

Auer, L. H. and Mihalas, D., 1972, *ApJSS*, **24**, 193

Azzopardi, M. and Vigneau, J., 1975, *A&AS*, **22**, 285

Azzopardi, M. and Vigneau, J., 1982, *A&AS*, **50**, 291

Bahcall, J. N. and Soneira, R. M., 1980, *ApJSS*, **44**, 73

Balona, L. A., 1994, *MNRAS*, **268**, 119

Bertin, E. and Arnouts, S., 1996, *A&AS*, **117**, 393

Bessell, M. S., 1983, *PASP*, **95**, 480

Bessell, M. S., 1990, *PASP*, **102**, 1181

Bessell, M. S., 1995, *PASP*, **107**, 672

Bessell, M. S., Castelli, F. and Plez, B., 1998, *A&A*, **333**, 231

Binney, J. and Merrifield, M., 1998, *Galactic Astronomy* (Princeton University Press, New Jersey)

Castelli, F. and Kurucz, R. L., 1994, *A&A*, **281**, 817

Charbonnel, C., Meynet, G., Maeder, A., Schaller, G. and Schaerer, D., 1993, *A&AS*, **101**, 415

Chlebowski, T. and Garmany, C. D., 1991, *ApJ*, **368**, 241

Conti, P. S., Garmany, C. D., de Loore, C. and Vanbevern, D., 1983, *ApJ*, **274**, 302

Cousins, A. W. J., 1980, *SAAOC*, **1**, 234

Crawford, D. L., 1966, in Lodén, K., Lodén, O., Sinnerstad, U. (ed.), *Spectral Classification and Multicolour Photometry*, IAU Symposium 24, p. 170

Elias, J. H., Frogel, J. A., Matthews, K. and Neugebauer, G., 1982, *AJ*, **87**, 1029

Elmegreen, B. G., 2004, *MNRAS*, **354**, 367

Evans, C. J., 2001, *PhD thesis* (University of London)

Evans, C. J., Howarth, I. D., Irwin, M. J., Burnley, A. W. and Harries, T. J., 2004, *MNRAS*, **353**, 601

Feast, M. W., Thackeray, A. D. and Wesselink, A. J., 1960, *MNRAS*, **121**, 337

Figer, D. F., 2005, *Nature*, **434**, 192

Fitzgerald, M. P., 1970, *A&A*, **4**, 234

Flower, P. J., 1977, *A&A*, **54**, 31

Flower, P. J., 1996, *ApJ*, **469**, 355

Gardiner, L. T. and Hatzidimitriou, D., 1992, *MNRAS*, **257**, 195

Garmany, C. D., Conti, P. S. and Chiosi, C., 1982, *ApJ*, **263**, 777

Gilmore, G. and Howell, D., 1998, *The Stellar Initial Mass Fuction, 38th Herstmonceux Conference* (A.S.P Conference Series, Vol. 142)

Gould, A., Bahcall, J. N. and Flynn, C., 1997, *ApJ*, **482**, 913

Grieve, G. R. and Madore, B. F., 1986, *ApJSS*, **62**, 427

Gullixson, C. A., 1992, in Howell, S. B. (ed.), *Astronomical CCD observing and Reduction Techniques*, ASP Conference Series Vol. 23, p. 130

Harries, T. J., Hilditch, R. W. and Howarth, I. D., 2003, *MNRAS*, **339**, 157

Harris, J. and Zaritsky, D., 2004, *AJ*, **127**, 1531

Henden, A. A. and Kaitchuck, R. H., 1982, *Astronomical Photometry* (van Nostrand Reinhold)

Hernandez, X., Valls-Gabaud, D. and Gilmore, G., 1999, *MNRAS*, **304**, 705

Hernandez, X., Valls-Gabaud, D. and Gilmore, G., 2000*a*, *MNRAS*, **316**, 605

Hernandez, X., Valls-Gabaud, D. and Gilmore, G., 2000*b*, *MNRAS*, **317**, 831

Hilditch, R. W., 2001, *An Introduction to Close Binary Stars* (Cambridge University Press)

Hilditch, R. W., Howarth, I. D. and Harries, T. J., 2005, *MNRAS*, **357**, 304

Hill, R. J., Madore, B. F. and Freedman, W. L., 1994*a*, *ApJSS*, **91**, 583

Hill, R. J., Madore, B. F. and Freedman, W. L., 1994*b*, *ApJ*, **429**, 192

Hill, R. J., Madore, B. F. and Freedman, W. L., 1994*c*, *ApJ*, **429**, 204

Hodge, P., 1986, *PASP*, **98**, 1113

Howarth, I. D., 1983, *MNRAS*, **203**, 301

Howarth, I. D., 2004, *private commuication*

Howarth, I. D. and Prinja, R. K., 1989, *ApJSS*, **69**, 527

Hubeny, I. and Lanz, T., 1995, *ApJ*, **439**, 875

Humphreys, R. M., 1983, *ApJ*, **265**, 176

Humphreys, R. M. and McElroy, D. B., 1984, *ApJ*, **284**, 565

Iben, I. J., 1965, *ApJ*, **141**, 993

Jacoby, G. H., Walker, A. R. and Ciardullo, R., 1990, *ApJ*, **365**, 471

Johnson, H. L., 1966, *AR&AA*, **4**, 193

Johnson, H. L. and Morgan, W. W., 1953, *ApJ*, **117**, 313

Johnson, H. L. and Sandage, A. R., 1956, *ApJ*, **124**, 379

Kahn, F. D., 1974, *A&A*, **37**, 149

Kennicutt, R. C. J., 1998, in Gilmore, G. and Howell, D. (ed.), *The Stellar Initial Mass Function, 38th Herstmonceux Conference*, ASP Conference Series Vol. 142, p. 1

Kilkenny, D., van Wyk, F., Roberts, G., Marang, F. and Cooper, D., 1998, *MNRAS*, **294**, 93

Kitchin, C. R., 2003, *Astrophysical Techniques* (Institute of Physics Publishing Bristol and Philadelphia)

Koornneef, J., 1983, *A&A*, **128**, 84

Kroupa, P., 2001, *MNRAS*, **322**, 231

Kroupa, P., Tout, C. A. and Gilmore, G., 1993, *MNRAS*, **262**, 545

Kurucz, R. L., 1979, *ApJSS*, **40**, 1

Kurucz, R. L., 1992, in Barbuy, B. and Renzini, A. (ed.), *The Stellar Populations of Galaxies*, IAU symp. 149, p. 225

Landolt, A. U., 1983, *AJ*, **88**, 439

Landolt, A. U., 1992, *AJ*, **104**, 340

Laney, C. D. and Stobie, R. S., 1986, *MNRAS*, **222**, 449

Lanz, T. and Hubeny, I., 2003, *ApJSS*, **146**, 417

Larsen, S. S., Clausen, J. V. and Storm, J., 2000, *A&A*, **364**, 455

Leach, R. W., Beale, F. L. and Eriksen, J. E., 1998, *SPIE*, **3355**, 512

Lequeux, J., Peimbert, M., Rayo, J. F., Serrano, A. and Torres-Peimbert, S., 1979, *A&A*, **80**, 155

Maeder, A. and Meynet, G., 1988, *A&AS*, **76**, 411

Maeder, A. and Meynet, G., 2001, *A&A*, **373**, 555

Maeder, A. and Meynet, G., 2003, *A&A*, **411**, 543

Maeder, A. and Meynet, G., 2004, *A&A*, **422**, 225

Martins, F., Schaerer, D. and Hiller, D. J., 2002, *A&A*, **382**, 999

Martins, F., Schaerer, D. and Hiller, D. J., 2005, *A&A*, **astro-ph/0503346**

Massey, P., 1997, *A User's Guide to CCD Reductions with IRAF*, NOAO, IRAF Manual

Massey, P., 2002, *ApJSS*, **141**, 81

Massey, P., Armandroff, T. E., Pyke, R., Patel, K. and Wilson, C. D., 1995*a*, *AJ*, **110**, 271

Massey, P. and Davis, L. E., 1992, *A User's Guide to Stellar CCD Photometry with IRAF*, NOAO, IRAF Manual

Massey, P. and Hunter, D., 1998, *ApJ*, **493**, 180

Massey, P. and Jacoby, G. H., 1992, in Howell, S. B. (ed.), *Astronomical CCD observing and Reduction Techniques*, ASP Conference Series Vol. 23, p. 240

Massey, P., Johnson, K. E. and DeGioia-Eastwood, K., 1995*b*, *ApJ*, **454**, 151

Massey, P., Lang, C. C., DeGioia-Eastwood, K. and Garmany, C. D., 1995*c*, *ApJ*, **438**, 188

McClure, R. D. and van den Bergh, S., 1968, *ApJ*, **73**, 313

McNamara, D. H. and Feltz, K. A. J., 1980, *PASP*, **92**, 578

Menzies, J. W., Cousins, A. W. J., Banfield, R. M. and Laing, J. D., 1989, *SAAOC*, **13**, 1

Menzies, J. W., Marang, F., Laing, J. D., Coulson, I. M. and Engelbrecht, C. A., 1991, *MNRAS*, **248**, 642

Méra, D., Chabrier, G. and Baraffe, I., 1996, *ApJ*, **459**, L87

Meynet, G. and Maeder, A., 1997, *A&AS*, **321**, 465

Meynet, G., Maeder, A., Schaller, G. and Charbonnel, C., 1994, *A&AS*, **103**, 97

Mihalas, D., 1970, *Stellar Atmospheres* (W.H. Freeman and Company, San Francisco)

Miller, G. E. and Scalo, J. M., 1979, *ApJSS*, **41**, 513

Mink, D. J., 1996, *ADASS*, **101**, 96

Mink, D. J., 1997, *ADASS*, **125**, 249

Mink, D. J., 1999, *ADASS*, **172**, 498

Mokiem, M. R., Martín-Hernández, N. L., Lenorzer, A., de Koter, A. d. and Tielens, A. G. G. M., 2004, *A&A*, **419**, 319

Olszewski, E. W., Suntzeff, N. B. and Mateo, M., 1996, *AR&AA*, **34**, 511

Pagel, B. E. J. and Tautvaišienė, G., 1998, *MNRAS*, **299**, 535

Palmer, J. and Davenhall, A. C., 1999, *The CCD Photometric Calibration Cookbook*, Starlink Project, PPARC, Starlink Cookbook 6.3

Phelps, R. L. and Janes, K. A., 1993, *AJ*, **106**, 1870

Philips, A. C., 1999, *The Physics of Stars* (Wiley)

Press, W. H., Teukolsky, S. A., Vetterling, W. T. and Flannery, B. P., 1992, *Numerical Recipes in Fortran* (Cambridge University Press)

Reid, I. N. and Gizis, J. E., 1997, *AJ*, **113**, 2246

Sagar, R. and Richtler, T., 1991, *A&A*, **250**, 324

Salpeter, E. E., 1955, *ApJ*, **121**, 161

Scalo, J. M., 1986, *Fund. Cosmic Phys.*, **11**, 1

Scalo, J. M., 1998, in Gilmore, G. and Howell, D. (ed.), *The Stellar Initial Mass Function, 38th Herstmonceux Conference*, ASP Conference Series Vol. 142, p. 201

Schaerer, D., Charbonnel, C., Meynet, G., Maeder, A. and Schaller, G., 1993*a*, *A&AS*, **102**, 339

Schaerer, D., Meynet, G., Maeder, A. and Schaller, G., 1993*b*, *A&AS*, **98**, 523

Schaller, G., Schaerer, D. Meynet, G. and Maeder, A., 1992, *A&AS*, **96**, 269

Schmidt-Kaler, T., 1982, in Schaifers, K. and Vogit, H. H. (ed.), *Londolt-Bornstein, Group VI*, volume 2b of *Numerical data and Functional Relationships in Science and Technology*, p. 1

Schönberg, M. and Chandrasekhar, S., 1942, *ApJ*, **96**, 161

Schultz, G. V. and Wiemer, W., 1975, *A&A*, **43**, 133

Shields, G. A. and Tinsley, B. M., 1976, *ApJ*, **203**, 66

Shobbrook, J. and Shobbrook, B., 2001, *40-INCH TELESCOPE (WFI) DIY MANUAL*, Mount Stromlo Observatory, Research School of Astronomy and Astrophysics, Internal Report

Sneden, C., Gehrz, R. D., Hackwell, J. A., York, D. G. and Snow, T. P., 1978, *ApJ*, **223**, 168

Stetson, P. B., 1987, *PASP*, **99**, 191

Stetson, P. B., 1991, in James, K. A. (ed.), *The Formation and Evolution of Star Clusters*, ASP Conference Series Vol. 13, p. 88

Stetson, P. B. and Harris, W. E., 1988, *AJ*, **96**, 909

Strömgren, B., 1963, in Strand, K. AA. (ed.), *Basic Astronomical Data* (University Chicago Press), p. 123

Strömgren, B., 1966, *AR&AA*, **4**, 433

Stryker, L. L., Da Costa, G. S. and Mould, J. R., 1985, *ApJ*, **298**, 544

Subramaniam, A. and Sagar, R., 1995, *A&A*, **297**, 695

Sung, H. K., 1995, *PhD thesis* (Seoul National University)

Tolstoy, E. and Saha, A., 1996, *ApJ*, **462**, 672

Udalski, A., Szymański, M., Kubiak, M., Pietrzyński, G., Woźniak, P. and Żebruń, K., 1998, *Acta Astron*, **48**, 147

Urban, S., Corbin, T. and Wycoff, G., 1997, *AAS*, **29**, 1306

Vacca, W. D., Garnany, C. D. and Shull, J. M., 1996, *ApJ*, **460**, 914

Valdes, F. G., 2002, in Gupta, R., Singh, H. P. and Bailer-Jones, C. A. L. (eds.), *Automated Data Analysis in Astronomy*, Narosa Publishing, p. 309

van den Bergh, S., 2000, *The Gallaxies of the Local Group* (Cambridge University Press.)

Wells, L. A., 1994, *Photometry using IRAF*, IRAF programming Group, NOAO, IRAF Manual

Westerlund, B. E., 1997, *The Magellanic Clouds* (Cambridge University Press)

Zaritsky, D., Harris, J., Thompson, I. B., Grebel, E. K. and Massey, P., 2002, *AJ*, **123**, 855